NUMERICAL METHODS AND COMPUTATIONAL SCIENCES APPLIED TO NUCLEAR ENERGY

EDITED BY: Yue Jin, Jun Wang, Haomin Yuan, Fulvio Mascari and Shripad T. Revankar

PUBLISHED IN: Frontiers in Energy Research

frontiers Research Topics

frontiers

Frontiers eBook Copyright Statement

The copyright in the text of individual articles in this eBook is the property of their respective authors or their respective institutions or funders. The copyright in graphics and images within each article may be subject to copyright of other parties. In both cases this is subject to a license granted to Frontiers.

The compilation of articles constituting this eBook is the property of Frontiers.

Each article within this eBook, and the eBook itself, are published under the most recent version of the Creative Commons CC-BY licence. The version current at the date of publication of this eBook is CC-BY 4.0. If the CC-BY licence is updated, the licence granted by Frontiers is automatically updated to the new version.

When exercising any right under the CC-BY licence, Frontiers must be attributed as the original publisher of the article or eBook, as applicable.

Authors have the responsibility of ensuring that any graphics or other materials which are the property of others may be included in the CC-BY licence, but this should be checked before relying on the CC-BY licence to reproduce those materials. Any copyright notices relating to those materials must be complied with.

Copyright and source acknowledgement notices may not be removed and must be displayed in any copy, derivative work or partial copy which includes the elements in question.

All copyright, and all rights therein, are protected by national and international copyright laws. The above represents a summary only. For further information please read Frontiers' Conditions for Website Use and Copyright Statement, and the applicable CC-BY licence.

ISSN 1664-8714
ISBN 978-2-83250-518-2
DOI 10.3389/978-2-83250-518-2

About Frontiers

Frontiers is more than just an open-access publisher of scholarly articles: it is a pioneering approach to the world of academia, radically improving the way scholarly research is managed. The grand vision of Frontiers is a world where all people have an equal opportunity to seek, share and generate knowledge. Frontiers provides immediate and permanent online open access to all its publications, but this alone is not enough to realize our grand goals.

Frontiers Journal Series

The Frontiers Journal Series is a multi-tier and interdisciplinary set of open-access, online journals, promising a paradigm shift from the current review, selection and dissemination processes in academic publishing. All Frontiers journals are driven by researchers for researchers; therefore, they constitute a service to the scholarly community. At the same time, the Frontiers Journal Series operates on a revolutionary invention, the tiered publishing system, initially addressing specific communities of scholars, and gradually climbing up to broader public understanding, thus serving the interests of the lay society, too.

Dedication to Quality

Each Frontiers article is a landmark of the highest quality, thanks to genuinely collaborative interactions between authors and review editors, who include some of the world's best academicians. Research must be certified by peers before entering a stream of knowledge that may eventually reach the public - and shape society; therefore, Frontiers only applies the most rigorous and unbiased reviews.
Frontiers revolutionizes research publishing by freely delivering the most outstanding research, evaluated with no bias from both the academic and social point of view. By applying the most advanced information technologies, Frontiers is catapulting scholarly publishing into a new generation.

What are Frontiers Research Topics?

Frontiers Research Topics are very popular trademarks of the Frontiers Journals Series: they are collections of at least ten articles, all centered on a particular subject. With their unique mix of varied contributions from Original Research to Review Articles, Frontiers Research Topics unify the most influential researchers, the latest key findings and historical advances in a hot research area! Find out more on how to host your own Frontiers Research Topic or contribute to one as an author by contacting the Frontiers Editorial Office: frontiersin.org/about/contact

NUMERICAL METHODS AND COMPUTATIONAL SCIENCES APPLIED TO NUCLEAR ENERGY

Topic Editors:
Yue Jin, Massachusetts Institute of Technology, United States
Jun Wang, University of Wisconsin-Madison, United States
Haomin Yuan, Argonne National Laboratory (DOE), United States
Fulvio Mascari, ENEA Bologna Research Centre, Italy
Shripad T. Revankar, Purdue University, United States

Citation: Jin, Y., Wang, J., Yuan, H., Mascari, F., Revankar, S. T., eds. (2022). Numerical Methods and Computational Sciences Applied to Nuclear Energy. Lausanne: Frontiers Media SA. doi: 10.3389/978-2-83250-518-2

Table of Contents

04 ***Validation of Doppler Temperature Coefficients and Assembly Power Distribution for the Lattice Code KYLIN V2.0.***
Lei Jichong, Xie Jinsen, Chen Zhenping, Yu Tao, Yang Chao, Zhang Bin, Zhao Chen, Li Xiangyang, Wu Jiebo, Zhang Huajian and Deng Nianbiao

12 ***Numerical Study on the Effect of Jet Cross Section Shape on the Corium Jet Breakup Behavior With Lattice Boltzmann Method***
Hui Cheng, Songbai Cheng and Jun Wang

22 ***Vessel Failure Analysis of a Boiling Water Reactor During a Severe Accident***
H. D. Wang, Y. L. Chen and W. Villanueva

38 ***Effects of Matrix Creep Properties on Effective Irradiation Swelling of U-10Mo/Zr Dispersion Nuclear Fuels***
Yong Li, Jing Zhang, Xiaobin Jian, Feng Yan, Shurong Ding and Yuanming Li

52 ***Pin-by-Pin Coupled Transient Monte Carlo Analysis Using the iMC Code***
HyeonTae Kim and Yonghee Kim

66 ***Mechanical Feasibility Analysis of the Surface Microstructure to Be Used in the Nuclear Reactor***
Shan Huang, Ti Yue, Pan Yuan, Fawen Zhu, Haoyu Wang, Menglong Liu, Chunlan Huang, Hua Li and Yun Li

76 ***Investigation of Nodal Numerical Adjoints From CMFD-Based Acceleration Methods***
Taesuk Oh and Yonghee Kim

88 ***Scalability of Nek5000 on High-Performance Computing Clusters Toward Direct Numerical Simulation of Molten Pool Convection***
Boshen Bian, Jing Gong and Walter Villanueva

98 ***Improved Radiation Heat Transfer Model in RELAP5 for Compact Fuel Rod Bundles by the Absorption Factor Modification***
Qian Sun, Yu Ji and Jun Sun

110 ***An Improved Model of the Heat Pipe Based on the Network Method Applied on a Heat Pipe Cooled Reactor***
Yuchuan Guo, Zilin Su, Zeguang Li, Kan Wang and Xuanyi Liu

126 ***An iDTMC-Based Monte Carlo Depletion of a 3D SMR With Intra-Pin Flux Renormalization***
Inhyung Kim, Inyup Kim and Yonghee Kim

139 ***Numerical Investigation of Heat Transfer Characteristics of Moderator Assembly Employed in a Low-Enriched Uranium Nuclear Thermal Propulsion Reactor***
Wei Li, Chaoran Guan, Houde Song, Xiang Chai and Xiaojing Liu

frontiers in Energy Research

ORIGINAL RESEARCH
published: 02 December 2021
doi: 10.3389/fenrg.2021.801481

Validation of Doppler Temperature Coefficients and Assembly Power Distribution for the Lattice Code KYLIN V2.0.

Lei Jichong[1], Xie Jinsen[1], Chen Zhenping[1], Yu Tao[1]*, Yang Chao[1], Zhang Bin[2], Zhao Chen[2], Li Xiangyang[2], Wu Jiebo[1], Zhang Huajian[1] and Deng Nianbiao[3]*

[1]School of Nuclear Science and Technology, University of South China, Hengyang, China, [2]Science and Technology on Reactor System Design Technology Laboratory, Nuclear Power Institute of China, Chengdu, China, [3]School of Resource Environment and Safety Engineering, University of South China, Hengyang, China

This work is interested in verifying and analyzing the advanced neutronics lattice code KYLIN V2.0. Assembly calculations are an integral part of the two-step calculation for core design, and their accuracy directly affects the results of the core physics calculations. In this paper, we use the Doppler coefficient numerical benchmark problem and CPR1000 AFA-3G fuel assemblies to verify and analyze the advanced neutronics lattice code KYLIN V2.0 developed by the Nuclear Power Institute of China. The analysis results show that the Doppler coefficients calculated by KYLIN V2.0 are in good agreement with the results of other well-known nuclear engineering design software in the world; the power distributions of AFA-3G fuel assemblies are in good agreement with the results of the RMC calculations, it's error distribution is in accordance with the normal distribution. It shows that KYLIN V2.0 has high calculation accuracy and meets the engineering design requirements.

Keywords: KYLIN V2.0, doppler temperature coefficient, power distribution, method of characteristic (MOC), AFA 3G

OPEN ACCESS

Edited by:
Shripad T. Revankar, Purdue University, United States

Reviewed by:
Donny Hartanto, University of Sharjah, United Arab Emirates
A. Abdelghafar Galahom, Higher Technological Institute, Egypt

****Correspondence:***
Yu Tao
yutao29@sina.com
Chen Zhenping
chzping@yeah.net

Specialty section:
This article was submitted to Nuclear Energy, a section of the journal Frontiers in Energy Research

Received: *25 October 2021*
Accepted: *08 November 2021*
Published: *02 December 2021*

Citation:
Jichong L, Jinsen X, Zhenping C, Tao Y, Chao Y, Bin Z, Chen Z, Xiangyang L, Jiebo W, Huajian Z and Nianbiao D (2021) Validation of Doppler Temperature Coefficients and Assembly Power Distribution for the Lattice Code KYLIN V2.0.. Front. Energy Res. 9:801481. doi: 10.3389/fenrg.2021.801481

INTRODUCTION

The main task of reactor physics analysis is to simulate various nuclear reaction processes in the core and to analyze various key parameters related to the "nuclear" in the nuclear reactor, including core criticality (reactivity), core three-dimensional power distribution, various reactivity coefficients, control rod values, shutdown margins, and isotope changes of various assemblies in the nuclear fuel, etc. The key to the physical analysis of the reactor is to solve the neutron transport equation and the fuel consumption equation. There are two methods to solve the neutron transport equation, one is the approximate method to solve the seven-dimensional equation, and the other is the probabilistic method to solve the neutron transport equation - Monte Carlo transport calculation method (Hammersley, 2013). However, the Monte Carlo method cannot be widely used in the engineering design of nuclear reactor core physics due to the large calculation rate and the difficulty of multi-physics coupling calculation (Lang et al., 1993).

Nuclear Power Institute of China (NPIC) has developed a software platform with independent property rights for nuclear power design and system safety analysis, NEPRI, in which the lattcie code KYLIN-V2.0 (Chai et al., 2017) is mainly used to calculate the few group constants for transport of single rods and assemblies of pressurized water reactors and the nucleon density of important nuclides for the core diffusion code for full core calculations. KYLIN-V2.0 uses the subgroup resonance calculation method to obtain effective resonance self-shielding cross sections, eliminating

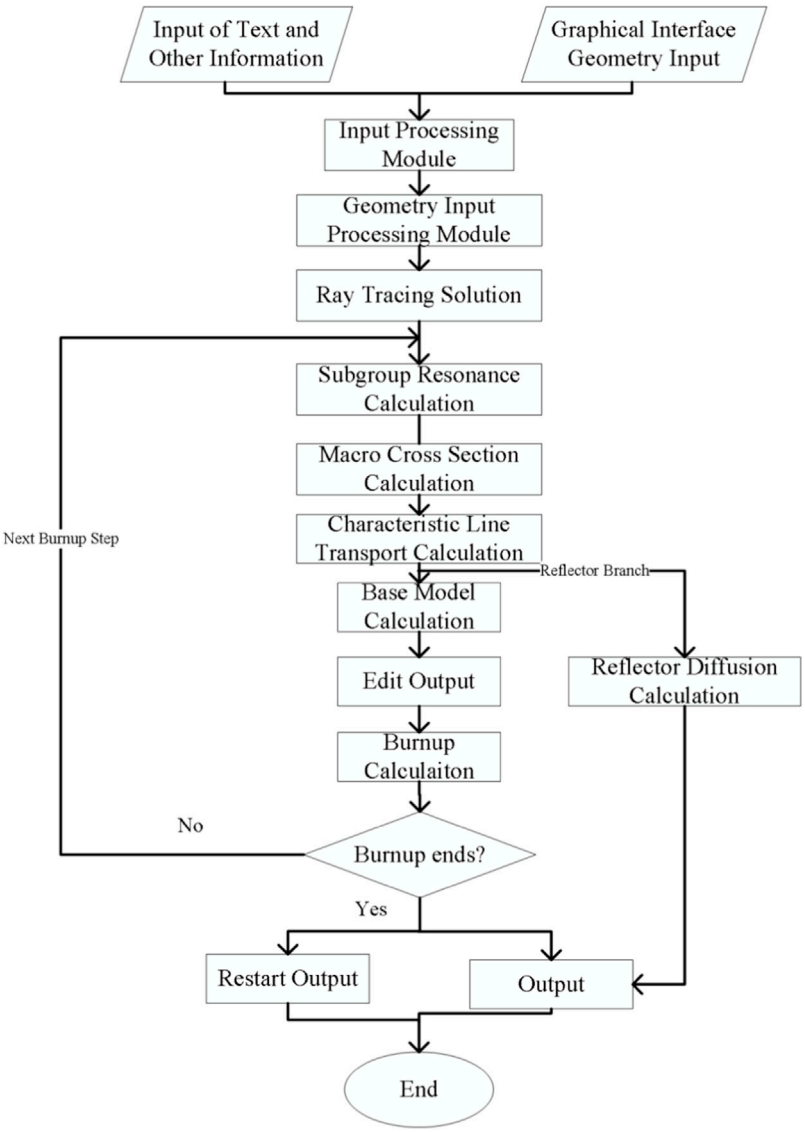

FIGURE 1 | Calculation flow chart of KYLIN-V2.0.

the limitations of lattice geometry and ensuring accuracy and efficiency, with multi-group energy structure in the cross section database. When multiple resonance nuclides are present, the Bondarenko iterative method is used to deal with resonance interference effects. The neutron transport calculation adopts the method of characteristics (MOC) (Douglas and Russell, 1982), the Chebyshev rational approximation method (CRAM) (Maria, 2016) with good computational accuracy and efficiency is used in the fuel burnup calculation in KYLIN V2.0 program. The KYLIN V2.0 program solves the multigroup diffusion equation by the fractional group diffusion theory and obtains the fewgroup parameters needed for the core procedure by parallel group homogenization.

In order to further confirm the engineering applicability of KYLIN V2.0 code and the credibility of the calculation results, an application study and additional validation experiments of the key nuclear power design software were conducted. In this paper, the Doppler temperature coefficient and neutron transport functions of the KYLIN V2.0 code are verified based on the Doppler temperature coefficient numerical benchmark problem and the AFA-3G fuel assembly problem.

KYLIN V2.0 SOFTWARE

The neutronics lattice calculation code KYLIN-V2.0 is an important program in the core design program system, which provides the homogenization parameters of two-dimensional components for the core design software CORCA 3D through the cross-section production software PACFAC. The calculation flow chart of KYLIN-V2.0 is shown in **Figure 1**, and the program uses the 45-group or 190-group multi-group cross-section library

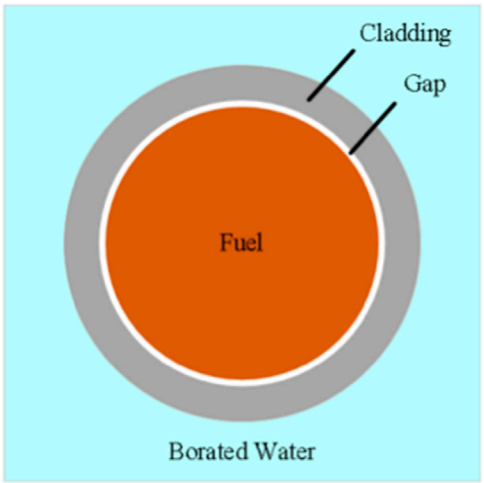

FIGURE 2 | Geometric structure diagram.

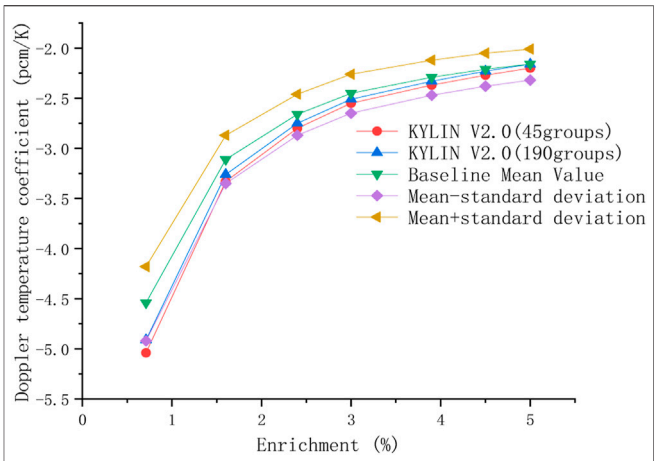

FIGURE 3 | Doppler coefficient trend graph.

TABLE 1 | Geometric data.

Parameters	Hot zero power (HZP)	Hot full power (HFP)
Outer Radius of Fuel/cm	0.39398	0.39433
Inner Radius of Cladding/cm	0.40266	0.40266
Outer Radius of Cladding/cm	0.45972	0.45972
Pitch/cm	1.26678	1.26678

TABLE 2 | Doppler coefficient calculation results.

Multigroup energy groups	Enrichment (%)	k_{inf} (600K)	k_{inf} (900K)	Changes from doppler loss in reactivity (pcm)	Doppler temperature coefficient (pcm/K)
45	0.711	0.63488	0.62884	−1,512.88	−5.04
	1.6	0.91961	0.91124	−998.82	−3.33
	2.4	1.05421	1.04496	−839.68	−2.80
	3.0	1.13051	1.12082	−764.74	−2.55
	3.9	1.19196	1.18196	−709.80	−2.37
	4.5	1.22678	1.21662	−680.73	−2.27
	5.0	1.25071	1.24045	−661.32	−2.20
190	0.711	0.63602	0.63012	−1,472.17	−4.91
	1.6	0.92159	0.91336	−977.73	−3.26
	2.4	1.05678	1.04765	−824.65	−2.75
	3.0	1.13352	1.12394	−751.96	−2.51
	3.9	1.19539	1.18550	−697.89	−2.33
	4.5	1.23048	1.22043	−669.23	−2.23
	5.0	1.25461	1.24447	−649.45	−2.16

generated by the NJOY code to calculate. KYLIN-V2.0 code uses the relevant computational procedures to rigorously solve the slowing down equations for homogeneous mixtures to obtain the effective resonance cross sections of resonant nuclides. Method of characteristics (MOC) is used to solve the neutron transport problem for two-dimensional steady-state multi-group neutron transport equation. The coarse mesh finite difference (CMFD) (Zhu et al., 2016) or generalized coarse mesh finite difference (GCMFD) (Yamamoto, 2005) are used to accelerate method of characteristics, and the P1 or B1 approximation to perform neutron leakage calculations to obtain the and group constants. The improved predictor-corrector method (PPC) (Wang et al., 2018) was used to solve the fuel consumption. KYLIN-V2.0 code is based on the PPC method. The log-linear

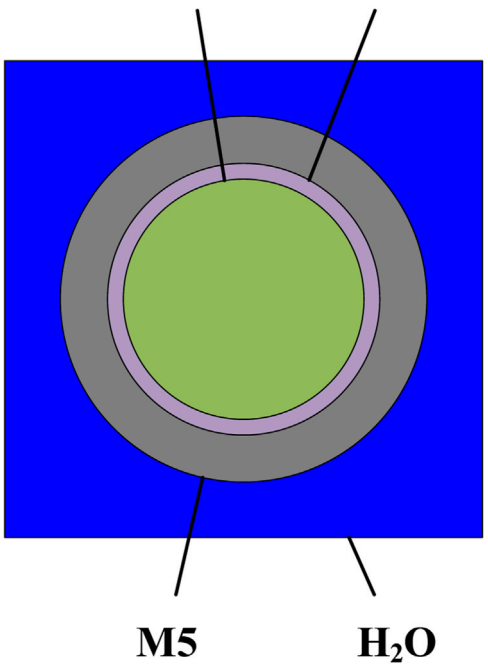

FIGURE 4 | Schematic diagram of the pin geometry.

extrapolation of the reaction rate is used for strong absorption nuclei such as ^{155}Gd and ^{157}Gd, and the Chebyshev rational approximation method (CRAM) is used to solve the fuel consumption equation.

BENCHMARK QUESTION VALIDATION

Doppler Temperature Coefficient Numerical Benchmark Problem

The data underlying the Doppler temperature coefficient benchmark question are obtained from Los Alamos National Laboratory, United States, which has been jointly approved by the American Nuclear Society's Division of Mathematics and Computation, Reactor Physics, and Radiation Protection Committees (Mosteller et al., 1991; Mosteller, 2007; Thilagam et al., 2007). The reactivity Doppler temperature coefficient is a key parameter for the reactivity evaluation of several transients in light water reactors (LWRs), including pressurized water reactor control rod ejection accidents and steam pipe rupture accidents. However, it is relatively small in magnitude. The Doppler feedback from hot zero power (HZP) to hot full power (HFP) produces a reactivity change in LWRs of only about 1,000 pcm. In addition, the reactivity change cannot be measured directly in an operating reactor, but must be derived from the derivation of other parameters.

The benchmark contains the corresponding gate element structures for the hot zero power (HZP) and hot full power (HFP) conditions. At HZP, the temperature of all fuels, cladding and moderators is a uniform 600K. At HFP, the fuel temperature

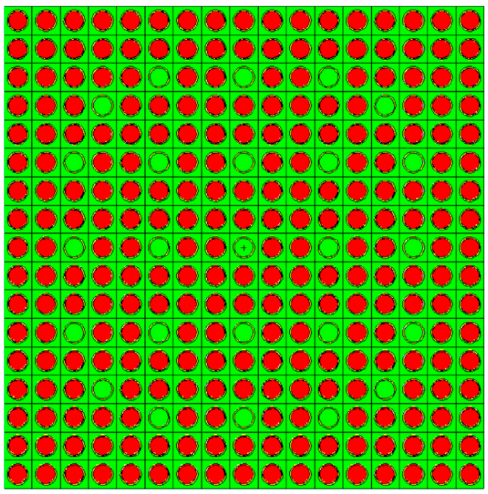

FIGURE 5 | Geometric arrangement of AFA-3G37000 type components.

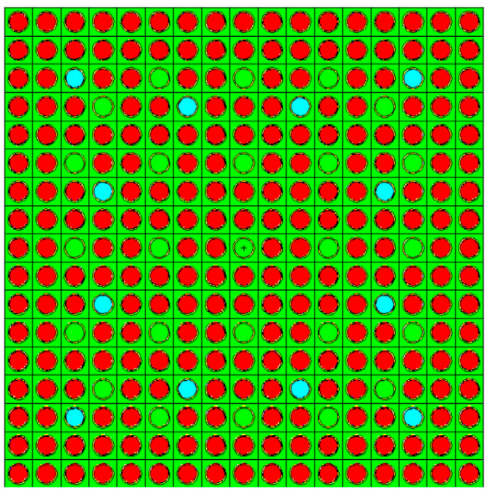

FIGURE 6 | Geometric arrangement of AFA-3G44512 type components.

is 900K, while all others remain at 600K. The reactivity difference between the HFP and HZP conditions is used to calculate the Doppler effect. The reactivity Doppler temperature coefficient is then determined as

$$DC = \frac{\Delta\rho_{Dop}}{\Delta T_{Fuel}}$$

where DC is the Doppler temperature coefficient, ΔT_{Fuel} is 300K, The changes from Doppler loss in reactivity is

$$\Delta\rho_{Dop} = \frac{k_{HFP} - k_{HZP}}{k_{HFP} * k_{HZP}}$$

The geometric structure of the benchmark problem is shown in **Figure 2**, and its geometric data are shown in **Table 1**.

TABLE 3 | Table of characteristic values of different depletion steps of AFA-3G assemblies calculated by KYLIN V2.0.

Assembly type	37,000			44,512		
Burnup (MWd/tU)	**KYLIN V2.0**	**RMC**	**Relative deviation**	**KYLIN V2.0**	**RMC**	**Relative deviation**
0	1.29253	1.28779	0.37%	1.19531	1.19153	0.32%
150	1.24934	1.24543	0.31%	1.16087	1.15786	0.26%
500	1.24164	1.23785	0.31%	1.15623	1.15331	0.25%
1,000	1.23544	1.23189	0.29%	1.15343	1.15049	0.26%
2000	1.22541	1.22210	0.27%	1.15019	1.14728	0.25%
4,000	1.20324	1.20051	0.23%	1.14268	1.14005	0.23%
6,000	1.18056	1.17819	0.20%	1.13465	1.13227	0.21%
10,000	1.13783	1.13598	0.16%	1.12209	1.11966	0.22%
16,000	1.08192	1.08030	0.15%	1.11211	1.10982	0.21%
20,000	1.04816	1.04697	0.11%	1.09046	1.08661	0.35%
30,000	0.97190	0.97209	–0.02%	1.01613	1.01317	0.29%
40,000	0.90535	0.90663	–0.14%	0.94946	0.94677	0.28%
50,000	0.84941	0.85139	–0.23%	0.88988	0.88745	0.27%
60,000	0.80556	0.80759	–0.25%	0.83892	0.83667	0.27%

The results of Doppler temperature coefficients obtained by KYLIN V2.0 refined modeling are shown in **Table 2**. Fifteen organizations in eight countries obtained 44 different solution sets based on different cross-sectional libraries using different software such as MCNP, KENO, CASMO, DRAGON, APPLLO, NEWT, HELIOS, and based on these solution sets, the Doppler mean value of temperature coefficients and the ±standard deviation range are obtained by bringing the solution set of KYLIN V2.0 to obtain the Doppler temperature coefficient trend graph.

Due to the microscopic cross-section in KYLIN V2.0 adopts ENDF/B-VIII.0 nuclear database, KYLIN V2.0 code provides overestimated values of FTC when compared to results of other codes. Through **Table 2** and **Figure 3**, it can be concluded that KYLIN V2.0 is within the standard deviation envelope when using the 45-group cross-section library, except for the Doppler temperature coefficient when the enrichment is 0.711%. The result is slightly lower than the benchmark mean-standard deviation, and all solutions are within the standard deviation envelope when using the 190-group cross-section library, and through the results, it can be concluded that KYLIN V2.0 is comparable to the standard deviation envelope in calculating the Doppler temperature coefficient. The accuracy of KYLIN V2.0 in calculating Doppler temperature coefficients is similar to that of international nuclear design related software, which meets the engineering design requirements.

AFA-3G Fuel Assembly Benchmark Questions

The base data of the AFA-3G fuel assembly benchmark question was obtained from the Chinese Electrical Engineering Dictionary, Volume 6 - Nuclear Power Generation Engineering. The benchmark question was established by referring to the operating parameters of units 3 and 4 of the Ningde Phase I project (Forat and Florentin, 1999; Lu et al., 2002; Ye et al., 2009; Lei et al., 2021). The AFA-3G fuel assembly continues the standard Westinghouse fuel assembly arrangement with a 17 × 17 square arrangement, and the burnable poison is selected as Gd_2O_3 with 9% by weight and ^{235}U enrichment of 0.711% in Gd rods (Wang et al., 2018). The AFA-3G fuel assembly, with the grid element geometry arrangement shown in **Figure 4**, is used in this paper for a ^{235}U enrichment of 3.7% without burnable poison rod assembly (37,000-type fuel assembly) and a ^{235}U enrichment of 4.45% with 12 burnable poison rods assembly (The 44,512 fuel assembly). **Figure 5** shows Geometric arrangement of AFA-3G37000 type assembly and **Figure 6** Geometric arrangement of AFA-3G44512 type assembly (the red grid element is the fuel grid element, the green grid element is the control rod conduit grid element, and the blue grid element is the combustible poison rod grid element).

According to the relevant references, the eigenvalues and relative errors of the assemblies at different depletion steps obtained by KYLIN V2.0 code and RMC code [9] based on the ENDF/B-VIII.0 database after refinement modeling are shown in **Table 3**. The relative errors between KYLIN V2.0 code and RMC code are within ±0.5% of the calculated eigenvalues, which meets the error requirement. According to **Figure 7**, where the power distribution is compared at the beginning (0 MWd/tU), middle (30,000 MWd/tU) and end (60,000 MWd/tU) of the life cycle.

Through **Figure 7**, it can be found that the errors of the rod power distribution between KYLIN V2.0 code and RMC code are between ±1%, which meets the international index ±5% error range. The error statistics of the relative distribution error of the rods of AFA-3G 37,000 fuel assembly and AFA-3G 445,12 fuel assembly are shown in **Figure 8**. The statistical results using the Owen factor method (Mosteller et al., 1991) show that the relative error 95/95 confidence interval is (0.001%, 0.054%). The results show that the errors of the rod power distribution between

A

RMC Calculated values
KYLIN V2.0 Calculated values
Relative Deviation/%

1.006	0.995							
1.006	0.997							
-0.004	0.200							
1.017	1.004	1.009						
1.020	1.006	1.010						
0.283	0.189	0.088						
	1.026	1.029						
	1.026	1.029						
	-0.010	-0.011						
1.029	1.014	1.024	1.041	1.032				
1.029	1.016	1.024	1.041	1.033				
-0.011	0.190	-0.010	-0.014	0.085				
1.031	1.020	0.802	1.045	1.047				
1.029	1.022	0.799	1.046	1.048				
-0.205	0.187	-0.302	0.080	0.079				
	1.029	1.035		1.038	1.031	0.785		
	1.028	1.036		1.038	1.032	0.781		
	-0.108	0.084		-0.014	0.085	-0.429		
1.019	1.002	1.003	1.019	1.001	0.989	0.983	0.972	
1.018	1.002	1.004	1.019	1.001	0.988	0.985	0.974	
-0.106	-0.003	0.096	-0.008	-0.003	-0.100	0.206	0.211	
0.998	0.995	0.995	0.997	0.993	0.987	0.981	0.980	0.993
0.996	0.995	0.995	0.995	0.992	0.986	0.983	0.981	0.993
-0.202	-0.001	-0.001	-0.202	-0.101	-0.100	0.207	0.105	0.000

Comparison of power distribution of 37000 type fuel assembly rods (0 MWd/tU)

B

RMC Calculated values
KYLIN V2.0 Calculated values
Relative Deviation/%

1.089	1.066							
1.085	1.066							
-0.378	-0.006							
1.101	1.067	1.059						
1.102	1.071	1.065						
0.116	0.401	0.592						
	1.084	1.074						
	1.084	1.075						
	-0.010	0.085						
1.070	1.017	0.974	1.050	1.051				
1.067	1.014	0.975	1.048	1.053				
-0.286	-0.286	0.123	-0.191	0.188				
1.047	0.965	0.352	1.008	1.071				
1.048	0.967	0.352	1.009	1.073				
0.095	0.230	-0.003	0.109	0.179				
	1.042	0.999		1.063	0.987	0.346		
	1.042	1.001		1.065	0.990	0.346		
	0.001	0.213		0.183	0.320	0.002		
1.074	1.045	1.035	1.065	1.032	0.983	0.923	0.961	
1.076	1.043	1.035	1.066	1.030	0.980	0.923	0.960	
0.178	-0.191	0.003	0.088	-0.190	-0.286	0.038	-0.079	
1.058	1.055	1.051	1.050	1.035	1.014	1.000	1.008	1.039
1.058	1.053	1.050	1.050	1.035	1.014	0.999	1.009	1.039
-0.004	-0.192	-0.097	-0.001	0.003	0.009	-0.087	0.109	0.002

Comparison of power distribution of 37000 type fuel assembly rods (30000 MWd/tU)

C

RMC Calculated values
KYLIN V2.0 Calculated values
Relative Deviation/%

1.003	0.995							
1.001	0.996							
-0.141	0.061							
1.009	0.999	1.000						
1.010	1.002	1.003						
0.108	0.311	0.310						
	1.011	1.010						
	1.009	1.009						
	-0.144	-0.045						
1.010	1.000	1.000	1.014	1.008				
1.009	0.999	1.000	1.013	1.011				
-0.045	-0.041	0.059	-0.046	0.351				
1.010	0.999	1.000	1.012	1.021				
1.009	0.999	1.000	1.011	1.020				
-0.045	0.059	0.059	-0.046	-0.049				
	1.009	1.000		1.017	1.008	0.988		
	1.007	1.008		1.016	1.006	0.991		
	-0.143	0.856		-0.048	-0.143	0.267		
1.007	0.997	0.995	1.007	0.994	0.986	0.981	0.976	
1.007	0.996	0.996	1.007	0.987	0.985	0.982	0.980	
0.055	-0.040	0.161	0.055	-0.740	-0.136	0.068	0.377	
0.995	0.994	0.997	0.996	0.994	0.990	0.989	0.987	0.996
0.994	0.996	0.995	0.995	0.994	0.990	0.989	0.988	0.997
-0.139	0.162	-0.240	-0.139	-0.038	-0.037	-0.036	0.065	0.161

Comparison of power distribution of 37000 type fuel assembly rods (60000 MWd/tU)

D

RMC Calculated values
KYLIN V2.0 Calculated values
Relative Deviation/%

1.002	0.994							
1.001	0.993							
-0.085	-0.083							
1.011	0.996	0.998						
1.015	1.002	1.005						
0.383	0.590	0.688						
	1.014	1.015						
	1.015	1.017						
	0.108	0.206						
1.016	1.001	1.004	1.023	1.018				
1.016	1.002	1.003	1.023	1.019				
0.009	0.114	-0.086	0.006	0.106				
1.017	1.001	1.005	1.023	1.029				
1.015	1.001	1.003	1.022	1.031				
-0.187	0.015	-0.185	-0.091	0.198				
	1.014	1.016		1.022	1.011	0.981		
	1.013	1.014		1.023	1.009	0.984		
	-0.088	-0.187		0.104	-0.186	0.328		
1.008	0.994	0.993	1.009	0.991	0.978	0.968	0.966	
1.009	0.995	0.995	1.009	0.992	0.977	0.969	0.965	
0.111	0.118	0.219	0.012	0.119	-0.078	0.131	-0.074	
0.995	0.991	0.993	0.993	0.985	0.980	0.977	0.976	0.987
0.990	0.991	0.990	0.990	0.986	0.979	0.976	0.975	0.987
-0.483	0.019	-0.283	-0.283	0.122	-0.078	-0.077	-0.077	0.021

Comparison of power distribution of 44512 type fuel assembly rods (0 MWd/tU)

E

RMC Calculated values
KYLIN V2.0 Calculated values
Relative Deviation/%

0.996	0.983							
0.998	0.985							
0.108	0.111							
1.017	0.992	0.996						
1.022	0.998	1.002						
0.453	0.559	0.557						
	1.023	1.027						
	1.026	1.029						
	0.298	0.199						
1.026	0.998	1.000	1.037	1.023				
1.027	1.002	1.004	1.039	1.028				
0.102	0.307	0.406	0.196	0.492				
1.023	0.999	1.000	1.040	1.048				
1.026	1.001	1.004	1.040	1.049				
0.298	0.107	0.306	0.004	0.098				
	1.022	1.024		1.034	1.105	0.972		
	1.023	1.025		1.036	1.017	0.976		
	0.103	0.103		0.197	-7.937	0.421		
1.013	0.988	0.989	1.013	0.982	0.966	0.952	0.946	
1.014	0.991	0.991	1.014	0.987	0.968	0.954	0.948	
0.105	0.210	0.109	0.105	0.415	0.218	0.222	0.224	
0.983	0.981	0.983	0.982	0.973	0.967	0.958	0.958	0.973
0.987	0.984	0.984	0.986	0.977	0.968	0.962	0.962	0.979
0.313	0.213	0.009	0.314	0.420	0.114	0.428	0.428	0.625

Comparison of power distribution of 44512 type fuel assembly rods (30000 MWd/tU)

F

RMC Calculated values
KYLIN V2.0 Calculated values
Relative Deviation/%

1.006	0.999							
1.007	1.001							
0.095	0.197							
1.013	1.003	1.007						
1.014	1.007	1.009						
0.073	0.373	0.173						
	1.017	1.017						
	1.014	1.015						
	-0.302	-0.204						
1.017	1.007	1.010	1.020	1.019				
1.015	1.008	1.010	1.020	1.017				
-0.204	0.094	-0.006	-0.008	-0.204				
1.015	1.009	0.874	1.020	1.027				
1.016	1.010	0.873	1.020	1.026				
0.091	0.094	-0.188	-0.008	-0.108				
	1.017	1.017		1.022	1.015	0.860		
	1.014	1.017		1.022	1.015	0.861		
	-0.302	-0.008		-0.009	-0.007	0.046		
1.012	1.003	1.002	1.010	1.001	0.991	0.991	0.987	
1.012	1.003	1.003	1.012	1.002	0.993	0.992	0.987	
-0.006	-0.004	0.096	0.192	0.097	0.201	0.101	0.001	
1.001	1.000	0.999	0.999	0.998	0.997	0.995	0.993	1.000
0.999	1.001	1.001	1.000	0.999	0.996	0.995	0.994	1.002
-0.202	0.097	0.197	0.097	0.098	-0.102	-0.001	0.100	0.197

Comparison of power distribution of 44512 type fuel assembly rods (60000 MWd/tU)

FIGURE 7 | Comparison of KYLIN V2.0 and RMC power distribution. **(A)** Comparison of power distribution of 37000 type **(B)** Comparison of power distribution of 37000 type fuel assembly rods (0 MWd/tU) fuel assembly rods (30000 MWd/tU) **(C)** Comparison of power distribution of 37000 type **(D)** Comparison of power distribution of 44512 type fuel assembly rods (60000 MWd/tU) fuel assembly rods (0 MWd/tU) **(E)** Comparison of power distribution of 44512 type **(F)** Comparison of power distribution of 44512 type fuel assembly rods (30000 MWd/tU) fuel assembly rods (60000 MWd/tU)

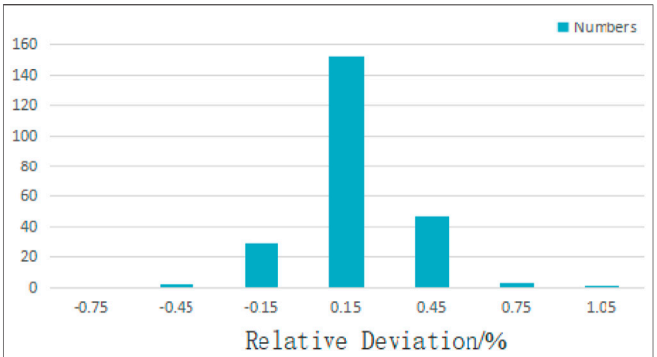

FIGURE 8 | Statistical chart of relative power distribution.

KYLIN V2.0 code and RMC code are normally distributed and the confidence interval is within the error range. From the error, two software are in good compliance, and indicates that KYLIN V2.0 is able to meet the requirements for calculating the eigenvalues. It shows that KYLIN V2.0 can meet the engineering design requirements in terms of calculating the eigenvalues and the assembly power distribution.

CONCLUSION

In this paper, the calculation scheme and theoretical model in KYLIN-V2.0 code are briefly introduced. And in order to verify the calculation ability of KYLIN-V2.0 code, the Doppler coefficient numerical benchmark problems, AFA-3G 37,000 gadolinium-free fuel and AFA-3G 44,512 gadolinium-containing fuel assembly problems from Ningde nuclear power plant are chosen. By comparing the results with reference results from benchmark and the reference program RMC, the main conclusions were drawn as follows:

a) For the Doppler temperature coefficient benchmark question, the calculated Doppler temperature coefficient is between the mean ± standard deviation of the calculated results from references, which is consistent with good.
b) For the calculation of AFA-3G fuel assemblies with gadolinium and fuel assemblies without gadolinium, RMC was selected as the reference procedure. The relative errors of eigenvalues calculated within ±0.5%, which is in accordance with error criteria; the relative errors of power distribution meet the error requirement of ±5%.
c) The relative power of fuel assembly rods based on KYLIN V2.0 code and RMC code with 95/95 confidence intervals of (0.001%,0.054%) was calculated by the Owen factor method, and the relative errors were in accordance with the normal distribution.
d) The KYLIN-V2.0 program is able to meet engineering design requirements in terms of calculating Doppler temperature coefficients, eigenvalues, and assembly power distributions.

DATA AVAILABILITY STATEMENT

The original contributions presented in the study are included in the article/Supplementary Material, further inquiries can be directed to the corresponding authors.

AUTHOR CONTRIBUTIONS

LJ and XJ: Conceptualization, Methodology, Software YC and CZ: Data curation, Writing—Original draft preparation. WJ, ZB, and ZC: Visualization, Investigation. XJ, YT, and LX: Supervision: ZH, LJ and DN: Writing—Reviewing and Editing.

FUNDING

This work is supported by the Scientific Research Project of Hunan Provincial Education Department (No. 19A422), Hunan Province Science and Technology Talent Support Project (No. 2020TJ-N02), 2020 Graduate Research and Innovation Project of Hunan Province, PR China (No. CX20200946), University of South China Innovation Foundation For Postgraduate (213YXC009), and the National Natural Science Foundation of China (No. 12175101) for their funding.

ACKNOWLEDGMENTS

The authors would like to show their great appreciation to NEAL (Nuclear Engineering and Application Laboratory) Team for its contribution to this research.

REFERENCES

Chai, X., Tu, X., Lu, W., Lu, Z., Yao, D., Li, Q., et al. (2017). The Powerful Method of Characteristics Module in Advanced Neutronics Lattice Code KYLIN-2[J]. *J. Nucl. Eng. Radiat. Sci.* 3 (3), 031004. doi:10.1115/1.4035934

Douglas, J., Jr, and Russell, T. F. (1982). Numerical Methods for Convection-Dominated Diffusion Problems Based on Combining the Method of Characteristics with Finite Element or Finite Difference Procedures. *SIAM J. Numer. Anal.* 19 (5), 871–885. doi:10.1137/0719063

Forat, C., and Florentin, F. (1999). *The AFA 3G Fuel Assembly: A Proven Design for High burnups[M].* LWR nuclear fuel highlights at the beginning of the third millennium.

Hammersley, J. (2013). *Monte Carlo methods[M]*. Berlin, Germany: Springer Science & Business Media.

Lang, G. H., Johnson, C. W., Koonin, S. E., and Ormand, W. E. (1993). Monte Carlo Evaluation of Path Integrals for the Nuclear Shell Model. *Phys. Rev. C* 48 (4), 1518–1545. doi:10.1103/physrevc.48.1518

Lei, J. C., Zhou, J. D., Zhao, Y. N., Chen, Z. P., Zhao, P. C., Xie, C., et al. (2021). Prediction of Burn-up Nucleus Density Based on Machine Learning[J]. *Int. J. Energ. Res.* 45, 14052. doi:10.1002/er.6660

Lu, H., Liu, T., Jiao, Y., and Pang, H. (2002). AFA 2G and AFA 3G Fuel Rod Performance Analysis[J]. *Nucl. Power Eng.* 23 (5), 58–61, 84.

Maria, P. (2016). Higher-Order Chebyshev Rational Approximation Method and Application to Burnup Equations. *Nucl. Sci. Eng.* 182 (3), 297–318. doi:10.13182/nse15-26

Mosteller, R. D., Eisenhart, L. D., Little, R. C., Eich, W. J., and Chao, J. (1991). Benchmark Calculations for the Doppler Coefficient of Reactivity. *Nucl. Sci. Eng.* 107 (3), 265–271. doi:10.13182/nse91-a23789

Mosteller, R. D. (2007). "The Doppler-Defect Benchmark: Overview and Summary of Results," in Joint International Topical Meeting on Mathematics & Computation and Supercomputing in Nuclear Applications (M&C + SNA 2007), Monterey, California, April 15–19, 2007.

Thilagam, L., Sunny, C. S., Subbaiah, K. V., Devan, K., Lee, Y. S., and Jagannathan, V. (2007). "Doppler Coefficient of Reactivity-Benchmark Calculations for Different Enrichments of UO2[C]," in Joint International Topical Meeting on Mathematics & Computation and Supercomputing in Nuclear Applications, Monterey, California.

Wang, B., Liu, Z., Chen, J., Zhao, C., Cao, L., and Wu, H. (2018). A Modified Predictor-Corrector Quasi-Static Method in NECP-X for Reactor Transient Analysis Based on the 2D/1D Transport Method. *Prog. Nucl. Energ.* 108, 122–135. doi:10.1016/j.pnucene.2018.05.014

Yamamoto, A. (2005). Generalized Coarse-Mesh Rebalance Method for Acceleration of Neutron Transport Calculations. *Nucl. Sci. Eng.* 151 (3), 274–282. doi:10.13182/nse151-274

Ye, Q. Z., Li, X. M., Yu, C. D., and Huang, X. (2009). *China Electrical Engineering Dictionary, Vol. 6. Nuclear Power Generation Engineering [M]*. China: China Electric Power Press.

Zhu, A., Jarrett, M., Xu, Y., Kochunas, B., Larsen, E., and Downar, T. (2016). An Optimally Diffusive Coarse Mesh Finite Difference Method to Accelerate Neutron Transport Calculations. *Ann. Nucl. Energ.* 95, 116–124. doi:10.1016/j.anucene.2016.05.004

Conflict of Interest: The authors declare that the research was conducted in the absence of any commercial or financial relationships that could be construed as a potential conflict of interest.

Publisher's Note: All claims expressed in this article are solely those of the authors and do not necessarily represent those of their affiliated organizations, or those of the publisher, the editors and the reviewers. Any product that may be evaluated in this article, or claim that may be made by its manufacturer, is not guaranteed or endorsed by the publisher.

Copyright © 2021 Jichong, Jinsen, Zhenping, Tao, Chao, Bin, Chen, Xiangyang, Jiebo, Huajian and Nianbiao. This is an open-access article distributed under the terms of the Creative Commons Attribution License (CC BY). The use, distribution or reproduction in other forums is permitted, provided the original author(s) and the copyright owner(s) are credited and that the original publication in this journal is cited, in accordance with accepted academic practice. No use, distribution or reproduction is permitted which does not comply with these terms.

frontiers in Energy Research

ORIGINAL RESEARCH
published: 10 February 2022
doi: 10.3389/fenrg.2022.834237

Numerical Study on the Effect of Jet Cross Section Shape on the Corium Jet Breakup Behavior With Lattice Boltzmann Method

Hui Cheng[1], *Songbai Cheng*[1]* *and Jun Wang*[2]*

[1]Sino-French Institute of Nuclear Engineering and Technology, Sun Yat-Sen University, Zhuhai, China, [2]College of Engineering, University of Wisconsin-Madison, Madison, WI, United States

In a core meltdown accident in light water reactors, molten corium may drop into the lower plenum of the pressure vessel and interact with water, which is called fuel–coolant interaction (FCI). The behavior of the corium jet breakup in water during FCIs is important for the in-vessel retention strategy and has been extensively studied. While in previous studies, the jet cross-section shapes are naturally assumed to be circular, which is actually not always the case, in this study, the breakup processes of the corium jets with four different elliptical cross-section shapes and three different penetration velocities are simulated with color-gradient lattice Boltzmann method. The effect of the cross-section shape on the hydrodynamic breakup behavior of the corium jet is analyzed in detail. It is found that the effect of the cross-section shape on the jet penetration depth is very limited. With the increase in the aspect ratio under the same penetration velocity, the jet breakup length decreases gradually. In general, the dimensionless corium surface area increases with the increase in the aspect ratio for the jets under the same penetration velocity.

Keywords: fuel–coolant interaction (FCI), corium jet breakup, effect of jet cross-section shape, lattice Boltzmann method, jet breakup length

OPEN ACCESS

Edited by:
Yixiang Liao,
Helmholtz Association of German Research Centres (HZ), Germany

Reviewed by:
Luteng Zhang,
Chongqing University, China
Rong Liu,
South China University of Technology, China

***Correspondence:**
Songbai Cheng
chengsb3@mail.sysu.edu.cn
Jun Wang
jwang564@wisc.edu

Specialty section:
This article was submitted to Nuclear Energy, a section of the journal Frontiers in Energy Research

Received: *13 December 2021*
Accepted: *12 January 2022*
Published: *10 February 2022*

Citation:
Cheng H, Cheng S and Wang J (2022) Numerical Study on the Effect of Jet Cross Section Shape on the Corium Jet Breakup Behavior With Lattice Boltzmann Method. Front. Energy Res. 10:834237. doi: 10.3389/fenrg.2022.834237

1 INTRODUCTION

During a core meltdown accident in light water reactors (LWRs), molten corium may drop into the lower plenum of the reactor vessel and interact with water, which is called fuel–coolant interaction (FCI). The design of the in-vessel retention (IVR) strategy requires the full understanding of the physical phenomena related to FCIs, especially the corium jet breakup process which will significantly affect the formation of the debris bed and the subsequent in-vessel cooling. The corium jet breakup behavior in water has been extensively studied with real core material experiments, simulant material experiments, and various simulations (Spencer et al., 1994;Burger et al., 1995;Dinh et al., 1999;Huhtiniemi et al., 1999;Abe et al., 2006;Thakre et al., 2015;Zhou et al., 2017;Iwasawa and Abe 2018;Saito et al., 2018;Shen et al., 2018;Cheng et al., 2019;Cheng et al., 2020; Cheng et al., 2021a;Cheng et al., 2021b). To the best of authors' knowledge, in almost all of the previous studies, the jet cross-section shapes are naturally assumed to be circular, which is actually not always the case. In fact, when the molten corium drops from the edge of the core, through the structures or the cracks of the corium crust, the corium jets are very likely to have different cross-section shapes depending on the specific situations (Corradini et al., 1988). This leads to the

investigation of the effect of jet cross-section shape on the corium jet breakup behavior, which was generally ignored in previous studies.

Since the interaction between the molten corium jet and water involves very complex thermal hydraulics phenomena such as boiling heat transfer, corium jet breakup, and corium solidification, it is not easy to get the effect of jet cross-section shape directly from the experimental results with such complex phenomena. On the other hand, more quantitative results can be directly extracted from the numerical results, among which the lattice Boltzmann method (LBM) has become a powerful tool in analyzing the complex multiphase flow in recent years (Saito et al., 2017). LBM is the so-called mesoscopic simulation method between the microscopic particle-based (molecular dynamics) and macroscopic Navier–Stokes–based methods. Compared with conventional CFD methods, it has the following advantages: 1) based on the molecular kinetic theory; 2) easy to program and parallelize; 3) interface tracking is not needed; and 4) applicable to complex geometries (Huang et al., 2015;Krüger et al., 2016). As one of the two-phase LBM methods, the color-gradient LBM employs two components to represent two immiscible fluids; one component is the red-colored fluid and the other is the blue-colored fluid. Its main advantages lie in strict mass conservation for each fluid and flexibility in adjusting the interfacial tension (Ba et al., 2016). To simplify the complex situation involved, in the current study, the hydrodynamic phenomena are decoupled from the thermal phenomena and studied separately for the corium jet breakup process with the state-of-the-art GPU-accelerated color-gradient LBM.

In this study, the breakup process of the corium jets with four different elliptical cross-section shapes and three different penetration velocities are simulated with color-gradient LBM. The effect of the cross-section shape on the hydrodynamic breakup behavior of the corium jet is analyzed in detail.

2 COLOR-GRADIENT LATTICE BOLTZMANN METHOD

In our previous studies, the improved color-gradient LBM with non-orthogonal central-moment MRT has been successfully developed and used to study the hydrodynamic breakup process of melt jets with circular cross-section in both sodium-cooled fast reactors (SFRs) (Cheng et al., 2020) and LWRs (Cheng et al., 2021b), thanks to its advantages in multiphase flow modeling and the enhanced numerical stability for flows with high Reynolds numbers. Here, this model is adopted in the current work to explore the effect of jet cross-section shape on the corium jet hydrodynamic breakup behavior. The details of the improved color-gradient LBM are introduced as follows.

The D3Q27 lattice is adopted; the discrete lattice velocity $\mathbf{c}_i$ in the D3Q27 framework is defined as

$$\mathbf{c}_i = \left(c_{ix}, c_{iy}, c_{iz}\right) = c\begin{bmatrix} 0 & 1 & -1 & 0 & 0 & 0 & 0 & 1 & -1 & 1 & -1 & 0 & 0 & 0 & 0 & 1 & -1 & 1 & -1 & 1 & -1 & 1 & -1 & 1 & -1 & 1 \\ 0 & 0 & 0 & 1 & -1 & 0 & 0 & 1 & -1 & -1 & 1 & 1 & -1 & 1 & -1 & 0 & 0 & 0 & 0 & 1 & -1 & 1 & -1 & -1 & 1 & -1 \\ 0 & 0 & 0 & 0 & 0 & 1 & -1 & 0 & 0 & 0 & 0 & 1 & -1 & -1 & 1 & 1 & -1 & -1 & 1 & 1 & -1 & -1 & 1 & 1 & -1 & -1 \end{bmatrix}, \tag{1}$$

where index $i = 0, 1, \ldots, 26$, $c = \delta_x/\delta_t$ is the lattice speed, δ_t is the time step, and δ_x is the lattice spacing.

Two immiscible fluids are represented by pseudo red fluid and blue fluid, respectively. The distribution function, f_i^k, is used to represent the fluid k, namely, $k = r$ denotes "red" color, $k = b$ denotes the "blue" color, and i is the index of the lattice-velocity direction. $f_i = f_i^r + f_i^b$ is the total distribution function with evolution equation defined as

$$f_i^k(\mathbf{x} + \mathbf{c}_i\delta_t,\ t + \delta_t) - f_i^k(\mathbf{x},\ t) = \Omega_i^k(\mathbf{x},\ t), \tag{2}$$

where x and t represent the position and time. The collision operator Ω_i^k is composed of the following sub-operators

$$\Omega_i^k = \left(\Omega_i^k\right)^{(3)}\left[\left(\Omega_i^k\right)^{(1)} + \left(\Omega_i^k\right)^{(2)}\right], \tag{3}$$

where $(\Omega_i^k)^{(1)}$ is the single-phase collision operator, $(\Omega_i^k)^{(2)}$ is the perturbation operator, and $(\Omega_i^k)^{(3)}$ is the recoloring operator.

2.1 Single-Phase Collision Operator

The single-phase collision operator with non-orthogonal central moment MRT is defined as

$$(\Omega)^{(1)}\left(|f\rangle\right) = |f\rangle - M^{-1}N^{-1}KNM\left(|f\rangle - |f^{(e)}\rangle\right) + |F\rangle, \tag{4}$$

where transformation matrix M transforms distribution functions from velocity space into raw moment space. The shift matrix N transfers raw moments to central moments. K represents the relaxation matrix. Here, "ket" operator $|.\rangle$ denotes the column vector. For details on the transformation matrix M, the shift matrix N, the non-orthogonal central-moment matrix NM, and the relaxation matrix K, refer to Cheng et al. (2021b). $|f\rangle$ denotes the discrete forcing term, which is given by

$$|F\rangle = M^{-1}N^{-1}\left(I - \frac{1}{2}K\right)NM|F'\rangle, \tag{5}$$

where I is a unit matrix, $|F\rangle = (F_0, F_1, \ldots, F_{26})^T$, and $|F\rangle' = (F_0', F_1', \ldots, F_{26}')^T$, $F_i'$is defined as

$$F_i' = \omega_i\left[3\frac{\mathbf{c}_i - \mathbf{u}}{c^2} + 9\frac{(\mathbf{c}_i \cdot \mathbf{u})\mathbf{c}_i}{c^4}\right] \cdot \mathbf{F}\delta_t, \tag{6}$$

where $\mathbf{F}$ is the body force.

In the single-phase collision operator, the enhanced equilibrium distribution function (Leclaire et al., 2017) is used

$$f_i^{(e)}(\rho, \mathbf{u}) = \rho\left\{\varphi_i + \omega_i\left[\frac{3}{c^2}(\mathbf{c}_i \cdot \mathbf{u}) + \frac{9}{2c^4}(\mathbf{c}_i \cdot \mathbf{u})^2 - \frac{3}{2c^2}\mathbf{u}^2 + \frac{9}{2c^6}(\mathbf{c}_i \cdot \mathbf{u})^3 - \frac{9}{2c^4}(\mathbf{c}_i \cdot \mathbf{u})\mathbf{u}^2\right]\right\} + \Phi_i. \tag{7}$$

The weights, ω_i, are as follows

$$\omega_i = \begin{cases} 8/27, & i = 0, \\ 2/27, & i = 1, 2, \ldots, 6, \\ 1/54, & i = 7, 8, \ldots, 18, \\ 1/216, & i = 19, 20, \ldots, 26. \end{cases} \tag{8}$$

Meanwhile, we have

$$\varphi_i = \begin{cases} \bar{\alpha}, & |\mathbf{c}_i|^2 = 0, \\ 2(1-\bar{\alpha})/19, & |\mathbf{c}_i|^2 = 1, \\ (1-\bar{\alpha})/38, & |\mathbf{c}_i|^2 = 2, \\ (1-\bar{\alpha})/152, & |\mathbf{c}_i|^2 = 3. \end{cases} \tag{9}$$

where $\bar{\alpha}$ interpolates between α_r and α_b are as follows:

$$\bar{\alpha} = \frac{\rho_r}{\rho_r + \rho_b}\alpha_r + \frac{\rho_b}{\rho_r + \rho_b}\alpha_b, \tag{10}$$

$$\Phi_i = \begin{cases} -3\bar{\nu}(\mathbf{u}\cdot\nabla\rho)/c, & |\mathbf{c}_i|^2 = 0, \\ +16\bar{\nu}(\mathbf{G}\colon c_i \otimes c_i)/c^3, & |\mathbf{c}_i|^2 = 1, \\ +4\bar{\nu}(\mathbf{G}\colon c_i \otimes c_i)/c^3, & |\mathbf{c}_i|^2 = 2, \\ +1\bar{\nu}(\mathbf{G}\colon c_i \otimes c_i)/c^3, & |\mathbf{c}_i|^2 = 3. \end{cases} \tag{11}$$

where $\otimes$ is the tensor product, ": " is the tensor contraction, $\bar{\upsilon}$ is the kinematic viscosity interpolating between red fluid viscosity υ_r and blue fluid viscosity υ_b as

$$\frac{1}{\bar{\upsilon}} = \frac{\rho_r}{\rho_r + \rho_b}\frac{1}{\upsilon_r} + \frac{\rho_b}{\rho_r + \rho_b}\frac{1}{\upsilon_b}. \tag{12}$$

ϕ represents the order parameter distinguishing two fluids given by

$$\phi(\boldsymbol{x}, t) = \frac{\rho_r(\boldsymbol{x}, t) - \gamma\rho_b(\boldsymbol{x}, t)}{\rho_r(\boldsymbol{x}, t) + \gamma\rho_b(\boldsymbol{x}, t)}, \tag{13}$$

where γ denotes the density ratio between the red fluid and blue fluid. $\phi = 1, -1, 0$ represent pure red fluid, pure blue fluid, and the interface. The tensor **G** in **Eq. 11** is given by

$$\mathbf{G} = \frac{1}{48}\left[\mathbf{u}\otimes\nabla\rho + (\mathbf{u}\otimes\nabla\rho)^T\right]. \tag{14}$$

To ensure stable interface, γ must satisfy the equation as

$$\gamma = \frac{\rho_r^0}{\rho_b^0} = \frac{1-\alpha_b}{1-\alpha_r}, \tag{15}$$

where the superscript "0" over ρ_r^0 or ρ_b^0 represents pure fluid density. The fluid pressure is given based on the D3Q27 isothermal equation of state

$$p_k = \rho_k\left(c_s^k\right)^2 = \rho_k\frac{9(1-\alpha_k)}{19}c^2. \tag{16}$$

In this study, we chose $\alpha_b = 8/27$, so that $c_s^b = \frac{c}{\sqrt{3}}$ (Saito et al., 2017).

2.2 Perturbation Operator

The interfacial tension in the color-gradient LBM is modeled with the perturbation operator given by

$$(\Omega)^{(2)}(f_i) = f_i + A|\nabla\phi|\left[\omega_i\frac{(\mathbf{c}_i\cdot\nabla\phi)^2}{|\nabla\phi|^2} - B_i\right], \tag{17}$$

where B_i represents the lattice dependent weight and is defined as

$$B_i = \begin{cases} -(10/27)c^2, & |\mathbf{c}_i|^2 = 0, \\ +(2/27)c^2, & |\mathbf{c}_i|^2 = 1, \\ +(1/54)c^2, & |\mathbf{c}_i|^2 = 2, \\ +(1/216)c^2, & |\mathbf{c}_i|^2 = 3. \end{cases} \tag{18}$$

The interfacial tension σ is defined as

$$\sigma = \frac{4}{9}A\tau c^4\delta_t, \tag{19}$$

where τ is the relaxation time, and it is assumed here that $A = A_r = A_b$.

2.3 Recoloring Operator

This operator is employed to maximize the amount of fluid k at interface near the fluid k side while remaining mass and momentum conservation laws. The recoloring operators are given by

$$(\Omega)^{(3)}(f_i^r) = \frac{\rho_r}{\rho}f_i + \beta\frac{\rho_r\rho_b}{\rho^2}\cos(\theta_i)f_i^{(e)}(\rho, 0), \tag{20}$$

$$(\Omega)^{(3)}\left(f_i^b\right) = \frac{\rho_b}{\rho}f_i - \beta\frac{\rho_r\rho_b}{\rho^2}\cos(\theta_i)f_i^{(e)}(\rho, 0), \tag{21}$$

where β is the segregation parameter related to the interface thickness, θ_i is the angle between the lattice velocity and the order parameter gradient.

$$\cos(\theta_i) = \frac{\mathbf{c}_i\cdot\nabla\phi}{|\mathbf{c}_i||\nabla\phi|}. \tag{22}$$

2.4 Streaming Operator

$$f_i^k(\mathbf{x} + \mathbf{c}_i\delta_t,\ t + \delta_t) = f_i^{k*}(\mathbf{x},\ t), \tag{23}$$

where $f_i^{k*}(\mathbf{x},\ t)$ is the post-collision distribution function.

2.5 Macro Properties and Gradient Operator

The density of each fluid and the total fluid are defined as

$$\rho_k = \sum_i f_i^k, \tag{24}$$

$$\rho = \sum_k \rho_k. \tag{25}$$

The total momentum is defined as

$$\rho\mathbf{u} = \sum_i f_i\mathbf{c}_i + \frac{1}{2}\mathbf{F}\delta_t. \tag{26}$$

The second-order isotropic central scheme is adopted to define the gradient operator for any function χ

$$\nabla\chi(\mathbf{x}, t) = \sum_{i\neq 0}\frac{\omega_i\chi(\mathbf{x} + \mathbf{c}_i\delta_t, t)\mathbf{c}_i}{c_s^2\delta_t}. \tag{27}$$

3 COMPUTATIONAL DOMAIN AND PARAMETERS

The computational domain for the corium jet breakup process is presented in **Figure 1**, which includes a water pool and an inlet at the top surface where the corium jet is penetrated. The other surfaces are set as convective boundary conditions so that the

dispersion of the corium will not be limited by the boundary of the computational domain. As an example, the convective boundary condition at the bottom surface is given by

$$\frac{\partial f_i^k}{\partial t} + u_z \frac{\partial f_i^k}{\partial z} = 0, \ at \ z = 0, \tag{28}$$

where $z = 0$ denotes the nodes at the bottom surface. Using the first-order explicit discrete scheme, we have

$$f_i^k(x, y, 0, t + \delta_t) = \frac{f_i^k(x, y, 0, t) - u_z(x, y, 1, t) * f_i^k(x, y, 1, t)}{1 - u_z(x, y, 1, t)}. \tag{29}$$

The body force is given by

$$\mathbf{F}(\mathbf{x}, t) = (\rho(\mathbf{x}, t) - \rho_b^0)\mathbf{g}, \tag{30}$$

where $\mathbf{g} = (0, 0, -9.81\ m/s^2)$.

To study the effect of the jet cross-section shape on the corium jet hydrodynamic breakup behavior, the penetration processes of the corium jets with four different elliptical cross-section shapes and three different penetration velocities are simulated. The parameters for all 12 cases are presented in **Table 1**, where "a" is the semi-major axis of the ellipse, "b" is the semi-minor axis of the ellipse, and "E = a/b" is the aspect ratio. All these elliptical cross-sections have the same area which is equal to a circular area with 10 mm diameter, so that the penetration flow rates remain the same for the corium jets with the same penetration velocity. The three penetration velocities V (2.21, 4.43, and 8.85 m/s) represent the typical free fall distances of the corium in the pressure vessel of LWRs ranging from 0.25 to 4.0 m.

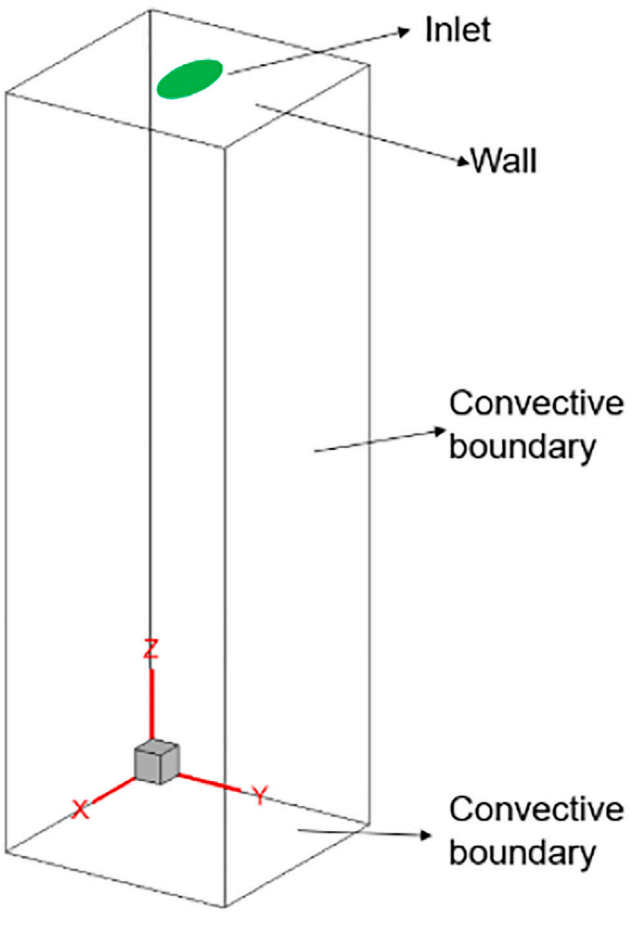

FIGURE 1 | Computational domain for the corium jet breakup process.

In the current simulations, the corium is set to a mixture of 80% UO_2 and 20% ZrO_2 (mol%) with a melting point of 2,600°C. It is assumed that corium jet at 3,000°C is penetrated into water at 70°C. The thermophysical properties of the corium at 3,000°C and water at 70°C are presented in **Table 2** (Schins1978; Kirillov2006; Kolev 2015; Kim et al., 2017).

To conduct the simulations with LBM, all parameters are converted from physical units to lattice units based on **Eqs 31–34**, where D is the area equivalent diameter, D^* represents the lattice number along the area equivalent inlet diameter, ρ_r and ρ_b are the density of the red and blue fluid, respectively, and the jet inlet velocity V^* and the jet density ρ_r^* are set to 0.1 and 1.0, respectively. The parameter β is set to 0.7.

$$\rho_b^* = \frac{\rho_b}{\rho_r}\rho_r^*, \tag{31}$$

$$\nu_r^* = \frac{D^* V^*}{DV}\nu_r, \tag{32}$$

$$\nu_b^* = \frac{D^* V^*}{DV}\nu_b, \tag{33}$$

$$g^* = \frac{DV^{*2}}{D^* V^2} g, \tag{33a}$$

$$\sigma^* = \frac{D^* V^{*2}\sigma}{DV^2 \rho_r}. \tag{34}$$

In our previous studies (Cheng et al., 2020; Cheng et al., 2021b), lattice number independent tests have been conducted by dividing the computational domain into 78*78*250,104*104*330, 130*130*410, and160*160*500 lattices, and it is found that the difference of the simulation results can be ignored for the last two; hence, 160*160*500 lattices with $D^* = 30$ are used in the simulation of jet breakup process. The parameters in both physical units and lattice units with this lattice number are shown in **Table 3**. Meanwhile, the ability of the color-gradient LBM model to precisely predict the jet breakup process has also been validated using the results of molten wood's metal jet breakup experiments; it is found that the morphologies of the melt jet at different times in the experiment and simulation match very well (Cheng et al., 2021b).

4 RESULTS AND DISCUSSION

4.1 Morphology of Corium Jet Breakup

The snap shots of corium jet breakup processes along both minor axis direction and major axis direction of the elliptical cross-section in the 12 cases are presented in **Figure 2**, where the interface between the corium and the

TABLE 1 | Parameters of the corium jets with four elliptical cross-sections and three velocities.

Case	Semi-major axis a (mm)	Semi-minor axis b (mm)	Aspect ratio E (-)	Penetration velocity V (m/s)
1	5.0000	5.0000	1	2.21
2	5.0000	5.0000	1	4.43
3	5.0000	5.0000	1	8.85
4	7.0711	3.5355	2	2.21
5	7.0711	3.5355	2	4.43
6	7.0711	3.5355	2	8.85
7	8.6603	2.8868	3	2.21
8	8.6603	2.8868	3	4.43
9	8.6603	2.8868	3	8.85
10	10.0000	2.5000	4	2.21
11	10.0000	2.5000	4	4.43
12	10.0000	2.5000	4	8.85

TABLE 2 | Thermophysical properties of the corium.

Thermophysical properties	$(UO_2)_{0.8}(ZrO_2)_{0.2}$	Water
Melting point [°C]	2,600	0
Temperature [°C]	3,000	70
Density [kg/m^3]	8,302	978
Density ratio to water	8.49	1.0
Kinematic viscosity [m^2/s]	7.35e-7	4.13e-7
Surface tension [N/m]	0.484	-

water is extracted from the simulation results. It can be seen that for all 12 cases under different conditions, a mushroom-shaped leading edge can be observed immediately after the penetration due to the drag force, and then both the jet leading edge and jet column start to break up under the effect of Rayleigh–Taylor instability and Kelvin–Helmholtz instability, respectively; lots of small fragments are generated along with the penetration process.

Qualitatively, it is easy to find that more fragments are generated with the increase in the penetration velocity for the corium jets with the same aspect ratio (e.g., comparing Case 1, Case 2, and Case 3). The effect of the aspect ratio on the generated fragments for the corium jets with the same penetration velocity is not directly based on these figures, which is further analyzed quantitatively in **Section 4.4** Nevertheless, it can be noticed that with the increase in the aspect ratio, the jet becomes more flat and more fragments are distributed along the major axis direction than along the minor axis direction.

4.2 Jet Penetration Depth

The penetration depth versus time of the corium jet under three different penetration velocities is presented in **Figure 3**. From these figures, it can be seen that the effect of the cross-section shape on the jet penetration depth is very limited. The penetration depth changes little even when the aspect ratio changes from 1 to 4. This is because the penetration depth is mainly affected by the drag force; though the aspect ratio changes a lot, the drag force still changes very little for jets with the same penetration velocity and cross-section area.

4.3 Jet Breakup Length

The jet breakup length, the distance from free surface to the breakup point, is an important parameter to evaluate whether molten corium will directly come in contact with the lower plenum of the pressure vessel before it sufficiently breaks up.

TABLE 3 | Parameters in physical units and lattice units.

	Parameters in physical units									
	D[m]	V[m/s]	ρ_r[kg/m^3]	ρ_b[kg/m^3]	ν_r[m^2/s]	ν_b[m^2/s]	g[m/s^2]	σ[N/m]	γ	Re
Case 1, 4, 7, 10	0.01	2.21	8,302	978	7.35e-7	4.13e-7	9.81	0.484	8.49	3.01e4
Case 2, 5, 8, 11	0.01	4.43	8,302	978	7.35e-7	4.13e-7	9.81	0.484	8.49	6.03e4
Case 3, 6, 9, 12	0.01	8.85	8,302	978	7.35e-7	4.13e-7	9.81	0.484	8.49	1.20e5
	Parameters in lattice units									
	D^*	V^*	ρ_r^*	ρ_b^*	ν_r^*	ν_b^*	g^*	σ^*	γ	Re
Case 1, 4, 7, 10	30	0.1	1	0.118	9.98e-5	5.61e-5	6.70e-6	3.58e-4	8.49	3.01e4
Case 2, 5, 8, 11	30	0.1	1	0.118	4.98e-5	2.80e-5	1.67e-6	8.91e-5	8.49	6.03e4
Case 3, 6, 9, 12	30	0.1	1	0.118	2.49e-5	1.40e-5	4.18e-7	2.23e-5	8.49	1.20e5

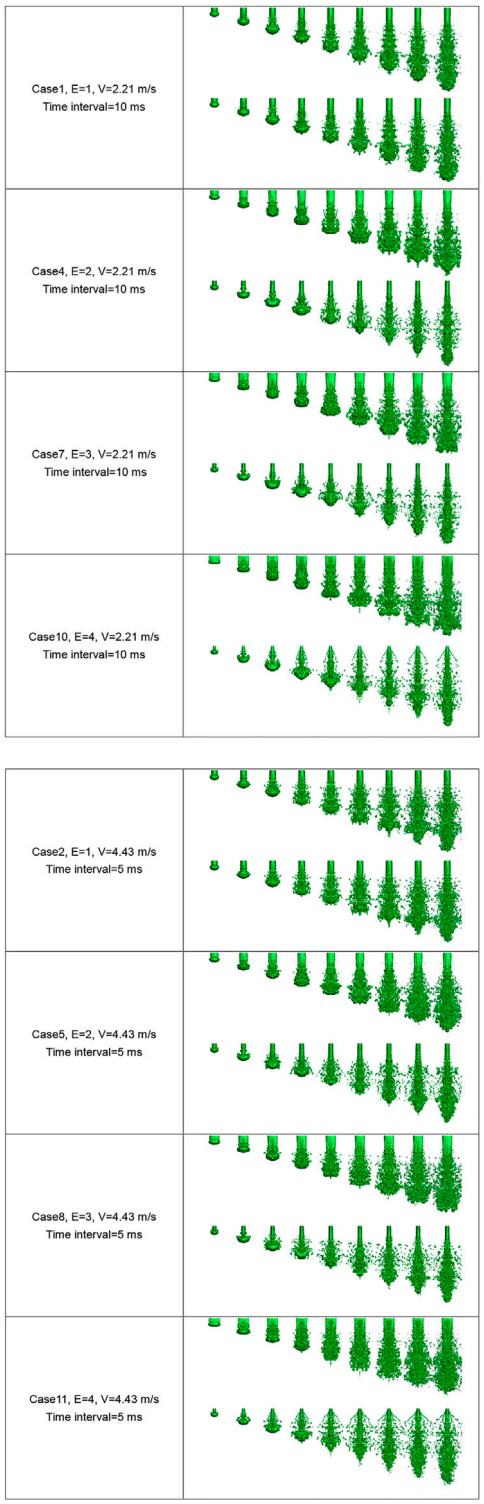

FIGURE 2 | Snap shots of corium jet breakup processes in the 12 cases.

Once the length is longer than the water depth, the pressure vessel is likely to be melted through by the molten corium, which might cause the radioactive material leakage (Iwasawa and Abe 2018). In the melt jet breakup experiments, the jet breakup length usually can hardly be measured directly from the observation because the jet column is covered by lots of fragments similar to those in **Figure 2**, while with the simulations in the current study, the jet breakup length can be easily extracted from the middle cross-sectional density contours as shown in **Figure 4**, where Case 4 and Case 10 are presented. The breakup position can be easily observed from these figures. It should be noted that the jet column may break up in one middle cross-section view (e.g., major axis direction) but actually still connect in another middle cross-section view (e.g., minor axis direction) since the jet morphology is not axially symmetric. Hence, the jet column should be disconnected in both views when checking the breakup point. Furthermore, the breakup point usually fluctuates during the penetration process; here, the maximum jet breakup length is used as the jet breakup length in this study.

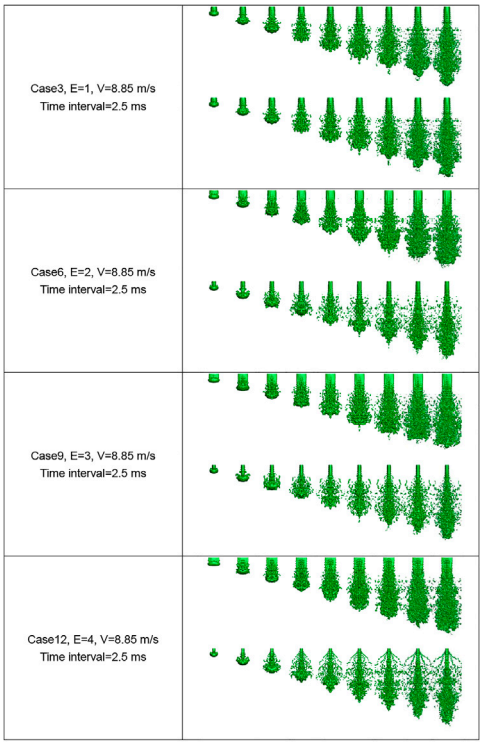

FIGURE 2 | (Continued).

The dimensionless jet breakup length is defined as

$$\frac{L_{brk}}{D}\Big/\left(\frac{\rho_j}{\rho_c}\right)^{0.5}, \tag{35}$$

where L_{brk} is the jet breakup length, the area equivalent diameter D is 10 mm for all 12 cases, ρ_j is the density of the jet, and ρ_c is the density of the water.

The dimensionless jet breakup length versus aspect ratio in the 12 cases is shown in **Figure 5**. First, it is clear that with the

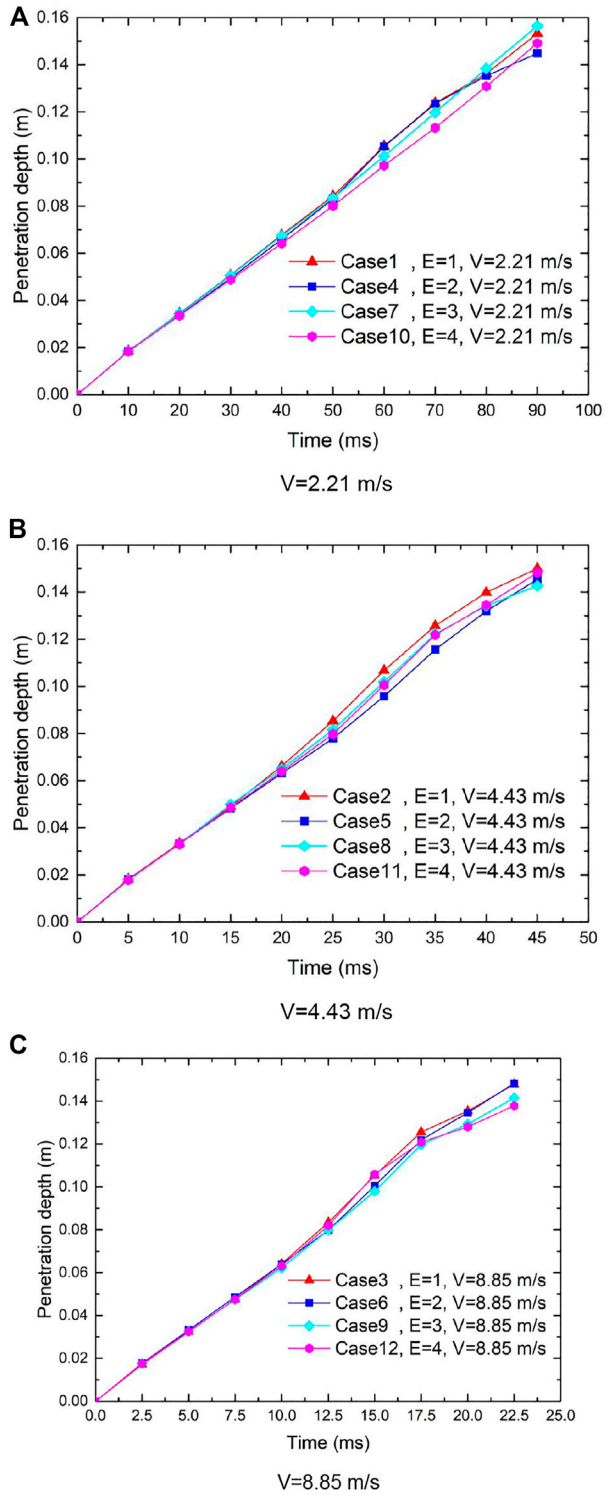

FIGURE 3 | Jet penetration depth vs. time.

increase in the penetration velocity under the same aspect ratio, the breakup length decreases gradually. This is because higher penetration velocity will enhance the stripping from the jet column due to the Kelvin–Helmholtz instability, and the material is removed from the jet column faster, which leads to the faster disconnection of the jet column and the shorter breakup length.

It can also be found that with the increase in the aspect ratio under the same penetration velocity, the jet breakup length decreases gradually. This can be explained as follows: The intensity of the stripping is determined not only by the penetration velocity but also by the contact area between the jet and water, since the contact area increases with the increase in the aspect ratio under the same cross-section area, namely, the jet becomes flat, and the stripping is enhanced. On the other hand, the thickness of the jet along the minor axis direction becomes smaller with the increase in the aspect ratio. Hence, the jet column is easier to break up due to stripping at a higher aspect ratio. This phenomenon can be clearly observed in **Figure 4** by comparing Case 4 and Case 10 with an aspect ratio of 2 and 4, respectively.

4.4 Degree of the Fragmentation

Since the fragments generated during the jet penetration process are mostly irregular as shown in **Figure 2**, direct measurement of the fragment size will introduce large errors. In this work, the dimensionless corium surface area is used to evaluate the degree of the jet fragmentation. First, the interface between the corium and water is extracted from the simulation results as shown in **Figure 2**; then, the interface area S is calculated, and the dimensionless corium surface area is given by

$$\bar{S} = \frac{S}{\pi D^2/4}. \tag{36}$$

The dimensionless corium surface area versus aspect ratio at approximately the same penetration depth (V*t) in the 12 cases is presented in **Figure 6**. It can be seen that the dimensionless corium surface area increases with the increase in the penetration velocity for the jets with the same aspect ratio, that is, smaller fragments are generated with the increase in the penetration velocity. This is because higher penetration velocity means stronger momentum exchange and stripping, leading to more fragments.

Another observation is that, in general, the dimensionless corium surface area increases with the increase in the aspect ratio for the jets under the same penetration velocity. This trend is not obvious at low penetration velocity (e.g., V = 2.21 m/s), but remarkable at high penetration velocities. The reason has been explained in Section 4.3, namely, with the increase in the aspect ratio under the same cross-section area, the contact area between the jet and water is increased, which enhances the stripping and facilitates the jet fragmentation.

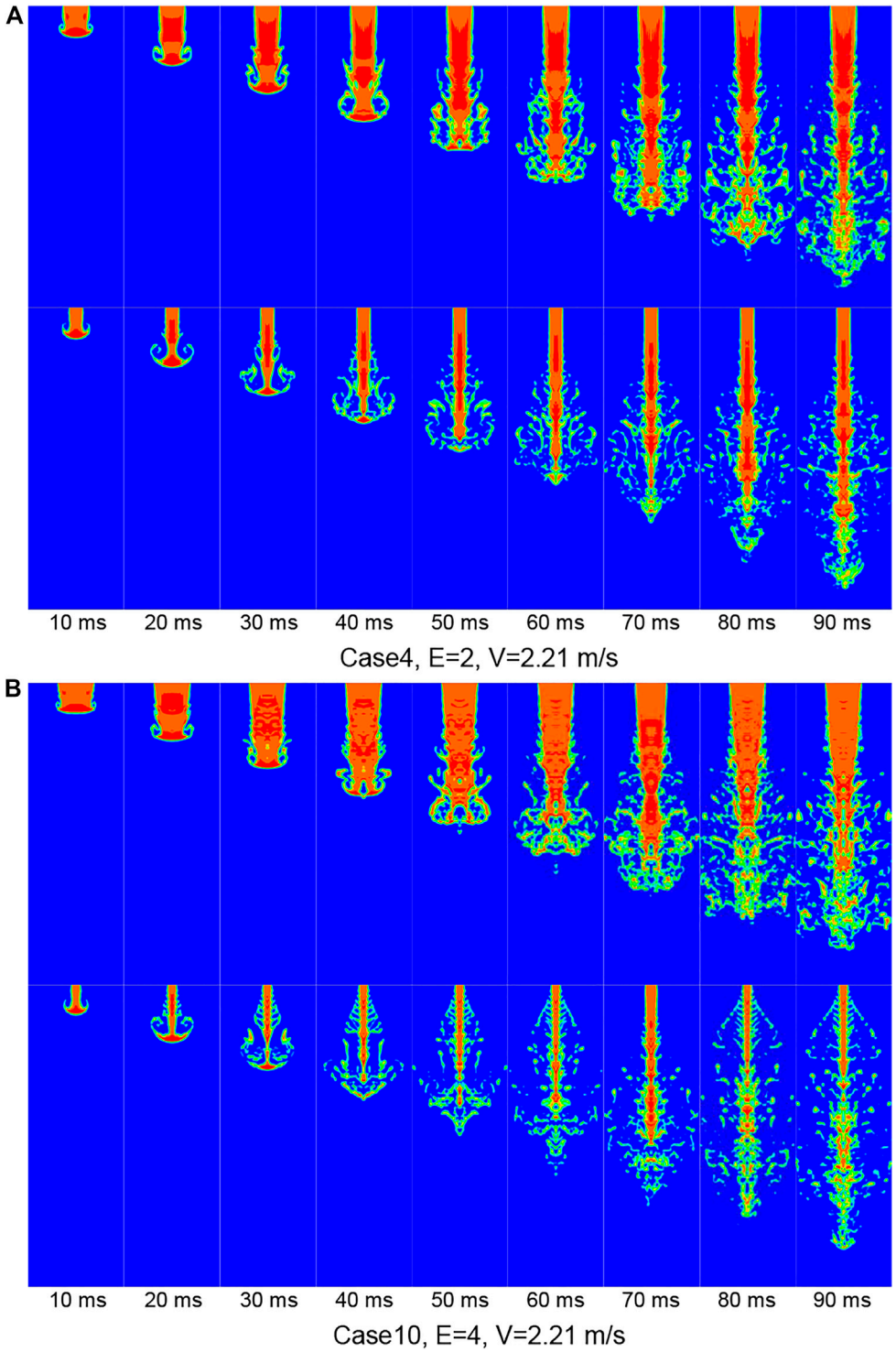

FIGURE 4 | Middle cross-sectional density contours along both major axis direction and minor axis direction.

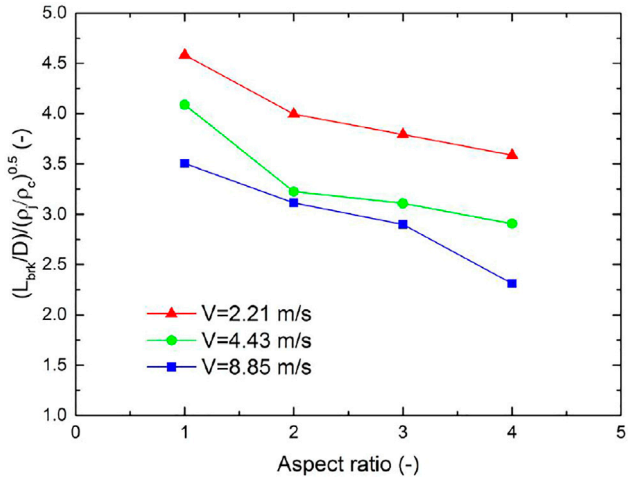

FIGURE 5 | Dimensionless jet breakup length vs. aspect ratio in the 12 cases.

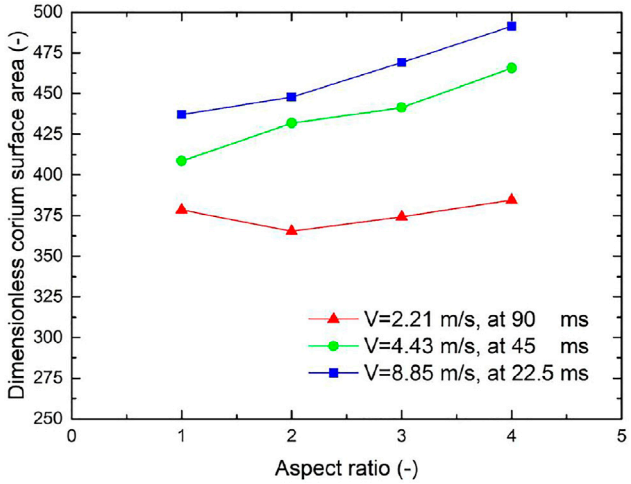

FIGURE 6 | Dimensionless corium surface area vs. aspect ratio at approximately the same penetration depth in the 12 cases.

5 CONCLUSION

In order to investigate the effect of jet cross-section shape on the corium jet breakup behavior, which is generally ignored in previous studies, in this study, the breakup processes of the corium jets with four different elliptical cross-section shapes and three different penetration velocities are simulated with the state-of-the-art GPU-accelerated color-gradient lattice Boltzmann method. The effect of the cross-section shape on the hydrodynamic breakup behavior of the corium jet is analyzed in detail. Three main conclusions drawn from the simulation results are as follows:

(1) The effect of the cross-section shape on the jet penetration depth is very limited because the change of the drag force is very small for jets with the same penetration velocity and cross-section area.
(2) With the increase in the aspect ratio under the same penetration velocity, the jet breakup length decreases gradually mainly due to the decrease in the thickness of the jet along the minor axis direction.
(3) In general, the dimensionless corium surface area increases with the increase in the aspect ratio for the jets under the same penetration velocity since the contact area increases with the increase in the aspect ratio under the same cross-section area.

DATA AVAILABILITY STATEMENT

The raw data supporting the conclusions of this article will be made available by the authors, without undue reservation.

AUTHOR CONTRIBUTIONS

HC contributed to the conception and simulations of this study and writing the manuscript; SC and JW contributed to manuscript revision and read and approved the submitted version.

FUNDING

This work was supported by the Fundamental Research Funds for the Central Universities of Sun Yat-sen University (No. 2021qntd12), the basic and applied basic research foundation of Guangdong province (No. 2021A1515010343), and the Science and Technology Program of Guangdong Province (No. 2021A0505030026).

REFERENCES

Abe, Y., Matsuo, E., Arai, T., Nariai, H., Chitose, K., Koyama, K., et al. (2006). Fragmentation Behavior during Molten Material and Coolant Interactions. *Nucl. Eng. Des.*236, 1668–1681. doi:10.1016/j.nucengdes.2006.04.008

Ba, Y., Liu, H., Li, Q., Kang, Q., and Sun, J. (2016). Multiple-relaxation-time Color-Gradient Lattice Boltzmann Model for Simulating Two-phase Flows with High Density Ratio. *Phys. Rev. E*94, 023310. doi:10.1103/PhysRevE.94.023310

Bürger, M., Cho, S. H., Berg, E. v., and Schatz, A. (1995). Breakup of Melt Jets as Pre-condition for Premixing: Modeling and Experimental Verification. *Nucl. Eng. Des.*155, 215–251. doi:10.1016/0029-5493(94)00875-y

Cheng, H., Chen, X., Ye, Y., and Cheng, S. (2021a). Systematic Experimental Investigation on the Characteristics of Molten lead-bismuth Eutectic Fragmentation in Water. *Nucl. Eng. Des.*371, 110943. doi:10.1016/j.nucengdes.2020.110943

Cheng, H., Cheng, S., and Zhao, J. (2020). Study on Corium Jet Breakup and Fragmentation in Sodium with a GPU-Accelerated Color-Gradient Lattice Boltzmann Solver. *Int. J. Multiphase Flow*126, 103264. doi:10.1016/j.ijmultiphaseflow.2020.103264

Cheng, H., Zhao, J., Saito, S., and Cheng, S. (2021b). Study on Melt Jet Breakup Behavior with Nonorthogonal central-moment MRTColor-Gradient Lattice Boltzmann Method. *Prog. Nucl. Energ.*136, 103725. doi:10.1016/j.pnucene.2021.103725

Cheng, H., Zhao, J., and Wang, J. (2019). Experimental Investigation on the Characteristics of Melt Jet Breakup in Water: The Importance of Surface Tension and Rayleigh-Plateau Instability. *Int. J. Heat Mass Transfer*132, 388–393. doi:10.1016/j.ijheatmasstransfer.2018.12.026

Corradini, M. L., Kim, B. J., and Oh, M. D. (1988). Vapor Explosions in Light Water Reactors: A Review of Theory and Modeling. *Prog. Nucl. Energ.*22, 1–117. doi:10.1016/0149-1970(88)90004-2

Dinh, T. N., Bui, V. A., Nourgaliev, R. R., Green, J. A., and Sehgal, B. R. (1999). Experimental and Analytical Studies of Melt Jet-Coolant Interactions: a Synthesis. *Nucl. Eng. Des.*189, 299–327. doi:10.1016/s0029-5493(98)00275-1

Huang, H., Sukop, M., and Lu, X. (2015). *Multiphase Lattice Boltzmann Methods: Theory and Application*.

Huhtiniemi, I., Magallon, D., and Hohmann, H. (1999). Results of Recent KROTOSFCI Tests: Alumina versus Corium Melts. *Nucl. Eng. Des.*189, 379–389. doi:10.1016/s0029-5493(98)00269-6

Iwasawa, Y., and Abe, Y. (2018). Melt Jet-Breakup and Fragmentation Phenomena in Nuclear Reactors: A Review of Experimental Works and Solidification Effects. *Prog. Nucl. Energ.*108, 188–203. doi:10.1016/j.pnucene.2018.05.009

Kim, W. K., Shim, J. H., and Kaviany, M. (2017). Thermophysical Properties of Liquid UO2, ZrO2 and Corium by Molecular Dynamics and Predictive Models. *J. Nucl. Mater.*491, 126–137. doi:10.1016/j.jnucmat.2017.04.030

Kirillov, P. (2006). *Thermo Physical Properties of Materials for Nuclear Engineering*. Obninsk: Institute for heat and mass transfer in nuclear power plants.

Kolev, N. I. (2015). *Multiphase Flow Dynamics 5: Nuclear thermal Hydraulics*. Springer.

Krüger, T., Kusumaatmaja, H., Kuzmin, A., Shardt, O., Silva, G., and Viggen, E. M. (2016). *The Lattice Boltzmann Method - Principles and Practice*.

Leclaire, S., Parmigiani, A., Malaspinas, O., Chopard, B., and Latt, J. (2017). Generalized Three-Dimensional Lattice Boltzmann Color-Gradient Method for Immiscible Two-phase Pore-Scale Imbibition and Drainage in Porous media. *Phys. Rev. E*95, 033306. doi:10.1103/PhysRevE.95.033306

Saito, S., Abe, Y., and Koyama, K. (2017). Lattice Boltzmann Modeling and Simulation of Liquid Jet Breakup. *Phys. Rev. E*96, 013317f. doi:10.1103/PhysRevE.96.013317

Saito, S., De Rosis, A., Festuccia, A., Kaneko, A., Abe, Y., and Koyama, K. (2018). Color-gradient Lattice Boltzmann Model with Nonorthogonal central Moments: Hydrodynamic Melt-Jet Breakup Simulations. *Phys. Rev. E*98, 013305. doi:10.1103/PhysRevE.98.013305

Schins, H. (1978). On the Surface Tension of Liquid UO2. *J. Nucl. Mater.*78, 215–216. doi:10.1016/0022-3115(78)90521-4

Shen, P., Zhou, W., Cassiaut-Louis, N., Journeau, C., Piluso, P., and Liao, Y. (2018). Corium Behavior and Steam Explosion Risks: A Review of Experiments. *Ann. Nucl. Energ.*121, 162–176. doi:10.1016/j.anucene.2018.07.029

Spencer, B., Wang, K., Blomquist, C., Mcumber, L., and Schneider, J. (1994). *Fragmentation and Quench Behavior of Corium Melt Streams in Water". Nuclear Regulatory Commission*. Washington, DCIL (United States)): United States. Div. of Systems Research; Argonne National Lab..

Thakre, S., Manickam, L., and Ma, W. (2015). A Numerical Simulation of Jet Breakup in Melt Coolant Interactions. *Ann. Nucl. Energ.*80, 467–475. doi:10.1016/j.anucene.2015.02.038

Zhou, Y., Chen, J., Zhong, M., Wang, J., and Lv, M. (2017). Numerical Simulation of Metal Jet Breakup, Cooling and Solidification in Water. *Int. J. Heat Mass Transfer*109, 1100–1109. doi:10.1016/j.ijheatmasstransfer.2017.02.083

Conflict of Interest: The authors declare that the research was conducted in the absence of any commercial or financial relationships that could be construed as a potential conflict of interest.

Publisher's Note: All claims expressed in this article are solely those of the authors and do not necessarily represent those of their affiliated organizations, or those of the publisher, the editors, and the reviewers. Any product that may be evaluated in this article, or claim that may be made by its manufacturer, is not guaranteed or endorsed by the publisher.

Copyright © 2022 Cheng, Cheng and Wang. This is an open-access article distributed under the terms of the Creative Commons Attribution License (CC BY). The use, distribution or reproduction in other forums is permitted, provided the original author(s) and the copyright owner(s) are credited and that the original publication in this journal is cited, in accordance with accepted academic practice. No use, distribution or reproduction is permitted which does not comply with these terms.

frontiers in Energy Research

ORIGINAL RESEARCH
published: 14 February 2022
doi: 10.3389/fenrg.2022.839667

Vessel Failure Analysis of a Boiling Water Reactor During a Severe Accident

H. D. Wang, Y. L. Chen and W. Villanueva*

Division of Nuclear Power Safety, Royal Institute of Technology (KTH), Stockholm, Sweden

In a postulated severe accident, the thermo-mechanical loads from the corium debris that has relocated to the lower head of the reactor pressure vessel (RPV) can pose a credible threat to the RPV's structural integrity. In case of a vessel breach, it is vital to predict the mode and timing of the vessel failure. This affects the ex-vessel accident progression and plays a critical role in the development of mitigation strategies. We propose a methodology to assess RPV failure based on MELCOR and ANSYS Mechanical APDL simulations. A Nordic-type boiling water reactor (BWR) is considered with two severe accident scenarios: i) SBO (Station Blackout) and ii) SBO + LOCA (Loss of Coolant Accident). In addition, the approach considers the dynamic ablation of the vessel wall due to a high-temperature debris bed with the use of the *element kill* function in ANSYS. The results indicate that the stress failure mechanism is the major cause of the RPV failure, compared to the strain failure mechanism. Moreover, the axial normal stress and circumferential normal stress make the dominant contributions to the equivalent stress σ at the lower head of RPVs. As expected, the region with high ablation is most likely the failure location in both SBO and SBO + LOCA. In addition, comparisons of the failure mode and timing between SBO and SBO + LOCA are described in detail. A short discussion on RPV failure between ANSYS and MELCOR is also presented.

Keywords: severe accident, reactor pressure vessel, structural integrity, finite element analysis, vessel failure criteria

OPEN ACCESS

Edited by:
Jun Wang,
University of Wisconsin-Madison, United States

Reviewed by:
Muritala Amidu,
Khalifa University, United Arab Emirates
Shanfang Huang,
Tsinghua University, China

****Correspondence:***
H. D. Wang
Hongdi@kth.se

Specialty section:
This article was submitted to Nuclear Energy, a section of the journal Frontiers in Energy Research

Received: *20 December 2021*
Accepted: *12 January 2022*
Published: *14 February 2022*

Citation:
Wang HD, Chen YL and Villanueva W (2022) Vessel Failure Analysis of a Boiling Water Reactor During a Severe Accident. Front. Energy Res. 10:839667. doi: 10.3389/fenrg.2022.839667

INTRODUCTION

The Fukushima nuclear accident occurred in 2011, stemming from a strong earthquake and a subsequent tsunami that induced a station blackout (SBO) scenario (Naitoh et al., 2013a; Kaneko et al., 2015; Pellegrini et al., 2016). In this scenario, the nuclear power plants (NPPs) experienced serious damage due to the loss of off-site power, resulting in the leakage of large amount of radioactive material to the environment. The reactor pressure vessel (RPV) of a light water reactor is one of the key safety barriers that prevent the release of radioactive substances to the environment. Thus, analyses of RPV failure are warranted to provide insights into the reactor's accident progression and develop effective mitigation strategies.

Abbreviations: ADS, automatic depressurization system; BWR, boiling water reactor; FE, finite lement; NPP, nuclear power plant; NISO, nonlinear isotropic; RPV, reactor pressure vessel; SA, severe accident; SBO, station blackout; SBO + LOCA, station blackout with loss of coolant accident.

TABLE 1 | Examples from the literature (Ikonen, 1999; Koundy et al., 2005; Villanueva et al., 2012b; Kaneko et al., 2015; Mao et al., 2016b; Mao et al., 2017) of strain- and stress-based failure criteria used in structural analysis of RPVs.

Authors	Objective	Platform/approach	Failure criteria
Mao et al. (2016b); Mao et al. (2017)	AP600	ABAQUS	Strain- and stress-based criteria
Koundy et al. (2005)	Generic PWR	Analytical FE models	Strain- and stress-based criteria
Kaneko et al. (2015)	Low-alloy steel of RPV	Codes for Nuclear Power Generation Facilities	Stress-based criterion
Villanueva et al. (2012b)	Nordic BWR	ANSYS APDL	Strain- and stress-based criteria
Ikonen, (1999)	RUPTHER# 14	PASULA	Strain- and stress-based criteria

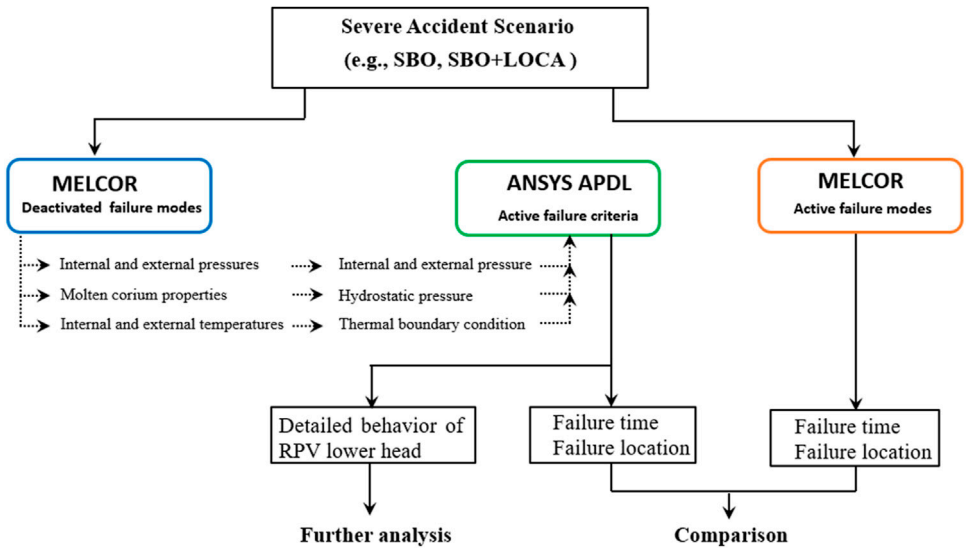

FIGURE 1 | Framework of thermo-mechanical analysis for a Nordic BWR with SBO and SBO + LOCA scenarios.

TABLE 2 | Major parameters and settings of the Nordic BWR in MELCOR.

Setting in MELCOR	State	Parameters	Values
Considered accident events	SBO/SBO + LOCA	Nominal power	3,000 MWth
Automatic depressurization system	On	Vessel lower plenum radius	3.2 m
Emergency core cooling system	Off	Vessel lower plenum height	5.398 m
Penetration model and failure	Off	Vessel lower head thickness	0.198 m
Mitigation strategies	Ex-vessel retention by cavity flooding	—	—

During a severe accident, molten core materials and internal structures, also known as corium, can relocate to the lower head of the RPV and form a debris bed. This debris bed can threaten the integrity of the RPV lower head with four possible failure modes: lower head global rupture, melt impingement and melt-through, penetration tube heats up and ruptures, and penetration tube ejection (Naitoh et al., 2013b; Herranz et al., 2015; Li et al., 2014; Mao et al., 2017; Yue et al., 2020; Willschütz et al., 2003; Siegele et al., 1999; Rempe et al., 1993). The structural behavior of the RPV is a complex phenomenon, including the macro-structural global deformation (i.e., the displacement of the RPV lower head) and the micro-structural stress-strain responses. From the global point of view, the failure deformation of the vessel lower head has not been explicitly characterized in the field of RPV structural integrity due to its different effects on various shapes and sizes of RPVs. So the deformation is commonly used as a supplementary in a specific RPV application (Mao et al., 2016a; Villanueva et al., 2012a) and a validation for the finite element analysis (FEA) (Sehgal et al., 2003; Devos et al., 1999). However, the material properties can be characterized by the tensile-creep tests under various temperatures and loadings, providing the limits of the stress and strain for certain carbon steel (Humphries and Chu, 2002). One can find that the stress and strain mechanisms are the major factors initiating the RPV failure, and the failure criterion based on the stress-strain response is widely implemented in the failure analysis of the RPV lower head (see **Table 1** for examples)

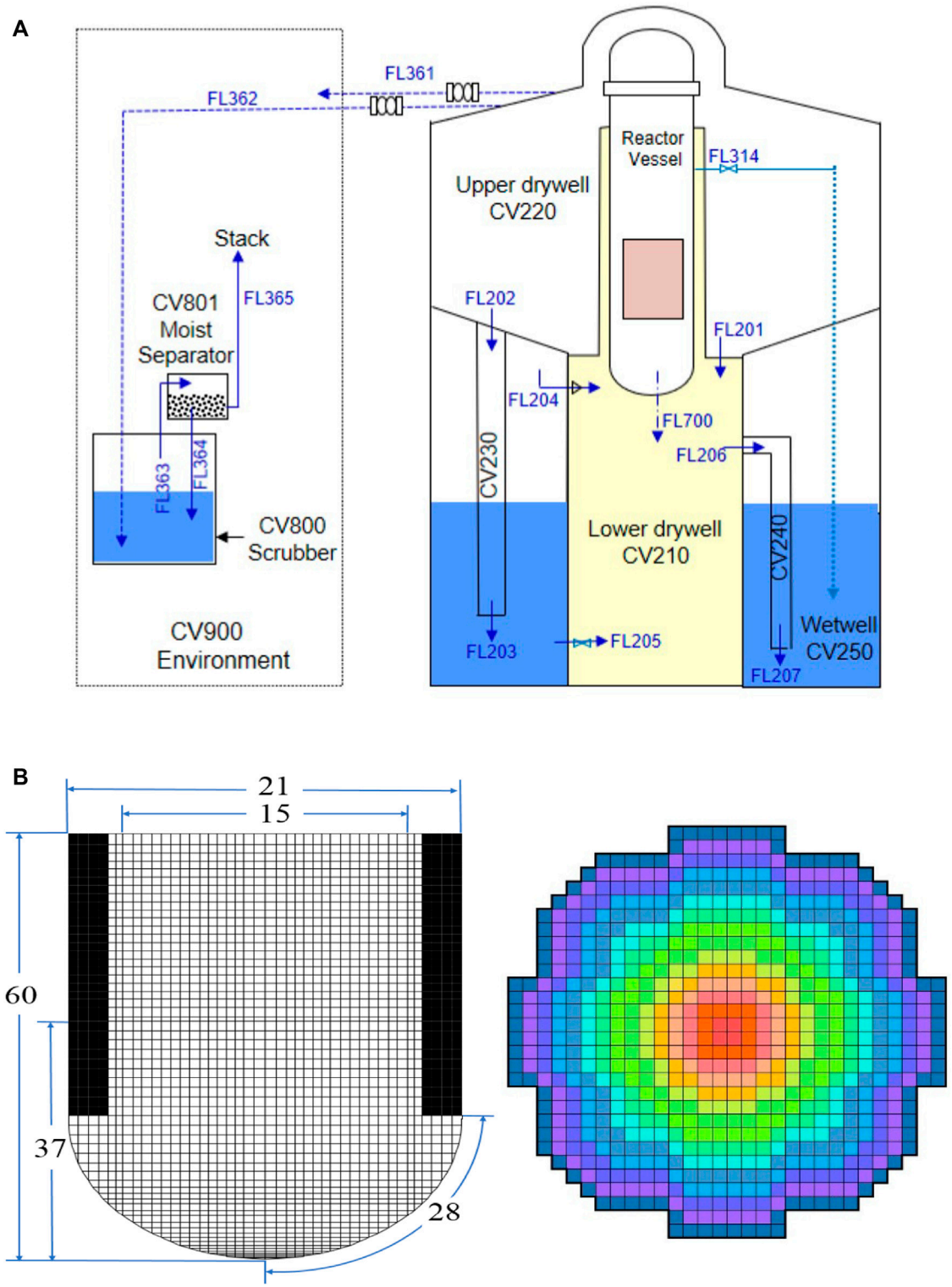

FIGURE 2 | (A) Schematic of the containment nodalization of a Nordic BWR, **(B)** fine nodalization in the COR package of MELCOR, and **(C)** group of fuel assemblies for radial rings (Chen et al., 2019).

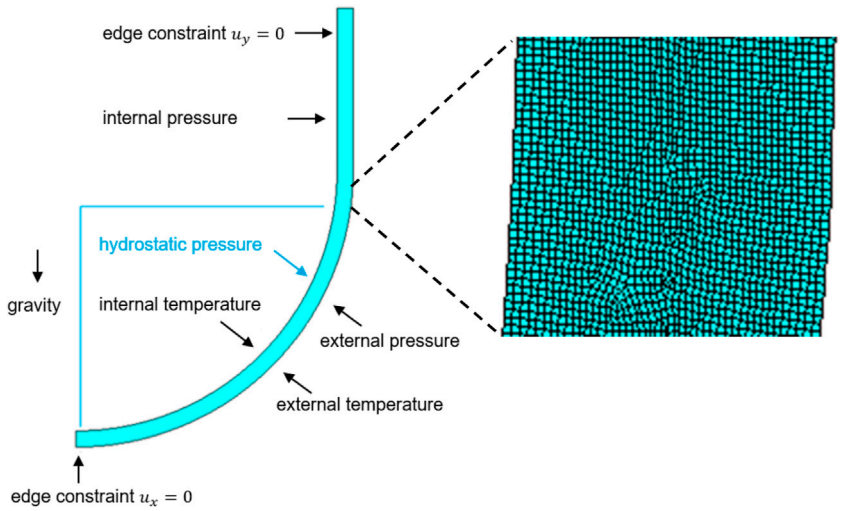

FIGURE 3 | 2D axisymmetric geometry of the ablated RPV, loads, constraints, and the mesh.

(Ikonen, 1999; Koundy et al., 2005; Villanueva et al., 2012b; Kaneko et al., 2015; Mao et al., 2016b; Mao et al., 2017). When the equivalent stress of the RPV lower head exceeds the material strength, RPV failure occurs. The creep strain also cannot be ignored because the vessel can undergo creep failure when the temperature exceeds a certain level for an extended period even at low pressures (Rempe et al., 1993; Callister and Rethwisch, 2011). In the present study, we pay particular attention to the failure mode and timing of a Nordic-type BWR vessel under the SBO and SBO + LOCA events from the perspective of micro-structural stress-strain responses, as well as considering its macro-structural global deformation. The heat exchange between the debris bed and the RPV wall is not constant; hence, the stress and the strain across the vessel wall behave in a transient way. To investigate the changing conditions of RPVs under accident scenarios, a one-way coupling method has been developed using MELCOR and ANSYS Mechanical APDL codes. By taking transient thermo-mechanical loadings as boundary conditions, the failure mechanism of the vessel lower head is investigated in detail, and its failure location and timing are also predicted for the worst scenarios (i.e., SBO and SBO + LOCA).

Since the temperature at the inner surface of the RPV may exceed the local melting of the vessel wall which can lead to an ablation of the wall, it is important to investigate the structural behavior of the RPV with an ablated profile. To simplify the calculation, the geometry of the ablated vessel wall is mostly assumed to be constant during the structural analysis in previous study (Sehgal et al., 2003; Wang et al., 2021). However, the temperature of the vessel wall has a gradient across the thickness and continues to increase due to the continuous heat transfer from the corium debris bed. This debris bed is expected to fill the ablated region in the wall and produce further ablation at the inner surface of the vessel wall (Zhan et al., 2018). Accordingly, the vessel wall becomes thinner and thinner as the accident progresses, which is supposed to be much weaker to withstand the certain loads than before (Matejovic et al., 2017). Thus, it is possibly accurate to take the change of vessel thickness into account when predicting the timing and mode of RPV failure. For that, the approach "element killing" is adopted in the structural analysis in the present study, updating the vessel profile regularly according to the transient temperature. The thermal and mechanical response of the RPV lower head is then investigated based on the dynamic ablation of the vessel wall.

METHODOLOGY AND MODELING

Considering the strengths of MELCOR in modeling accident progression and ANSYS in simulating the structural behavior, the thermo-mechanical analysis is developed based on these two tools. The structural analysis of RPV was implemented in ANSYS while the thermal loads and mechanical loads (i.e., the applied boundary conditions on the RPV in ANSYS) from the debris bed were calculated using MELCOR. In the following sections, the procedure is outlined for this thermo-mechanical analysis, and descriptions of modeling in MELCOR and the Finite Element (FE) model in ANSYS APDL are also presented.

Framework of the Thermo-Mechanical Analysis

MELCOR, as an integral code for severe accidents in an NPP, includes various models or packages [e.g., Core (COR) Package, Decay Heat (DCH) Package, and Cavity (CAV) Package]. These packages can simulate a variety of severe accident phenomena in a severe accident, such as core degradation, fission product release, and hydrodynamics. However, some of these models or packages are simplified to ensure a computationally efficient simulation (Dietrich et al., 2015; Humphries et al., 2017). In this case, some other codes and approaches are adapted to a specific phenomenon in a severe accident, whose

TABLE 3 | Accident progression for the case with deactivated failure modes in MELCOR.

Accident progression	SBO	SBO + LOCA
Initiating accident	0 s	0 s
Downcomer low water level signal state parameters	1,057 s ≈ 18 min	59 s ≈ 1 min
Start of cavity flooding (same with ADS activation)	1,657 s ≈ 28 min	660 s ≈ 11 min
Gap release	2,750 s ≈ 46 min	1,542 s ≈ 26 min
First failure of support plate (the start of core relocation)	7,913 s ≈ 2.20 h	6,183 s ≈ 1.72 h
Last failure of support plate (the end of core relocation)	27296 s ≈ 7.58 h	24659 s ≈ 6.85 h

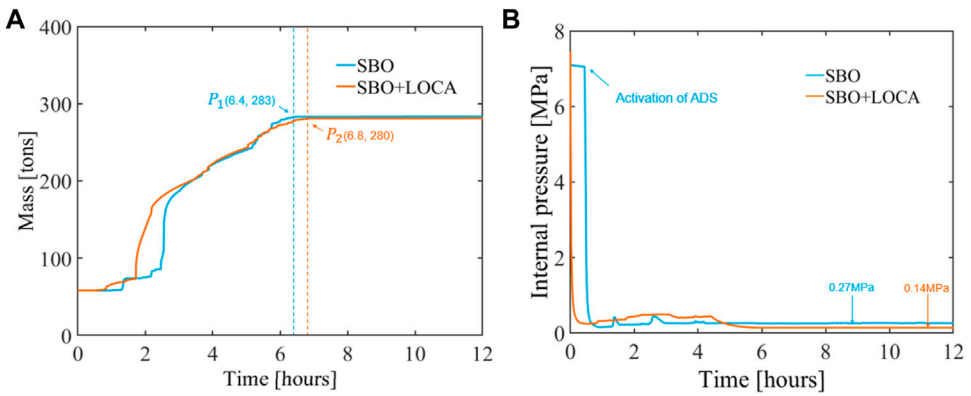

FIGURE 4 | (A) Evolution of total mass in the RPV lower head under SBO and SBO + LOCA scenarios. The total mass stabilizes at $\boldsymbol{P}_1$ and $\boldsymbol{P}_2$ in SBO and SBO + LOCA scenarios, respectively. **(B)** Evolution of RPV internal pressure under SBO and SBO + LOCA scenarios.

roles are complementary to those of MELCOR (Amidu et al., 2021a; Amidu et al., 2021b). In this work, the first aim is to investigate the vessel state (e.g., the stress and the strain) during the Severe Accident (SA), and the second task is to assess the timing and location of RPV failure. In terms of the failure analysis of the RPV lower head, MELCOR has two failure modes (i.e., creep failure based on a life-fractional rule and the yield stress failure criterion), with a description of the failure time and location of RPV failure in the form of an output text file. Thus, detailed information on the structural response of the RPV lower head is limited. In contrast, ANSYS allows users to perform detailed nonlinear analyses using the Finite Element Method (FEM). The FEM can divide the RPV lower head into a finite number of subdomains, addressing the constitutive behavior in each subdomain and recombining them into a global system for the final calculation. This method allows ANSYS to provide more information than just the timing and location of RPV failure for the whole transient calculation. Both global deformation and the stress-strain responses at different locations of the vessel can be accessed for the entire accident progression, which are also important in the assessment of severe accidents and accident mitigation strategies (Humphries and Chu, 2002).

In assessing the structural integrity of the RPV, it is necessary to set up failure criteria. One can take the yield stress or ultimate stress as the stress-based criterion in engineering practice. Compared to the yield stress failure criterion, the ultimate stress failure criterion is a more popular application of RPV failure (Humphries and Chu, 2002; Koundy et al., 2008; Kaneko et al., 2015; Villanueva et al., 2020). This criterion assumes that the structural failure is determined by the material necking. In addition, the strain-based failure criteria are also considered in the present thermo-mechanical analysis because the RPV can undergo strain failure at an elevated temperature even under moderate stresses (Rempe et al., 1993; Callister and Rethwisch, 2011; Villanueva et al., 2012b). That is, we declare RPV failure if any one of the following is satisfied: 1) the von Mises stress exceeds the ultimate stress, 2) creep strain exceeds 20%, or 3) total strain exceeds 25% (Rempe et al., 1993; Wang et al., 2021).

Figure 1 shows the general framework of this research. Given that the occurrence of RPV failure will lead to the release of corium from the RPV to the cavity in MELCOR simulation, we deactivated the failure modes first to simulate the SBO progression, thereby obtaining the thermo-mechanical loads during a longer period. Then these loads are transferred as the boundary conditions for the transient structural analysis with ANSYS, further investigating the behavior of the vessel and predicting its failure time and location based on the failure criteria mentioned above. Also, the accident scenario (i.e., SBO accident or SBO + LOCA accident) with the same conditions was simulated again in MELCOR with the failure modes, and some information about RPV failure can be given using the MELCOR platform. By comparing the timing and location of RPV failure predicted by these two codes, respectively, some insights into the failure analysis on the vessel lower head are provided in the succeeding section.

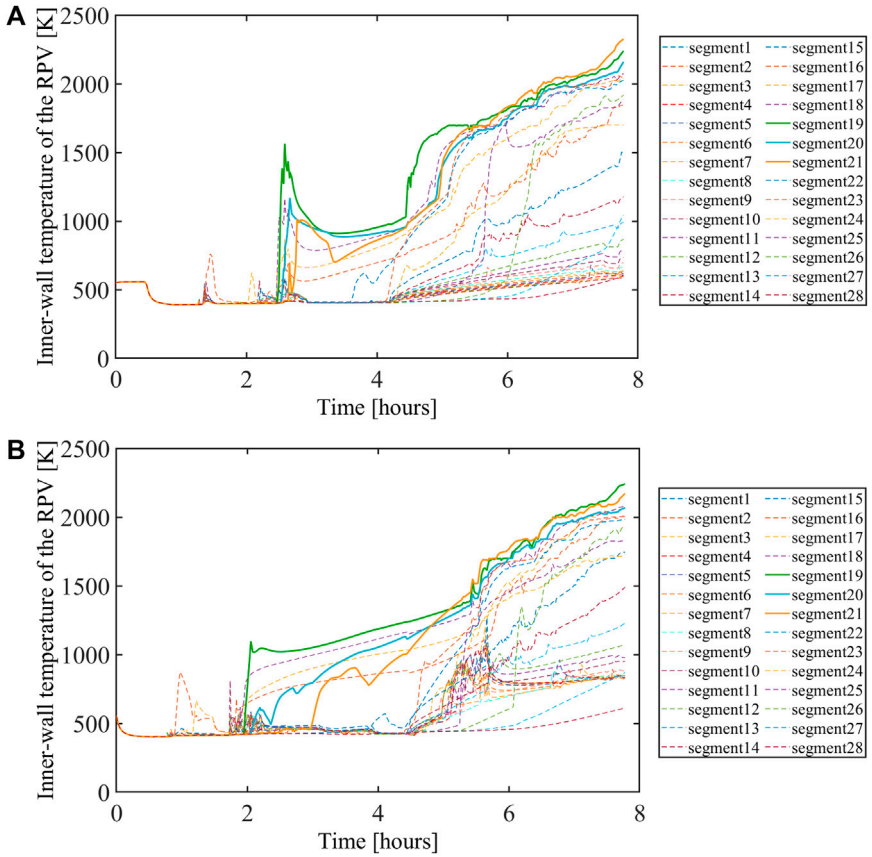

FIGURE 5 | Evolution of **(A)** the inner-wall temperature of the RPV in the SBO case and **(B)** the inner-wall temperature of the RPV in the SBO + LOCA case.

TABLE 4 | Range of polar angles for each segment in the MELCOR model.

Segment number	1	2	3	4	5	6	7
Angle range (°)	0–3.13	3.13–6.27	6.27–8.88	8.88–11.35	11.35–14.13	14.13–16.78	16.78–19.39
Segment number	8	9	10	11	12	13	14
Angle range (°)	19.39–22.46	22.46–25.45	25.45–28.61	28.61–31.94	31.94–35.10	35.10–38.83	38.83–42.28
Segment number	15	16	17	18	19	20	21
Angle range (°)	42.28–46.21	46.21–49.37	49.37–52.74	52.74–55.35	55.35–57.88	57.88–60.93	60.93–63.89
Segment number	22	23	24	25	26	27	28
Angle range (°)	63.89–67.81	67.81–71.62	71.62–75.57	75.57–79.45	79.45–83.28	83.28–87.09	87.09–90

Description of MELCOR Model

The SBO and SBO + LOCA scenarios were assumed to occur in a Nordic BWR with a 3,000 MWth nominal power (Pershagen, 1996). The major parameters of the Nordic BWR and settings in MELCOR are summarized in **Table 2**. The severe accident strategy employed by the Nordic BWR is cavity flooding, which is also considered in the MELCOR simulation. This accident strategy is assumed to activate when the water level in the vessel is below a critical value.

In MELCOR, the thermal-hydraulic response of this reactor was calculated by means of modeling its nodalization (see **Figure 2A**). **Figures 2B,C** show the mesh configuration for the COR package nodalization, which is used to simulate the degradation and relocation of the core in the RPV. As indicated in **Figure 2B**, there are 28 uneven segments along the vessel lower plenum and 21 rings in the radial direction. These radial rings are depicted by various cells and colors, as shown in **Figure 2C**, representing different fuel assemblies and ring groups, respectively.

Description of FE Model

The numerical simulation of the RPV was performed in a 2D axisymmetric geometry as shown in **Figure 3**. As stated above,

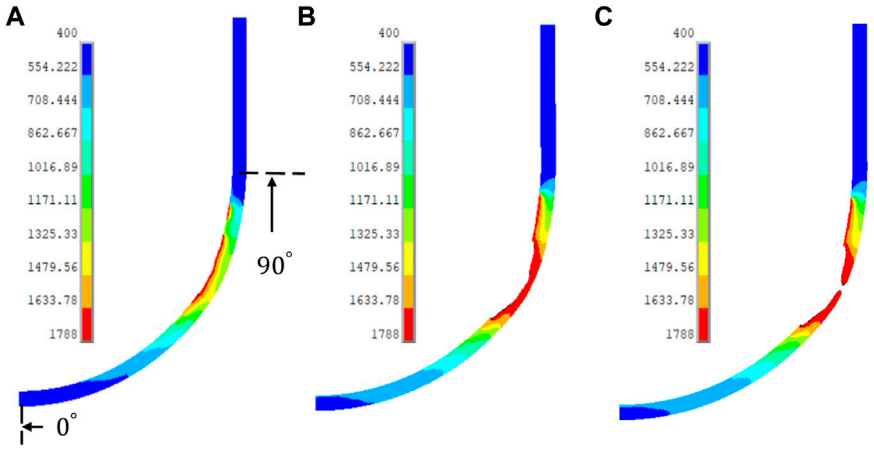

FIGURE 6 | Dynamic ablation for the SBO case: temperature distribution (K) at time **(A)** t = 6 h, **(B)** t = 7.16, and **(C)** t = 7.22 h.

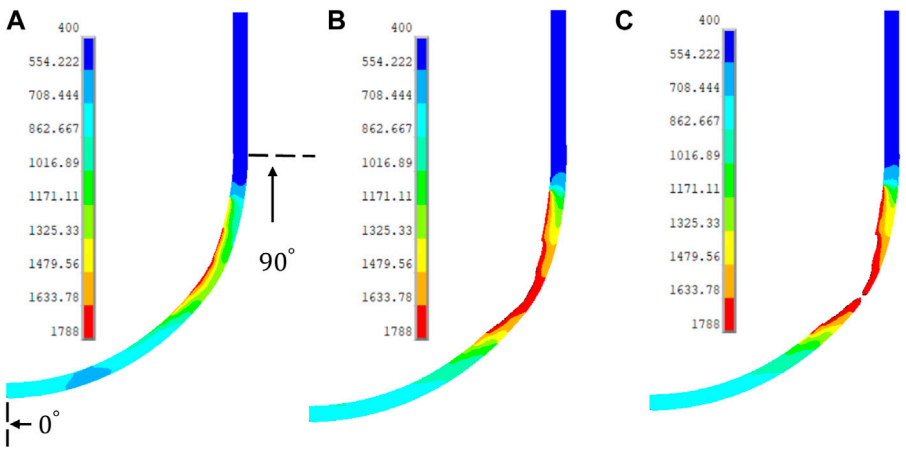

FIGURE 7 | Dynamic ablation for the SBO + LOCA case: temperature distribution (K) at time **(A)** t = 6 h, **(B)** t = 7.16, and **(C)** t = 7.33 h.

the output data from MELCOR (e.g., internal and external surface temperatures of the vessel, internal and external pressures, and the molten corium properties) were transferred as loads and constraints on the RPV for the structural analysis using ANSYS.

Furthermore, the temperature of the vessel wall has a gradient across the thickness and continues to increase due to the continuous heat transfer from the debris bed. This debris bed is expected to fill the ablated region in the wall and produce further ablation at the inner surface of the vessel wall (Zhan et al., 2018). Here, the thermal and mechanical response of the RPV lower head is investigated based on a dynamic ablation process of the vessel wall. First, the RPV geometry is modeled in ANSYS Mechanical APDL with an initial thickness of 0.198 m. Then the "element killing" method is implemented in ANSYS to simulate the dynamic state of vessel ablation, updating the ablated profile of the RPV regularly based on the temperature distribution. In addition, a sufficiently fine mesh (40 element layers across the vessel wall) with a characteristic length of 0.005 m is considered, which is necessary to describe the detailed profile during the ablation process (see **Figure 3**).

Material Properties

The material properties of SA533B1 are considered and adopted from the study by (Rempe et al., 1993), which are all temperature-dependent, including the density, thermal conductivity, specific heat capacity, ultimate strength, coefficient of thermal expansion, and modulus of elasticity. Since most of these data are limited at temperatures of up to 1373K in the reference, a constant-valued extrapolation of the material properties of SA533B1 is used for temperatures above 1373K.

The maximum temperature on the surface of the RPV is beyond the melting point of the vessel material. It is well known that creep occurs when the temperature is higher than 0.3–0.4 times the melting temperature of the material (Gandy, 2007). To account for the creep effect, a modified time hardening model is used and is given by the following:

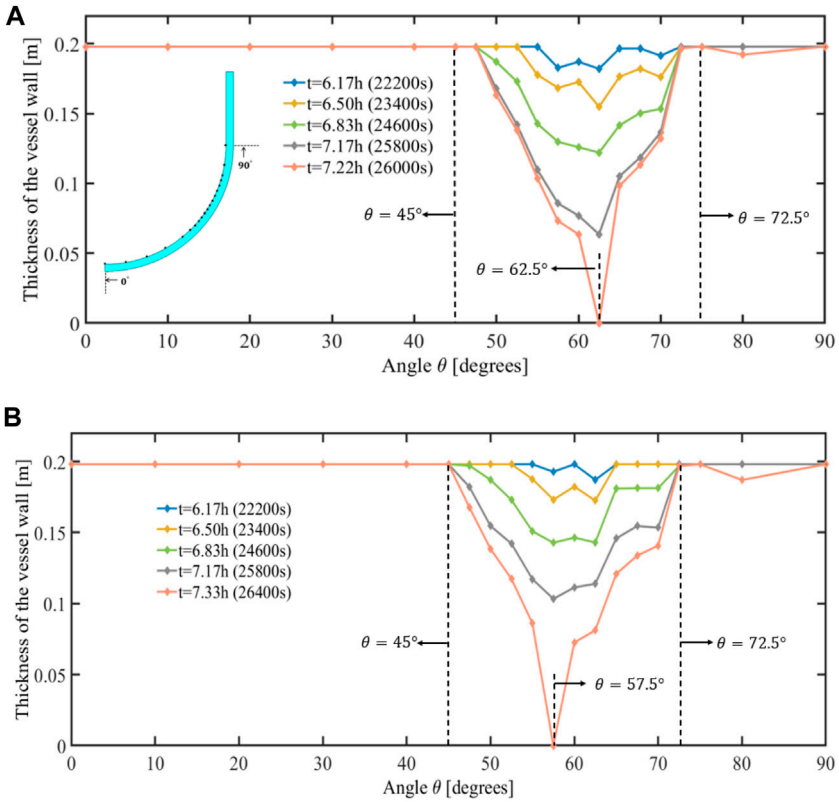

FIGURE 8 | Thickness of the RPV lower head at $t = 6.17$ h, $t = 6.50$ h, $t = 6.83$ h, $t = 7.17$ h, and $t = 7.22$h/7.33 h (the time of melt-through) for **(A)** SBO and **(B)** SBO + LOCA cases.

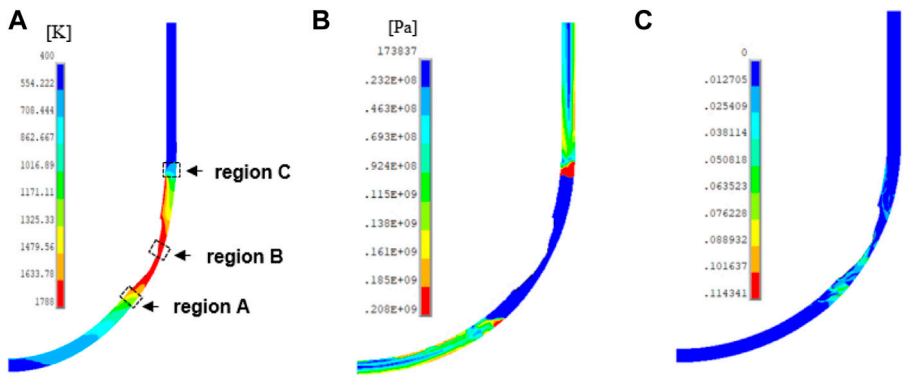

FIGURE 9 | (A) Temperature distribution (K), **(B)** von Mises stress distribution (Pa), and **(C)** creep strain distribution of the vessel wall at time = 7.16 h for the SBO case.

$$\varepsilon_{cr} = \frac{c_1 \sigma^{C_2} t^{C_3+1}}{c_3 + 1} \quad c_1 > 0 \tag{1}$$

where ε_{cr} is equivalent creep strain, t corresponds to the time in seconds at the end of sub-step, δ is the equivalent stress in Pa, and c_i are constants.

In addition to the creep behavior, the elasto-plastic behavior of this material is governed by a nonlinear isotropic (NISO) hardening model (see **Eq. 2**). The detailed values of the parameters and validations of these two models are given in the study by (Wang et al., 2021).

$$\delta_Y = \sigma_0 + R_0 \hat{\varepsilon}^{pl} + R_\infty \left(1 - \exp\left(-b\hat{\varepsilon}^{pl}\right)\right) \tag{2}$$

where δ_Y is the current yield stress, σ_0 is the initial yield stress, $\hat{\varepsilon}^{pl}$ is the accumulated equivalent plastic strain, and R_∞, R_0, and b are material constants.

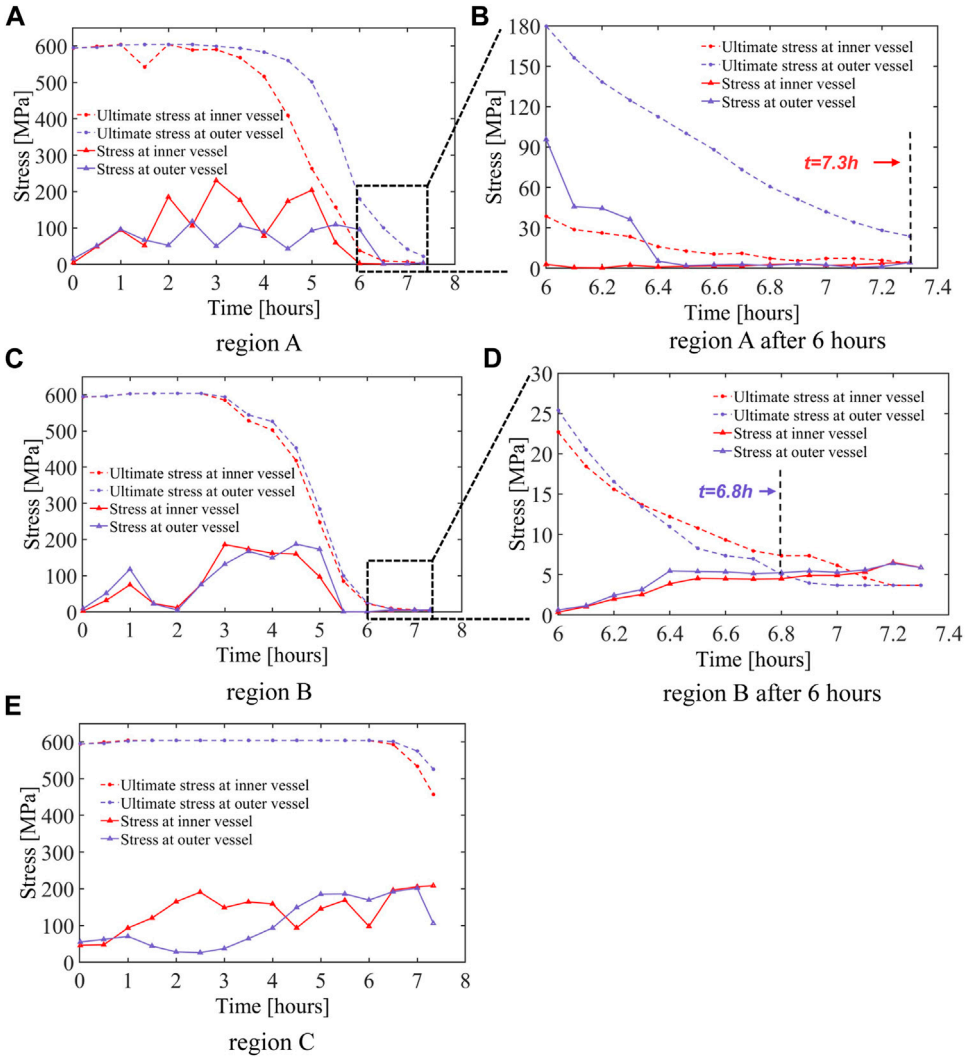

FIGURE 10 | Comparison of von Mises stress of the vessel and SA533B1 ultimate stress at the critical regions for the SBO case; **(A)** region A, **(B)** zoomed-in version of region A after 6 h, **(C)** region B, **(D)** zoomed-in version of region B after 6 h, and **(E)** region C.

RESULTS AND DISCUSSIONS

System Analysis With MELCOR

In this section, some observations are briefly given for the case with deactivated failure modes in MELCOR, as mentioned previously in the framework (see **Figure 1**). The main events of accident progression are listed in **Table 3**.

It should be noted that these output data from MELCOR are used as the input conditions for the detailed structural analysis using ANSYS Mechanical. In **Figure 4A**, the total mass accumulated in the lower head is provided for both SBO and SBO + LOCA cases. The initial mass comprises intact supporting structures and penetration guide tubes. The abrupt increase happens earlier in the SBO + LOCA case, before 2 h, but both follow the same trend after 3 h onward and stabilize around 280 tons after 6 h.

Figure 4B shows the internal pressure evolution of the RPV at the first 12 h. For the SBO case (marked in blue line), the automatic depressurization system (ADS) is active at about half an hour, and the internal pressure before that is maintained at the level of 7 MPa due to the operation of safety relief valves. Subsequently, it dramatically reduces at 0.27 MPa and stabilizes. For the SBO + LOCA case, the vessel pressure decreases dramatically at the very beginning of the accident due to rapid steam release to the containment through the initial break at the main steam line. The ADS system has no effect in this case. The pressure stabilizes at around 0.14 MPa.

Figures 5A,B show the internal temperature evolution for the SBO and SBO + LOCA cases. A significant decrease in temperatures is shown at t = 0.5 h for the SBO case in conjunction with activation of the ADS (see **Figure 5A**). An earlier decrease in temperatures is also shown for the

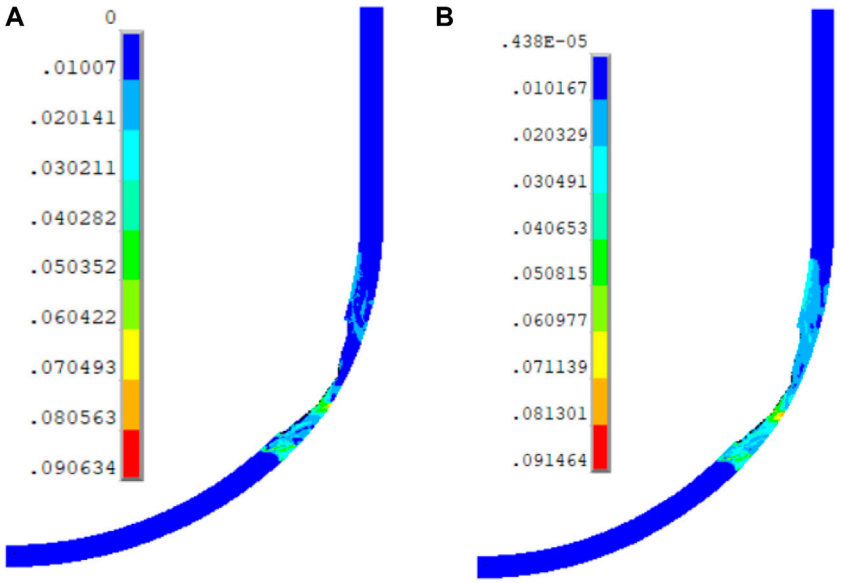

FIGURE 11 | (A) Equivalent creep strain and **(B)** total strain of the vessel wall at time = 6.8 h for the SBO case.

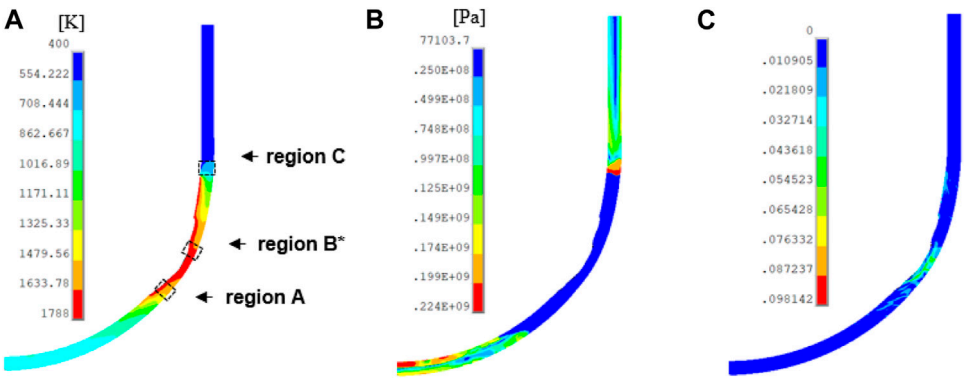

FIGURE 12 | (A) Temperature distribution (K), **(B)** von Mises stress distribution (Pa), and **(C)** creep strain distribution of the vessel wall at time = 7.16 h for the SBO + LOCA case.

SBO + LOCA case due to the main steam line break (see **Figure 5B**). For both SBO and SBO + LOCA cases, segments 19–21 (marked with solid lines in both figures) show higher internal temperatures at the late stage and reach the melting temperature earlier than other segments, at 1789K at 5.88 h and 6.05 h, respectively. Given these data from MELCOR, the temperature of each segment is used as the boundary condition for the vessel surface with a different range of polar angles in the structural analysis (see **Table 4**).

Compared with the SBO case, the steam line breach in SBO + LOCA can accelerate the coolant vaporization and take away some heat (Chen et al., 2019). Accordingly, the results showed significant difference for these two cases from the corium mass, internal pressure, and temperature to the time of melt-through, as well as the external pressure and temperature (not shown). The effect of these differences on the behavior of the RPV is investigated from the structural analyses in the following sections.

Reactor Pressure Vessel Structural Analysis With ANSYS APDL

Reactor Pressure Vessel Ablation

The RPV undergoes an ablation caused by the thermal load from the debris bed, and hence, the thickness of the vessel wall changes during the accident progression. In MELCOR, the residual thickness profile is determined by the inner-wall temperatures, resulting from the debris temperature distribution and heat fluxes directed into the vessel wall. As for the determination of the vessel ablated profile in ANSYS, these inner-wall temperatures as a function of time are directly used as the thermal boundary condition imposed on the vessel wall, deactivating the

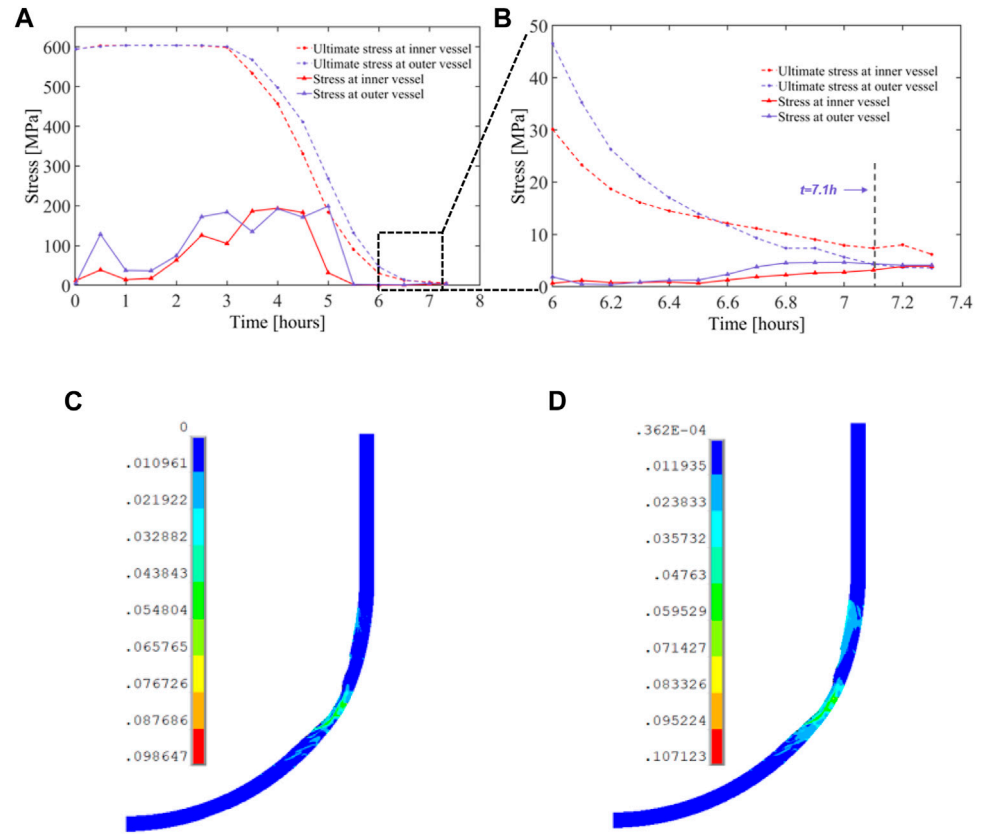

FIGURE 13 | Comparison of von Mises stress of the vessel and SA533B1 ultimate stress at the critical regions for the SBO + LOCA case; **(A)** region B* and **(B)** zoomed-in version of region B* after 6 h. The strain distribution of the vessel at time = 7.1 h for the SBO + LOCA case; **(C)** equivalent creep strain and **(D)** total strain.

elements with zero stiffness when its temperature is higher than the melting point of this material (i.e., the element killing method). Here, the ablated profile of the RPV is updated regularly by eliminating the elements when their corresponding temperature exceeded 1789K, which is the melting point of material SA533B1 (Rempe et al., 1993).

Figures 6, **7** show the dynamic process of RPVs' ablation and temperature distribution and their corresponding times. As expected, the ablation of the vessel wall occurs approximately after t = 6 h for both SBO and SBO + LOCA and becomes worse as time progresses. These severe ablations are concentrated on the upper surface of the RPV lower head, and eventually, a melt-though on the vessel wall happens after 7.22 h for the SBO case and 7.33 h for the SBO + LOCA case.

Figure 8 shows a sequence of five snapshots illustrating the ablation process; these snapshots are obtained by describing the residual thickness at interval 10° along the RPV lower head and 2.5° in the high-ablated area (see the points in **Figure 8A**, inset). The first snapshot is 6.17 h (marked in blue line), at which time the ablation occurred slightly at angle 55°–70° for the SBO case and 55°–65° for the SBO + LOCA case. Furthermore, as the accident progresses, the range of the ablation expands to both sides within the range 45°–72.5°. Similar ablation can be found in the SBO + LOCA case, although the thinnest region in the SBO case (θ = 62.5°) is always higher than the one in the SBO + LOCA case (θ = 57.5°) during the entire time. Close observation of **Figure 8** reveals that at any stage, the thinnest region is always at the same angle and, in addition, melt-through occurs at this angle. The orange lines in **Figures 8A,B** show the location of the RPV breach, at 7.22 and 7.33 h, respectively. These breach times are consistent with the escalation of the internal temperatures in each case (see **Figures 5A,B**).

Stress and Strain Response

As the accident progresses, the stresses and strains of the vessel wall change in time and are both strongly dependent on the temperature. To illustrate the complex and nonlinear behavior of the RPV, we present snapshots of the stress and strain responses of the RPV during the ablation.

The results of temperature, von Mises stress, and creep strain of the vessel wall for the SBO case at t = 7.16 h are shown in **Figure 9**. In **Figure 9A**, the highly ablated area corresponds to the region with higher temperature, where the creep strain is also larger (see **Figure 9C**). However, it is found that the von Mises stress is lower in these regions due to the significant yielding in the regions with high temperature (see **Figure 9B**). Since the thermo-mechanical response of the vessel wall is quite complex,

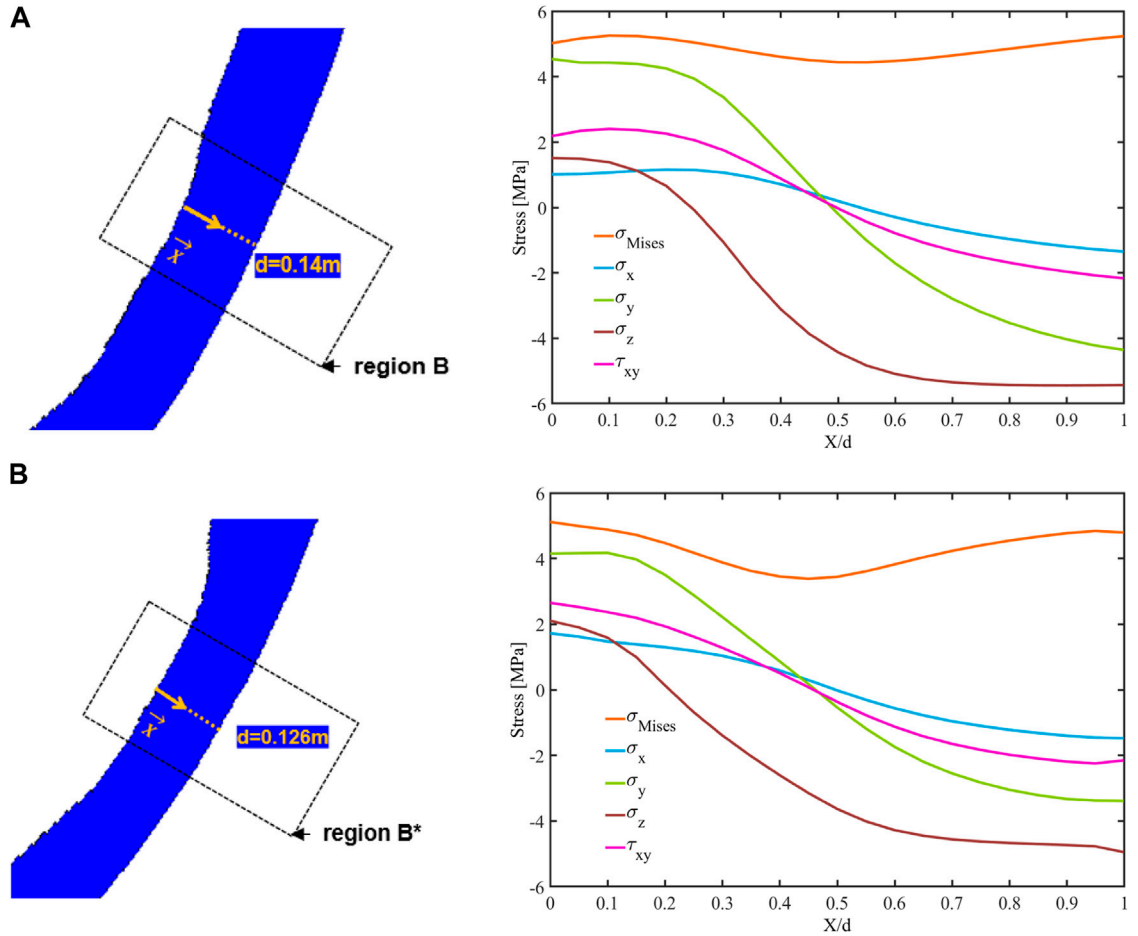

FIGURE 14 | (A) The stress component distributions along the thinnest region (region B) of the RPV lower head for the SBO case at failure time t = 6.8 h. **(B)** The stress component distributions along the thinnest region (region B*) of the RPV lower head for the SBO + LOCA case at failure time t = 7.1 h.

we took three locations on the vessel wall to further investigate the vessel behavior. They correspond to the high-creep strain (region A at angle 46°–49°), high-ablation and high-temperature (region B at angle 60°–63°), and high-stress (region C at angle 83°–87°).

Figure 10 gives the comparison of von Mises stress of the vessel (the solid lines) and SA533B1 ultimate stress (the dotted lines) at the critical regions. It can be seen in **Figures 10A,B** that the stresses at region A remain below the ultimate stress of the vessel steel until t = 7.3 h. The results of region B are depicted in **Figure 10C** with a zoomed-in plot in **Figure 10D**, which shows that the von Mises stress at the outer wall exceeds the ultimate stress of the steel at t = 6.8 h and the inner wall thereafter. Compared to the other two segments, region C has the highest stress after 6 h (see **Figure 10E**). However, a larger safety margin between the vessel stress and the stress limit can be seen in this region. This is because the ultimate stress is temperature-dependent, and hence, the stress limit of region C is relatively high due to its low local temperature.

As mentioned before, the RPV failure mechanism includes the stress and strain responses according to the two failure criteria in *Framework of the Thermo-Mechanical Analysis*. From **Figure 10**, it was found that RPV failure occurs at 6.8 h in region B when considering the stress limit of the vessel steel. To check whether there is a strain failure before the stress failure, snapshots of creep and total strains at t = 6.8 h are shown in **Figure 11**. The maximum creep strain and maximum total strain have values of 9% and 9.1%, respectively, located at the region with high ablation. Both are sufficiently below the limits set in the strain-based failure criteria (i.e., 20% creep strain and 25% total strain). Accordingly, RPV failure for the SBO case at 6.8 h is due to the stress failure mechanism. In addition, the failure location is in region B (angle 60°–63°), which has ablated the most in comparison with other parts of the RPV lower head (see **Figure 8A**).

Next, we present the structural analysis of the RPV with the SBO + LOCA case, similar to the SBO case. **Figure 12** shows the results of temperature, von Mises stress, and creep strain of the vessel wall for the SBO + LOCA case at t = 7.16 h. Like the SBO case, the highly ablated area shows higher temperature, higher creep strain, and higher stress. Given the distribution of the stresses along the vessel wall, it can be noted that high stresses are in the same region as in the SBO case, that is, in region C at angle 83°–87°, while high-creep and high-temperature values occur at the thinnest region of the RPV

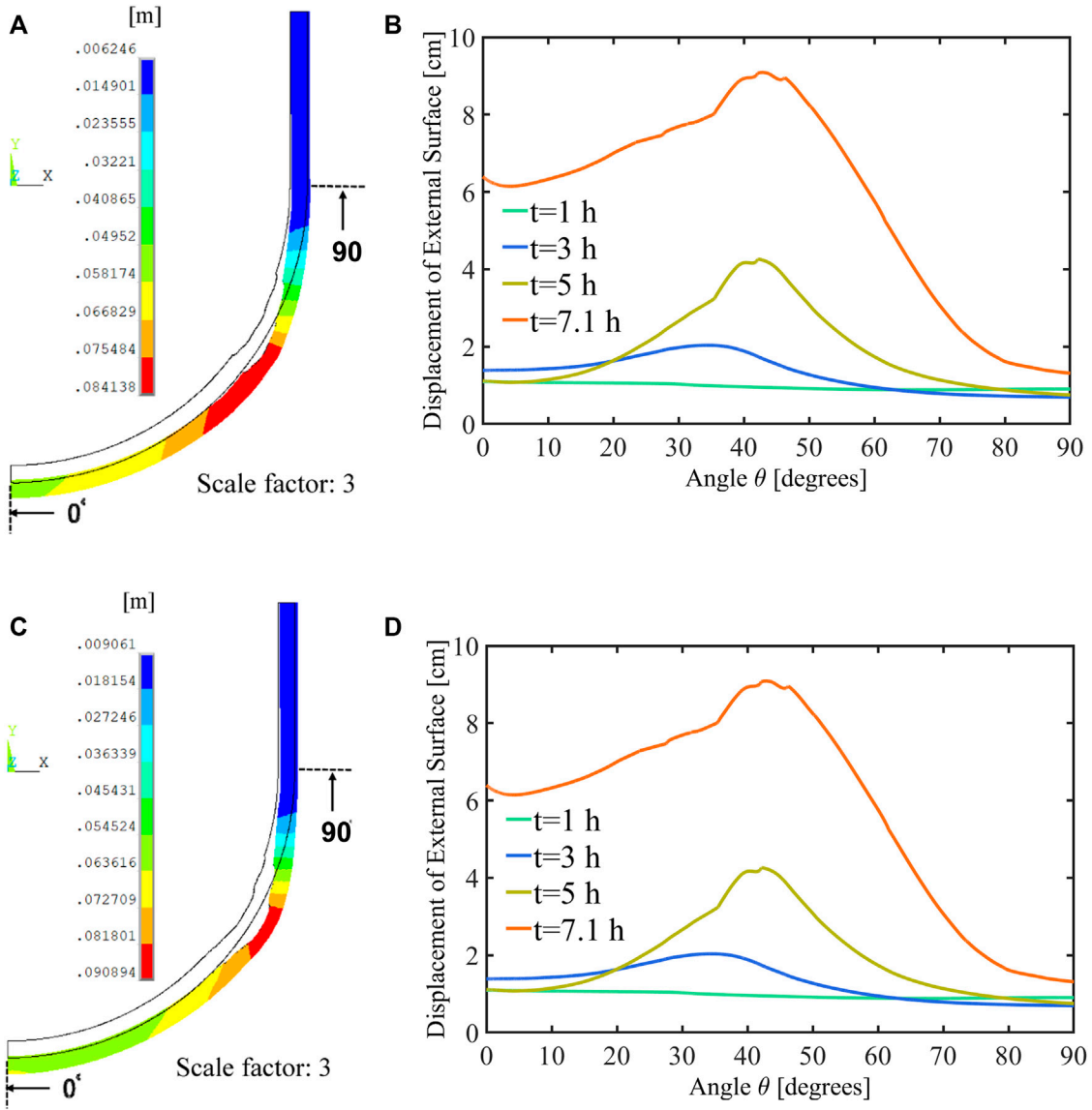

FIGURE 15 | (A) Vector sum of displacement (scale factor = 3) at t = 6.8 h (failure time) for the SBO case. **(B)** Displacement of the external vessel surface at t = 1, 2, 3, and 6.8 h for the SBO case. **(C)** Vector sum of displacement (scale factor = 3) at t = 7.1 h (failure time) for the SBO + LOCA case. **(D)** Displacement of the external vessel surface at t = 1, 2, 3, and 7.1 h for the SBO + LOCA case.

TABLE 5 | Relevant information of RPV failure from MELCOR and ANSYS.

Accident scenarios	**SBO case**		**SBO + LOCA case**	
Simulation tool	MELCOR	ANSYS	MELCOR	ANSYS
Failure time	t = 6.7 h	t = 6.8 h	t = 6.9 h	t = 7.1 h
Failure location	60.93°–63.89°	60°–63°	55.35°–57.88°	55°–58°
Failure reason	Thru-wall yielding	Breach of ultimate stress	Thru-wall yielding	Breach of ultimate stress

Note: however that MELCOR, cannot provide the transient structural responses (i.e., stresses, strains, and global deformation) which may provide insights on how to develop measures to mitigate the accident. In addition, inclusion of important lower head features such as vessel penetrations is straightforward in ANSYS, although it is not done here yet and should be in 3D. Nevertheless, MELCOR, can provide acceptable results where transient structural responses of the RPV, is not needed.

lower head, that is, in region B* at angle 55°–58°. Note that region B* in **Figure 12** and region B in **Figure 9** are at different angles, but both correspond to the regions with high ablation for the SBO + LOCA and SBO cases, respectively.

Next, a comparison of von Mises stress of the vessel and the SA533B1 ultimate stress at the critical regions (see **Figure 12**) is shown to investigate the timing and region of RPV failure in the SBO + LOCA case. It can be observed that the von Mises stresses do not exceed the allowable stress for the given temperature at region A and region C (not shown here). However, as temperature is quite high in region B*, the stress limit of this region (specifically the outer part of the vessel) is reached at t = 7.1 h (see **Figure 13A, B**).

Figures 13C,D show the distribution of creep and total strains of the RPV in the SBO + LOCA case at the (stress) failure time (t = 7.1 h). As expected, the highly ablated area has maximum creep and total strains, the rate being 9.8% and 10.7%, respectively. Accordingly, we can conclude that the stress failure mechanism, rather than the strain failure mechanism, is the dominant mechanism leading to RPV failure both in the SBO case and the SBO + LOCA case. Furthermore, the results indicate that the thinnest region of the RPV lower head can fail before melt-through.

To further investigate the stress profile of the vessel upon failure, **Figure 14** illustrates the contribution of each stress component to the von Mises stress across the thinnest regions of the RPVs for the SBO and SBO + LOCA cases at their failure time. The axial normal stress σ_y and circumferential normal stress σ_z are generally larger than the other two components, both contributing dominantly to the von Mises stress σ along the vessel thickness. In addition, as shown in both figures, the σ_y and σ_z are in the positive direction (outward of the surface of the vessel) at the inner vessel, while in the negative direction (toward the surface of the vessel) at the outer vessel. It means that the RPV undergoes a compression process at the inner surface and a tension process at the outer surface. As it has already been discussed that the RPV would fail at the outer surface for both SBO and SBO + LOCA cases (see **Figure 10D**; **Figure 13B**), the state of stress components at the outer surface (X/d = 1) should be given more attention. In **Figure 14A**, we can see that at the outer surface of the vessel wall, the circumferential normal stress σ_z (5.4 MPa in the negative direction) is the largest stress component, followed by the axial normal stress σ_y (4.3 MPa in the negative direction), and the radial normal stress σ_x and shear stress τ_{xy} are relatively lower. Similar results can also be found in **Figure 14B**. Accordingly, in the case of vessel breach, the RPV tends to produce a vertical crack instead of a circumferential crack.

Reactor Pressure Vessel Deformation

To supplement the analysis of RPV structural response at the time of failure, **Figures 15A, C** show the deformation of the vessel lower head, reaching 8.4 cm in the SBO case and 9 cm in the SBO + LOCA case. Although the limit of deformation for the vessel lower head has not been explicitly defined here and elsewhere (as far as the authors know), the degree of deformation in these two accidents (i.e., 8.4 cm and 9 cm) is considered to pose a significant threat to the RPV structural integrity. For the same accident scenarios but with external cooling (Wang et al., 2021), it can be noted that these values are more than three times the values predicted at 12 h, which are 2.8 cm and 2.9 cm, respectively. The location of the large deformation (above 8 cm) for the SBO case is in the 24° to 42° section of the vessel (see **Figure 15B**), which is slightly outside and below the ablated region in the latitudinal direction. For the SBO + LOCA case (see **Figure 15D**) the section of the vessel with large displacement (35°–51°) partly overlaps with the ablated region at angle 45°–51°. Hence, it can be inferred that the ablated region in the SBO + LOCA case is considered weaker than that in the SBO case given the macro-structural global deformation of the RPV.

Comparison of the Reactor Pressure Vessel Failure Between ANSYS and MELCOR

Recall that in the structural analysis with ANSYS, the boundary conditions are transferred continuously from the output data in MELCOR by deactivating the failure modes. On the other hand, both SBO and SBO + LOCA accidents are simulated again in MELCOR with the failure modes, and the time and location of RPV failure can be extracted from the MELCOR output file. **Table 5** compares the relevant information of RPV failure from MELCOR and ANSYS. In MELCOR, the vessel fails at t = 6.7 and 6.9 h, respectively, under these two accidents, resulting from the thru-wall yielding. This is the default failure criterion in MELCOR, indicating that the stress of the vessel wall exceeds the yield stress. Although MELCOR uses a different failure criterion, the failure time is close to the one obtained using ANSYS. Furthermore, the highly ablated regions, 60.93°–63.89° (segment 21) and 55.35°–57.88° (segment 19), are also identified as the failure location of the vessel wall, consistent with the results from ANSYS.

CONCLUSION

In this study, a framework involving the ANSYS and MELCOR platforms is established to study the behavior of a Nordic RPV lower head under SBO and SBO + LOCA. This one-way coupled method is particularly useful when the detailed investigation on the RPV behaviors is needed. Two failure criteria, the stress-based failure criterion and the strain-based failure criterion, have been used in assessing the mode and timing of RPV failure. In addition, a transient boundary condition (i.e., internal and external temperatures) is considered to simulate the dynamic process of vessel ablation. From the structural analysis, it is found that RPV failure initially occurs at 6.8 h in the SBO case and 7.1 h in the SBO + LOCA case, both attributed to a stress failure mechanism. Moreover, the axial normal stress σ_y and circumferential normal stress σ_z are generally larger than the other two components, contributing dominantly to the von Mises stress σ along the vessel thickness. Furthermore, the weakest part of the vessel wall is in the region with high temperature, which occurs at an angle around $\theta = 62.5°$ from the bottom for the SBO case and angle $\theta = 57.5°$ for the SBO + LOCA case. Due to high

temperature, the corresponding ultimate stress limits in this region are much lower than in colder regions. In this case, the von Mises stresses have surpassed these limits for both the SBO and SBO + LOCA cases. In addition, the creep and total strains and the ablation on the RPV are also found to be significant in this region. Finally, both ANSYS and MELCOR results indicate that the region with high ablation is most likely the failure location, as expected.

The framework and methodology presented here can be used in assessing structural integrity of the RPV in other types of nuclear reactor designs and provide the vessel failure analysis during a severe accident progression. It can also be used in analyzing the feasibility of different severe accident mitigation strategies with consideration of vessel thermo-mechanical behavior. In the future, the vessel penetrations (e.g., pump nozzles, Control Rod Guide Tubes, and Instrumentation Guide Tubes) on the RPV lower head will be considered to investigate other modes of vessel failure. This study provides a preliminary comparison of the RPV failure from ANSYS and MELCOR with their commonly used or default failure criteria; however, further investigation on RPV failure between these two codes is required with a unified failure criterion.

DATA AVAILABILITY STATEMENT

The raw data supporting the conclusion of this article will be made available by the authors, without undue reservation.

AUTHOR CONTRIBUTIONS

HW: writing—original draft preparation, methodology, and software. YC: MELCOR software and reviewing. WV: funding acquisition, supervision, writing, and reviewing.

FUNDING

This work is supported by the Swedish Radiation Safety Authority (SSM) Diarienr SSM2019-7689 and SSM2020-1192, the Swiss Federal Nuclear Safety Inspectorate (ENSI), and the Consortium of SSM and NPPs in Sweden (APRI). The authors are also grateful to the PhD scholarship awarded by the China Scholarship Council (CSC).

REFERENCES

Amidu, M. A., Addad, Y., Lee, J. I., Kam, D. H., and Jeong, Y. H. (2021). Investigation of the Pressure Vessel Lower Head Potential Failure under IVR-ERVC Condition during a Severe Accident Scenario in APR1400 Reactors. *Nucl. Eng. Des.* 376, 111107. doi:10.1016/j.nucengdes.2021.111107

Amidu, M. A., Olatubosun, S. A., Ayodeji, A., and Addad, Y. (2021). Severe Accident in High-Power Light Water Reactors: Mitigating Strategies, Assessment Methods and Research Opportunities. *Prog. Nucl. Energ.*, 104062.

Callister, W. D., and Rethwisch, D. G. (2011). *Materials Science and Engineering*, 5. NY: John Wiley & Sons.

Chen, Y., Zhang, H., Villanueva, W., Ma, W., and Bechta, S. (2019). A Sensitivity Study of MELCOR Nodalization for Simulation of In-Vessel Severe Accident Progression in a Boiling Water Reactor. *Nucl. Eng. Des.* 343, 22–37. doi:10.1016/j.nucengdes.2018.12.011

Devos, J., Sainte Catherine, C., Poette, C., and Burlet, H. (1999). CEA Programme to Model the Failure of the Lower Head in Severe Accidents. *Nucl. Eng. Des.* 191 (1), 3–15. doi:10.1016/s0029-5493(99)00049-7

Dietrich, P., Kretzschmar, F., Miassoedov, A., Class, A., Villanueva, W., and Bechta, S. (2015). *Extension of the Nuclear Safety Code MELCOR*. Pisa, Italy: Proc. 5th International Youth Conference on Energy IYCE.

Gandy, D. (2007). *Carbon Steel Handbook*. Palo Alto, CA: Electric Power Research Institute EPRI.

Herranz, L. E., Fontanet, J., Fernández, E., and López, C. (2015). Influence of the Wet-Well Nodalization of a BWR3 Mark I on the Containment thermal-hydraulic Response during an SBO Accident. *Nucl. Eng. Des.* 295, 138–147. doi:10.1016/j.nucengdes.2015.09.031

Humphries, L., and Chu, T.-Y. (2002). *OECD Lower Head Failure Project Final Report*. Albuquerque, NM: Sandia National Laboratories, 87185–91139.

Humphries, L. L., Beeny, B. A., Gelbard, F., Louie, D. L., and Phillips, J. (2017). *MELCOR Computer Code Manuals*, Vol. 2. Albuquerque, NM: Reference Manual.

Ikonen, K. (1999). *Revisa Rupther #14 Post-Test Analysis*. Espoo, Finland: VTT Energy.

Kaneko, T., Tanaka, N., Yamaoka, T., Masaki, H., Masuda, Y., Iwanami, M., et al. (2015). Evaluation of Corrosion Behaviors for Reactor Pressure Vessels/primary Containment Vessels in Fukushima Daiichi Units 1-3 Nuclear Power Plant. *J. Nucl. Sci. Techn.* 52 (6), 773–783. doi:10.1080/00223131.2014.994048

Koundy, V., Durin, M., Nicolas, L., Combescure, A., et al. (2005). Simplified Modeling of a PWR Reactor Pressure Vessel Lower Head Failure in the Case of a Severe Accident. *Nucl. Eng. Des.* 235, 835–843. doi:10.1016/j.nucengdes.2004.11.012

Koundy, V., Fichot, F., Willschuetz, H.-G., Altstadt, E., Nicolas, L., Lamy, J.-S., et al. (2008). Progress on PWR Lower Head Failure Predictive Models. *Nucl. Eng. Des.* 238 (9), 2420–2429. doi:10.1016/j.nucengdes.2008.03.004

Li, L., Wang, M., Tian, W., Su, G., and Qiu, S. (2014). Severe Accident Analysis for a Typical PWR Using the MELCOR Code. *Prog. Nucl. Energ.* 71, 30–38. doi:10.1016/j.pnucene.2013.10.014

Mao, J. F., Zhu, J. W., Bao, S. Y., Luo, L. J., and Gao, Z. L. (2016). Investigation on Multilayer Failure Mechanism of RPV with a High Temperature Gradient from Core Meltdown Scenario. *Nucl. Eng. Des.* 310, 39–47. doi:10.1016/j.nucengdes.2016.10.005

Mao, J. F., Zhu, J. W., Bao, S. Y., Luo, L. J., and Gao, Z. L. (2016). Study on Structural Failure of RPV with Geometric Discontinuity under Severe Accident. *Nucl. Eng. Des.* 307, 354–363. doi:10.1016/j.nucengdes.2016.07.027

Mao, J., Hu, L., Bao, S., Luo, L., and Gao, Z. (2017). Investigation on the RPV Structural Behaviors Caused by Various Cooling Water Levels under Severe Accident. *Eng. Fail. Anal.* 79, 274–284. doi:10.1016/j.engfailanal.2017.04.029

Matejovic, P., Barnak, M., Bachraty, M., Vranka, L., and Berky, R. (2017). Adoption of In-Vessel Retention Concept for VVER-440/V213 Reactors in Central European Countries. *Nucl. Eng. Des.* 314, 93–109. doi:10.1016/j.nucengdes.2017.01.015

Naitoh, M., Pellegrini, M., Mizouchi, H., Suzuki, H., and Okada, H. (2013). Analysis of Accident Progression of Fukushima Daiichi NPPs with SAMPSON Code. in" International Conference on Nuclear Engineering. Chengdu, China: American Society of Mechanical Engineers (ASME). doi:10.1115/icone21-16805

Naitoh, M., Pellegrini, M., Mizouchi, H., Suzuki, H., and Okada, H. (2013). *Analysis of Accident Progression of Fukushima Daiichi NPPs with SAMPSON codeInternational Conference on Nuclear Engineering*. Chengdu, China: American Society of Mechanical Engineers (ASME), V006T015A023.

Pellegrini, M., Dolganov, K., Herranz, L. E., Bonneville, H., Luxat, D., Sonnenkalb, M., et al. (2016). Benchmark Study of the Accident at the Fukushima Daiichi NPS: Best-Estimate Case Comparison. *Nucl. Techn.* 196 (2), 198–210. doi:10.13182/nt16-63

Pershagen, B. (1996). *Light Water Reactor Safety*. second. Oxford: Pergamon Press.

Rempe, J.-L., Chavez, S.-A., and Thinnes, G. L. (1993). *Light Water Reactor Lower Head Failure Analysis*. Washington, DC (United States): Nuclear Regulatory CommissionDiv. of Systems Research.

Sehgal, B.-R., Theerthan, A., Giri, A., Karbojian, A., Willschütz, H. G., Kymäläinen, O., et al. (2003). Assessment of Reactor Vessel Integrity (ARVI). *Nucl. Eng. Des.* 221 (1-3), 23–53. doi:10.1016/s0029-5493(02)00343-6

Siegele, D., Hodulak, L., Varfolomeyev, I., and Nagel, G. (1999). Failure Assessment of RPV Nozzle under Loss of Coolant Accident. *Nucl. Eng. Des.* 193, 265–272. doi:10.1016/s0029-5493(99)00184-3

Villanueva, W., Filippov, A., Jules, S., Lim, K., Jobst, M., Bouydo, A., et al. (2020). Thermo-mechanical Modelling of Reactor Pressure Vessel during Core Melt In-Vessel Retention. in" Proc. of the International Seminar on In-vessel retention: outcomes of the IVMR project . France: Juan-les-Pins.

Villanueva, W., Tran, C.-T., and Kudinov, P. (2012). Coupled Thermo-Mechanical Creep Analysis for Boiling Water Reactor Pressure Vessel Lower Head. *Nucl. Eng. Des.* 249, 146–153. doi:10.1016/j.nucengdes.2011.07.048

Villanueva, W., Tran, C. T., and Kudinov, P. (2012). *Analysis of Instrumentation Guide Tube Failure in a BWR Lower Head*. Lausanne, Switzerland: NUTHOS-9.

Wang, H., Villanueva, W., Chen, Y., Kulachenko, A., and Bechta, S. (2021). Thermo-mechanical Behavior of an Ablated Reactor Pressure Vessel wall in a Nordic BWR under In-Vessel Core Melt Retention. *Nucl. Eng. Des.* 379, 111196. doi:10.1016/j.nucengdes.2021.111196

Willschütz, H. G., Altstadt, E., Sehgal, B., and Weiss, F. P. (2003). Simulation of Creep Tests with French or German RPV-Steel and Investigation of a RPV-Support against Failure. *Ann. Nucl. Energ.* 30, 1033–1063. doi:10.1016/S0306-4549(03)00036-7

Yue, Y., Villanueva, W., Wang, H., and Wang, D. (2020). Thermo-mechanical Analysis of Instrumentation Guide Tube Failure during a Severe Accident in a Nordic Boiling Water Reactor.in" Proc. Of the 28th International Conference on Nuclear Engineering (ICONE-28). Paper 16236, Virtual Conference. Online, USA.

Zhan, D., Liu, F., Zhang, X., Chen, H., and Li, J. (2018). Ablation and thermal Stress Analysis of RPV Vessel under Heating by Core Melt. *Nucl. Eng. Des.* 330, 550–558. doi:10.1016/j.nucengdes.2018.02.008

Conflict of Interest: The authors declare that the research was conducted in the absence of any commercial or financial relationships that could be construed as a potential conflict of interest.

Publisher's Note: All claims expressed in this article are solely those of the authors and do not necessarily represent those of their affiliated organizations, or those of the publisher, the editors, and the reviewers. Any product that may be evaluated in this article, or claim that may be made by its manufacturer, is not guaranteed or endorsed by the publisher.

Copyright © 2022 Wang, Chen and Villanueva. This is an open-access article distributed under the terms of the Creative Commons Attribution License (CC BY). The use, distribution or reproduction in other forums is permitted, provided the original author(s) and the copyright owner(s) are credited and that the original publication in this journal is cited, in accordance with accepted academic practice. No use, distribution or reproduction is permitted which does not comply with these terms.

frontiers in Energy Research

ORIGINAL RESEARCH
published: 17 March 2022
doi: 10.3389/fenrg.2022.851747

Effects of Matrix Creep Properties on Effective Irradiation Swelling of U-10Mo/Zr Dispersion Nuclear Fuels

Yong Li[1], Jing Zhang[1], Xiaobin Jian[1], Feng Yan[1], Shurong Ding[1] and Yuanming Li[2]**

[1]Department of Aeronautics and Astronautics, Institute of Mechanics and Computational Engineering, Fudan University, Shanghai, China, [2]Science and Technology on Reactor System Design Technology Laboratory, Nuclear Power Institute of China, Chengdu, China*

A meso-mechanical model is established for the homogenized irradiation swelling of U-10Mo/Zr dispersion fuels, with an equivalent sphere chosen as the representative volume element (RVE). In the simulation, a mechanistic model for the fission gas swelling of U-10Mo particles and the creep model for Zr matrix with different values of the creep amplification factor are included. Based on the developed method, the results of effective irradiation swelling of U-10Mo/Zr dispersion fuels are obtained by finite element simulation. Additionally, the effects of matrix creep properties on the effective irradiation swelling are investigated. The numerical results indicate that 1) the Zr matrix has the function of restraining and compensating the irradiation swelling of fuel particles by the mechanical interactions between the fuel particles and the matrix; 2) with the increase in the creep amplification factor of the matrix, the effective irradiation swelling increases while the stresses in the fuel particles and the matrix decrease. The enhanced creep rate of the matrix is apt to result in less restraint of the effective irradiation swelling, but reduces the risk of radial crack initiation and propagation in the matrix; 3) based on the results of finite element simulation, a mathematic model for the effective irradiation swelling of U-10Mo/Zr dispersion fuels is fitted to correlate the effective irradiation swelling with different values of the matrix creep amplification factor under the considered irradiation conditions. The creep property of the matrix should be optimized because of its evident effects on the effective irradiation swelling and stresses of the U-10Mo/Zr dispersion fuels.

Keywords: U-10Mo/Zr dispersion fuel, mechanistic fission gas swelling model, creep property of matrix, effective irradiation swelling, numerical simulation

OPEN ACCESS

Edited by:
Yue Jin,
Massachusetts Institute of Technology, United States

Reviewed by:
Chenglong Wang,
Xi'an Jiaotong University, China
Jinbiao Xiong,
Shanghai Jiao Tong University, China
Xingang Zhao,
Oak Ridge National Laboratory (DOE), United States

****Correspondence:***
Shurong Ding
dingshurong@fudan.edu.cn
Yuanming Li
lym_npic@126.com

Specialty section:
This article was submitted to Nuclear Energy, a section of the journal Frontiers in Energy Research

Received: *10 January 2022*
Accepted: *15 February 2022*
Published: *17 March 2022*

Citation:
Li Y, Zhang J, Jian X, Yan F, Ding S and Li Y (2022) Effects of Matrix Creep Properties on Effective Irradiation Swelling of U-10Mo/Zr Dispersion Nuclear Fuels. Front. Energy Res. 10:851747. doi: 10.3389/fenrg.2022.851747

INTRODUCTION

Dispersion nuclear fuels, with fissionable fuel particles dispersed in the non-fissionable matrix (Ding et al., 2018), are widely used in research and test reactors, advanced nuclear systems, and disposal of nuclear wastes (Duyn, 2003; Carmack et al., 2006; Lombardi et al., 2008; Gong et al., 2013). Tri-structural isotropic particle–based dispersion fuels have been used in high-temperature gas-cooled reactors and have a promising application prospect in advanced pressurized water reactors (Xiang et al., 2014; Zhang T. et al., 2021; Lou et al., 2022). With the non-fissionable matrix encompassing fuel particles, dispersion nuclear fuels possess a more stable swelling behavior and allow higher burnup than traditional homogeneous fuels (Neeft et al., 2003a; Savchenko et al., 2006). Moreover, certain properties of dispersion fuels such as high strength, high thermal conductivity, good corrosion

resistance, and good performances under transient conditions can be designed by a proper choice of fuel and matrix materials (Holden, 1967; Savchenko et al., 2007; Savchenko et al., 2010).

In the 1980s, the US Department of Energy Office launched the Reduced Enrichment for Research and Test Reactors (RERTR) program to reduce the threat of nuclear proliferation worldwide, through the conversation of research and test reactors from highly enriched uranium to low-enriched uranium fuels (Meyer et al., 2002; Liu et al., 2011). With the development of the RERTR program, U-Mo/Al dispersion fuels have attracted numerous attention as the low-enriched uranium fuels for research and test reactors (Van den Berghe and Lemoine, 2014), due to their advantages of high uranium density, low neutron capture cross sections, good irradiation stability, and high thermal conductivity (Meyer et al., 2002; Jian et al., 2019a). Early experimental results demonstrated that U-Mo/Al dispersion fuels have good irradiation performance under low power and low burnup (Kim et al., 2002; Meyer et al., 2002). However, excessive local swelling occurred in U-Mo/Al dispersion fuels under high power and high burnup irradiation conditions (Leenaers et al., 2004; Van den Berghe and Lemoine, 2014), due to the formation of an amorphous interaction layer (IL) between U-Mo fuel particles and the Al alloy matrix (Van den Berghe et al., 2008; Oh et al., 2016). Under the irradiation conditions, the IL grows and shows poor fission gas solubility and high diffusivity of fission gas atoms, leading to large bubbles, which induces excessive irradiation swelling (Lee et al., 1997; Huber et al., 2018; Saoudi et al., 2022). To prevent the growth of the IL, some methods were implemented, such as modifying the Al matrix by adding Si (Leenaers et al., 2011; Keiser et al., 2014), coating U-Mo fuel particles with Si or ZrN, and developing monolithic fuels with a Zr layer inserted between U-Mo fuel foil and Al alloy clad (Leenaers et al., 2013; Keiser et al., 2015; Leenaers et al., 2015). An alternative method to eliminate the IL of U-Mo/Al is replacing the Al alloy matrix with some other inert alloys. Zirconium alloys are promising alternative matrixes for U-Mo–based fuels because they have a low reactivity with U and Mo, high melting point, high strength, good corrosion resistance, and low neutron capture cross-section for thermal neutrons (Cox, 2005; Nakamura et al., 2007; Gonzalez et al., 2015). Moreover, zirconium alloys have long been used as fuel matrix and cladding in nuclear reactors (Moorthy, 1969; Savchenko et al., 2007; Savchenko et al., 2010) with extensive knowledge of their material properties and processing technologies, so they would be a good choice to minimize the qualification testing required to introduce a new matrix material for U-Mo–based dispersion fuels (Hagrman et al., 1995; Hayes and Kassner, 2006; Hales et al., 2016; Pasqualini et al., 2016).

Under the irradiation conditions, U-Mo fuel particles undergo irradiation swelling due to the accumulation of solid and gaseous fission products, namely, fission solid swelling and fission gas swelling (Kim and Hofman, 2011). As irradiation swelling is considered the important factor dominating the behavior and service life of nuclear fuels, it is necessary to investigate and model the swelling behavior of U-Mo/Zr dispersion fuels to evaluate its serviceability. Varied knowledge of irradiation swelling behavior of U-Mo alloy has been accumulated through experimental investigation (Kim and Hofman, 2011; Van den Berghe et al., 2012). The fission solid swelling of U-Mo alloy is proportional to the fission density (Kim and Hofman, 2011). The fission gas swelling is complex and related to the fission density, the grain size, the temperature, the external hydrostatic pressure, and the progression of irradiation-induced recrystallization. Kim and Hofman built an empirical model for fission gas swelling by fitting the experiment data (Kim and Hofman, 2011). The empirical model is simple, but it could not reflect the critical influencing parameters mentioned above. Rest built a mechanistic model reflecting the influence of those parameters except the external hydrostatic pressure (Rest, 2005). Cui et al. modified the mechanistic model with consideration of external hydrostatic pressure and re-solution of intergranular gas atoms (Cui et al., 2015). Jian et al. (Jian et al., submitted) further developed the fission gas swelling mechanistic model for U-10Mo fuels, which has been validated by comparing the model results, including the fission gas swelling, the evolution rules of the bubble density, and the bubble size with the experimental results. The newly developed fission gas swelling model could reflect the dependence of external hydrostatic pressure more reasonably. To better understand and study the irradiation swelling behavior of U-Mo/Zr dispersion fuels, it is necessary to adopt the improved mechanistic model of fission gas swelling for fuel particles. For dispersion fuels with numerous fuel particles, it is difficult and expensive to establish a finite element model for the whole fuel element with all particles involved (Schappel et al., 2018). An effective way is to homogenize the thermal-mechanical performances of the dispersion fuels based on homogenization theory, including its effective irradiation swelling behavior (Rest and Hofman, 1997; Zhao et al., 2014; Liu et al., 2018). Zhang J. et al. established an equivalent spherical model to investigate the effective irradiation swelling of PuO_2/Zr dispersion fuels (Zhang J. et al., 2021). The simulation results indicate that the creep behavior of the Zr matrix has an evident influence on the effective irradiation swelling of PuO_2/Zr dispersion fuels. As the creep properties of zirconium alloys are related to alloy compositions, microstructure, process conditions, and service conditions (Krishnan and Asundi, 1980; Hayes and Kassner, 2006; Kim et al., 2021), it is essential and necessary to investigate the effects of Zr matrix creep properties on the effective irradiation swelling of U-Mo/Zr dispersion fuels and provide a reference for the optimization design and advanced manufacture. Meanwhile, the relative research studies are currently limited.

In this study, the three-dimensional finite element simulation for the developed equivalent spherical model is performed for the further homogenization of the effective irradiation swelling of U-10Mo/Zr dispersion fuels. The newly improved mechanistic model of fission gas swelling (Jian et al., submitted) is adopted, which could reflect the significant influences of external hydrostatic pressure. The effects of Zr matrix creep properties on the effective irradiation swelling of U-10Mo/Zr dispersion fuels are investigated with different creep amplification factors imposed on a typical creep model. The irradiation swelling model and creep model are given in *Material Properties*. The three-dimensional finite element

model and the validity of the fission gas swelling model are presented in *Results and Discussion*. The effective irradiation swelling results are obtained by finite element simulation, and the influence mechanisms are analyzed in *Finite Element Modelling*. Based on the simulated results, a mathematical model of effective irradiation swelling is described with different values of creep amplification factors.

The acronyms and symbols used in the paper are summarized in **Appendix A** for better readability.

MATERIAL PROPERTIES

In this section, the irradiation swelling model for U-10Mo fuel particles and the creep strain rate model for the Zr matrix correlated with the creep amplification factor are given. The other material property models for U-10Mo and the Zr matrix, such as the elastic constants and plasticity model are described in Refs. (Zhao et al., 2014; Jian et al., 2019b). The mechanical constitutive relations for fuel particles and the matrix are introduced to commercial software ABAQUS through user-defined subroutines, based on the stress update algorithms in our previous studies (Zhao et al., 2015; Kong et al., 2018).

The Irradiation Swelling Model for U-10Mo Fuels

The irradiation swelling of U-10Mo consists of fission solid swelling and fission gas swelling, expressed as follows:

$$\frac{\Delta V}{V_0} = \frac{\Delta V_{solid}}{V_0} + \frac{V_{bubble}}{V_0} \tag{1}$$

The fission solid swelling is proportional to the fission density, expressed as follows (Kim et al., 2015):

$$\frac{\Delta V_{solid}}{V_0} = 4.0 \times 10^{-29} \cdot F_d \tag{2}$$

where V_0 is the initial fuel volume in m^3, F_d depicts the fission density in fission/m^3, and ΔV_{solid} is the absolute volume change caused by solid fission products in m^3.

The fission gas swelling is measured by the fraction of identified inter-granular bubbles through SEM, while the intra-granular bubbles are invisible (Kim and Hofman, 2011). Thus, the fission gas swelling is only regarded as the contribution of inter-granular bubbles in the newly developed model (Jian et al., submitted). The fission gas swelling is described as follows:

$$\frac{V_{bubble}}{V_0} = \frac{N_{bubble} \times 4/3\pi\bar{R}^3}{V_0} \tag{3}$$

where V_{bubble} is the total volume of inter-granular bubbles in m^3; N_{bubble} is the total number of inter-granular bubbles in the recrystallized and un-recrystallized areas with a new description by Jian et al. (Jian et al., submitted), which could reflect the significant influence of external pressure, and the obtained evolution results of the bubble density and the bubble size have been demonstrated in the same magnitude order as the related experimental results; $\bar{R}$ is the average radius of inter-granular bubbles.

The average radius of inter-granular bubbles is determined using the modified van der Waals gas law (Jian et al., submitted) as follows:

$$\left(\frac{2\gamma}{\bar{R}} + P_h\right)\left(\frac{4}{3}\pi\bar{R}^3 - h_s b_v \bar{N}\right) = \bar{N}kT \tag{4}$$

where $\frac{2\gamma}{\bar{R}}$ is the surface tension–induced pressure, in Pa; P_h is the external hydrostatic pressure in Pa, involved when positive; h_s is the fitting parameter to make the van der Waals equation equivalent to the hard-sphere equation of state in the value of 0.6; $b_v = 8.5 \times 10^{-29}$ m^3/atom is the van der Waals gas constant of Xe; $\bar{N}$ is the average number of fission gas atoms in each inter-granular bubble; $k = 1.38 \times 10^{-23}$ J/K is the Boltzmann constant and T is the temperature in K.

The numbers of inter-granular bubbles in the recrystallized and un-recrystallized areas are defined as $N_{bubble1}$ and $N_{bubble2}$, respectively, expressed as follows (Jian et al., submitted):

$$N_{\text{bubble1}} = 2\pi r_{gr}^2 \cdot C_b \cdot \eta_{F_d} \tag{5}$$

$$N_{\text{bubble2}} = \frac{2\pi r_{gr0}^3 \cdot \eta_r}{r_{grx}} \cdot C_{bx} \cdot \eta_{F_d} \tag{6}$$

$$\eta_{F_d} = \begin{cases} 1 & F_d < F_{d0} \\ \left(\frac{F_{d0}}{F_d}\right)^2 & F_d \geq F_{d0} \end{cases} \tag{7}$$

where C_b and C_{bx} are the defined grain-boundary bubble concentration of the un-recrystallization region and the fine grain region in Refs. (Rest, 2005; Cui et al., 2015), respectively; η_{F_d} is the modified factor for the gas bubble number; $F_{d0} = 4.7 \times 10^{27}$ fissions/m^3.

The Creep Model of Zr Matrix

The effects of different creep properties are investigated based on the creep model of Zircaloy-2 alloy (Macdonald and Thompson, 1976). The creep model of the Zr matrix consists of thermal creep and irradiation creep, expressed as follows:

$$\dot{\varepsilon}_m^{cr} = \beta\left(\dot{\varepsilon}^{ss} + \dot{\varepsilon}^{ir}\right) \tag{8}$$

where β is the creep amplification factor in the values of 0.01, 0.1, 1, 10, and 100; $\dot{\varepsilon}^{ss}$ and $\dot{\varepsilon}^{ir}$ are the thermal creep strain rate and the irradiation creep strain rate, respectively, in 1/s.

The thermal creep strain rate is described as follows:

$$\dot{\varepsilon}^{ss} = A_0\left(\frac{\sigma_m}{G}\right)^n e^{\left(\frac{-Q}{RT}\right)} \tag{9}$$

where R is the gas constant in J/(mol·K) with a value of 8.314 J/(mol·K); T is temperature in K; σ_m is the Mises equivalent stress in Pa and G is the shear modulus in Pa; $Q = 27{,}000$ J/mol is the activation energy; $A_0 = 3.14 \times 10^{26}$ s^{-1} and $n = 5$ are the used material constants in this study.

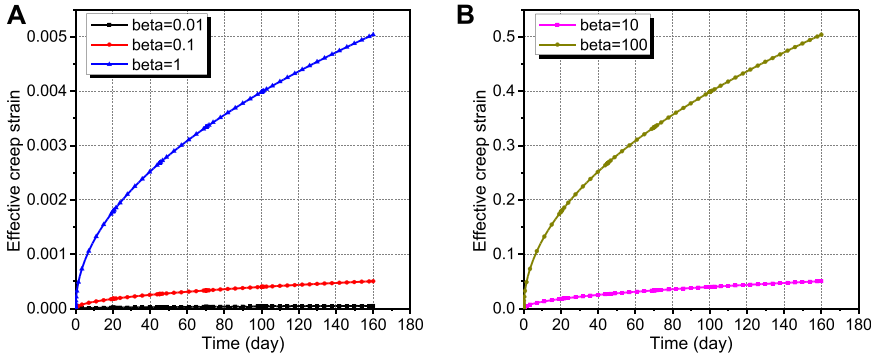

FIGURE 1 | Creep curves for the Zr matrix with β = 0.01, 0.1, 1 **(A)** and β = 10, 100 **(B)**.

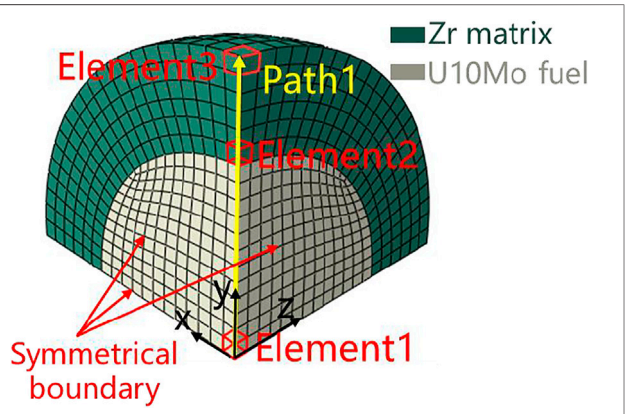

FIGURE 2 | FE model of an equivalent sphere.

The irradiation creep strain rate is described as follows:

$$\dot{\varepsilon}^{ir} = K\phi\left(\sigma + Be^{C\sigma_m}\right)\exp\left(-10000/RT\right)t^{-0.5} \quad (10)$$

where $\dot{\varepsilon}^{ir}$ is the irradiation creep strain rate in 1/s; σ_m is the Mises equivalent stress in Pa and ϕ is the fast neutron flux in n/(m^2·s), with the constants $K = 5.129 \times 10^{-27}$, $B = 7.252 \times 10^{2}$, and $C = 4.967 \times 10^{-8}$ in this study.

Figure 1 displays the creep curves of the Zr matrix with different values of β under the condition of 373 K, with a Von Mises stress of 50 MPa and a fast neutron flux of 1.9128×10^{18} n/(m^2·s). It can be found that the creep strain rate decreases with time. For cases of β = 100 and β = 0.01, the effective creep strains after irradiation of 160 days reach 0.5 and 5×10^{-5}, respectively.

FINITE ELEMENT MODELING

In this section, the FE (finite element) model for a respective volume element (RVE) of U-10Mo/Zr dispersion fuels with the fuel particle, matrix part, and the applied boundary conditions are presented. The irradiation conditions are chosen according to those of RERTR programs. The effective irradiation swelling of U-10Mo/Zr dispersion fuels is defined and presented in a formula form. To validate the fission gas swelling model, the fission gas swelling results calculated by the model used in this study are compared with the experiment results in the references.

Finite Element Model

The equivalent spherical model has been adopted to study the irradiation swelling behavior of polycrystalline nuclear fuels (Wood and Kear, 1983; Rest, 2010) and the effective irradiation swelling of dispersion fuels (Zhang J et al., 2021). In this study, an equivalent spherical model containing the fuel particle and the matrix is selected as the RVE to obtain the effective irradiation swelling of U-10Mo/Zr dispersion fuels. The initial particle volume fraction of the equivalent spherical model is set as 30% in this study. According to the symmetry in geometry and loading, 1/8 part of the equivalent spherical model is ultimately selected as the FE model shown in **Figure 2**, including the particle part with a radius of 50 μm and a matrix-shell part.

The bonding between the fuel particle and the matrix is assumed to be perfect with continuous displacements and interfacial stresses. Symmetrical boundary conditions are applied to the surfaces of x = 0, y = 0, and z = 0, which are the symmetrical surfaces of the 1/8 part of the RVE. Constant pressure in a magnitude of 2.5 MPa is applied to the outer surface of the RVE, according to the pressure of the reactor coolant for RERTR (Salvato et al., 2018). A uniform steady-state temperature of 373 K is set. The fission rate in the fuel particle is set as 6×10^{20} fission/(m^3·s) and the fast neutron flux is set as 1.9128×10^{18} n/(m^2·s) in this study, according to irradiation conditions of research and test reactors (Perez et al., 2011). The total irradiation time is 160 days, on which the recrystallization process is completed.

To ensure the computation precision and efficiency, three mesh cases are adopted with 1472, 4,147, and 7,868 elements, respectively. The obtained effective irradiation swelling results of the RVE and Mises stress of the matrix for the case of β = 1 are shown in **Figure 3**. The maximum relative error of the effective irradiation swelling results and Mises stress between Mesh 2 and Mesh 3 is less than 0.11 and 0.14%, respectively. So the effective irradiation swelling and stress results of Mesh 2 have converged, and Mesh 2 is adopted in the following studies.

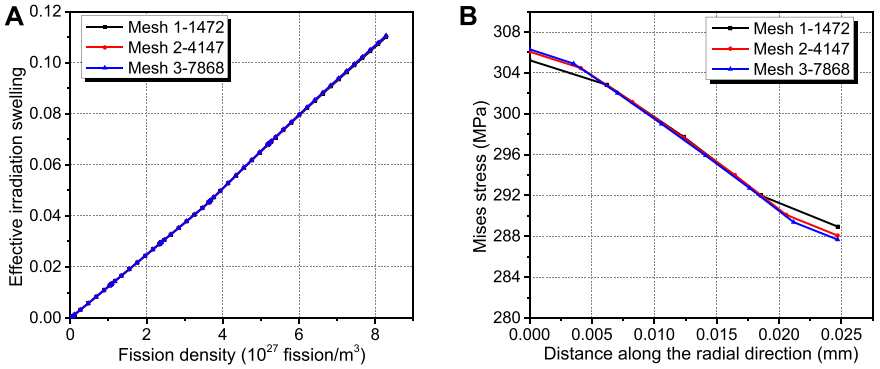

FIGURE 3 | Convergence of effective irradiation swelling of the RVE **(A)** and Mises stress of the matrix **(B)** to meshes.

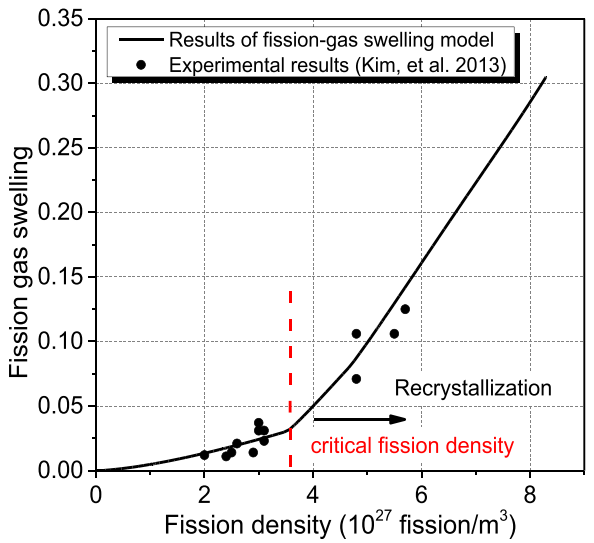

FIGURE 4 | Comparison of the simulation results with the experimental results for the fission gas swelling of U-10Mo fuel particles in U-10Mo/Al dispersion fuels.

The effective irradiation swelling of U-10Mo/Zr dispersion fuels is calculated as follows:

$$\frac{\Delta V}{V_0} = \frac{V - V_0}{V_0} = \frac{r^3 - r_0^3}{r_0^3} \tag{11}$$

where V is the calculated post-irradiation volume of the equivalent sphere; V_0 is the initial spherical volume; r is the post-irradiation outer spherical radius, obtained from the FE model displacement results; r_0 is the initial outer spherical radius.

Verification of the Used Fission Gas Swelling Model

The irradiation swelling model for the fuel particles is vitally important for calculating the effective irradiation swelling of U-10Mo/Zr dispersion fuels. The fission solid swelling model is directly obtained from the reference (Kim and Hofman, 2011). Meanwhile, the fission gas swelling model considering the critical physical mechanisms will be validated with the experiment results. The plate elements, consisting of Al-alloy cladding and the fuel meat with U-Mo particles dispersed in the aluminum matrix, were irradiated in the advanced test reactor for the test campaigns of RERTR-1~5 (Kim et al., 2013). The fuel temperature during the test was in the range of 339–431 K, and the achieved fission density was in the range of 2.0 × 10^{27}–5.7 × 10^{27} fission/m^3. The post-irradiation samples were punched out at the plate center to measure the fission gas swelling by scanning electron microscopy. Ignoring the constraint of the IL on U-10Mo particles, the subjected hydrostatic pressure of the fuel particles in the middle zone of fuel plates could be considered as that of the reactor coolant. So, the temperature is ultimately set as 373 K and the hydrostatic pressure is set as 2.5 MPa in this study. The results of the calculated fission gas swelling are compared with the experimental results of RERTR1~5, shown in **Figure 4**. It can be seen that the predictions agree well with the experimental results. So, the fission gas swelling model used in this study is effective.

RESULTS AND DISCUSSION

Adopting the FE model in **Figure 2**, numerical simulation of the irradiation-induced mechanical behavior is implemented, considering different values of β of the Zr matrix. Here, the deformations and stresses of the FE model and the effective irradiation swelling for cases with different values of β are obtained, and the influence mechanisms for effective irradiation swelling are analyzed. A mathematical model correlating the effective irradiation swelling with different values of β is fitted at last.

Deformation and Effective Irradiation Swelling of RVE

The Deformation and Stress Analysis

Due to the irradiation swelling of U-10Mo fuel particles under the irradiation environments, the intensive mechanical interactions

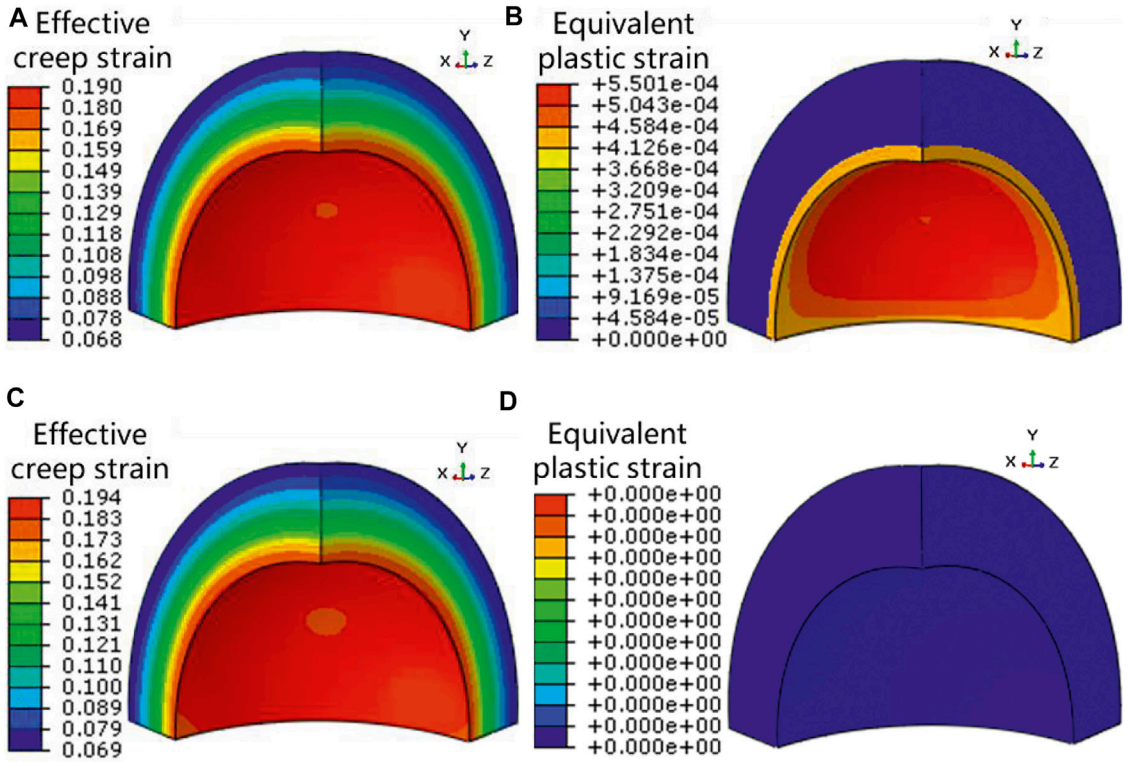

FIGURE 5 | Effective creep strain contour plot **(A)**, the equivalent plastic strain contour plot **(B)** of the matrix for the case of $\beta = 0.01$ and the effective creep strain contour plot **(C)**, and the equivalent plastic strain contour plot **(D)** of the matrix for the case of $\beta = 1$ at the fission density of 8.3×10^{27} fission/m^3.

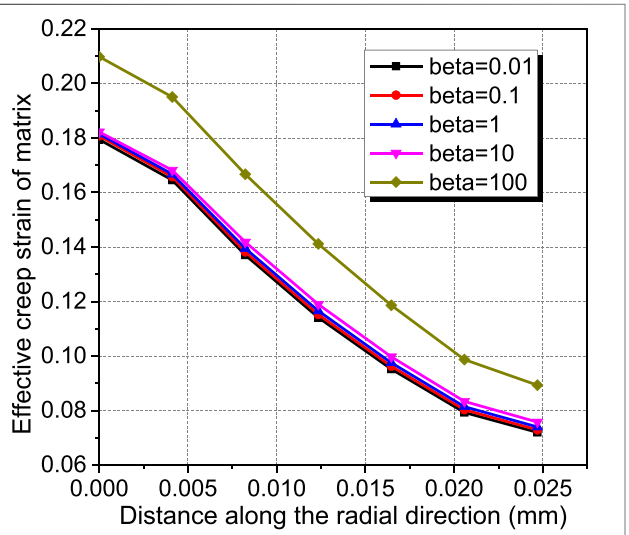

FIGURE 6 | Distributions of matrix effective creep strain along the radial direction at the fission density of 8.3×10^{27} fission/m^3 for the cases with different values of β

are aroused between the fuel particles and the matrix. These mechanical interactions could result in creep and plastic deformations of the matrix. The value of β has a direct influence on the creep deformation of the matrix. **Figure 5** gives the contour plots of effective creep strain and equivalent plastic strain of the matrix at the fission density of 8.3×10^{27} fission/m^3 for the cases of $\beta = 0.01$ and $\beta = 1$. It is noted that the other cases with different values of β have similar effective creep strain distributions. The effective creep strain field of the matrix is spherically symmetric on the whole, and the largest effective creep strain occurs at the interface of the matrix with the fuel particle. The plastic deformation of the matrix only occurs in the case of $\beta = 0.01$, with the maximum value of 0.055%, excluding the other cases with β ranged from 0.1 to 100. **Figure 6** compares the distributions of effective creep strain of the matrix along the radial direction at the fission density of 8.3×10^{27} fission/m^3, for different values of β. One can see that the effective creep strain of the matrix decreases along the radial direction for all cases and grows with the increase in β. For the cases with β in the range of 0.01–10, the effective creep strain of the matrix has a small difference with a relative deviation of less than 1.2%. When β is amplified to 100, the maximum effective creep strain of the matrix is about 21%, with a relative increase of ~20% compared to the result of $\beta = 0.01$.

Figure 7 gives the contour plots of Mises stress and the first principal stress of the matrix at a fission density of 8.3×10^{27} fission/m^3 for the case of $\beta = 0.01$. The largest Mises stress occurs at the interface of the matrix with the fuel particle, while the largest first principal stress occurs at the outer surface of the matrix. **Figure 8** compares the evolution results of Mises stress of Element 2 and the first principal stress of Element 3 for the cases

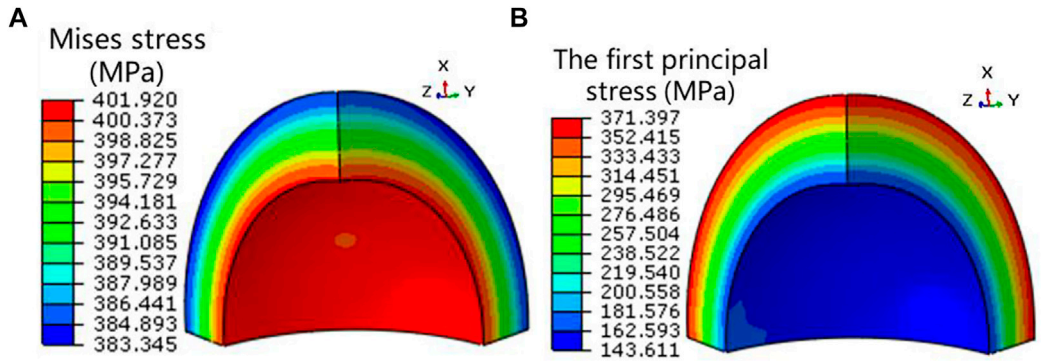

FIGURE 7 | Mises stress contour plot **(A)** and the first principal stress contour plot **(B)** of the matrix for the case of β = 0.01 at the fission density of 8.3 × 10^{27} fission/m^3.

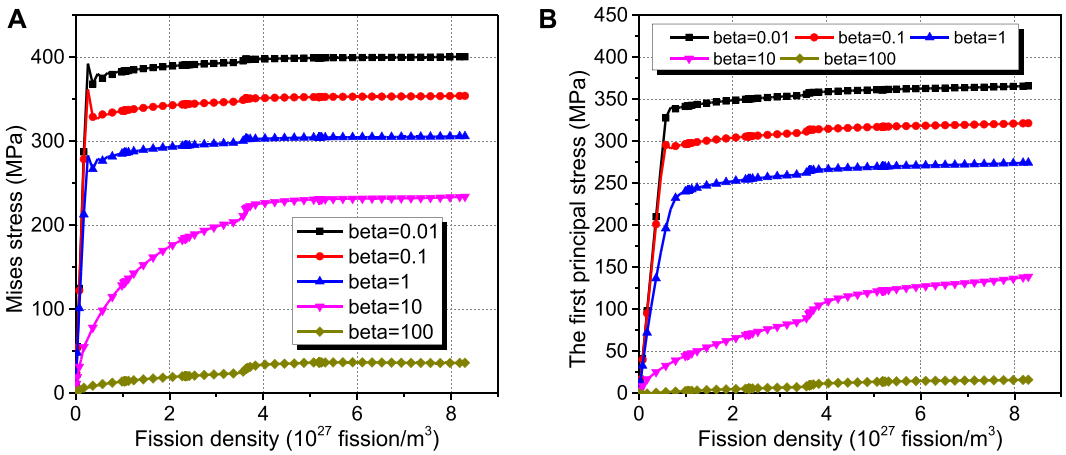

FIGURE 8 | Evolution results of **(A)** Mises stress of Element 2 and **(B)** the first principal stress of Element 3.

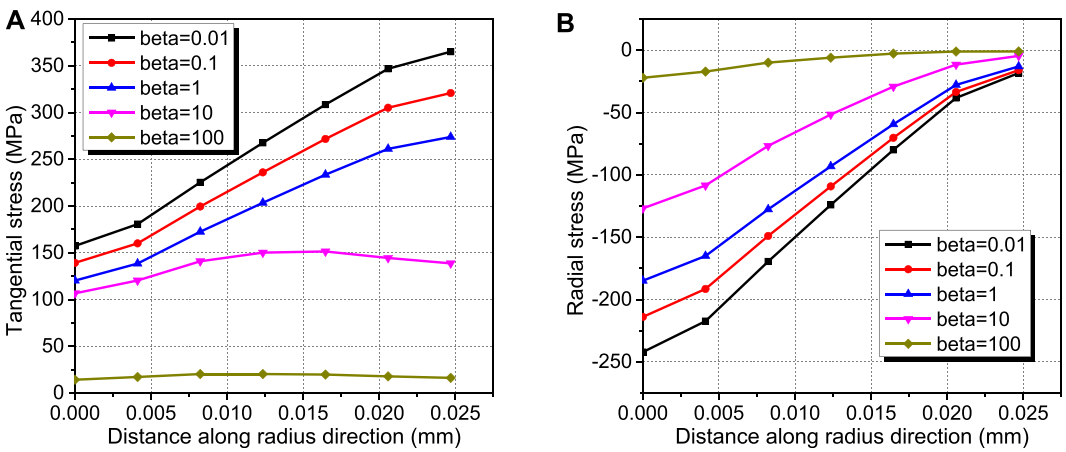

FIGURE 9 | Distributions of matrix **(A)** tangential stress and **(B)** radial stress along the radial direction at the fission density of 8.3 × 10^{27} fission/m^3 for the cases with different values of β.

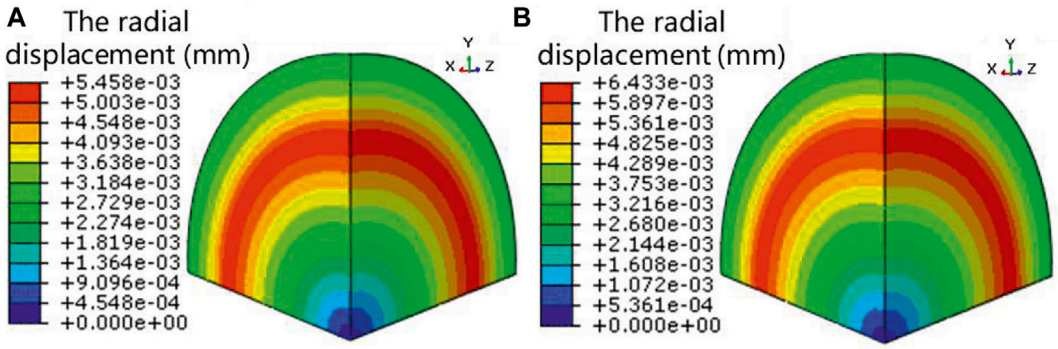

FIGURE 10 | Radial displacement contour plot of the FE model at the fission density of 8.3×10^{27} fission/m^{3}for the case of $\beta = 0.01$ **(A)** and the case of $\beta = 100$ **(B)**.

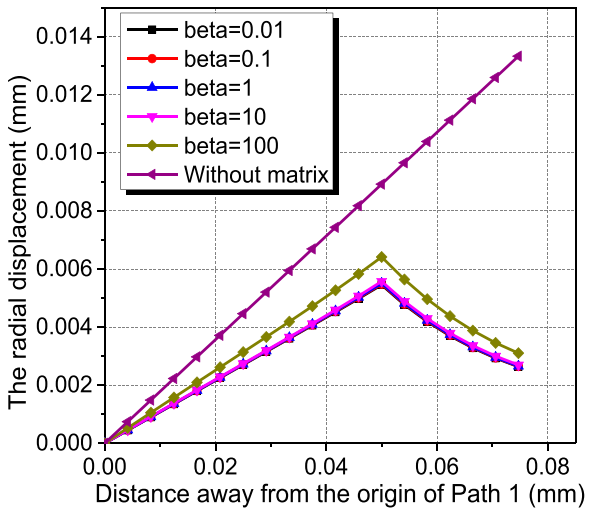

FIGURE 11 | Distributions of the radial displacement along Path 1 at the fission density of 8.3×10^{27} fission/m^3 for the cases with different values of β and the case without the matrix.

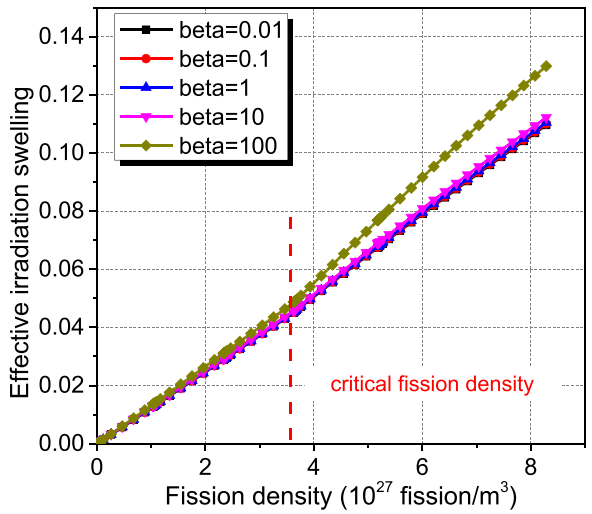

FIGURE 12 | Evolution results of effective irradiation swelling of RVE with different values of β

with different values of β. It can be found that the stresses of the matrix increase quickly in the preliminary stage of irradiation and tend to be stable at higher burnup levels. As β increases from 0.01 to 100, the maximum Mises stress decreases from 402 to 40 MPa, with a relative reduction of 90%, and the maximum first principal stress decreases from 366 to 16 MPa, with a relative reduction of 96%. As neutron radiations will result in the loss of ductility of the matrix and the formation of the fission fragment damage zone (Duyn, 2003), there is a possibility for the brittle fracture of the matrix. Thus, the increase in β has the positive consequence that the stresses of the matrix decrease, which could reduce the risk of stress-induced failure. To further predict the possible form of crack initiation and propagation, **Figure 9** compares the distributions of tangential and radial stress of the matrix along the radial direction at the fission density of 8.3×10^{27} fission/m^3, for different values of β. One can see that the radial stress of the matrix is compressive, while the tangential stress is tensile stress approximately equal to the first principal stress. The tangential stress of the matrix decreases with the increase in β. Thus, radial cracks are susceptible to generating and propagating in the matrix, and the enhanced creep rate could prevent the stress-induced cracks of the matrix, similar to the conclusion from the experimental investigation (Neeft et al., 2003b).

The Radial Displacement Analysis

Under the irradiation conditions, U-10Mo fuel particles undergo irradiation swelling, presented as positive radial displacements. **Figure 10** displays the radial displacement contour plot of the FE model at a fission density of 8.3×10^{27} fission/m^3 for the cases of $\beta = 0.01$ and $\beta = 100$. It is noted that similar displacement contour plots appear for the other cases with different values of β. The radial displacements of the fuel particle increase along the radial direction. As β increases from 0.01 to 100, the maximum radial displacement, located at the particle surface to be connected with the matrix, increases from 5.5 to 6.4 μm, with a relative increase of ~18%. The radial displacements of the matrix part are smaller than the

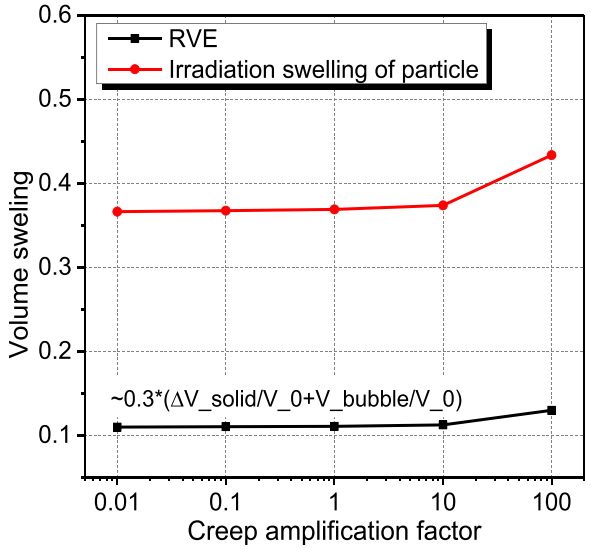

FIGURE 13 | Comparison of effective irradiation swelling of RVE with the irradiation swelling of fuel particles for the cases with different values of β.

maximum of the particle. **Figure 11** compares the distributions of radial displacement along Path 1 at the fission density of 8.3 × 10^{27} fission/m^3, for the cases with different values of β and the case without the constraint of the matrix condition. The case without the matrix part means that the original matrix part in **Figure 2** is occupied by the particle material. The radial displacements of the FE model along path1 keep increasing for the case without the matrix. Meanwhile, those of the other cases display a decreasing trend along the radial direction across the matrix part, due to the through-thickness shrinking of the matrix. It demonstrates that the Zr matrix has the effects of restraining and compensating the irradiation swelling of U-10Mo fuel particles, and the effects are promoted with the decrease in β. As analyzed in *The Deformation and Stress Analysis*, the matrix with lower values of β is susceptible to be fractured, which will result in the reduced restraint effect after failure. So, a compromise should be determined in the actual design and fabrication.

The Irradiation Swelling Analysis

Irradiation swelling of nuclear fuels proceeds with the increase in fission density (Kim and Hofman, 2011; Cui et al., 2015). **Figure 12** depicts the effective irradiation swelling evolutions of dispersion fuels, calculated using **Eq. 11** for the cases with different values of β. The curve of effective irradiation swelling can be divided into two parts with the critical fission density F_{dx}. Beyond F_{dx}, the effective irradiation swelling is accelerated. One can also see that the effective irradiation swelling increases with the rise of β. For the cases with β ranged in 0.01–10, the differences of effective irradiation swelling at the fission density of 8.3 × 10^{27} fission/m^3 are small, not more than 2.5%. For the case of β = 100, the effective irradiation swelling is 13%, with a relative increase of 18% compared to that of the case with β = 0.01.

The effective irradiation swelling of dispersion fuels is driven by the irradiation swelling of fuel particles and is approximately equal to the product of the initial particle volume fraction and the sum of fission solid swelling and fission gas swelling, as shown in **Figure 13**. The evolutions of fission solid swelling and fission gas swelling of Element 1 in the part of the fuel particle are shown in **Figure 14**. The fission solid swelling in **Figure 14A** linearly increases with the fission density independent of β, as expressed in **Eq. 2**. The results of fission gas swelling in **Figure 14B** rise with the increase in β. The fission gas swelling at the fission density of 8.3 × 10^{27} fission/m^3 for β = 0.01 is 3.44%, becoming 10.2% for β = 100, and they are both less than the fission solid swelling of 33%. So, the discrepancies of effective irradiation swelling for U-10Mo/Zr dispersion fuels are mainly dependent on the difference of fission gas swelling for various values of β. The obtained fission gas swelling predictions here are less than the measured results for U-10Mo/Al dispersion fuels in Ref. (Kim et al., 2013). It is mainly due to the occurrence of the IL between the U-10Mo fuel particles and the Al matrix, which weakens the restraint effect of the matrix and can be interpreted as the high creep rate of the IL (Jeong et al., 2020). Moreover, according to our previous studies, the fission gas swelling increases with the decrease in hydrostatic pressure in fuel particles (Cui et al., 2015; Jian et al., 2019a; Zhang J. et al., 2021). The particles selected to measure the fission gas swellings (Kim et al., 2013) are near the middle region of U-10Mo/Al dispersion fuel plates, and the hydrostatic pressures of these particles are close to the coolant pressure of ~2.5 MPa, which are much lower than the experienced hydrostatic pressure of the particles in U-10Mo/Zr dispersion fuels, as presented in *Fission Gas Swelling of Fuel Particles and the Influencing Mechanisms*.

Fission Gas Swelling of Fuel Particles and the Influencing Mechanisms

It can be known from *The Irradiation Swelling Model for U-10Mo Fuels* that the fission gas swelling behavior of nuclear fuels is influenced by the external hydrostatic pressure. **Figure 15** displays the evolution results of hydrostatic pressure of Element 1 for the cases with different values of β. It can be found that the hydrostatic pressure of the fuel particle increases quickly in the preliminary stage of irradiation and tend to be stable at higher burnup levels. As β increases from 0.01 to 100, the maximum hydrostatic pressure decreases from 299 to 24 MPa, with a relative reduction of ~92%. Creep deformation of the matrix could relax the mechanical interactions between the fuel particles and the matrix (Zhang J. et al., 2021). A larger value of β will result in enlarged matrix creep deformations, as shown in **Figure 6**, and the stress relaxation effect will be enhanced to result in lower hydrostatic pressure in the fuel particle, as shown in **Figure 15**.

According to **Eq. 4**, the average radius of inter-granular bubbles is correlated with hydrostatic pressure and the average number of fission gas atoms in each inter-granular bubble. **Figure 16** depicts the average radius predictions of the inter-granular bubbles of Element 1 for the cases with different values of β. One can observe that the average radius of inter-granular

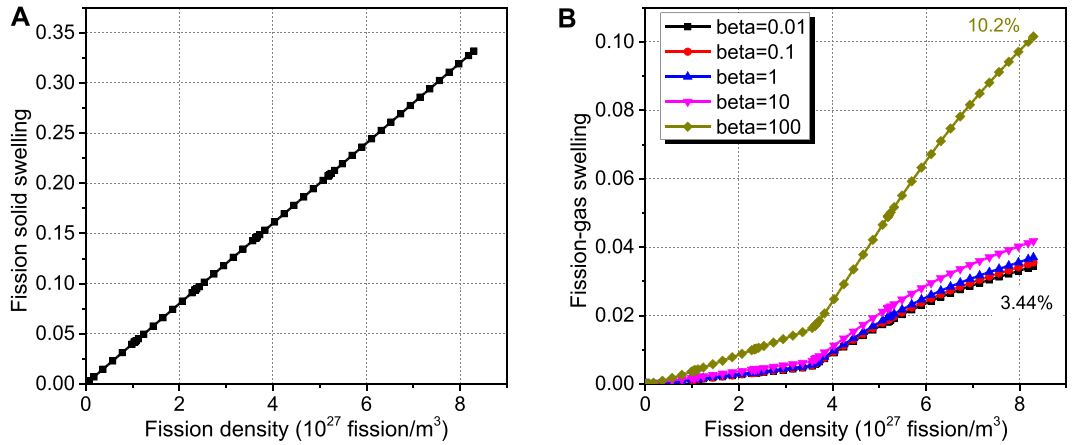

FIGURE 14 | Evolution results of **(A)** fission-solid swelling and **(B)** fission-gas swelling of Element 1.

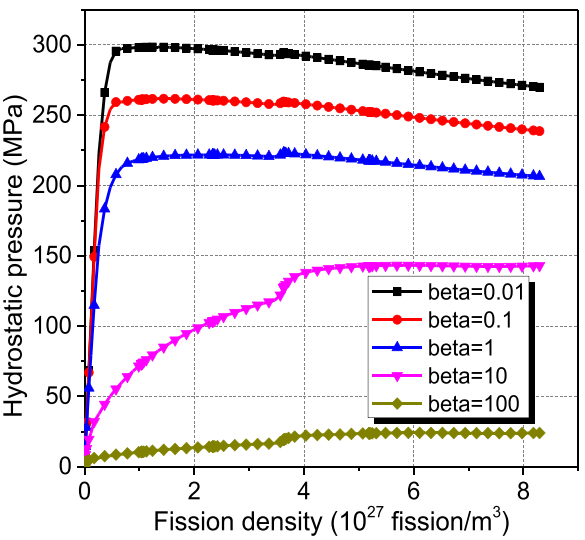

FIGURE 15 | Evolution results of hydrostatic pressure of Element 1 for the cases with different values of β.

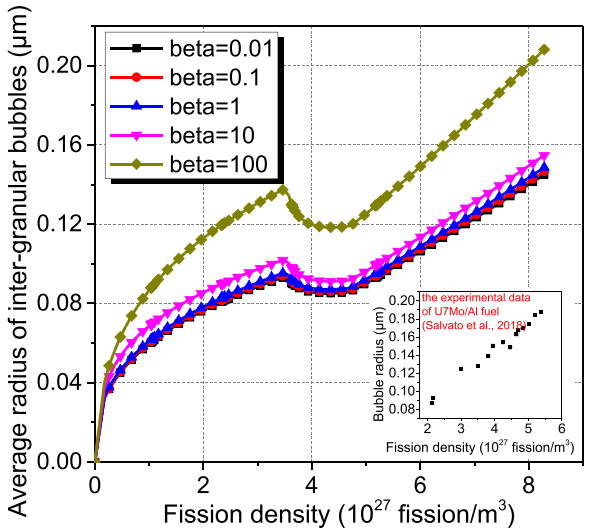

FIGURE 16 | Evolution results of the average radius of inter-granular bubbles of Element 1 for the cases with different values of β.

bubbles increases with the fission density overall, due to the increase in fission gas atoms. As β increases, the average radius of inter-granular bubbles increases because of the lowered hydrostatical pressure. The predicted radius of inter-granular bubbles is in the same magnitude order with experimental results of U-7Mo fuels (Salvato et al., 2018), so that the external hydrostatical pressure effects could be well reflected.

According to **Eq. 3**, the fission gas swelling also depends on the number of inter-granular bubbles or the bubble density $\frac{N_{bubble}}{V_0}$. The cases with different values of β have the same results of the bubble density. One can find from **Figure 17** that the number of inter-granular bubbles does not show significant changes before recrystallization. After recrystallization, the number of inter-granular bubbles increases sharply, due to the increased grain-boundary area per unit volume (Rest, 2005). As the fission density increases further, the inter-granular bubbles begin to coalesce (Meyer et al., 2002) and the predicted number of inter-granular bubbles decreases. The predictions of bubble density match the evolution traits of the experimental results (Salvato et al., 2018). The different fission gas swelling results in **Figure 14B** for the varied cases of β can be known to stem mainly from the discrepancy of inter-granular bubble size influenced by hydrostatic pressure.

Fitted Mathematic Model for the Effective Irradiation Swelling

The effective irradiation swelling is defined as the relative volume variation to the initial volume of the RVE, calculated using **Eq. 11**.

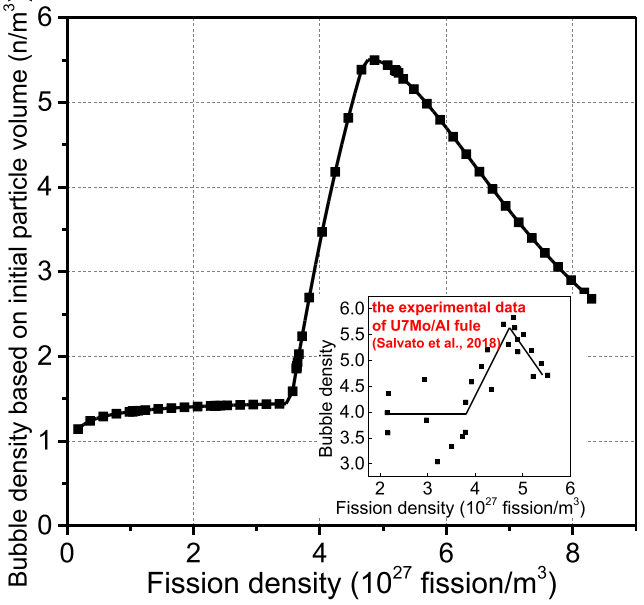

FIGURE 17 | Evolution results of bubble density of Element 1 for all the considered cases.

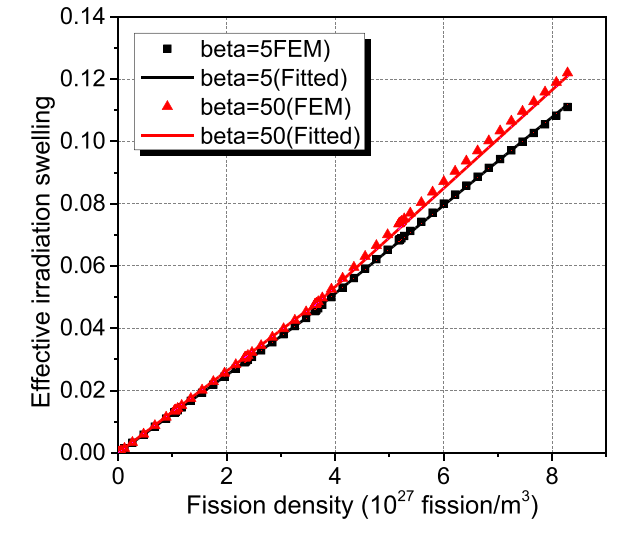

FIGURE 18 | Verification of the fitted model for the effective irradiation swelling of U-10Mo/Zr dispersion fuels.

Considering the temperature of RVE as 373 K and the subjected homogenization pressure as 2.5 MPa, a mathematic model for the effective irradiation swelling of U-10Mo/Zr dispersion fuels is fitted as follows:

$$SW_{eff} = \begin{cases} (-1.1858 \times 10^{-7}\beta^2 + 2.1160 \times 10^{-5}\beta + 1.2375 \times 10^{-2})F_d, & F_d < 3.54 \\ (3.6481 \times 10^{-5}\beta + 1.3978 \times 10^{-2})F_d & \\ -9.8148 \times 10^{-5}\beta - 5.0011 \times 10^{-3}, & F_d \geq 3.54 \end{cases} \quad (12)$$

where SW_{eff} is the effective irradiation swelling; β is the creep amplification factor in the range of 0.01–100; F_d is fission density in 10^{27} fission/m^3; The critical fission density of 3.54×10^{27} fission/m^3 is dependent on fission rate $\dot{f}$, calculated as $4 \times 10^{24}(\dot{f})^{2/15}$.

The comparison of finite element simulation results and the fitted model results is shown in **Figure 18**, for the cases with different values of β. The relative error is less than 0.8% at the fission density of 8.3×10^{27} fission/m^3. So the fitted model is acceptable and could be used to obtain the effective irradiation swelling for U-10Mo/Zr dispersion fuels with the values of β ranged in 0.01–100, under the irradiation condition mentioned in *Finite Element Model*.

It should be mentioned that the homogenization pressures of dispersion fuel foil in the plate-type fuel elements are distributed heterogeneously and vary with the burnup levels and also depend on the matrix creep and the particle volume fractions. As a result, it will be possible for the homogenization pressures to differ greatly from the coolant pressure. Further research should be carried out to obtain a comprehensive mathematic model for usage in the numerical simulations of the irradiation-induced thermal-mechanical behaviors in dispersion fuel elements or assemblies.

CONCLUSION

In this study, a meso-mechanical model is established for the homogenized irradiation swelling of U-10Mo/Zr dispersion fuels. An equivalent sphere is chosen as the RVE, with an initial particle volume fraction of 30% and a temperature of 373 K. A newly developed fission gas swelling mechanistic model for U-10Mo is involved and validated with the experimental results in literatures. To investigate the effect of Zr matrix creep properties on effective irradiation swelling of U-10Mo/Zr dispersion fuels, different creep amplification factors are imposed on a typical creep model. Based on the developed method, the results of effective irradiation swelling for U-10Mo/Zr dispersion fuels are obtained and analyzed. The main conclusions are as follows:

1) The Zr matrix has the effects of restraining and compensating for the irradiation swelling of fuel particles. The effective irradiation swelling of U-10Mo/Zr dispersion fuels increases with the increase of the creep amplification factor of the Zr matrix due to the stress relaxation effect of matrix creep deformations. When the creep amplification factor increases from 0.01 to 100, the effective irradiation swelling at the fission density of 8.3×10^{27} fission/m^3 increases from 11 to 13%, with a relative increase of 18%.
2) Although the effective irradiation swelling increases with the increase of the creep amplification factor, the stresses in the matrix of U-10Mo/Zr dispersion fuels decrease to result in a reduction of the risk of radial crack initiation and propagation. So, the creep properties of the Zr matrix need to be optimized according to design requirements and service conditions.
3) When the creep amplification factor increases from 0.01 to 100, the maximum hydrostatic pressure of the fuel particle decreases from 299 to 24 MPa, with a reduction of 92%. The different fission gas swelling results for the varied cases of the creep amplification factor stems mainly from the discrepancy of inter-granular bubble size influenced by hydrostatic pressure.

4) Based on the results of finite element simulation, a mathematic model for the effective irradiation swelling of U-10Mo/Zr dispersion fuels is fitted and verified. The fitted model is acceptable under the adopted irradiation condition and the selected parameter ranges.

In reality, the initial particle volume fraction and the temperature could be different under different irradiation environments or in different positions. The mechanical interaction between particles and between fuel meat and cladding could also lead to the external equilibrium hydrostatic pressure. So, wide future research studies should be performed.

DATA AVAILABILITY STATEMENT

The original contributions presented in the study are included in the article/Supplementary Material, further inquiries can be directed to the corresponding authors.

AUTHOR CONTRIBUTIONS

YoL: Software, Validation, Formal analysis, Investigation, Data Curation, Writing, Original Draft, Visualization. JZ: Software, Validation, Formal analysis, Investigation, Review & Editing. XJ, FY: Software, Validation, Formal analysis. SD: Conceptualization, Methodology, Software, Resources, Writing, Review & Editing, Supervision, Project administration. YuL: Conceptualization, Supervision, Formal analysis.

FUNDING

The authors are very grateful for the support of the National Natural Science Foundation of China (No. 12132005, 12102094, and 12135008) and the support of the Foundation from Science and Technology on Reactor System Design Technology Laboratory. This study is also sponsored by Shanghai Sailing Program (21YF1402200).

REFERENCES

Carmack, W. J., Todosow, M., Meyer, M. K., and Pasamehmetoglu, K. O. (2006). Inert Matrix Fuel Neutronic, Thermal-Hydraulic, and Transient Behavior in a Light Water Reactor. *J. Nucl. Mater.* 352, 276–284. doi:10.1016/j.jnucmat.2006.02.098

Cox, B. (2005). Some Thoughts on the Mechanisms of In-Reactor Corrosion of Zirconium Alloys. *J. Nucl. Mater.* 336, 331–368. doi:10.1016/j.jnucmat.2004.09.029

Cui, Y., Ding, S., Chen, Z., and Huo, Y. (2015). Modifications and Applications of the Mechanistic Gaseous Swelling Model for UMo Fuel. *J. Nucl. Mater.* 457, 157–164. doi:10.1016/j.jnucmat.2014.11.065

Dai, X., Cao, X., Yu, S., and Zhu, C. (2014). Conceptual Core Design of an Innovative Small PWR Utilizing Fully Ceramic Microencapsulated Fuel. *Prog. Nucl. Energ.* 75, 63–71. doi:10.1016/j.pnucene.2014.04.010

Ding, S. R., Gong, X., Zhao, Y. M., Huo, Y. Z., and Wei, H. Y. (2018). Key Mechanical Problems in Dispersion Nuclear Fuels during Their Burning Evolution Process. *Chin. Q. Mech.* 039 (001), 1–21. doi:10.15959/j.cnki.0254-0053.2018.01.001

Duyn, L. (2003). Evaluation of the Mechanical Behavior of a Metal-Matrix Dispersion Fuel for Plutonium Burning. [master's thesis]. Atlanta: Georgia Institute of Technology.

Gong, X., Ding, S., Zhao, Y., Huo, Y., Zhang, L., and Li, Y. (2013). Effects of Irradiation Hardening and Creep on the Thermo-Mechanical Behaviors in Inert Matrix Fuel Elements. *Mech. Mater.* 65, 110–123. doi:10.1016/j.mechmat.2013.05.008

Gonzalez, A. G., Muñoz, C. A., and Arnaldo, G. J. (2015). Metallographic Study on Alloy Zircaloy-4 of Nuclear Use. *Proced. Mater. Sci.* 8, 494–501. doi:10.1016/j.mspro.2015.04.101

Hagrman, D. T., Allison, C. M., and Berna, G. A. (1995). SCDAP/RELAP5/MOD 3.1 Code Manual: MATPRO, A Library of Materials Properties for Light-Water-Reactor Accident Analysis. *Off. scientific Tech. Inf. Tech. Rep.* 4, 212–449. doi:10.2172/100327

Hales, D. J., Williamson, R. L., Novascone, S. R., Pastore, G., Spencer, B. W., Stafford, D. S., et al. (2016). *Bison Theory Manual the Equations behind Nuclear Fuel Analysis*. Idaho Falls, Idaho National Laboratory. doi:10.2172/1374503

Hayes, T. A., and Kassner, M. E. (2006). Creep of Zirconium and Zirconium Alloys. *Metall. Mat Trans. A.* 37 (8), 2389–2396. doi:10.1007/BF02586213

Holden, A. N. (1967). *Dispersion Fuel elements[M]*. New York: Gordon and Breach Science Publishers Inc. doi:10.1016/0029-554X(68)90177-8

Huber, T. K., Breitkreutz, H., Burkes, D. E., Casella, A. J., Casella, A. M., Elgeti, S., et al. (2018). Thermal Conductivity of Fresh and Irradiated U-Mo Fuels. *J. Nucl. Mater.* 503 (C), 304–313. doi:10.1016/j.jnucmat.2018.01.056

Jeong, G. Y., Kim, Y. S., and Park, J. (2020). Analytical Local Stress Model for UMo/Al Dispersion Fuel. *J. Nucl. Mater.* 528, 151881. doi:10.1016/j.jnucmat.2019.151881

Jian, X., Kong, X., and Ding, S. (2019a). A Mesoscale Stress Model for Irradiated U 10Mo Monolithic Fuels Based on Evolution of Volume Fraction/Radius/Internal Pressure of Bubbles. *Nucl. Eng. Technol.* 51 (6), 1575–1588. doi:10.1016/j.net.2019.04.011

Jian, X., Yan, F., Kong, X., and Ding, S. (2019b). Effects of U-Mo Irradiation Creep Coefficient on the Mesoscale Mechanical Behavior in U-Mo/Al Monolithic Fuel Plates. *Nucl. Mater. Energ.* 21, 100706. doi:10.1016/j.nme.2019.100706

Keiser, D. D., Jr., Jue, J.-F., Miller, B., Gan, J., Robinson, A., Medvedev, P., et al. (2015). Microstructural Characterization of the U-9.1Mo Fuel/AA6061 Cladding Interface in Friction-Bonded Monolithic Fuel Plates Irradiated in the RERTR-6 Experiment. *Metallurgical Mater. Trans. E* 2, 173–189. doi:10.1007/s40553-015-0055-8

Keiser, D. D., Jr., Jue, J. F., Miller, B. D., Gan, J., Robinson, A. B., Medvedev, P., et al. (2014). Scanning Electron Microscopy Analysis of Fule/matirx Interaction Layers in Highly-Irradiation U-Mo Dispersion Fuel Plates with Al and Al-Si alloy Matrices. *Nucl. Eng. Technol.* 46 (2), 147–158. doi:10.5516/NET.07.2014.704

Kim, D., Hong, J., Kim, H., Kim, J., and Kim, H. (2021). Study of the Mechanical Properties and Effects of Particles for Oxide Dispersion Strengthened Zircaloy-4 via a 3D Representative Volume Element Model. *Nucl. Eng. Technol.*, 1–11. doi:10.1016/j.net.2021.10.044

Kim, K., Park, J., Kim, C. L., Hofman, G., and Meyer, M. K. (2002). Irradiation Behavior of Atomized U-10wt.% Mo alloy Aluminum Matrix Dispersion Fuel Meat at Low Temperature. *Nucl. Eng. Des.* 211 (2-3), 229–235. doi:10.1016/S0029-5493(01)00459-9

Kim, Y. S., Hofman, G. L., and Cheon, J. S. (2013). Recrystallization and Fission-Gas-Bubble Swelling of U-Mo Fuel. *J. Nucl. Mater.* 436, 14–22. doi:10.1016/j.jnucmat.2013.01.291

Kim, Y. S., and Hofman, G. L. (2011). Fission Product Induced Swelling of U-Mo Alloy Fuel. *J. Nucl. Mater.* 419 (1), 291–301. doi:10.1016/j.jnucmat.2011.08.018

Kim, Y. S., Jeong, G. Y., Park, J. M., and Robinson, A. B. (2015). Fission Induced Swelling of U-Mo/Al Dispersion Fuel. *J. Nucl. Mater.* 465, 142–152. doi:10.1016/j.jnucmat.2015.06.006

Kong, X., Tian, X., Yan, F., Ding, S., Hu, S., and Burkes, D. E. (2018). Thermo-Mechanical Behavior Simulation Coupled with the Hydrostatic-Pressure-Dependent Grain-Scale Fission Gas Swelling Calculation for a Monolithic UMo Fuel Plate under Heterogeneous Neutron Irradiation. *Open Eng.* 8, 243–260. doi:10.1515/eng-2018-0029

Krishnan, R., and Asundi, M. K. (1980). Zirconium Alloys in Nuclear Technology [J]. *Proc. Indian Acad. Sci.* 4, 41–56. doi:10.1007/BF02843474

Lee, D. B., Kim, K. H., and Kim, C. K. (1997). Thermal Compatibility Studies of Unirradiated U-Mo Alloys Dispersed in Aluminum. *J. Nucl. Mater.* 250, 79–82. doi:10.1016/S0022-3115(97)00252-3

Leenaers, A., Van den Berghe, S., and Detavernier, C. (2013). Surface Engineering of Low Enriched Uranium-Molybdenum. *J. Nucl. Mater.* 440, 220–228. doi:10.1016/j.jnucmat.2013.04.068

Leenaers, A., Van den Berghe, S., Koonen, E., Jarousse, C., Huet, F., Trotabas, M., et al. (2004). Post-Irradiation Examination of Uranium–7wt% Molybdenum Atomized Dispersion Fuel. *J. Nucl. Mater.* 335 (1), 39–47. doi:10.1016/j.jnucmat.2004.07.004

Leenaers, A., Van den Berghe, S., Koonen, E., Kuzminov, V., and Detavernier, C. (2015). Fuel Swelling and Interaction Layer Formation in the Selenium Si and ZrN Coated U(Mo) Dispersion Fuel Plates Irradiated at High Power in BR2. *J. Nucl. Mater.* 458, 380–393. doi:10.1016/j.jnucmat.2014.12.073

Leenaers, A., Van den Berghe, S., Van Renterghem, W., Charollais, F., Lemoine, P., Jarousse, C., et al. (2011). Irradiation Behavior of Ground U(Mo) Fuel with and without Si Added to the Matrix. *J. Nucl. Mater.* 412 (1), 41–52. doi:10.1016/j.jnucmat.2011.02.002

Liu, M., Lee, Y., and Rao, D. V. (2018). Development of Effective thermal Conductivity Model for Particle-Type Nuclear Fuels Randomly Distributed in a Matrix. *J. Nucl. Mater.* 508, 168–180. doi:10.1016/j.jnucmat.2018.05.044

Liu, X., Lu, T. C., Xing, Z. H., and Qian, D. Z. (2011). Modeling the Swelling Performance of UMo Alloys for Al-Matrix Dispersion Fuel. *J. Alloys Compd.* 509, 6589–6594. doi:10.1016/j.jallcom.2011.03.099

Lombardi, C., Luzzi, L., Padovani, E., and Vettraino, F. (2008). Thoria and Inert Matrix Fuels for a Sustainable Nuclear Power. *Prog. Nucl. Energ.* 50 (8), 944–953. doi:10.1016/j.pnucene.2008.03.006

Lou, L., Chai, X. M., Yao, D., Wang, L. J., Li, M. C., Chen, L., et al. (2022). Theoretically Modified Optical Length Research on the Physical Boundary of the Double-Heterogeneous System. *Front. Energ. Res.* 9, 1–10. doi:10.3389/fenrg.2021.773067

Macdonald, P. E., and Thompson, L. B. (1976). Matpro: A Handbook of Materials Properties for Use in the Analysis of Light Water Reactor Fuel Rod Behavior. *Specif. Nucl. Reactors Associated Plants*, 134–140. doi:10.2172/6442256

Meyer, M. K., Hofman, G. L., Hayes, S. L., Clark, C. R., Wiencek, T. C., Snelgrove, J. L., et al. (2002). Low-Temperature Irradiation Behavior of Uranium-Molybdenum Alloy Dispersion Fuel. *J. Nucl. Mater.* 304 (2), 221–236. doi:10.1016/S0022-3115(02)00850-4

Moorthy, K. B. (1969). Current Trends in the Use of Zirconium Alloys. *Metallurgy*, 181–187.

Nakamura, S., Harada, H., Raman, S., and Koehler, P. E. (2007). Thermal Neutron Capture Cross Sections of Zirconium-91 and Zirconium-93 by Prompt γ-ray Spectroscopy. *J. Nucl. Sci. Technol.* 44 (1), 21–28. doi:10.1080/18811248.2007.9711252

Neeft, E., Bakker, K., Belvroy, R. L., Tams, W. J., Schram, R. P. C., Conrad, R., et al. (2003b). Mechanical Behaviour of Macro-Dispersed Inert Matrix Fuels. *J. Nucl. Mater.* 317, 217–225. doi:10.1016/S0022-3115(03)00096-5

Neeft, E., Bakker, K., Schram, R., Conrad, R., and Konings, R. (2003a). The EFTTRA-T3 Irradiation Experiment on Inert Matrix Fuels. *J. Nucl. Mater.* 320 (1), 106–116. doi:10.1016/S0022-3115(03)00176-4

Oh, J.-Y., Kim, Y. S., Tahk, Y.-W., Kim, H.-J., Kong, E.-H., Yim, J.-S., et al. (2016). Modeling a Failure Criterion for U-Mo/Al Dispersion Fuel. *J. Nucl. Mater.* 473, 68–74. doi:10.1016/j.jnucmat.2016.02.015

Pasqualini, E. E., Robinson, A. B., Porter, D. L., Wachs, D. M., and Finlay, M. R. (2016). Fabrication and Testing of U-7Mo Monolithic Plate Fuel with Zircaloy Cladding. *J. Nucl. Mater.* 479, 402–410. doi:10.1016/j.jnucmat.2016.07.034

Perez, D. M., Lillo, M. A., Chang, G. S., Roth, G. A., Woolstenhulme, N. E., and Wachs, D. M. (2011). RERTR-9 Summary Report. *Off. scientific Tech. Inf. Tech. Rep*, 1–28. doi:10.2172/1023454

Rest, J. (2010). An Analytical Study of Gas-Bubble Nucleation Mechanisms in Uranium-alloy Nuclear Fuel at High Temperature. *J. Nucl. Mater.* 402 (2-3), 179–185. doi:10.1016/j.jnucmat.2010.05.022

Rest, J. (2005). A Model for the Effect of the Progression of Irradiation-Induced Recrystallization from Initiation to Completion on Swelling of UO2 and U-10Mo Nuclear Fuels. *J. Nucl. Mater.* 346 (2-3), 226–232. doi:10.1016/j.jnucmat.2005.06.012

Rest, J., and Hofman, G. L. (1997). DART Model for Irradiation-Induced Swelling of Dispersion Fuel Elements Including Aluminum-Fuel Interaction. *Trans. Am. Nucl. Soc.* 77, 1–4.

Salvato, D., Leenaers, A., Van den Berghe, S., and Detavernier, C. (2018). Pore Pressure Estimation in Irradiated UMo. *J. Nucl. Mater.* 510, 472–483. doi:10.1016/j.jnucmat.2018.08.039

Saoudi, M., Barry, A., Lang, J., Boyer, C., Rogge, R. B., Corbett, S., et al. (2022). Post-irradiation Examination of U-7Mo/Mg and U-10Mo/Mg Dispersion Fuels Irradiated in the NRU Reactor. *J. Nucl. Mater.* 558, 153343. doi:10.1016/j.jnucmat.2021.153343

Savchenko, A., Konovalov, I., Vatulin, A., Morozov, A., Orlov, V., Uferov, O., et al. (2007). Dispersion Type Zirconium Matrix Fuels Fabricated by Capillary Impregnation Method. *J. Nucl. Mater.* 362, 356–363. doi:10.1016/j.jnucmat.2007.01.211

Savchenko, A., Vatulin, A., Morozov, A., Sirotin, V., Dobrikova, I., Kulakov, G., et al. (2006). Inert Matrix Fuel in Dispersion Type Fuel Elements. *J. Nucl. Mater.* 352 (1-3), 372–377. doi:10.1016/j.jnucmat.2006.03.003

Savchenko, A., Vatulin, A., Konovalov, I., Morozov, A., Sorokin, V., and Maranchak, S. (2010). Fuel of Novel Generation for PWR and as Alternative to MOX Fuel. *Energ. Convers. Manage.* 51 (9), 1826–1833. doi:10.1016/j.enconman.2010.01.027

Schappel, D., Terrani, K., Powers, J. J., Snead, L. L., and Wirth, B. D. (2018). Modeling the Performance of TRISO-Based Fully Ceramic Matrix (FCM) Fuel in an LWR Environment Using BISON. *Nucl. Eng. Des.* 335 (C), 116–127. doi:10.1016/j.nucengdes.2018.05.018

Van den Berghe, S., and Lemoine, P. (2014). Review of 15 Years of High Density Low Enriched UMo Dispersion Fuel Development for Research Reactors in Europe. *Nucl. Eng. Technol.* 46, 125–146. doi:10.5516/NET.07.2014.703

Van den Berghe, S., Parthoens, Y., Charollais, F., Kim, Y. S., Leenaers, A., Koonen, E., et al. (2012). Swelling of U(Mo)-Al(Si) Dispersion Fuel under Irradiation-Non-Destructive Analyses of the Leonidas E-Future Plates. *J. Nucl. Mater.* 430, 246–258. doi:10.1016/j.jnucmat.2012.06.045

Van den Berghe, S., Van Renterghem, W., and Leenaers, A. (2008). Transmission Electron Microscopy Investigation of Irradiated U-7wt% Mo Dispersion Fuel. *J. Nucl. Mater.* 375 (3), 340–346. doi:10.1016/j.jnucmat.2007.12.006

Wood, M. H., and Kear, K. L. (1983). On the In-Pile Nucleation and Growth of Grain-Boundary Bubbles. *J. Nucl. Mater.* 118, 320–324. doi:10.1016/0022-3115(83)90240-4

Zhang, J., Wang, H., Wei, H., Zhang, J., Tang, C., Lu, C., et al. (2021). Modelling of Effective Irradiation Swelling for Inert Matrix Fuels. *Nucl. Eng. Technol.* 53, 2616–2628. doi:10.1016/j.net.2021.02.019

Zhang, T., Yin, H., Li, X., She, D., Pan, Q., He, D., et al. (2021). Studies on Calculation Models of ASTRA Critical Facility Benchmark Using OpenMC. *Ann. Nucl. Energ.* 158, 108291. doi:10.1016/j.anucene.2021.108291

Zhao, Y., Gong, X., Ding, S., and Huo, Y. (2014). A Numerical Method for Simulating the Non-homogeneous Irradiation Effects in Full-Sized Dispersion Nuclear Fuel Plates. *Int. J. Mech. Sci.* 81, 174–183. doi:10.1016/j.ijmecsci.2014.02.012

Zhao, Y., Gong, X., and Ding, S. (2015). Simulation of the Irradiation-Induced Thermo-Mechanical Behaviors Evolution in Monolithic U-Mo/Zr Fuel Plates under a Heterogeneous Irradiation Condition. *Nucl. Eng. Des.* 285, 84–97. doi:10.1016/j.nucengdes.2014.12.030

Conflict of Interest: The authors declare that the research was conducted in the absence of any commercial or financial relationships that could be construed as a potential conflict of interest.

Publisher's Note: All claims expressed in this article are solely those of the authors and do not necessarily represent those of their affiliated organizations, or those of the publisher, the editors, and the reviewers. Any product that may be evaluated in this article, or claim that may be made by its manufacturer, is not guaranteed or endorsed by the publisher.

Copyright © 2022 Li, Zhang, Jian, Yan, Ding and Li. This is an open-access article distributed under the terms of the Creative Commons Attribution License (CC BY). The use, distribution or reproduction in other forums is permitted, provided the original author(s) and the copyright owner(s) are credited and that the original publication in this journal is cited, in accordance with accepted academic practice. No use, distribution or reproduction is permitted which does not comply with these terms.

APPENDIX A. LIST OF THE INVOLVED ACRONYMS AND SYMBOLS

RVE representative volume element

RERTR Reduced Enrichment for Research and Test Reactors

IL interaction layer

FE finite element

F_d fission density

C_b the defined grain-boundary bubble concentration of un-recrystallization region

C_{bx} the defined grain-boundary bubble concentration of fine grain region

η_{F_d} the modified factor for the gas bubble number

h_s the fitting parameter to make the Van der Waals equation equivalent to the hard-sphere equation of state

b_v the Van der Waals gas constant of Xe

P_h the external hydrostatic pressure

$\boldsymbol{k}$ the Boltzmann constant

$\bar{N}$ the average number of fission gas atoms in each inter-granular bubble

β the creep amplification factor

$\dot{\varepsilon}_m^{cr}$ creep strain rate of Zr matrix

$\dot{\varepsilon}^{ss}$ thermal creep strain rate

$\dot{\varepsilon}^{ir}$ irradiation creep strain rate

$\boldsymbol{Q}$ the activation energy

ϕ the fast neutron flux

frontiers in Energy Research

ORIGINAL RESEARCH
published: 18 March 2022
doi: 10.3389/fenrg.2022.853222

Pin-by-Pin Coupled Transient Monte Carlo Analysis Using the iMC Code

*HyeonTae Kim and Yonghee Kim**

Korea Advanced Institute of Science and Technology, Daejeon, South Korea

In this article, we present a coupled multi-physics Monte Carlo reactor transient analysis framework implemented in the KAIST Monte Carlo iMC code. In the multi-physics framework, the time-dependent neutron transport calculation and the transient heat transfer analysis are done based on the predictor–corrector quasi-static Monte Carlo method and the three-dimensional finite element method, respectively. Using this high-fidelity analysis framework, we demonstrated the negative temperature feedback effect in two pressurized water reactor (PWR) transient scenarios. First, a 3-D burnable absorber-loaded fuel assembly was considered with all reflective boundary conditions. In this simple problem, a positive reactivity-induced transient was analyzed to characterize the reactor responses in view of the pin-wise power and temperature distribution. Second, the iMC multi-physics analysis is applied to a control rod withdrawal transient in the TMI-1 mini core problem, and detailed time-dependent results were provided and compared with the Serpent/SUBCHANFLOW analysis. In both cases, independent MC runs were performed to quantify the uncertainty of the multi-physics MC transient analysis.

Keywords: transient Monte Carlo, multi-physics coupled analysis, centrally shielded burnable absorber (CSBA), iMC code, predictor–corrector quasi-static method

OPEN ACCESS

Edited by:
Yue Jin,
Massachusetts Institute of Technology, United States

Reviewed by:
Tengfei Zhang,
Shanghai Jiao Tong University, China
Shanfang Huang,
Tsinghua University, China

****Correspondence:***
Yonghee Kim
yongheekim@kaist.ac.kr

Specialty section:
This article was submitted to Nuclear Energy, a section of the journal Frontiers in Energy Research

Received: *12 January 2022*
Accepted: *07 February 2022*
Published: *18 March 2022*

Citation:
Kim H and Kim Y (2022) Pin-by-Pin Coupled Transient Monte Carlo Analysis Using the iMC Code. Front. Energy Res. 10:853222. doi: 10.3389/fenrg.2022.853222

1 INTRODUCTION

It is a non-disputable fact that the nuclear reactor is a complex multi-physics system with neutronics, thermal hydraulics, thermo-mechanics, and chemistry interdependency. It is also well-known that a stand-alone physics simulation cannot predict the accurate and reliable dynamic behavior of a given nuclear system, yet many works had been focused on specific physics simulation mostly due to the lack of computational power.

Nowadays, a great portion of researchers in the high-fidelity reactor physics community is focusing on the establishment of a coupled multi-physics analysis framework for transient situations. The time-dependent coupled multi-physics simulations are largely based on neutronics codes with the diffusion or deterministic transport method coupled with reactor hydraulics codes (Fiorina et al., 2015; Cherezov et al., 2020; Park et al., 2020; Wang et al., 2021). In most cases, reactivity feedback effects have been deterministically applied directly to the reactivity, while the feedback constants were independently evaluated from Monte Carlo branch calculations. It is reasonable that the early multi-physics approaches are based on the deterministic neutronics methods as the time-dependent neutronics analysis itself is considered computationally exhaustive.

Despite its computation cost, the explicit Monte Carlo neutron transport method is generally accepted as the most accurate and reliable tool that takes into account various reactor feedbacks that possibly affect the dynamic behavior of a nuclear system in the most explicit way. For pursuing the high-fidelity simulation of transient nuclear systems, a few attempts have been made successfully by Serpent 2 and Tripoli-4 in combination with the SUBCHANFLOW thermal-hydraulics (TH) code

(Ferraro et al., 2019; Ferraro et al., 2020a; Ferraro et al., 2020b; Ferraro et al., 2020c; Ferraro et al., 2020d). To our best knowledge, they are so far the only published research outcomes regarding the time-dependent Monte Carlo transport analysis coupled with TH features.

Unlike the Serpent/SUBCHANFLOW framework, the iMC code utilizes intra-pin power distribution for the temperature analysis to provide an enhanced fuel integrity study for a complex fuel element such as the centrally shielded burnable absorber (CSBA) (Nguyen et al., 2019). From a previous study (Kim and Kim, 2020), we found the use of detailed power distribution critical for accurate temperature analysis. We also suggested using the intra-pellet power shape from a separate pin-cell transport calculation in which the effect of neighboring guide thimble can hardly affect the temperature distribution (Kim, 2022).

In this article, we present the iMC simulation results on pressurized water reactor (PWR) problems using the multi-physics coupled scheme. In **Section 2**, the basic framework of the coupled numerical analysis is introduced. The formulation of the predictor–corrector quasi-static Monte Carlo (PCQS-MC) for the transient neutron transport method, the three-dimensional (3-D) finite element transient heat transfer analysis, and a simplified coolant model for the current analysis are explained. The numerical results are presented in **Section 3**, showing that the negative temperature effect of fuel and coolant on reactivity successfully moves the given reactor system to a steady state in a reactivity insertion transient.

2 FRAMEWORK OF TRANSIENT MULTI-PHYSICS REACTOR ANALYSIS IN IMC

2.1 Predictor–Corrector Quasi-Static Monte Carlo Method

In this section, we discuss the key features for establishing the PCQS-MC method. Guo et al. (2021) implemented the PCQS-MC framework in the RMC based on random samplings of delayed sources within a given time bin and kinetic parameter polynomial fitting method. Meanwhile, Jo and Cho (Jo et al., 2016) used analytic linear interpolation of delayed fission source and exponential transformation method. The iMC adopted the latter approach as we found it mathematically concrete and straightforward to implement.

2.1.1 Transient Fixed Source Iteration for Prediction Step

The time-dependent neutron transport equation includes the time derivative of flux term which is often disregarded in steady-state analyses by defining the multiplication factor. The complete governing equation in the space and time domain requires the following transport equation and precursor concentration equation:

$$\frac{1}{\nu(E)}\frac{\partial\psi\left(\vec{r},E,\vec{\Omega},t\right)}{\partial t}=-L\psi\left(\vec{r},E,\vec{\Omega},t\right)-T\psi\left(\vec{r},E,\vec{\Omega},t\right)+S\psi\left(\vec{r},E,\vec{\Omega},t\right)+\frac{1}{k_0}\frac{\chi_p(E)}{4\pi}(1-\beta)F\psi\left(\vec{r},E,\vec{\Omega},t\right)+\sum_{d=1}^{G_d}\frac{\chi_d(E)}{4\pi}\lambda_d C_d\left(\vec{r},t\right), \tag{1}$$

$$\frac{\partial C_d\left(\vec{r},t\right)}{\partial t}=\frac{1}{k_0}\beta_d F\psi\left(\vec{r},E,\vec{\Omega},t\right)-\lambda_d C_d\left(\vec{r},t\right),\quad d=1\,to\,G_d. \tag{2}$$

Here, ψ is the neutron flux, ν is the energy-dependent neutron speed, k_0 is the initial neutron multiplication factor, β is the aggregate delayed neutron fraction, C_d is the precursor concentration of delayed group d, λ_d is the decay constant, G_d is the number of precursor group, andχ_p and χ_d are the prompt and delayed neutron fission energy spectrum, respectively. The operators are defined as follows:

$$L\psi\left(\vec{r},E,\vec{\Omega},t\vec{r},E,\vec{\Omega},t\right)=\vec{\Omega}\cdot\nabla\psi\left(\vec{r},E,\vec{\Omega},t\right), \tag{3}$$

$$T\psi\left(\vec{r},E,\vec{\Omega},t\right)=\sigma_t\left(\vec{r},E,t\right)\psi\left(\vec{r},E,\vec{\Omega},t\right), \tag{4}$$

$$S\psi\left(\vec{r},E,\vec{\Omega},t\right)=\int dE'\int d\vec{\Omega}'\sigma_s\left(\vec{r},E'\rightarrow E,\vec{\Omega}'\cdot\vec{\Omega},t\right)\psi\left(\vec{r},E',\vec{\Omega}',t\right), \tag{5}$$

$$F\psi\left(\vec{r},E,\vec{\Omega},t\right)=\int dE'\int d\vec{\Omega}'\nu\sigma_f\left(\vec{r},E',t\right)\psi\left(\vec{r},E',\vec{\Omega}',t\right), \tag{6}$$

where σ_t, σ_s, and σ_f are the macroscopic total, scattering, and fission cross section, respectively. Applying the implicit Euler scheme in the time domain gives the discretized form of transport equation:

$$\frac{\psi\left(\vec{r},E,\vec{\Omega},t_s\right)-\psi\left(\vec{r},E,\vec{\Omega},t_{s-1}\right)}{\nu(E)\Delta t}=-L\psi\left(\vec{r},E,\vec{\Omega},t\right)-T\psi\left(\vec{r},E,\vec{\Omega},t_s\right)+S\psi\left(\vec{r},E,\vec{\Omega},t_s\right)+\frac{1}{k_0}\frac{\chi_p(E)}{4\pi}(1-\beta)F\psi\left(\vec{r},E,\vec{\Omega},t_s\right)+\sum_{d=1}^{G_d}\frac{\chi_d(E)}{4\pi}\lambda_d C_d\left(\vec{r},t_s\right). \tag{7}$$

Rearranging the equation and sorting in terms of time-step flux leads to the following transport equation.

$$(L+T_{PCQS}-S)\psi\left(\vec{r},E,\vec{\Omega},t_s\right)=\frac{1}{k_0}\frac{\chi_p(E)}{4\pi}(1-\beta)F\psi\left(\vec{r},E,\vec{\Omega},t_s\right)+\sum_{d=1}^{G_d}\frac{\chi_d(E)}{4\pi}\lambda_d C_d\left(\vec{r},t_s\right)+\frac{\psi\left(\vec{r},E,\vec{\Omega},t_{s-1}\right)}{\nu(E)\Delta t}. \tag{8}$$

Here, the modified transport operator for PCQS formulation is defined as follows:

$$T_{PCQS}\psi\left(\vec{r},E,\vec{\Omega},t_s\right)=\left(\sigma_t\left(\vec{r},E,t_s\right)+\frac{1}{\nu(E)\Delta t}\right)\psi\left(\vec{r},E,\vec{\Omega},t_s\right). \tag{9}$$

Meanwhile, the delayed neutron source distribution at $t = t_s$ can be determined by integrating **Eq. 2** in the given time interval.

$$S_d\left(\vec{r}, E, \vec{\Omega}, t_s\right) = S_d\left(\vec{r}, E, \vec{\Omega}, t_{s-1}\right)()e^{-\lambda_d \Delta t_s} + \int_{t_{s-1}}^{t_s} \frac{\lambda_d \chi_d(E)}{4\pi} \frac{\beta_d F\psi\left(\vec{r}, E, \vec{\Omega}, t'\right)}{k_0} e^{-\lambda_d\left(t_s - t'\right)} dt'. \tag{10}$$

The integration term in **Eq. 10** can be converted into an approximated form by linearly interpolating the fission source density in the time bin.

$$F\psi\left(\vec{r}, E, \vec{\Omega}, t\right) \approx F\psi\left(\vec{r}, E, \vec{\Omega}, t_{s-1}\right)\frac{t_s - t}{\Delta t} + F\psi\left(\vec{r}, E, \vec{\Omega}, t_s\right)\frac{t - t_{s-1}}{\Delta t}, \quad (t_{s-1} \le t < t_s). \tag{11}$$

Applying **Eq. 11** to **Eq. 10** provides the following form of the delayed neutron source distribution:

$$S_d\left(\vec{r}, E, \vec{\Omega}, t_s\right) = S_d\left(\vec{r}, E, \vec{\Omega}, t_{s-1}\right) f_{1,d} + \frac{\chi_d(E)}{4\pi} \frac{\beta_d F\psi\left(\vec{r}, E, \vec{\Omega}, t_{s-1}\right)}{k_0} f_{2,d} + \frac{\chi_d(E)}{4\pi} \frac{\beta_d F\psi\left(\vec{r}, E, \vec{\Omega}, t_s\right)}{k_0} f_{3,d}, \tag{12}$$

where weight factors are defined as follows:

$$f_{1,d} = e^{-\lambda_d \Delta t}, \tag{13}$$

$$f_{2,d} = \frac{1 - e^{-\lambda_d \Delta t} - \lambda_d \Delta t e^{-\lambda_d \Delta t}}{\lambda_d \Delta t}, \tag{14}$$

$$f_{3,d} = \frac{e^{-\lambda_d \Delta t}\left(1 - e^{-\lambda_d \Delta t} + \lambda_d \Delta t e^{-\lambda_d \Delta t}\right)}{\lambda_d \Delta t}. \tag{15}$$

Substituting **Eq. 12** to **Eq. 7** results in the following modified transport equation with three delayed neutron source terms:

$$\left(L + T_{PCQS} - S\right)\psi\left(\vec{r}, E, \vec{\Omega}, t_s\right) = \sum_{d=1}^{G_d} \frac{\chi_d(E)}{4\pi} \lambda_d C_d\left(\vec{r}, t_{s-1}\right) f_{1,d} + \sum_{d=1}^{G_d} \frac{\chi_d(E)}{4\pi} \frac{\beta_d F\psi\left(\vec{r}, E, \vec{\Omega}, t_{s-1}\right)}{k_0} f_{2,d} + \frac{\psi\left(\vec{r}, E, \vec{\Omega}, t_{s-1}\right)}{v(E)\Delta t} + \sum_{d=1}^{G_d} \frac{\chi_d(E)}{4\pi} \frac{\beta_d F\psi\left(\vec{r}, E, \vec{\Omega}, t_s\right)}{k_0} f_{3,d} + \frac{1}{k_0} \frac{\chi_p(E)}{4\pi} (1 - \beta) F\psi\left(\vec{r}, E, \vec{\Omega}, t_s\right). \tag{16}$$

The left-hand side of **Eq. 16** represents the transport operation of the given particle, while the right-hand side terms are the sources. **Eq. 16** can be rewritten to be more understandable in terms of the standard Monte Carlo source iteration framework.

$$\left(L + T_{PCQS} - S\right)\psi^{(\ell)}\left(\vec{r}, E, \vec{\Omega}, t_s\right) = \sum_{d=1}^{G_d} \frac{\chi_d(E)}{4\pi} \lambda_d C_d\left(\vec{r}, t_{s-1}\right) f_{1,d} + \sum_{d=1}^{G_d} \frac{\chi_d(E)}{4\pi} \frac{\beta_d F\psi\left(\vec{r}, E, \vec{\Omega}, t_{s-1}\right)}{k_0} f_{2,d} + \frac{\psi\left(\vec{r}, E, \vec{\Omega}, t_{s-1}\right)}{v(E)\Delta t} + \sum_{d=1}^{G_d} \frac{\chi_d(E)}{4\pi} \frac{\beta_d F\psi^{(\ell-1)}\left(\vec{r}, E, \vec{\Omega}, t_s\right)}{k_0} f_{3,d} + \frac{1}{k_0} \frac{\chi_p(E)}{4\pi} (1 - \beta) F\psi^{(\ell-1)}\left(\vec{r}, E, \vec{\Omega}, t_s\right), \tag{17}$$

where ℓ denotes the iteration step. The last two source terms with a superscript $(\ell - 1)$ are iteratively updated at every PCQS source iteration step. The first three source terms are sampled from the previous time step, often from the last iteration step.

2.1.2 Exponential Transformation

Due to the presence of delayed neutron precursors, the reactor period during transient becomes long, which makes the nuclear reactor controllable. However, this caused the simulation to cover an accordingly long period, leading to a choice between accuracy and computation time depending on the number of time steps. If one chooses a large time step size to reduce the computation time, the truncation error becomes an issue with conventional discretization schemes.

The exponential transformation method applied to the reactor kinetics equation has been shown to greatly reduce truncation error caused by time discretization (Reed and Hansen, 1969; Reed and Hansen, 1970). With a properly chosen frequency in the time domain, the number of time bins for a given physical time simulation can be reasonably small since the allowable time step size is increased. Here, the change of variable is introduced for neutron flux in a time interval $t \in [t_{s-1}, t_s]$ as follows:

$$\psi\left(\vec{r}, E, \vec{\Omega}, t\right) = \phi\left(\vec{r}, E, \vec{\Omega}, t\right)e^{\gamma_s t}. \tag{18}$$

Then, the time derivative of the flux becomes

$$\frac{\partial \psi\left(\vec{r}, E, \vec{\Omega}, t\right)}{\partial t} = \frac{\partial \phi\left(\vec{r}, E, \vec{\Omega}, t\right)}{\partial t} e^{\gamma_s t} + \gamma_s e^{\gamma_s t} \phi\left(\vec{r}, E, \vec{\Omega}, t\right), \tag{19}$$

where γ_s is the exponential transformation frequency.

By substituting **Eq. 19** to **Eq. 1** and applying the implicit Euler method in the time domain, the following discretized form of the transient fixed source transport equation at time step t_s is obtained.

$$\left(L + \tilde{T}_{PCQS} - S\right)\psi\left(\vec{r}, E, \vec{\Omega}, t_s\right) = \sum_{d=1}^{G_d} \frac{\chi_d(E)}{4\pi} \lambda_d C_d\left(\vec{r}, t_{s-1}\right) f_{1,d} + \sum_{d=1}^{G_d} \frac{\chi_d(E)}{4\pi} \frac{\beta_d F\psi\left(\vec{r}, E, \vec{\Omega}, t_{s-1}\right)}{k_0} f_{2,d} + \frac{\psi\left(\vec{r}, E, \vec{\Omega}, t_{s-1}\right)e^{\gamma_s \Delta t}}{v(E)\Delta t} + \sum_{d=1}^{G_d} \frac{\chi_d(E)}{4\pi} \frac{\beta_d F\psi\left(\vec{r}, E, \vec{\Omega}, t_s\right)}{k_0} f_{3,d} + \frac{1}{k_0} \frac{\chi_p(E)}{4\pi} (1 - \beta) F\psi\left(\vec{r}, E, \vec{\Omega}, t_s\right), \tag{20}$$

where

$$\tilde{T}_{PCQS}\psi\left(\vec{r},E,\vec{\Omega},t_s\right)=\left(\sigma_t\left(\vec{r},E,t_s\right)+\frac{1}{v(E)\Delta t}+\frac{\gamma_s}{v(E)}\right)\psi\left(\vec{r},E,\vec{\Omega},t_s\right). \quad (21)$$

Frequency γ_s can be estimated by assuming that the frequencies do not change a lot over the time interval Δt. Then the approximation can be expressed as

$$e^{\gamma_s\Delta t}\int dE'\int d\vec{\Omega}'\psi\left(\vec{r},E',\vec{\Omega}',t_{s-1}\right)=\int dE'\int d\vec{\Omega}'\psi\left(\vec{r},E',\vec{\Omega}',t_s\right), \quad (22)$$

or

$$\gamma_s=\frac{1}{\Delta t}\ln\left(\frac{\int dE'\int d\vec{\Omega}'\psi\left(\vec{r},E',\vec{\Omega}',t_s\right)}{\int dE'\int d\vec{\Omega}'\psi\left(\vec{r},E',\vec{\Omega}',t_{s-1}\right)}\right). \quad (23)$$

2.1.3 Point Kinetics Model for Correction Step

The basic motivation of the correction step is to provide a better amplitude value calculated from a smaller time step value. The point kinetic equation can be derived by factorizing the neutron angular flux into the amplitude function $n(t)$ and the shape function $\varphi(\vec{r},E,\vec{\Omega},t)$:

$$\psi\left(\vec{r},E,\vec{\Omega},t\right)=n(t)\varphi\left(\vec{r},E,\vec{\Omega},t\right). \quad (24)$$

Here, the shape function is normalized based on the initial angular flux distribution as follows:

$$\int dV\int d\vec{\Omega}\int dE\,W\left(\vec{r},E,\vec{\Omega}\right)\frac{\varphi\left(\vec{r},E,\vec{\Omega},t\right)}{v(E)}=\int dV\int d\vec{\Omega}\int dE\,W\left(\vec{r},E,\vec{\Omega}\right)\frac{\psi\left(\vec{r},E,\vec{\Omega},t_0\right)}{v(E)}. \quad (25)$$

We obtain the above equation by assuming $\frac{\partial}{\partial t}\langle W(\vec{r},E,\vec{\Omega}),\frac{\varphi(\vec{r},E,\vec{\Omega},t_s)}{v(E)}\rangle=0$, where $W(\vec{r},E,\vec{\Omega})$ is an arbitrary weighting function.

Substituting **Eq. 24** to **Eqs 1**, **2**, and performing weighted integration over space, angle, and time results in the following point kinetic (PK) equations for the amplitude function and the weighted integrals of precursor density functions:

$$\frac{dn(t)}{dt}=\alpha_p(t)n(t)+\sum_{d=1}^{G_d}\lambda_d\bar{C}_d(t), \quad (26)$$

$$\frac{d\bar{C}_d(t)}{dt}=-\lambda_d\bar{C}_d(t)+\frac{\beta(t)}{\Lambda(t)}n(t),\quad d=1\,to\,G_d. \quad (27)$$

where ρ is the reactivity, β is the delayed neutron fraction, Λ is the neutron generation time, λ_d is the delayed neutron precursor decay constant, and $\bar{C}_d$ is the precursor concentration. The PK parameters are defined as

$$\alpha_p(t)\equiv\frac{\rho(t)-\beta(t)}{\Lambda(t)}, \quad (28)$$

$$\rho(t)=1-\frac{k_0}{k(t)},\ with\,k(t)=\frac{\langle W\left(\vec{r},E,\vec{\Omega}\right),\frac{\chi(E)}{4\pi}F\varphi\left(\vec{r},E,\vec{\Omega},t\right)\rangle}{\langle W\left(\vec{r},E,\vec{\Omega}\right),(L+T-S)\varphi\left(\vec{r},E,\vec{\Omega},t\right)\rangle}, \quad (29)$$

$$\beta(t)=\sum_{d=1}^{G_d}\beta_d(t),\ with\,\beta_d(t)=\frac{\langle W\left(\vec{r},E,\vec{\Omega}\right),\frac{\chi_d(E)}{4\pi}\beta_dF\varphi\left(\vec{r},E,\vec{\Omega},t\right)\rangle}{\langle W\left(\vec{r},E,\vec{\Omega}\right),\frac{\chi_d(E)}{4\pi}F\varphi\left(\vec{r},E,\vec{\Omega},t\right)\rangle}, \quad (30)$$

$$\Lambda(t)=\frac{\langle W\left(\vec{r},E,\vec{\Omega}\right),\frac{1}{v(E)}\varphi\left(\vec{r},E,\vec{\Omega},t\right)\rangle}{\langle W\left(\vec{r},E,\vec{\Omega}\right),\frac{1}{k_0}\frac{\chi_d(E)}{4\pi}F\varphi\left(\vec{r},E,\vec{\Omega},t\right)\rangle}, \quad (31)$$

$$\bar{C}_d(t)=\frac{\langle W\left(\vec{r},E,\vec{\Omega}\right),\frac{\chi_d(E)}{4\pi}C_d\left(\vec{r},t\right)\rangle}{\langle W\left(\vec{r},E,\vec{\Omega}\right),\frac{1}{v(E)}\varphi\left(\vec{r},E,\vec{\Omega},t\right)\rangle}, \quad (32)$$

where W is an arbitrary weighting function, and a constant weighting function is used in the current iMC.

The above PK parameters are tallied and averaged through PCQS source iterations. After the source iterations are completed, the PKE is solved based on the tallied PK parameters and PCQS micro time step δt. Here, $\alpha_p(t)$ is linearly interpolated between time t_{i-1} and t_i. For the discretization of the differential equation, the implicit Euler method is preferred for numerical stability.

The shape function at time step t_s is calculated based on the predicted flux distribution as follows:

$$\varphi\left(\vec{r},E,\vec{\Omega},t_s\right)=\psi^{predictor}\left(\vec{r},E,\vec{\Omega},t_s\right)\frac{1}{Z(t_s)}, \quad (33)$$

where normalization factor $Z(t_s)$ is defined from the normalization condition of **Eq. 25**.

$$Z(t_s)\equiv\frac{\langle W\left(\vec{r},E,t_s\right),\frac{\psi^{predictor}\left(\vec{r},E,\vec{\Omega},t_s\right)}{v(E)}\rangle}{\langle W\left(\vec{r},E,t_s\right),\frac{\psi\left(\vec{r},E,\vec{\Omega},t_0\right)}{v(E)}\rangle}. \quad (34)$$

Finally, the corrected flux distribution for the next source iteration is determined by using the amplitude function $n(t_s)$ in the following way:

$$\psi^{corrector}\left(\vec{r},E,\vec{\Omega},t_s\right)=\psi^{predictor}\left(\vec{r},E,\vec{\Omega},t_s\right)\frac{n(t_s)}{Z(t_s)}. \quad (35)$$

2.2 Finite Element Fuel Temperature Analysis

Based on the cell-wise power density tallied from the MC transport simulation, the FEM heat transfer calculation is performed for the fuel element temperature evaluation. The 3-D time-dependent heat conduction equation is obtained as follows:

$$\frac{\partial}{\partial x}\left(k_x\frac{\partial T(x,y,z,t)}{\partial x}\right)+\frac{\partial}{\partial y}\left(k_y\frac{\partial T(x,y,z,t)}{\partial y}\right)+\frac{\partial}{\partial z}\left(k_z\frac{\partial T(x,y,z,t)}{\partial z}\right)+Q(x,y,z,t)=C_p\frac{\partial T(x,y,z,t)}{\partial t}, \tag{36}$$

where T is the position-dependent temperature, Q is the heat source, k is the conductivity, and C_p is the heat capacity.

For the finite element analysis, a linear interpolation function is applied for each tetrahedron with an interpolation function (N) defined for four nodes:

$$N(x,y,z)=\begin{bmatrix}N_1 & N_2 & N_3 & N_4\end{bmatrix}, \tag{37}$$

$$N_i=\frac{1}{6V}(a_i+b_ix+c_iy+d_iz),\quad i=1,\ 2,\ 3,\ 4, \tag{38}$$

where V is the tetrahedron volume and (x_i, y_i, z_i) are coordinates of node i. From the interpolation function, the temperature gradient in the element is obtained in terms of nodal temperatures as

$$\begin{bmatrix}\frac{\partial T}{\partial x}\\ \frac{\partial T}{\partial y}\\ \frac{\partial T}{\partial z}\end{bmatrix}=\begin{bmatrix}\frac{\partial N_1}{\partial x} & \frac{\partial N_2}{\partial x} & \frac{\partial N_3}{\partial x} & \frac{\partial N_4}{\partial x}\\ \frac{\partial N_1}{\partial y} & \frac{\partial N_2}{\partial y} & \frac{\partial N_3}{\partial y} & \frac{\partial N_4}{\partial y}\\ \frac{\partial N_1}{\partial z} & \frac{\partial N_2}{\partial z} & \frac{\partial N_3}{\partial z} & \frac{\partial N_4}{\partial z}\end{bmatrix}\begin{bmatrix}T_1\\ T_2\\ T_3\\ T_4\end{bmatrix}. \tag{39}$$

Using the Galerkin method, **Eq. 36** is rewritten in the following form:

$$\int_V\left(k\frac{\partial^2T}{\partial x^2}+k\frac{\partial^2T}{\partial y^2}+k\frac{\partial^2T}{\partial z^2}-Q+C_p\frac{\partial T}{\partial t}\right)N_i dV=0,\quad i=1,\ 2,\ 3,\ 4. \tag{40}$$

Applying **Eq. 39** to **Eq. 40** gives a system of linear equations defined for every nodal temperature.

$$[C]\frac{\{T^{(\ell+1)}-T^{(\ell)}\}}{\delta t}+([K_c]+[K_h])\{T^{(\ell+1)}\}=\{R_q\}, \tag{41}$$

where ℓ denotes the time step index and

$$[B]=\frac{1}{6V}\begin{bmatrix}\frac{\partial N_i}{\partial x} & \frac{\partial N_j}{\partial x} & \frac{\partial N_k}{\partial x} & \frac{\partial N_m}{\partial x}\\ \frac{\partial N_i}{\partial y} & \frac{\partial N_j}{\partial y} & \frac{\partial N_k}{\partial y} & \frac{\partial N_m}{\partial y}\\ \frac{\partial N_i}{\partial z} & \frac{\partial N_j}{\partial z} & \frac{\partial N_k}{\partial z} & \frac{\partial N_m}{\partial z}\end{bmatrix},\quad [C]=\int_v C_p[N]^T[N]dv,\quad [K_c]=\int_v k[B]^T[B]dv,\quad [K_h]=\int_v h_f[N]^T[N]dv,\quad \{R_q\}=\int_v Q[N]^Tdv.$$

For the case of defining one million tetrahedrons, approximately 200,000 nodal temperatures are defined. To solve such a large matrix equation, the iMC uses the Intel math kernel library *dgesv* routine to achieve the least burden.

2.3 Coolant Model

Before coupling with an all-inclusive subchannel program, an internal coolant model is considered for a preliminary evaluation. The active-core region coolant is lumped into a point model, considering inlet, outlet, and average temperature only. The coolant temperature and the corresponding density is the major driving factor of coolant reactivity feedback, and this is governed by the average coolant temperature in this simulation model. The lumped coolant model is illustrated in **Figure 1**, where the control volume envelopes the entire coolant region.

In a steady-state condition, the energy balance equation is as follows:

$$\dot{m}c_p(T_{out}-T_{in})=\dot{Q}, \tag{42}$$

and the outlet coolant temperature is simply obtained as

$$T_{out}=T_{in}+\frac{\dot{Q}}{\dot{m}c_p}, \tag{43}$$

where $\dot{m}$ is the coolant mass flow rate, c_p is the specific heat capacity of the coolant, h is the coolant enthalpy, T_{wall} is the cladding wall temperature, T_f is the coolant bulk temperature, and $\dot{Q}$ is the thermal power of the fuel element. The average coolant temperature is defined as an average of the inlet and outlet coolant temperatures:

$$T_f=\frac{1}{2}(T_{out}+T_{in}). \tag{44}$$

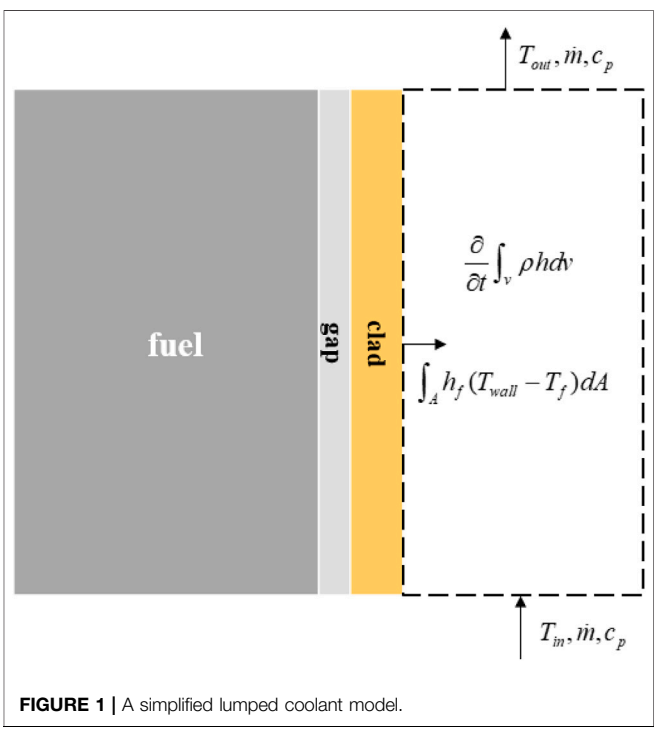

FIGURE 1 | A simplified lumped coolant model.

For a time-dependent problem, the energy balance equation for the given control volume includes an additional time derivative term:

$$\frac{\partial}{\partial t}\int_{v}\rho h dv = \frac{\partial}{\partial t}\left(\rho h V\right) = \dot{m}\left(h_{in} - h_{out}\right) + \dot{Q}. \tag{45}$$

Assuming a constant mass flow rate and the total mass is also constant as $\rho V = M$, the time derivative of the control volume's enthalpy is

$$\frac{\partial}{\partial t}\left(\rho h V\right) = \rho V\frac{\partial h}{\partial t} = \rho V\frac{\partial h}{\partial T}\frac{\partial T_f}{\partial t} = \rho V c_p\frac{\partial T_f}{\partial t}, \tag{46}$$

where $c_p \equiv \frac{\partial h}{\partial T_f}$.

Applying **Eq. 46** to **Eq. 45**, the time-dependent heat balance equation becomes

$$Mc_p\frac{\partial T}{\partial t} = \dot{m}c_p\left(T_{in} - T_{out}\right) + h_f A\left(T_{wall} - T_f\right). \tag{47}$$

To numerically solve the equation, we may apply the implicit Euler scheme:

$$Mc_p\frac{T_f^{(\ell)} - T_f^{(\ell-1)}}{\Delta t} = \dot{m}c_p\left(T_{in} - T_{out}\right) + h_f A\left(T_{wall} - T_f^{(\ell)}\right). \tag{48}$$

The coolant temperature at the current time step is then expressed as follows:

$$T^{(\ell)} = \frac{\frac{Mc_p}{\Delta t}T^{(\ell-1)} + 2\dot{m}c_p T_{in} + h_f A T_{wall}}{\left(\frac{Mc_p}{\Delta t} + 2\dot{m}c_p + h_f A\right)}. \tag{49}$$

2.4 Coupled Analysis Framework

The data exchange between the neutronics and the thermal-hydraulics part in the iMC code does not require an additional file exchange protocol since each calculation module is implemented in a single platform. The neutron transport simulation generates a user-specified thermal power distribution which is to be used in the heat transfer calculation. The thermal-hydraulics module performs the heat transfer analysis to provide the temperature evolution through the time step for the next time step neutron transport simulation.

Before the onset of the transient simulation, the system is needed to be in a steady state. The reactor system is first assumed to have a nominal constant temperature, and a steady-state neutron transport simulation calculates the local power distribution and global reactivity based on the arbitrary system condition. Using the neutronics output, a subsequent steady-state thermal-hydraulics simulation determines the corresponding temperature of all materials of interest. The temperature is then used in the next neutron transport simulation. Through this steady-state coupled iteration, material temperatures on a pin-by-pin basis are determined with the steady-state reactor power distribution.

Once the steady condition of the given reactor system is found, the transient simulation is commenced. Just like in the previous steady-state condition search iteration, the neutronics and the thermal-hydraulics coupled analysis is performed in every time bin, except the simulation schemes are based on the time-dependent formulation. The overall calculation flow of the coupled analysis is described in **Figure 2**.

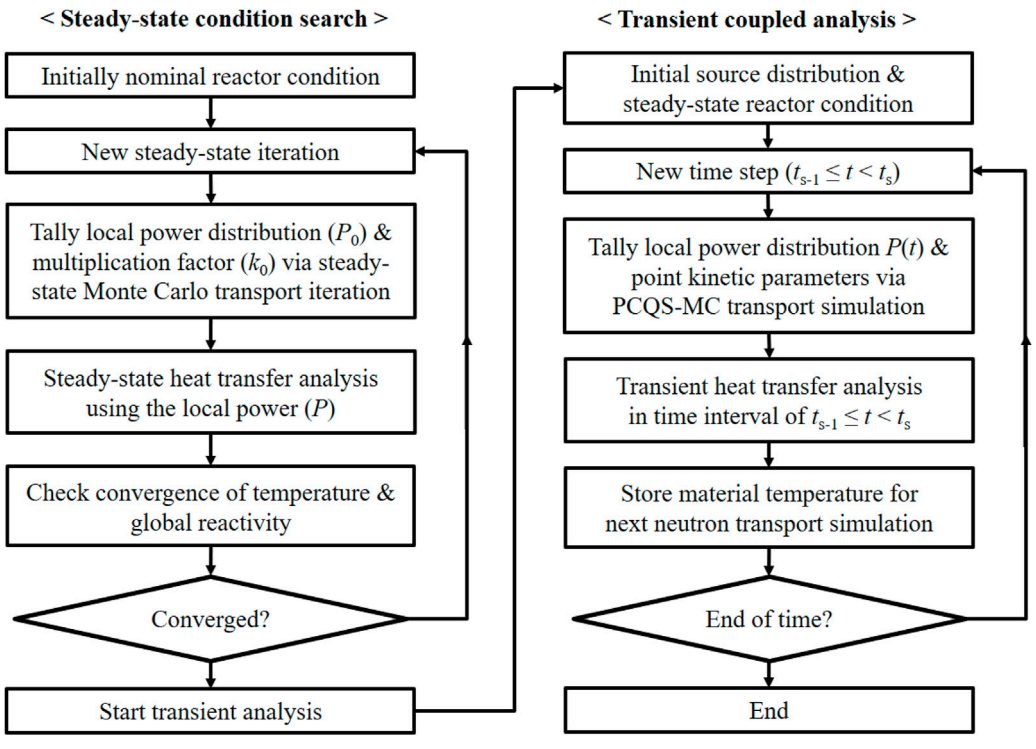

FIGURE 2 | Flowchart of coupled analysis framework.

3 NUMERICAL RESULTS

3.1 CSBA-Loaded Fuel Assembly

For a preliminary study on the multi-physics feedback transient analysis, a CSBA-loaded fuel assembly is designed. In this model, a 17-by-17 PWR fuel assembly is composed of CSBA-loaded fuel pellets in place of the conventional plain UO_2 fuel. Also, four control rods are initially inserted into the fuel assembly as a means to impose a reactivity transient. A discretized single CSBA pellet model and the CSBA-loaded assembly are illustrated in **Figure 3**. The mesh was generated from Gmsh (Geuzaine and Remacle, 2009) software for the finite element heat transfer analysis. Detailed information about the CSBA model is presented in the study by Kim and Kim (2021b).

To simplify the problem, a single layer of CSBA-inserted fuel is considered and the assembly is considered to be subjected to all reflective boundary conditions in four radial sides, top, and bottom. In the iMC, a user can provide reactivity transient scenarios in two different ways: changing material cross section by mixing or replacing with predefined materials or deforming the geometry by tuning surface parameters. In either case, the time-dependent parameter values are given in a user-defined function of time. To simulate the control rod withdrawal transient in this problem, we linearly mixed the coolant with

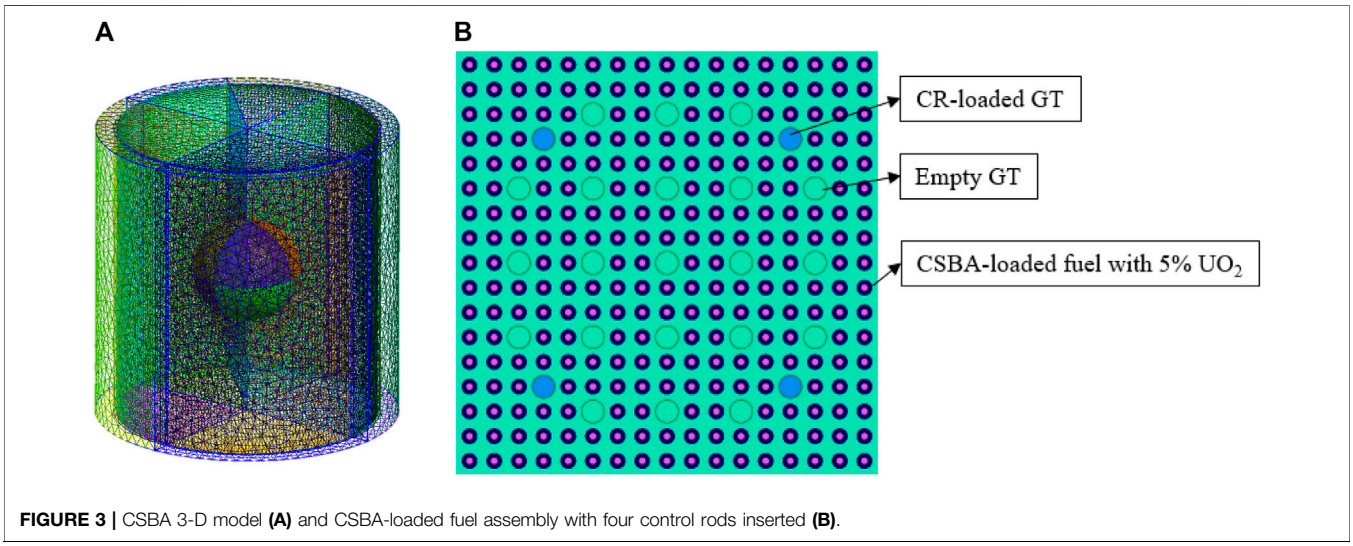

FIGURE 3 | CSBA 3-D model **(A)** and CSBA-loaded fuel assembly with four control rods inserted **(B)**.

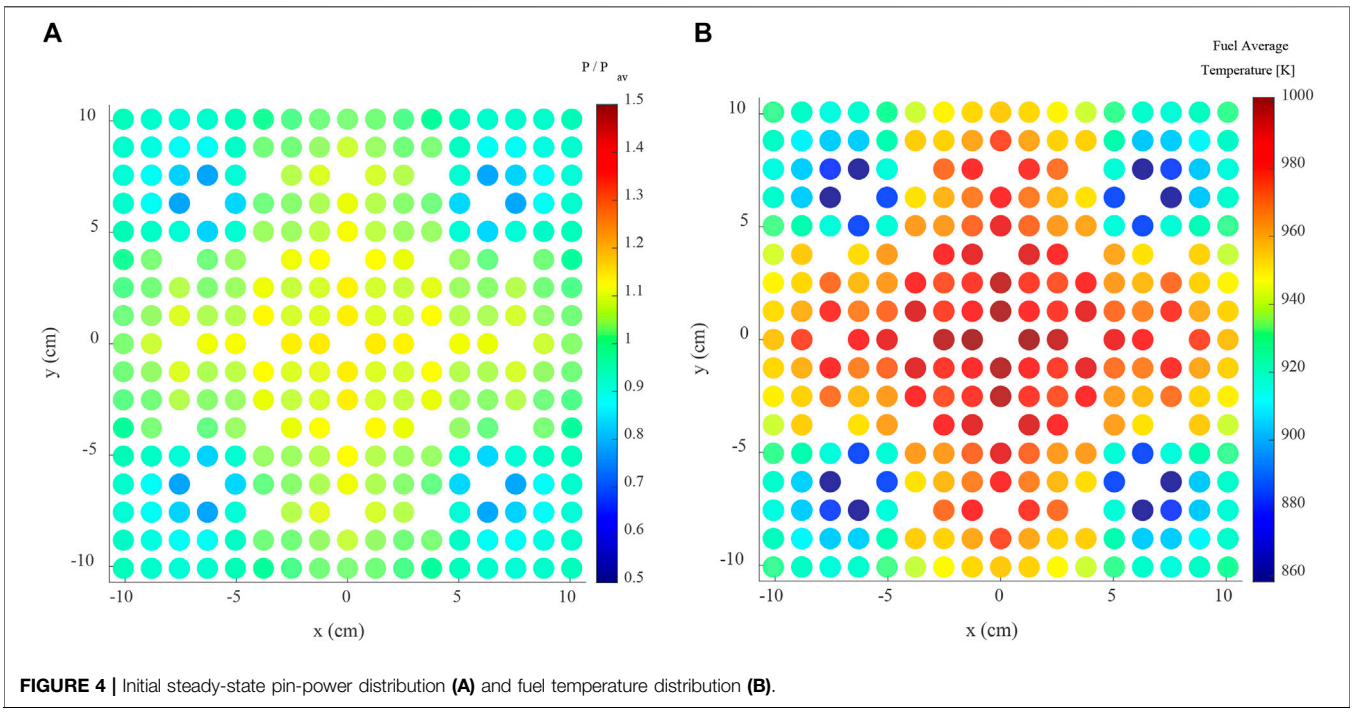

FIGURE 4 | Initial steady-state pin-power distribution **(A)** and fuel temperature distribution **(B)**.

TABLE 1 | CSBA fuel pellet analysis condition.

	—	—
Geometry (cm)	Fuel height	1.00000
	Fuel radius	0.40958
	CSBA sphere radius	0.16900
	Gas gap	0.00915
	Cladding thickness	0.05727
	Pin pitch	1.25984
Materials	Fuel/BA/gap/cladding	UO_2/Gd_2O_3/He/zircaloy-4
	Fuel enrichment	5 w/o
Convective heat transfer	Convective heat transfer coefficient	0.96 W/cm^2-K
	Inlet coolant temperature	558 K
	Coolant mass flow rate	49.39 kg/s
Monte Carlo transport	Number of histories per cycle	200,000
	Number of PCQS inactive/active cycles	200/200
	Number of independent batch runs	25
	Macro/micro time step size (sec)	0.1/0.001

TABLE 2 | Computation burden for major functions.

Functions		Fractional time (%)	CPU hours per time step
PCQS-MC	Source set	0.286	0.16
	Source comb	0.046	—
	Particle transport	95.77	54
	PKE solver	0.002	—
Transient heat transfer		3.899	2.2

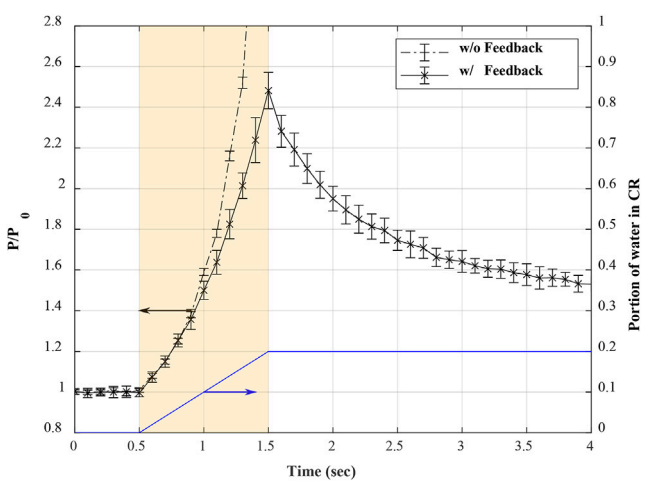

FIGURE 5 | Time-dependent reactor power without feedback (dashed line) and with feedback (solid line) under a given portion of water mixed with control rods (blue line).

the control rod material instead of geometric movement. The time-dependent mixing ratio is given in terms of volume fraction, and the corresponding new density is calculated in the iMC.

Before the transient simulation, a series of feedback iterations is performed to find an initial steady-state reactor

TABLE 3 | Critical boron concentrations from different conditions and codes.

	Simplified TH model	SUBCHANFLOW TH model Sanchez et al. (2010)
Serpent 2	1,480 ppm Ferraro et al. (2019)	1,272 ppm Ferraro et al. (2020a)
Tripoli-4	1,493 ppm Ferraro et al. (2019)	1,305 ppm Faucher et al. (2021)
iMC	1,450 ppm	—

system with the initial thermal power of 36 W/gU. The initial intra-pin temperature distribution and coolant average temperature are set as a constant value for the first steady-state transport simulation. With the obtained power distribution, the detailed temperature is updated. The iteration quickly converged to a steady-state after 2–3 iterations. The obtained pin-power distribution and pin average fuel temperature distribution are shown in **Figure 4**. The CSBA model used in this simulation is described in **Table 1**, and material properties used in the analysis are identical to those in the study by Kim and Kim (2020).

Starting from the initial material temperature and coolant density, the PCQS-assisted Monte Carlo transient calculation is done. The control rod material is linearly mixed with water from 0.5 to 1.5 s up to 20% of water volume fraction; 25 independent batch runs were performed to evaluate the uncertainty of the simulation. The reactor thermal power profile over the transient is shown in **Figure 5**. Without adequate temperature feedback from fuel, burnable absorber, and coolant, the reactor power increases exponentially with the given positive reactivity as the dashed line in **Figure 5**. However, the negative feedback effects of fuel and moderator temperatures suppressed the power excursion right after the end of additional reactivity insertion; the reactor power started to converge toward another stable state.

Figure 6 presents the fuel and moderator average temperature evolution with respect to the given thermal power transient. The fuel temperature response is rather prompt, although there is a

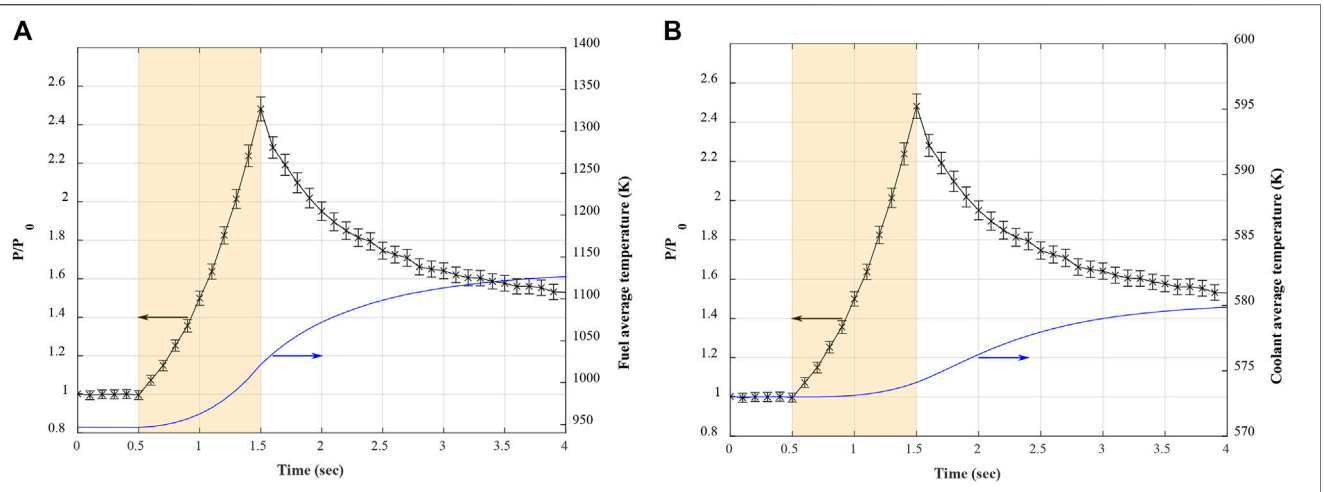

FIGURE 6 | Time-dependent fuel average temperature **(A)** and coolant average temperature **(B)**.

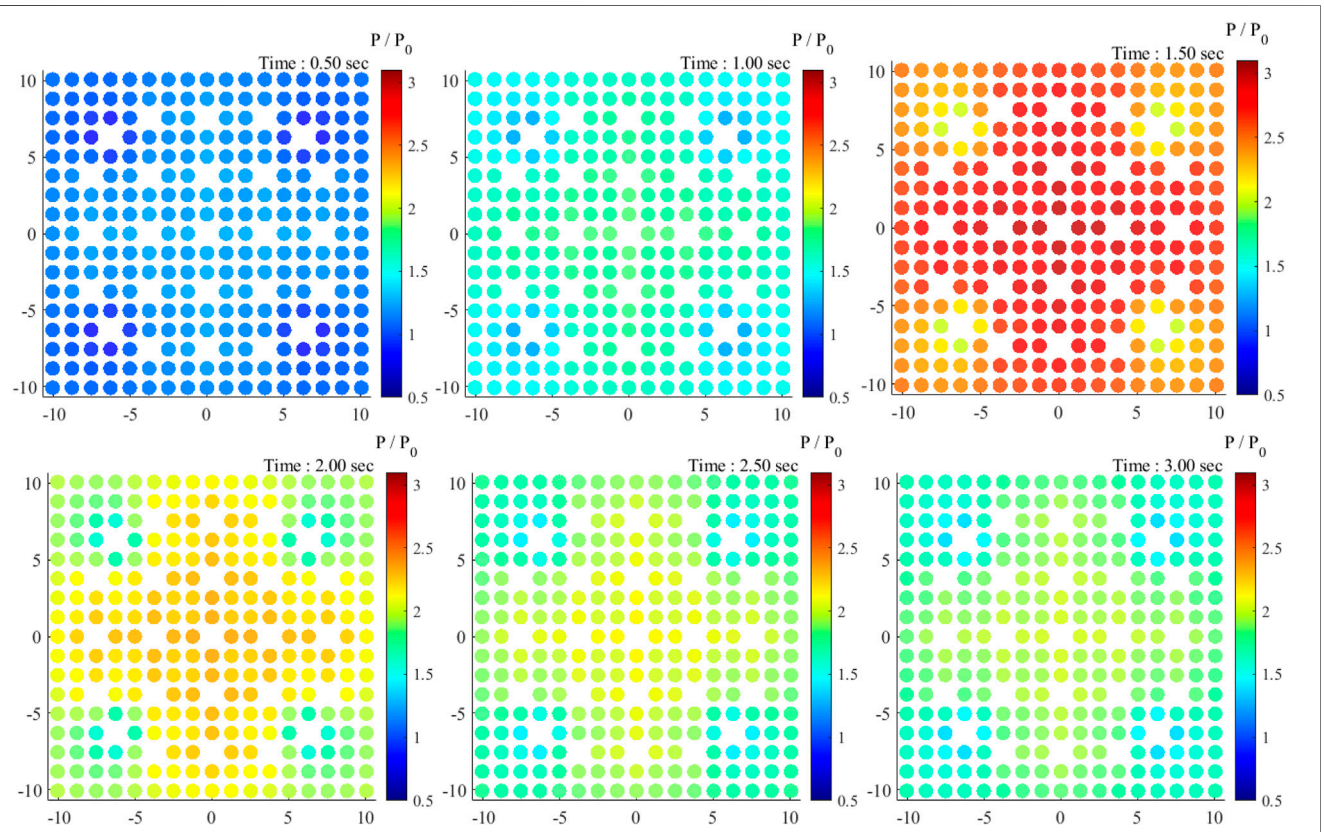

FIGURE 7 | Time-dependent pin-power distribution from 0.5 to 3 s.

slight lag to reach a stable state. This lag is largely due to the thermal inertia of the fuel and the heat dissipation delay from the fuel to the coolant. The coolant temperature response was clearly slower than that of the fuel since it is the last material of the heat transfer process. These temperature responses are also shown in local power and temperature in **Figures 7**, **8**. The peak pin-power occurred at 1.5 s and decreased afterward, while the pin-wise fuel temperature monotonically increases to reach a plateau.

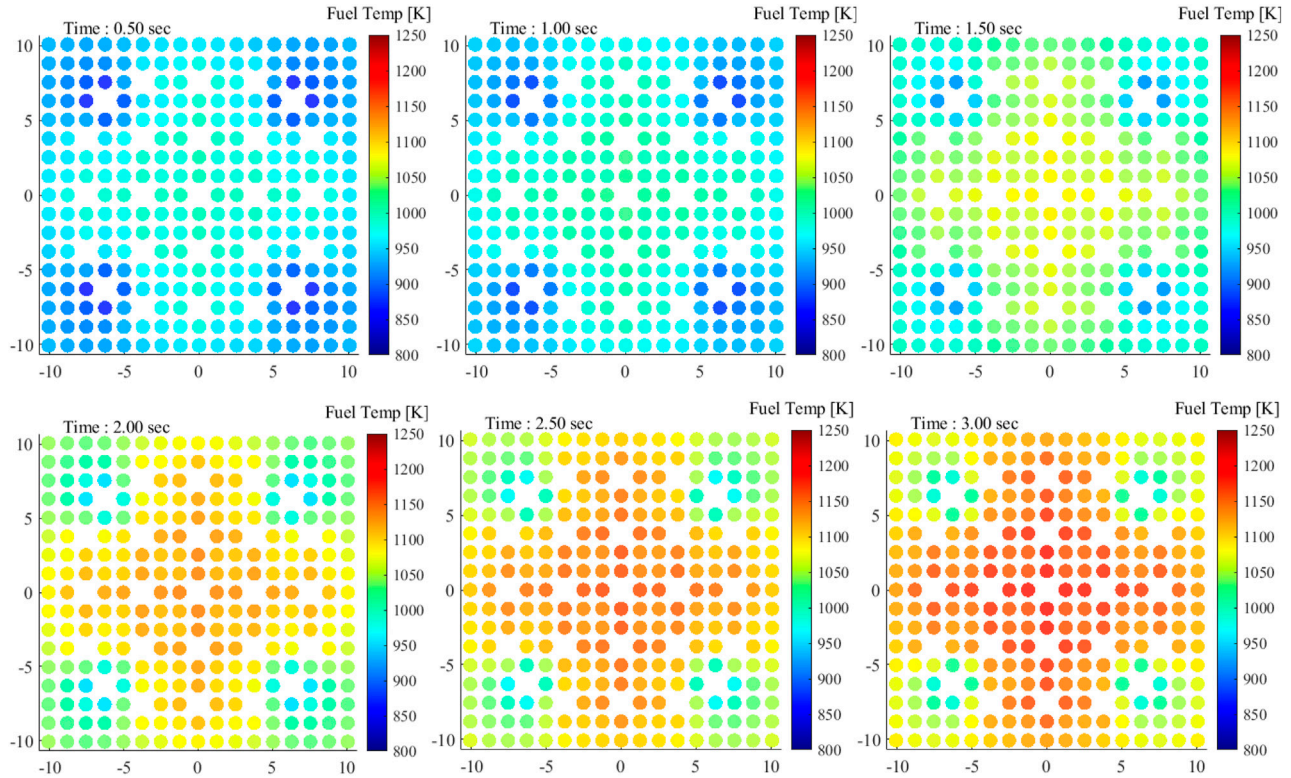

FIGURE 8 | Time-dependent fuel temperature distribution from 0.5 to 3 s.

Table 2 shows the computation burden for major functions in a fraction of total computation time. The particle transport occupies most of the resources in the multi-physics simulation. The source list setting and combing takes less than 1% of the total burden, and the PK equation solving time is negligible. The FEM heat transfer calculation for each fuel pin is rather significant, implying a possibility of acceleration and algorithmic improvement for the matrix operation for larger problems.

3.2 PWR Mini-Core Problem

This numerical study is for the verification of the iMC multi-physics coupled transient analysis framework. The only currently available Monte Carlo coupled analysis result is provided by the Serpent/SUBCHANFLOW framework. The TMI-1 mini-core problem provided in Ref (Ivanov et al., 2013) is considered for the iMC analysis, and the results are compared against the Serpent/SUBCHANFLOW analysis result presented in Refs. (Ferraro et al., 2019) and (Ferraro et al., 2020a). The TMI-1 mini-core problem consists of 15-by-15 PWR fuel assemblies in a 3-by-3 configuration as shown in **Figure 9**. In the center fuel assembly, 16 Ag-In-Cd control rods are initially fully inserted.

The coolant contains soluble boron to make the system critical. The critical boron concentration (CBC) depends on the thermal-hydraulic model since the temperature and grid structure of the coolant channel are directly related to the borated coolant density. In the study by Ferraro et al. (2019), Serpent 2 and Tripoli-4 used a point-wise coolant model and neglected time delay in heat transfer from the fuel to the coolant, and the iMC obtained a similar value as in **Table 3**. When the coolant model is based on the detailed subchannel analysis code, the CBC value is lowered by about 200 ppm from the simple model due to the aforementioned reason.

The simplified TH model in Ref. (Ferraro et al., 2019) assumes no thermal inertia of the fuel element, exhibiting no time delay of heat deposition inside the fuel by neglecting the time derivative term of the transient heat transfer equation. Since the iMC considers time-dependent heat transfer inside the fuel element without any approximation (but point model for the coolant), comparing the iMC analysis result with the simplified fuel heat transfer model is not adequate. Instead, we proposed to compare with the Serpent/SUBCHANFLOW coupled analysis model while the amount of static reactivity insertion is set to be identical. The static reactivity inserted in the Serpent/SUBCHANFLOW analysis is 354 pcm, with control rods withdrawn by 30 cm. We evaluated the equivalent control rod withdrawal length in the iMC that provides a similar static reactivity (**Table 4**). The critical boron concentration of the iMC model is determined on a trial basis iteration.

The reactor transient starts from 0.2 s by pulling out the 16 control rods from the active core with a constant speed pre-calculated in **Table 4** for 1 s. The reactor is axially divided into

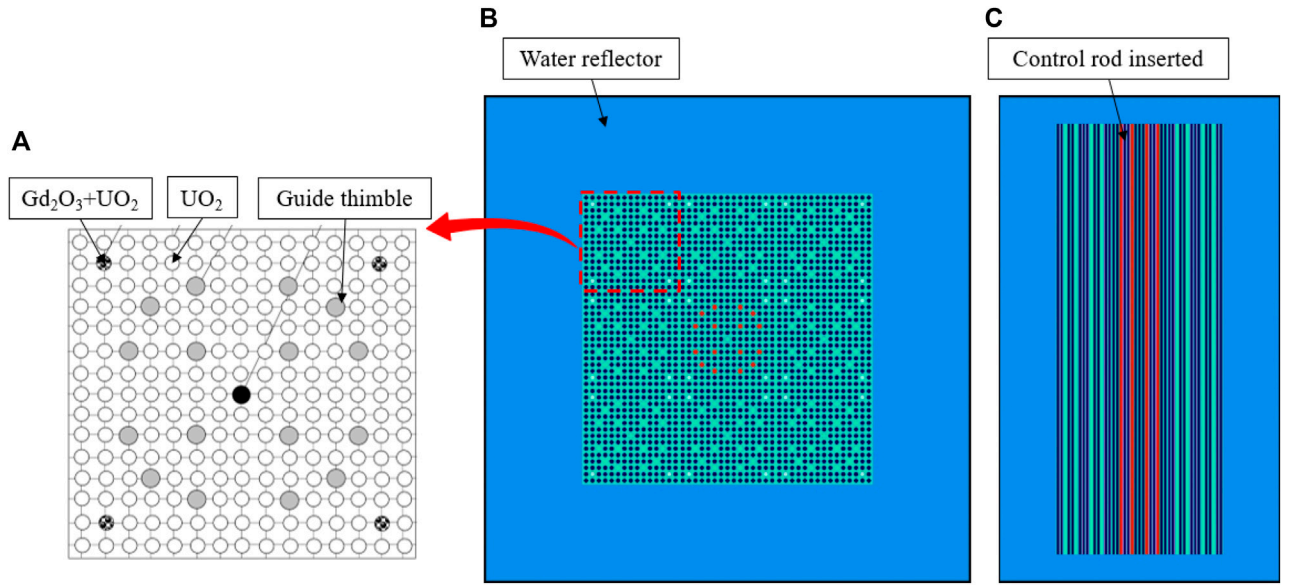

FIGURE 9 | TMI-1 mini-core fuel assembly **(A)**, x–y cut **(B)**, and x–z cut **(C)** (not to scale).

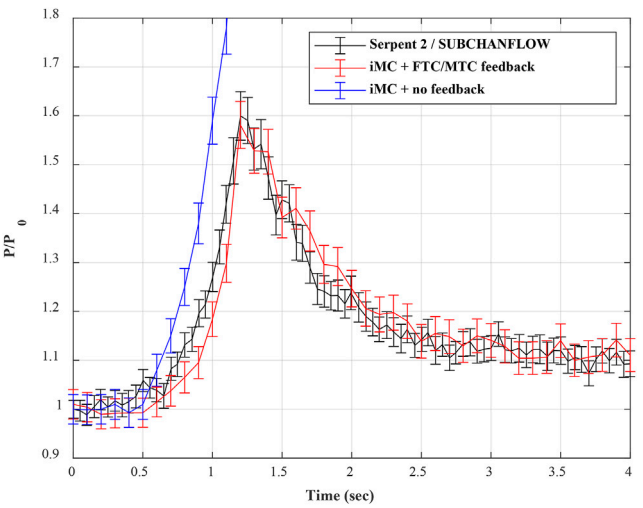

FIGURE 10 | Comparison of Serpent/SUBCHANFLOW and iMC multi-physics using TMI-1 mini-core problem.

10 meshes for the fuel temperature modeling to follow the fuel temperature evaluation model in the SUBCHANFLOW analysis. In this calculation, the iMC used a volume-averaged temperature of each material in a single TH mesh as in the Serpent analysis. The simulation used 0.1 M histories per cycle, 200 PCQS inactive/active cycles, and 15 independent batch runs were performed for the evaluation of the uncertainties. The comparison of the calculated thermal power transient from the two codes and required computation time are presented in **Figure 10** and **Table 5**, respectively.

TABLE 4 | Control rod assembly withdrawal speed for Serpent 2 and iMC.

	CR withdrawal (cm)	Static reactivity (pcm)
Serpent 2	30	354 ± 7
iMC	38.2	360 ± 22

TABLE 5 | Calculation time and condition for the TMI-1 mini-core problem.

	CPU time per time step (min)	Machine
Serpent 2	~5,000	Intel Xeon E5-2660 2.6 Ghz (1,000 CPUs)
iMC	~12,000	Intel Xeon E5-2697 2.6 GHz (196 CPUs)

As shown in **Figure 10**, without the negative temperature feedback of the reactor system, the thermal power exhibited an exponential excursion with the positive reactivity insertion. The iMC and Serpent simulation agreed well with each other except for the power evolution in response to the initial control rod withdrawal. This is because the control rod differential worth is slightly different in the two cases, albeit identical total reactivity insertion. Since the differential control rod reactivity worth becomes more significant as it approaches the active core center, the power growth is steeper in the iMC model as the withdrawal length is longer. The total reactivity insertion was similar in both cases (not exactly the same due to temperature difference), so the peak thermal power is

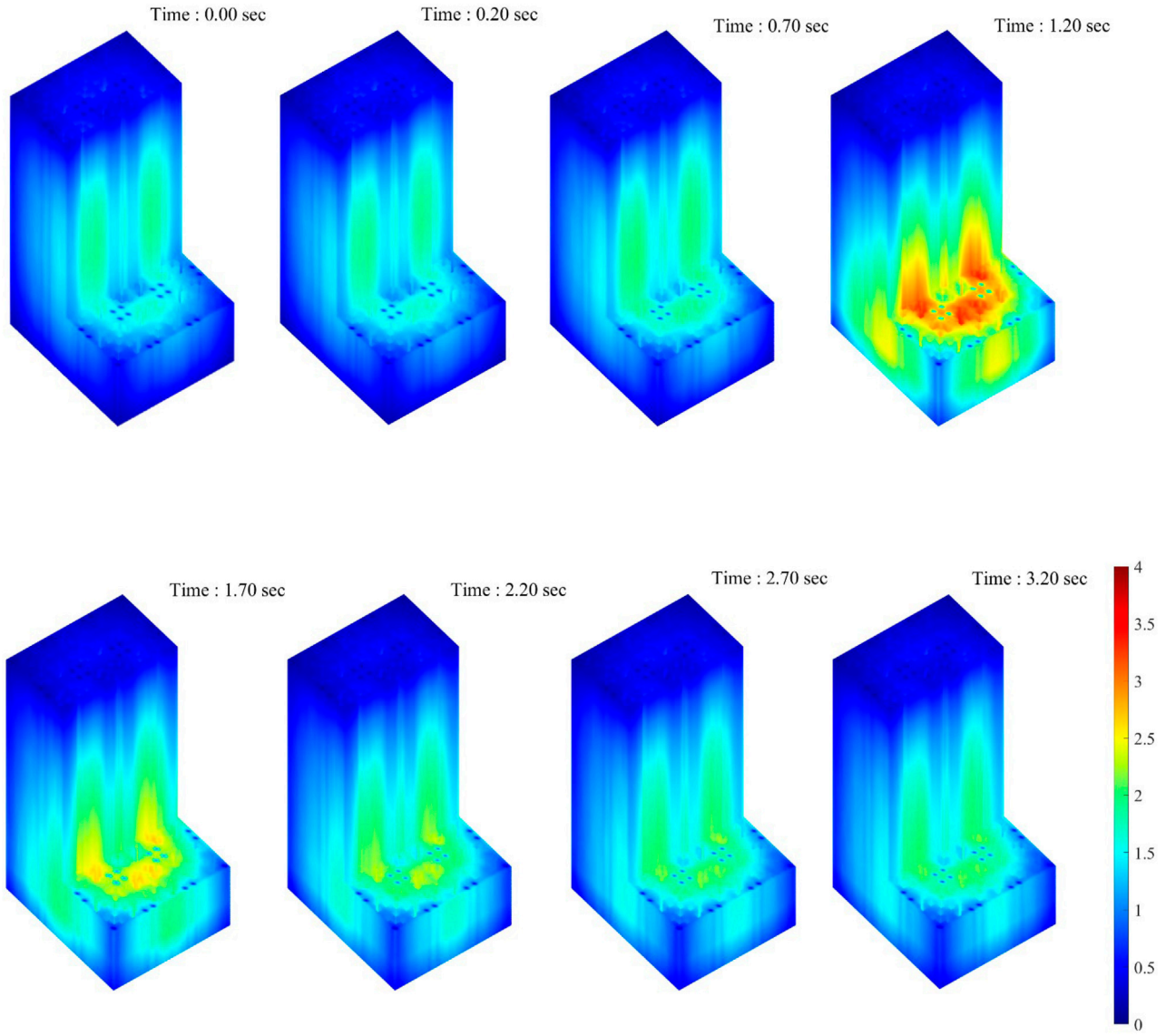

FIGURE 11 | Transient pin-power distribution of the mini-core problem.

evaluated to be very similar in the two codes. **Figure 11** illustrates the local power transient of the mini-core problem. After 0.2 s of stable null transient, the control rod assembly is withdrawn from the bottom of the core for 1 s at a constant speed and stopped afterward. The axial power peak shifts toward the bottom of the core, and the local power transient behavior well agrees with the point reactor power result. Meanwhile, the time-dependent fuel pin temperature shown in **Figure 12** monotonically increases during the period of the entire transient similar to the CSBA-loaded fuel assembly study. Also, the temperature peak skews toward the bottom of the core as the upward withdrawal of the control rod bank induces more bottom-skewed axial power profile.

The computation time required for the simulation is relatively large compared to the steady-state simulation even for the Serpent. The Serpent Monte Carlo transport simulation is based on the dynamic Monte Carlo method, so the computation time is less affected by the time step size. Although the two analyses were performed in different calculation conditions, the iMC transport simulation time is still much longer than that of the Serpent using a longer macro time step size. However, this performance gap can be reduced by adopting the coarse-mesh acceleration methods to reduce inactive cycles and the ray-tracing improvement of the iMC transport function itself. Future effort on algorithmic enhancement is needed for such a demanding process along with a sufficient amount of computation

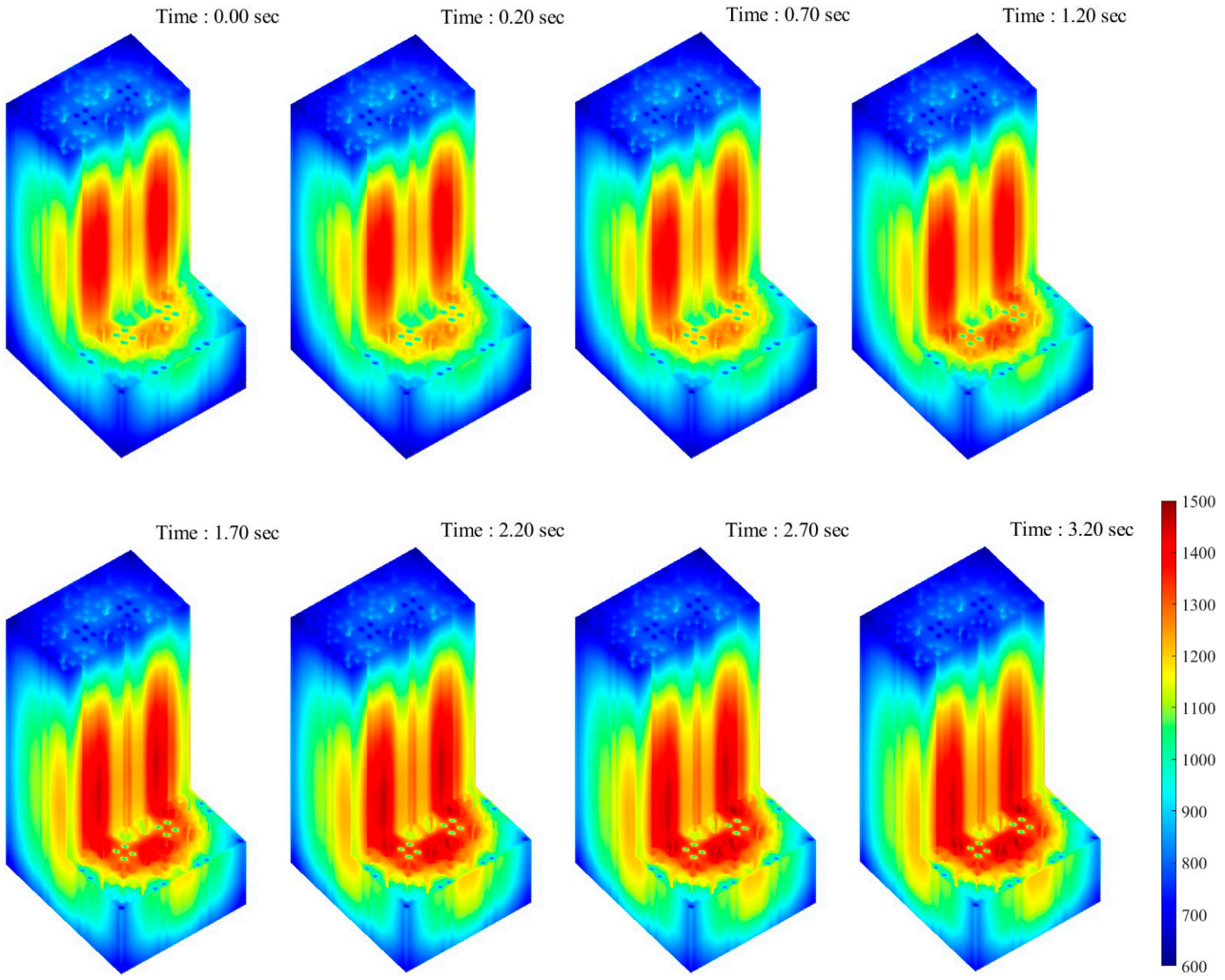

FIGURE 12 | Transient fuel pin temperature distribution of the mini-core problem.

resources for practical use of the Monte Carlo transient analysis.

4 CONCLUSION

In this work, we presented a multi-physics framework implemented in the iMC. The PCQS-MC-based transient neutron transport simulation and the finite element heat transfer are solved in a coupled framework to account for the temperature feedback effects in the time domain. The multi-physics framework is tested for a CSBA-loaded PWR fuel assembly when external reactivity is inserted *via* control rod removal from the system. The feedback correction of material cross-sections with adjusted temperature and density suppressed the additional reactivity and led the system to a stable state. The temperature responses of the system showed a slight lag from the initial perturbation due to the heat transfer delay, resulting in the power overshoot before the stabilization. The iMC multi-physics framework was also compared with the Serpent/SUBCHANFLOW coupled analysis framework on the TMI-1 mini-core problem for verification. The calculated time-dependent power evolutions from the two codes matched well, except for a minor discrepancy in the initial reactivity insertion period due to the different differential worth of the control rod.

The iMC analysis framework is especially useful for the 3-D complex fuel element as it can utilize the Gmsh-generated unstructured mesh grid for spatial discretization. For a more realistic reactor system simulation, the iMC multi-physics framework will adopt a subchannel analysis program in the near future. As we have demonstrated, such detailed analysis is essential for the accurate safety analysis of various fuel

designs. We expect the applicability of the iMC multi-physics feature can be far extended for advanced PWR fuel elements that are continuously being developed and even for the molten salt reactor analysis.

DATA AVAILABILITY STATEMENT

The raw data supporting the conclusion of this article will be made available by the authors, without undue reservation.

AUTHOR CONTRIBUTIONS

HK developed the program and carried out the result under the supervision of YK.

FUNDING

This work was supported by the National Research Foundation of Korea Grant funded by the Korean government (NRF-2016R1A5A1013919) and BK21 FOUR (Fostering Outstanding Universities for Research) Project NO. 4120200313637.

REFERENCES

Cherezov, A., Park, J., Kim, H., Choe, J., and Lee, D. (2020). A Multi-Physics Adaptive Time Step Coupling Algorithm for Light-Water Reactor Core Transient and Accident Simulation. *Energies* 13 (23), 6374. doi:10.3390/en13236374

Faucher, M., Mancusi, D., and Zoia, A. (2021). Multi-physics Transient Simulations with TRIPOLI-4. *EPJ Web of Conferences* 247, 7019. doi:10.1051/epjconf/202124707019

Ferraro, D., Faucher, M., Mancusi, D., and Zoia, A. (2019). "Serpent and TRIPOLI-4® Transient Calculations Comparisons for Several Reactivity Insertion Scenarios in a 3D PWR Minicore Benchmark," in International Conference on Mathematics and Computational Methods applied to Nuclear Science and Engineering, Portland, Oregon, USA, August 25–29, 2019, 1734–1743.

Ferraro, D., García, M., Valtavirta, V., Imke, U., Tuominen, R., Leppänen, J., et al. (2020). Serpent/SUBCHANFLOW Pin-By-Pin Coupled Transient Calculations for a PWR Minicore. *Ann. Nucl. Energ.* 137, 107090. doi:10.1016/j.anucene.2019.107090

Ferraro, D., García, M., Valtavirta, V., Imke, U., Tuominen, R., Leppänen, J., et al. (2020). Serpent/SUBCHANFLOW Pin-By-Pin Coupled Transient Calculations for the SPERT-IIIE Hot Full Power Tests. *Ann. Nucl. Energ.* 142, 107387. doi:10.1016/j.anucene.2020.107387

Ferraro, D., Valtavirta, V., García, M., Imke, U., Tuominen, R., Leppänen, J., et al. (2020). OECD/NRC PWR MOX/UO2 Core Transient Benchmark Pin-By-Pin Solutions Using Serpent/SUBCHANFLOW. *Ann. Nucl. Energ.* 147, 107745. doi:10.1016/j.anucene.2020.107745

Ferraro, M., Valtavirta, V., Tuominen, R., Imke, U., Leppänen, J., and Sanchez-Espinoza, V. (2020). Serpent2-SUBCHANFLOW Pin-By-Pin Modelling Capabilities for VVER Geometries. *Ann. Nucl. Energ.* 135, 106955. doi:10.1016/j.anucene.2019.106955

Fiorina, C., Clifford, I., Aufiero, M., and Mikityuk, K. (2015). GeN-Foam: a Novel OpenFOAM Based Multi-Physics Solver for 2D/3D Transient Analysis of Nuclear Reactors. *Nucl. Eng. Des.* 294, 24–37. doi:10.1016/j.nucengdes.2015.05.035

Geuzaine, C., and Remacle, J.-F. (2009). Gmsh: A 3-D Finite Element Mesh Generator with Built-In Pre- and post-processing Facilities. *Int. J. Numer. Meth. Engng.* 79 (11), 1309–1331. doi:10.1002/nme.2579

Guo, X., Shang, X., Song, J., Shi, G., Huang, S., and Wang, K. (2021). Kinetic Methods in Monte Carlo Code RMC and its Implementation to C5G7-TD Benchmark. *Ann. Nucl. Energ.* 151, 107864. doi:10.1016/j.anucene.2020.107864

Ivanov, K., Avramova, M., Kamerow, S., Kodeli, I., Sartori, E., Ivanov, E., et al. (2013). *Benchmarks for Uncertainty Analysis in Modelling (UAM) for the Design, Operation and Safety Analysis of LWRs-Volume I: Specification and Support Data for Neutronics Cases (Phase I)*. Organisation for Economic Co-Operation and Development.

Jo, Y., Cho, B., and Cho, N. Z. (2016). Nuclear Reactor Transient Analysis by Continuous-Energy Monte Carlo Calculation Based on Predictor-Corrector Quasi-Static Method. *Nucl. Sci. Eng.* 183 (2), 229–246. doi:10.13182/nse15-100

Kim, H. T. (2022). *Study of Steady-State and Time-Dependent Monte Carlo Neutron Transport Coupled Multi-Physics Reactor Analysis in the iMC Code*. Doctoral dissertation. Korea Advanced Institute of Science and Technology.

Kim, H., and Kim, Y. (2021). Unstructured Mesh-Based Neutronics and Thermomechanics Coupled Steady-State Analysis on Advanced Three-Dimensional Fuel Elements with Monte Carlo Code iMC. *Nucl. Sci. Eng.* 195 (5), 464–477. doi:10.1080/00295639.2020.1839342

Kim, H., and Kim, Y. (2020). Unstructured Mesh-Grid Multi-Physics Analysis with Monte Carlo iMC Code for Advanced Fuel Elements. *Trans. Am. Nucl. Soc.* 122 (1), 738–741. doi:10.13182/t122-32434

Nguyen, X. H., Kim, C., and Kim, Y. (2019). An Advanced Core Design for a soluble-boron-free Small Modular Reactor ATOM with Centrally-Shielded Burnable Absorber. *Nucl. Eng. Techn.* 51 (2), 369–376. doi:10.1016/j.net.2018.10.016

Park, I. K., Lee, J. R., Choi, Y. H., and Kang, D. H. (2020). A Multi-Scale and Multi-Physics Approach to Main Steam Line Break Accidents Using Coupled MASTER/CUPID/MARS Code. *Ann. Nucl. Energ.* 135, 106972. doi:10.1016/j.anucene.2019.106972

Reed, W. H., and Hansen, K. F. (1970). Alternating Direction Methods for the Reactor Kinetics Equations. *Nucl. Sci. Eng.* 41 (3), 431–442. doi:10.13182/nse41-431

Reed, W. H., and Hansen, K. F. (1969). *Finite Difference Techniques for the Solution of the Reactor Kinetics Equations Massachusetts Inst. Of Tech*. Cambridge: Dept. of Nuclear Engineering. doi:10.2172/4782171

Sanchez, V., Imke, U., Ivanov, A., and Gomez, R. (2010). *SUBCHANFLOW: A thermal Hydraulic Sub-channel Program to Analyse Fuel Rod Bundles and Reactor Cores*. Cancun, Mexico: 17th Pacific Basin Nuclear Conference.

Wang, Y., Schunert, S., Ortensi, J., Laboure, V., DeHart, M., Prince, Z., et al. (2021). Rattlesnake: A MOOSE-Based Multiphysics Multischeme Radiation Transport Application. *Nucl. Techn.* 207 (7), 1047–1072. doi:10.1080/00295450.2020.1843348

Conflict of Interest: The authors declare that the research was conducted in the absence of any commercial or financial relationships that could be construed as a potential conflict of interest.

Publisher's Note: All claims expressed in this article are solely those of the authors and do not necessarily represent those of their affiliated organizations, or those of the publisher, the editors, and the reviewers. Any product that may be evaluated in this article, or claim that may be made by its manufacturer, is not guaranteed or endorsed by the publisher.

Copyright © 2022 Kim and Kim. This is an open-access article distributed under the terms of the Creative Commons Attribution License (CC BY). The use, distribution or reproduction in other forums is permitted, provided the original author(s) and the copyright owner(s) are credited and that the original publication in this journal is cited, in accordance with accepted academic practice. No use, distribution or reproduction is permitted which does not comply with these terms.

frontiers in Energy Research

ORIGINAL RESEARCH
published: 23 March 2022
doi: 10.3389/fenrg.2022.843212

Mechanical Feasibility Analysis of the Surface Microstructure to Be Used in the Nuclear Reactor

Shan Huang, Ti Yue, Pan Yuan, Fawen Zhu, Haoyu Wang, Menglong Liu, Chunlan Huang, Hua Li and Yun Li*

Science and Technology on Reactor System Design Technology Laboratory, Nuclear Power Institute of China, Chengdu, China

With the continuous improvement of nuclear reactor power, the use of surface microstructures to enhance the heat exchange between the coolant and the solid surface has become the research focus of many researchers. However, the extreme environment inside the core, especially the continuous impact of the high-velocity liquid on the solid surface, poses a severe challenge to the reliable service of the microstructure. To this end, this paper establishes a numerical calculation method for the droplet scouring the solid wall to analyze and evaluate the mechanical feasibility and reliability of the surface microstructure under the impact of high-speed droplets. First of all, the physical process of the liquid droplet scouring the solid surface was described and analyzed, then the mathematical equations which describe the physical process were built by coupling the key physical parameters of the interface such as displacement and stress. Finally, the internal stress distribution and its change trend with and without the microstructure were obtained. The calculation results show that during the process of a droplet hitting the solid surface, due to the superposition of shock waves inside the droplet, there will be a stress field distribution on the solid side that cannot be ignored. The introduction of the surface microstructure will significantly change the stress field distribution on the solid side. The liquid film formed on the surface of the microstructure has a significant buffering effect on the impact of the droplets, which greatly reduces the stress level in the solid. The maximum stress level in the solid with microstructure is only about 50% of that in the solid without the microstructure. Therefore, it can be judged that the surface microstructure can meet the mechanical performance requirements under the condition of droplet scouring.

Keywords: microstructure, liquid-solid impact, numerical simulation, impact stress, feasibility

OPEN ACCESS

Edited by:
Haomin Yuan,
Argonne National Laboratory (DOE), United States

Reviewed by:
Jinbiao Xiong,
Shanghai Jiao Tong University, China
Luteng Zhang,
Chongqing University, China

****Correspondence:***
Shan Huang
18691635713@163.com

Specialty section:
This article was submitted to Nuclear Energy, a section of the journal Frontiers in Energy Research

Received: *25 December 2021*
Accepted: *17 February 2022*
Published: *23 March 2022*

Citation:
Huang S, Yue T, Yuan P, Zhu F, Wang H, Liu M, Huang C, Li H and Li Y (2022) Mechanical Feasibility Analysis of the Surface Microstructure to Be Used in the Nuclear Reactor. Front. Energy Res. 10:843212. doi: 10.3389/fenrg.2022.843212

1 INTRODUCTION

With the development of nuclear energy technology, the power of nuclear reactors has also continued to increase. As a result, the heat flux density on the surface of the fuel element has also risen sharply. How to improve the heat transfer efficiency between the surface of the fuel element and the coolant has become an urgent problem for front-line researchers.

Recent studies have shown that surface engineering technology is a means with great potential to enhance heat transfer and increase the value of CHF (Critical Heat Flux). Zhukov's study

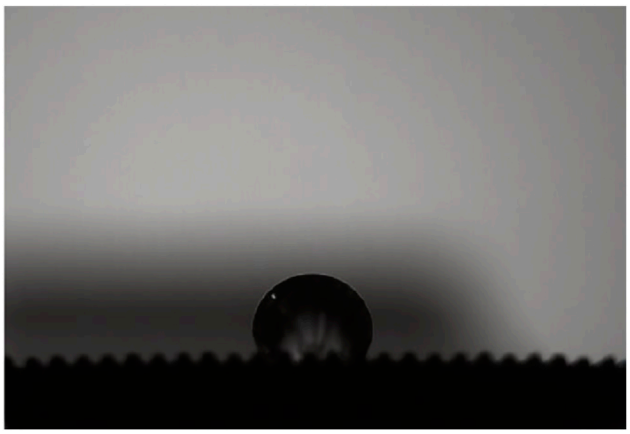

FIGURE 1 | The jagged microstructure in surface wettability experiment.

demonstrates that the use of a microstructured surface produced by a 3D laser printer leads to a 3.5-fold increase of the heat transfer coefficient in the regimes of bubble boiling and the critical heat fluxes (CHF) on the capillary-porous coating increase with the increasing height of the liquid layer (Zhukov et al., 2020). Wang investigated the boiling heat transfer properties of a copper surface with different microstructures and the effect of size and heat transfer area on heat transfer performance is studied by experiment and simulation. The studies have shown, the surface with microstructure can effectively promote boiling heat transfer and the heat transfer effect of multi-scale T surface is always the best, 1.31 times of single scale surface, 2.38 times of smooth surface (Wang et al., 2021). Tokunaga used a microstructured surface with a wettability gradient to enhance the condensation heat transfer and they fabricated a bi-public microgroove surface with a wettability gradient which could enhance the heat transfer by three times compared with the straight microgroove (Tokunaga and Tsuruta, 2020). Liu found that a straight fin microstructured surface has a higher heat transfer performance of pulsed spray cooling than a smooth surface, but it decreases the surface temperature uniformity. Then mixed surfactants were used to greatly improve the temperature uniformity of the microstructured surface (Liu et al., 2020). Zhu used the microstructure to enhance the heat transfer performance of nitrogen condensation on the vertical plate and the rivulet at the bottom of the micro fin indicates the curved surface structure could change the uniform distribution of the liquid film of the micro fin to accelerate the condensate drainage (Zhu et al., 2021). Shi's research team has designed the SCGS (supersonic cold gas spray technique) modified surfaces to enhance the downward-facing boiling and the conical pin microstructure shows significant CHF enhancement. The mechanism of CHF enhancement mainly brought by a synergy of Multi-scale structures was also preliminarily analyzed (Shi et al., 2021). In Sun's research, novel microstructured surfaces were fabricated with spatially-controlled mixed wettability to improve the pool boiling performance and the Synergistic enhancement mechanism was also explored by optimally utilizing the combined effects of mixed wettability and microstructures (Sun et al., 2022). Lei studied the heat transfer performance of block-divided surfaces in the pool boiling heat transfer and all block-divided surfaces show better heat transfer performance than a smooth surface. In his work, MP-3 has the smallest microstructure area but the highest CHF and a modified model to predict the CHFs was proposed (Lei et al., 2020). Park modified outer boiling and inner condensation surfaces of a two-phase heat exchanger tube with electroplated porous microstructures and dip-coated hydrophobic thin film and a significant increase in heat

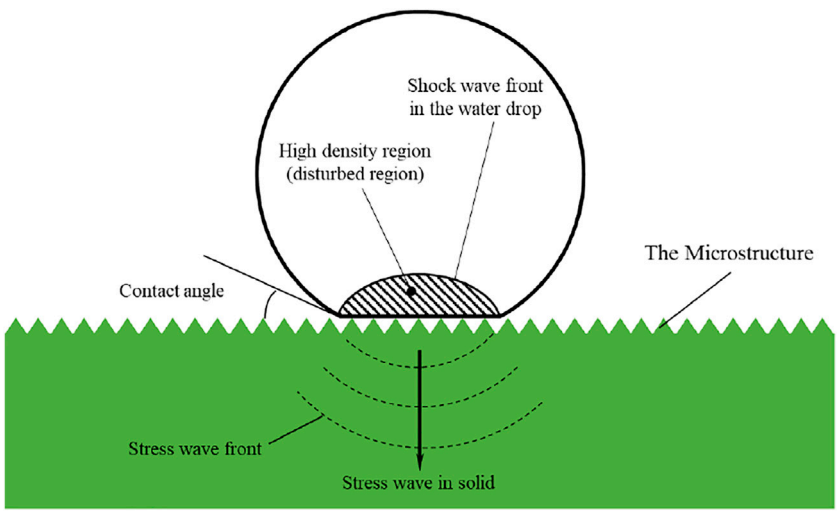

FIGURE 2 | The schematic of the liquid-solid impact process.

TABLE 1 | the physical properties involved in the calculation.

	Water	Solid
Density (m^3/kg)	1000	4090
Poisson's ratio		0.28
Sonic speed (m/s)	1430	4268
Flexure (tensile) strength (MPa)		75.4
Acoustic impedance (kg/m^2s)	1.430×10^6	1.75×10^7
Compressive strength (MPa)		1300
Young's modulus (Pa)	—	74.5×10^9

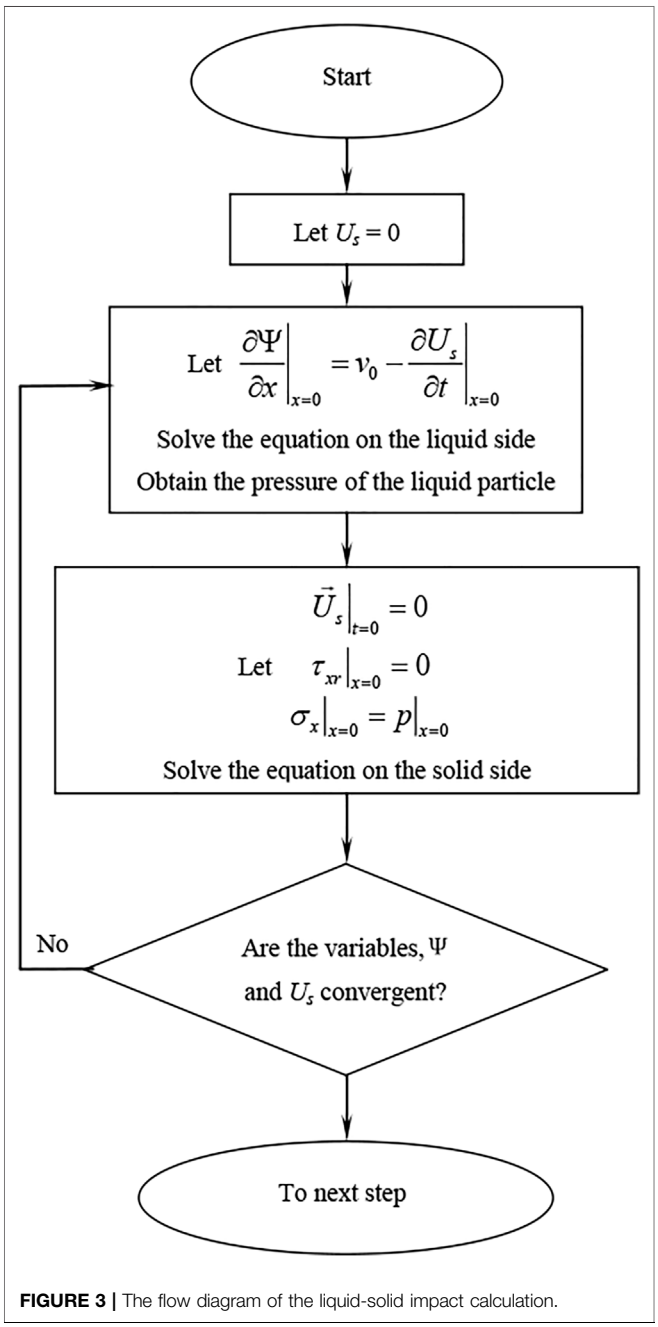

FIGURE 3 | The flow diagram of the liquid-solid impact calculation.

transfer performance of the heat exchanger tube were achieved (Park et al., 2019).

At the same time, the development of advanced manufacturing processes such as 3D printing has made it possible to successfully manufacture some complex surface microstructures. In Kang's research, microstructures on boiling surfaces were fabricated by 3D microprinting and the boiling heat transfer on surfaces with 3D-printing microstructures was studied (Kang and Wang, 2018). The experimental results showed that the microstructure which generates more nucleation sites can have higher heat flux during the saturated nucleate boiling which is the heat transfer situation in nuclear power plants.

All of these advancements are pushing surface engineering from research to engineering. However, the fuel elements of nuclear reactors have a long-term operation under strong radiation and high temperature and high-pressure water environment, and at the same time, they are subject to water chemical corrosion and fluid erosion. For this reason, the microstructure provided on the surface of the cladding must also have a sufficiently high structural strength to adapt to such a harsh environment. Damage to the surface microstructure will not only cause a reduction in heat exchange efficiency but is also closely related to the safety of nuclear reactors. For this reason, it is necessary to provide support for the selection and demonstration of surface microstructures from the perspective of structural mechanics.

However, at present, apart from experimental methods, there are no particularly effective methods to quickly analyze the mechanical feasibility of microstructures. To better analyze and verify the feasibility of surface microstructures in nuclear reactors, especially the mechanical stability under high-velocity scouring environments. This paper analyzes the physical process of the surface microstructure being washed by high-speed fluid and establishes a mathematical model on this basis. Then, the velocity transmission is used to couple the governing equations of the liquid with the governing equations of the solid, and the entire calculation area is solved by the discrete iterative method to obtain the stress distribution inside the surface microstructure. By comparing and analyzing the internal stress distribution law of different microstructure sizes during high-speed fluid scouring, it provides suggestions and ideas for improving the mechanical stability of the surface microstructure.

2 PHYSICAL PROCESS DESCRIPTION

Obtaining the real-time stress distribution inside the microstructure under the condition of high-speed fluid scouring is the key to this article. To calculate and analyze this process, we need to sort out the physical process of the impact of high-speed fluid on the surface microstructure. To facilitate the subsequent calculation and analysis, we need to define a specific microstructure form. Our research team has designed and processed a variety of surface microstructures. We will select a typical one as the object of subsequent analysis, that is the jagged microstructure, as shown in **Figure 1**.

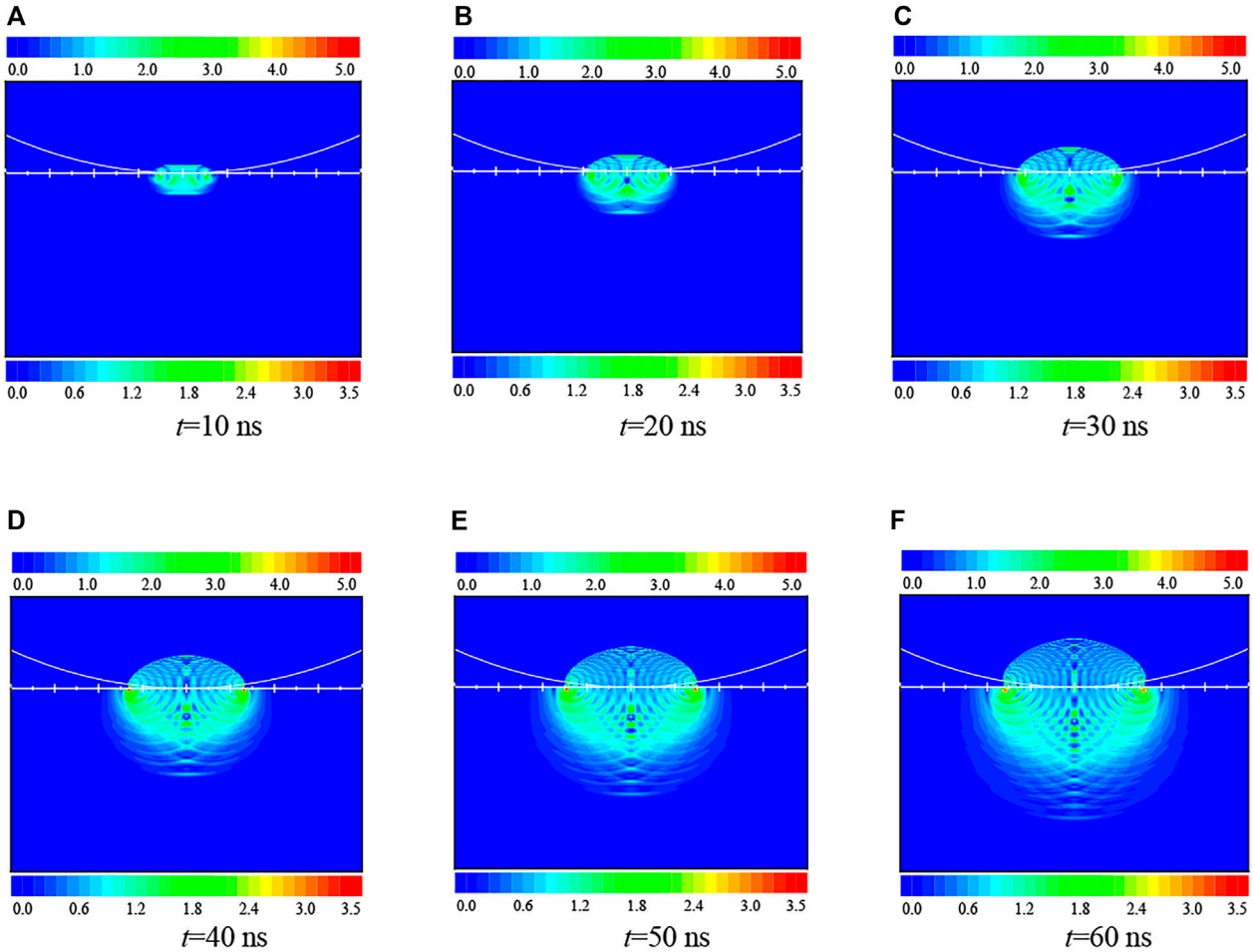

FIGURE 4 | The transient stress distribution in the solid. **(A)** t = 10 ns, **(B)** t = 20 ns, **(C)** t = 30 ns, **(D)** t = 40 ns, **(E)** t = 50 ns, **(F)** t = 60 ns.

After analysis, it is found that the process of fluid scouring the surface microstructure at high speed is a process in which countless liquid droplets hit the microstructure at a high speed. Although the droplet hits the microstructure in many directions, it can be known by Newton's second law: when the direction of the droplet's motion is perpendicular to the plane where the microstructure is located, the microstructure will receive the greatest impact, and the stress level of the microstructure will be the largest at this time. This is also the working condition that we should consider.

After clarifying the specific form of the microstructure, a simplified physical process model can be obtained, as shown in **Figure 2**. The circle in the figure represents the liquid drop, the green part represents the solid part, and the continuous triangle represents the jagged microstructure. The angle between the droplet and the solid is called the contact angle, and this angle is also constant as the impact process progresses. When a droplet hits a solid page at a relatively fast speed, a shock wave will be generated inside the droplet due to the deformation and compression of the droplet. The shock wave is generated on the liquid-solid contact surface and starts to propagate inside the droplet. The place where the shock wavefront passes is called the high-density zone (disturbed area). The shock wave generated by the liquid-solid impact process will cause a pressure distribution within the droplet that varies with space and time. According to the principle of force and reaction force, the pressure change of the droplet will cause the corresponding stress wave to propagate inside the solid, so the inside of the solid will also produce a corresponding stress distribution that changes with space and time.

Compared with the smooth surface of the solid, the microstructure may change the stress distribution on the solid side. If there is a large stress distribution inside or near the microstructure, it may cause the microstructure to fall off and break. In our study, the maximum stress in the solid is our focus and it has been proved that the internal pressure of the droplet will have a maximum value before the lateral jet forms in the liquid drop (Heymann, 1969; Field, 1999), so we only pay attention to the process before the broke of the liquid droplet. So, the shape and volume change of the droplet can be negligible during this period. Therefore, the focus of our research is to get the stress distribution in

the microstructure before the droplet breaks and compare the changes in the stress field on the solid side with and without the microstructure.

3 GOVERNING EQUATION

This phenomenon of droplets hitting and scouring solid surfaces at high speed not only in the nuclear reactor but also exists in other industries, like the turbine in the coal power plant and the propeller of the ship, and the base solid may be broken by the continuous water drops with relatively high velocity (Lee, 2002). A significant transient stresses distribution can be produced by the high-speed, micron-sized water droplets where the liquid impacts the solid. And in Denis's research, these impaction jets can travel at up to 40 times the velocity of the impact (Bartolo et al., 2006). Because of the small volume and high flow velocity of liquid droplets, the stress distribution in the solid can't be measured easily by the experiment. Therefore, it is necessary to establish a numerical model to obtain the stress.

At first, the classical model of the impact between a liquid flow and solid was built by Cook, and the numerical model was set to be solved under one dimensional (Cook, 1928). Then, a hydrodynamic analysis review of the cylinder under impact was presented by Cointe (Cointe and Armand, 1987). Many researchers' assumptions and results, such as Wagner (Wagner, 1932), were discussed and analyzed. Then, in 1992 and 1994, Korobkin investigated the impact process of the blunt-body between two completely different liquid surfaces, and the pressure and the velocity inside the liquid computed region were obtained (Korobkin, 1992; Korobkin, 1994).

With the quick development of high-speed photography, there were more experimental researches on the impact process between liquid and solid. But, most of them are focused on the pressure distribution on the liquid side. In 2003, Kim set up an experimental system, and the process of a droplet with high-velocity impacts on a solid surface was imaged (Kim et al., 2003). However, there is little research focus on the calculation of stress distribution in the solid. In 2008, Li and Zhou built a numerical model which considers the compressibility of liquid (Li et al., 2008), and the stress in the solid was finally obtained in the liquid-solid impact process (Zhou et al., 2008). In 2016, Semenov and Wu also got the hydrodynamic force caused by the impact when they investigated the impact process of a free surface flow and a permeable solid (Semenov and Wu, 2016). From 2010, Xiong has been focused on the numerical analysis of liquid-solid impingement by the method of moving particle semi-implicit. And their impact pressure in the liquid obtained by the numerically calculation has a very good agreement with the Heymann correlation and lateral jet which would cause a big shear stress has also been proved (Xiong et al., 2010). Their research team also carried an investigation on the mitigation effect of the water film in the liquid droplet impingement onto a wet rigid wall, and the results of which will provide obvious support for our calculation results analysis (Xiong et al., 2011). And Xiong also proposed a new correlation for the pressure load caused by the sodium impingement, which was in good consistent with the simulation results (Xiong et al., 2012). But all the research above has not taken the effect of microstructure into consideration.

In this paper, we use the 2-D wave equations developed from Li's work (Li et al., 2008) to describe the liquid-solid impact process and the governing equations which couple the liquid and solid can be got as follows:

$$\begin{cases} Liquid \begin{cases} \dfrac{\partial^2\Psi}{\partial x^2}+\dfrac{1}{r}\dfrac{\partial}{\partial r}\left(r\dfrac{\partial\Psi}{\partial r}\right)=\dfrac{1}{c^2}\dfrac{\partial\Psi}{\partial t^2} \\ \Psi|_{t=0}=0 \\ \left.\dfrac{d\Psi}{dx}\right|_{x=0}=\left.\dfrac{du_s}{dt}\right|_{x=0} \end{cases} \\ Solid \begin{cases} (\lambda+2\mu)\dfrac{\partial^2 u_s}{\partial x^2}+\mu\dfrac{\partial^2 u_s}{\partial r^2}+(\lambda+\mu)\dfrac{\partial^2 v_s}{\partial x\partial r}+\lambda\dfrac{\partial}{\partial x}\left(\dfrac{v_s}{r}\right)+\dfrac{\mu}{r}\left(\dfrac{\partial v_s}{\partial x}+\dfrac{\partial u_s}{\partial r}\right)=\rho_s\dfrac{d^2u_s}{dt^2} \\ \mu\dfrac{\partial^2 v_s}{\partial x^2}+(\lambda+2\mu)\dfrac{\partial^2 v_s}{\partial r^2}+(\lambda+\mu)\dfrac{\partial^2 u_s}{\partial x\partial r}+\lambda\dfrac{\partial}{\partial r}\left(\dfrac{v_s}{r}\right)+\dfrac{2\mu}{r}\left(\dfrac{\partial v_s}{\partial r}-\dfrac{v_s}{r}\right)=\rho_s\dfrac{d^2v_s}{dt^2} \\ u_s|_{t=0}=0 \\ v_s|_{t=0}=0 \\ \left.\dfrac{du_s}{dx}\right|_{x=0}=\dfrac{1}{E_1}\left.\dfrac{d\Psi}{dt}\right|_{x=0} \\ \left.\dfrac{dv_s}{dx}\right|_{x=0}=0 \end{cases} \end{cases} \tag{1}$$

In our research, the physical process was treated as an asymmetrical process because of the symmetry of the spherical droplet. And the coupling between the liquid and solid was done by the connection of the solid particle displacement and the liquid particle velocity on the interface. Through the equations and settings above, the solid particles displacement can be obtained, and then we can get the stress and strain by the equations below:

$$\begin{cases} \varepsilon_x=\dfrac{\partial u_s}{\partial x} \\ \varepsilon_r=\dfrac{\partial v_s}{\partial r} \\ \varepsilon_\phi=\dfrac{v_s}{r} \\ \gamma_{xr}=\dfrac{\partial v_s}{\partial x}+\dfrac{\partial u_s}{\partial r} \\ \theta=\varepsilon_x+\varepsilon_r+\varepsilon_\phi \end{cases} \qquad \begin{cases} \sigma_x=\lambda\theta+2\mu\varepsilon_x \\ \sigma_r=\lambda\theta+2\mu\varepsilon_r \\ \sigma_\phi=\lambda\theta+2\mu\varepsilon_\phi \\ \tau_{xr}=\mu\gamma_{xr} \end{cases} \tag{2}$$

Then, the 4th strength theory was used to convert all these different components of stress in the solid side into equivalent stress:

$$\sigma_e=\sqrt{\sigma_1^2+\sigma_2^2+\sigma_3^2-\sigma_1\sigma_2-\sigma_2\sigma_3-\sigma_1\sigma_3} \tag{3}$$

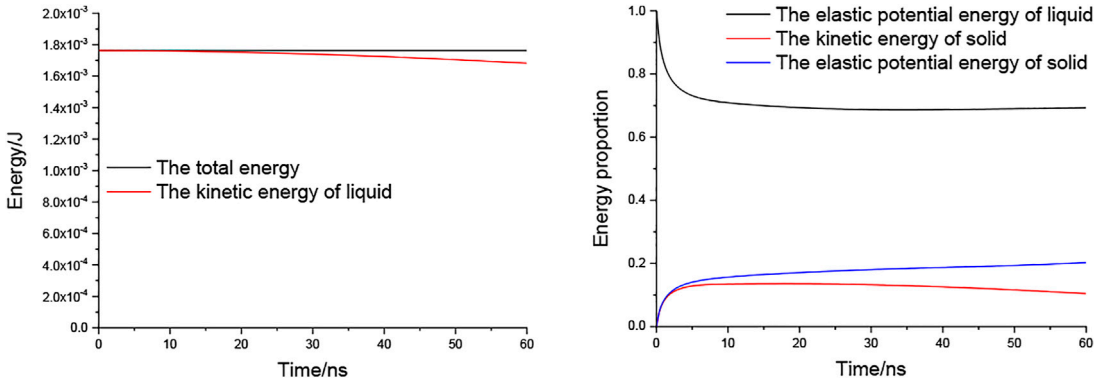

FIGURE 5 | The energy conversion process of the impact process.

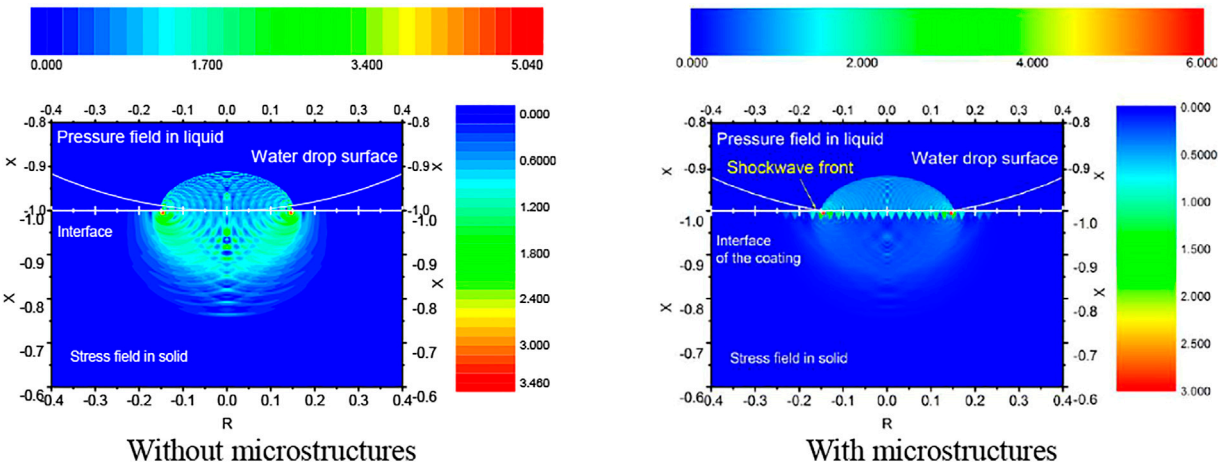

FIGURE 6 | The transient stress distribution in the solid (t = 50 ns).

$$\sigma_e = \sqrt{\frac{\left(\sigma_x - \sigma_y\right)^2 + \left(\sigma_x - \sigma_z\right)^2 + \left(\sigma_z - \sigma_y\right)^2 + 6\left(\tau_{xy}^2 + \tau_{yz}^2 + \tau_{xz}^2\right)}{2}} \tag{4}$$

and define the dimensionless equivalent stress:

$$\sigma_{eq} = \frac{\sigma_e}{\rho_0 c_0 v_0} \tag{5}$$

The denominator in the formula represents the magnitude of the water hammer force (Lee, 2002), which mainly considers the density and velocity of the droplets. Unless otherwise specified, the stress mentioned later is dimensionless equivalent stress。

In this paper, the finite difference method (Le Bot et al., 2015; Peng and Cao, 2016) is used to solve the liquid-solid interaction problems. And we use the 2th-order accuracy backward difference scheme for the discretization of the time-derivative term:

$$\frac{\delta^2 \phi}{\delta t^2}\Big)_{i,j,n} = \frac{9\phi_{i,j}^n - 24\phi_{i,j}^{n-1} + 22\phi_{i,j}^{n-2} - 8\phi_{i,j}^{n-3} + \phi_{i,j}^{n-4}}{4(\Delta t)^2} + O(\Delta t^2) \tag{6}$$

And for the space-derivative terms, $\frac{\partial^2 \Psi}{\partial x^2}$ and $\frac{1}{r}\frac{\partial}{\partial r}\left(r\frac{\partial \Psi}{\partial r}\right)$, the 4th-order accuracy central difference scheme was used for the discretization:

$$\frac{\delta^2 \phi}{\delta x^2}\Big)_{i,j,n} = \frac{-\phi_{i-2,j}^n + 16\phi_{i-1,j}^n - 30\phi_{i,j}^n + 16\phi_{i+1,j}^n - \phi_{i+2,j}^n}{12(\Delta x)^2} + O(\Delta x^4) \tag{7}$$

$$\frac{1}{r}\frac{\partial}{\partial r}\left(r\frac{\partial \phi}{\partial r}\right)\Big|_{i,j,n} = \frac{1}{r_{i,j}}\left(\frac{-(r\phi)_{i,j-2}^n + 16(r\phi)_{i,j-1}^n - 30(r\phi)_{i,j}^n + 16(r\phi)_{i,j+1}^n - (r\phi)_{i,j+2}^n}{12(\Delta r)^2} - \frac{\phi_{i,j-2}^n - 8\phi_{i,j-1}^n + 8\phi_{i,j+1}^n - \phi_{i,j+2}^n}{12\Delta r}\right) + O(\Delta r^4) \tag{8}$$

At last, TDMA which stands for the tridiagonal matrix algorithm was used to solve the discretized equations, and the Guass-Sidel

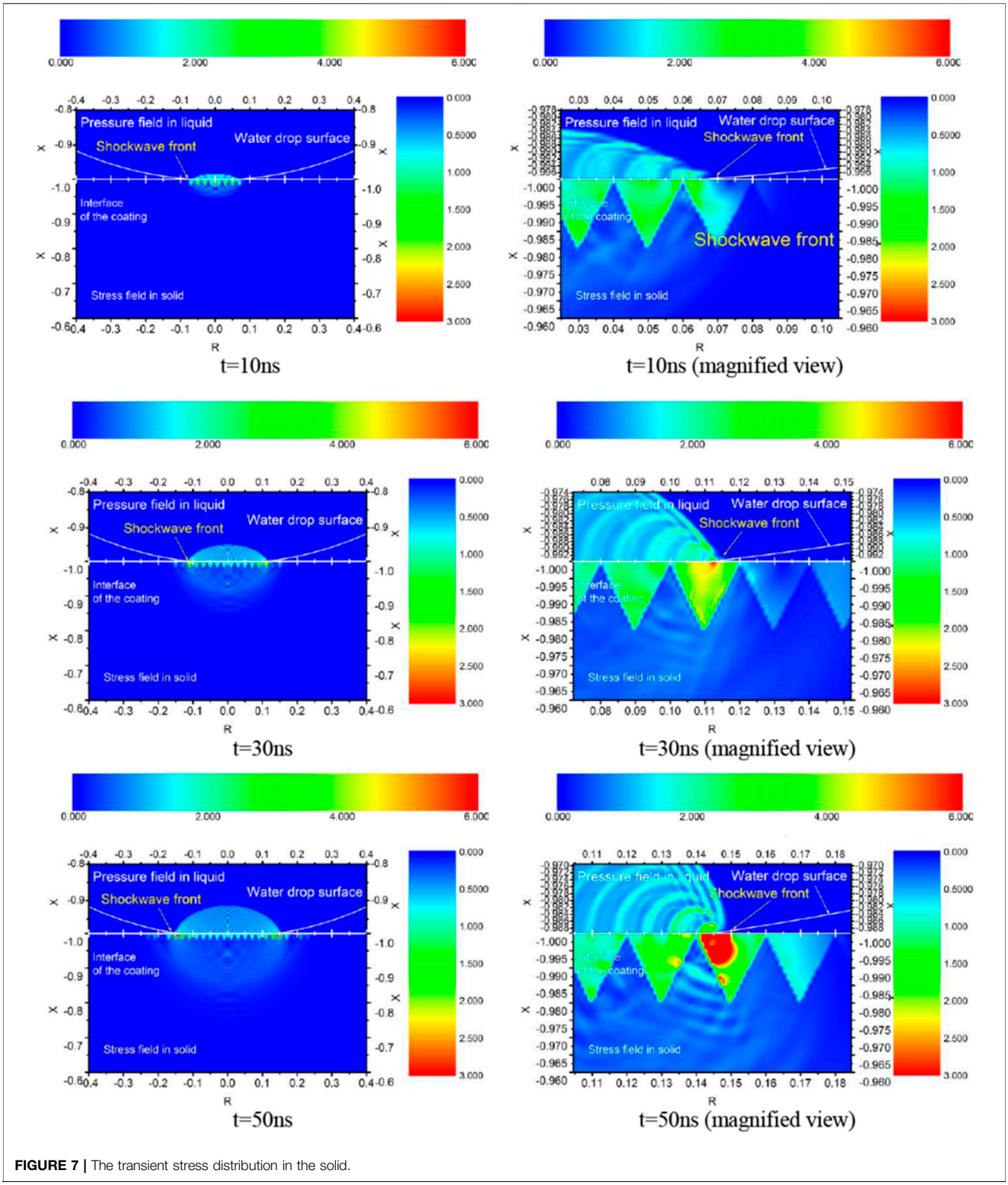

FIGURE 7 | The transient stress distribution in the solid.

iteration method was also employed. The key part of this calculation process is to set the pressure of the liquid particle on the boundary as the boundary condition of the solid side calculation to get the velocity. Like the discretize way above, the Lame equation can also be discretized. And, the flow diagram of the liquid-solid impact calculation can be expressed as in **Figure 3**.

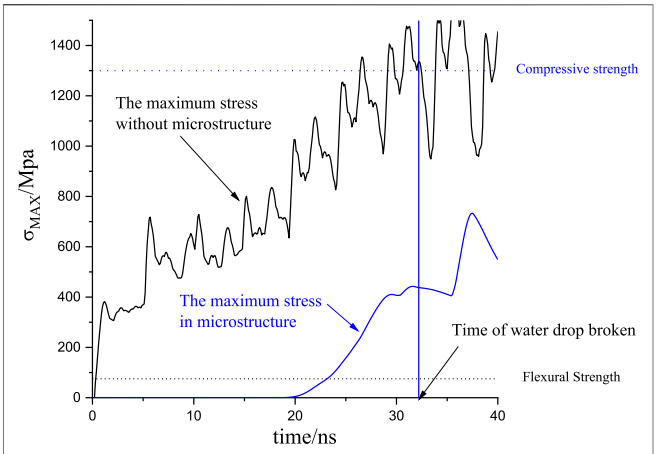

FIGURE 8 | The tendency of the maximum equivalent stress.

4 CALCULATION RESULTS ANALYSIS

4.1 Without Microstructure

According to the previous control equations and solution settings, we have carried out the relevant calculations. To compare the stress of the microstructure more intuitively, we first calculated the process of the droplet impacting the smooth wall (when there is no microstructure).

Table 1 gives the physical properties of solids and water. In the calculation, the initial diameter of the water drop was set to be 1 mm and the impact velocity was set to 50 m/s.

Figure 4 shows stress calculation results in the solid when time is ranging from 10 to 60 ns before the broke of the liquid droplet. And white lines were used to stand for the structure shapes, the horizontal line stands for the surface of the impacted solid while the arc line stands for the shape of the liquid droplet.

The impact of the water droplet causes a coronal disturbed zone in the liquid and the shock front inside the droplet forms. The density and modulus of the disturbed liquid are higher than the normal liquid, and thanks to that the propagation speed of the sound wave in the disturbed zone is much higher than that in the undisturbed zone. The difference in the propagation speed would result in wave superposition. While the propagation speed of the wave in the solid side would be influenced less, so the stress distribution in the solid side mainly takes over a spherical zone.

We also analyzed the energy conversion in the liquid-solid impact process, including the relationship among the total energy, the energy in the liquid and the energy in the solid. The computation results are shown in see **Figure 5**. And we can see that the total energy remains constant and it does not change with the time, and this phenomenon is well explained by the law of energy conservation. For the total kinetic energy in the liquid side, it has a small decrease at the end which indicates some liquid kinetic energy transforms into other energy. In our research, the impact velocity is relatively high and the total deformation of the liquid droplet is very small, about 0.3%. So, the decrease of liquid kinetic energy is on the same order which is good agreement with this number.

The lost kinetic energy of liquid has turned into other energy forms, including the elastic potential energy of liquid, the kinetic energy of solid and the elastic potential energy of solid. And because of the difference of the elastic modulus between the liquid and solid, the liquid gets a more obvious deformation than the solid, the elastic potential energy of liquid is much higher than the elastic potential energy of solid. Although the energy has transferred from the liquid to the solid, the elastic potential energy of liquid is still much higher than the elastic potential energy of solid. And the kinetic energy of solid is also restricted to a low level due to the restriction of the solid particles' displacement. As we can conclude, the lost kinetic energy of liquid has most turns into the elastic potential energy of liquid, only a small part of them results in the energy stored in the solid.

4.2 With Microstructure

Then, we calculated the situation with microstructures. The transient stress distribution in the solid with equilateral triangle microstructure, which has a 25 μm apex height, was shown in **Figure 6**. Comparing the calculation results before and after the introduction of the microstructure, it is obvious that the existence of the microstructure can change the stress distribution inside the solid greatly: the stress level of the base solid has dropped significantly, and the original stress concentration point in the base solid is no longer exist; the stress level of the microstructure on the surface is roughly the same as that of the base solid, but there seems to be a certain degree of stress concentration in the liquid film on the outside of the microstructure.

Figure 7 shows an enlarged view of the stress distribution in the solid. The existence of the microstructure makes a liquid film form which exists on the interactive surface, and the liquid film not only fills the gaps of the microstructures but there may also be a certain thickness of the liquid film layer in the space above the microstructure. This liquid film has a buffering effect on the impact process, so the stress level inside the base solid and the microstructure are not high.

The liquid stored in the microstructure is the main reason for buffering. At the same time, the liquid between the microstructure gaps also bears the greatest stress distribution. Although there will be a large pressure concentration in this part of the liquid, the stress level of the pressure concentrated feedback to the solid or microstructure is not high.

4.3 Quantitative Analysis

The tendency of the maximum equivalent stress was shown in **Figure 8**. The maximum equivalent stress in solid with or without the microstructure. When there is no microstructure, the maximum internal stress in the base solid increases with the impact progressing, and the overall trend is that the oscillation increases linearly. The maximum stress change trend with the microstructure is shown by the blue line in the figure. It can be seen that the stress level inside the base material is extremely low at the beginning of the impact. Due to the influence of stress

concentration inside the liquid film in the later stage, the maximum stress inside the microstructure also rises. Although the maximum stress inside the microstructure increased significantly in the later period, and the rate of increase was also faster. But in general, the maximum stress level inside the solid after the introduction of microstructures is only 50% of that without microstructures.

5 CONCLUSION

In this paper, the mechanical feasibility of applying the surface microstructure to improve the heat transfer efficiency in nuclear reactor is evaluated by establishing a numerical model of the liquid-solid impact process. First, the physical process of the liquid droplet scouring the solid surface was described, then the liquid-solid impact mathematical governing equation coupling the two phases was obtained by passing the pressure of liquid and displacement of solid on the interface. Through this calculation, the stress distribution in the solid and microstructure was analyzed and compared. The main results and conclusions obtained are as follows:

(1) When the droplet impacts continuously on the solid surface, due to the superposition of the shock waves inside the liquid, the kinetic energy lost by the droplets is finally converted into the elastic potential energy of the liquid, the kinetic energy of the solid and elastic potential energy of the solid, so a stress field distribution which cannot be ignored exists inside the solid.
(2) The surface microstructure can significantly change the distribution of the stress field inside the solid. The hydrophobic effect of the microstructure makes some liquid of the droplet form a liquid film in and above the microstructure. The buffering effect of the liquid film can greatly reduce the stress level in the solid. Although a certain degree of stress concentration in the liquid film causes the increase of the stress inside the microstructure, the maximum stress level inside the microstructure is only about 50% of that in the base solid without the microstructure.

The results in this paper show that the surface microstructure can not only meet the mechanical performance requirements under the condition of droplet impacting but also reduce the stress level inside the entire solid. Once again, the microstructure was proved to be with great potential in the heat transfer enhancement considering the perspective of mechanical feasibility.

DATA AVAILABILITY STATEMENT

The original contributions presented in the study are included in the article/Supplementary Material, further inquiries can be directed to the corresponding author.

AUTHOR CONTRIBUTIONS

SH: the physical model and numerical governing equations. TY, PY, and FZ: data processing. HW: writing-editing. ML and CH: project administration. HL and YL: funding.

FUNDING

This work was supported by National Key R&D Program of China (Grant No. 2018YFE0116100) and Natural Science Foundation of China (Grant No. 12105273).

REFERENCES

Bartolo, D., Josserand, C., and Bonn, D. (2006). Singular Jets and Bubbles in Drop Impact. *Phys. Rev. Lett.* 96, 124501. doi:10.1103/physrevlett.96.124501

Cointe, R., and Armand, J.-L. (1987). Hydrodynamic Impact Analysis of a Cylinder. *J. Offshore Mech. Arctic Eng.* 109, 237–243. doi:10.1115/1.3257015

Cook, S. S. (1928). Erosion by Water-Hammer. *Proc. R. Soc. Lond. Ser. A Contain. Pap. a Math. Phys. Character* 119, 481–488.

Field, J. E. (1999). ELSI Conference: Invited Lecture. *Wear* 233-235, 1–12. doi:10.1016/s0043-1648(99)00189-1

Heymann, F. J. (1969). High-Speed Impact between a Liquid Drop and a Solid Surface. *J. Appl. Phys.* 40, 5113–5122. doi:10.1063/1.1657361

Kang, Z., and Wang, L. (2018). Boiling Heat Transfer on Surfaces with 3D-Printing Microstructures. *Exp. Therm. Fluid Sci.* 93, 165–170. doi:10.1016/j.expthermflusci.2017.12.021

Kim, H.-Y., Park, S.-Y., and Min, K. (2003). Imaging the High-Speed Impact of Microdrop on Solid Surface. *Rev. Scientific Instr.* 74, 4930–4937. doi:10.1063/1.1614860

Korobkin, A. (1992). Blunt-body Impact on a Compressible Liquid Surface. *J. Fluid Mech.* 244, 437–453. doi:10.1017/s0022112092003136

Korobkin, A. (1994). Blunt-body Impact on the Free Surface of a Compressible Liquid. *J. Fluid Mech.* 263, 319–342. doi:10.1017/s0022112094004131

Le Bot, C., Vincent, S., Meillot, E., Sarret, F., Caltagirone, J.-P., and Bianchi, L. (2015). Numerical Simulation of Several Impacting Ceramic Droplets with Liquid/solid Phase Change. *Surf. Coat. Techn.* 268, 272–277. doi:10.1016/j.surfcoat.2014.10.047

Lee, M.-K., Kim, W.-W., Rhee, C.-K., and Lee, W.-J. (2002). An Analysis of Stress Waves in 12Cr Steel, Stellite 6B and TiN by Liquid Impact Loading. *Nucl. Eng. Des.* 214, 183–193. doi:10.1016/s0029-5493(02)00053-5

Lei, Z., Liu, B., Xu, P., Zhang, Y., and Wei, J. (2020). The Pool Boiling Heat Transfer and Critical Vapor Column Coalescence Mechanism of Block-Divided Microstructured Surfaces. *Int. J. Heat Mass Transfer* 150, 119362. doi:10.1016/j.ijheatmasstransfer.2020.119362

Li, N., Zhou, Q., Chen, X., Xu, T., Hui, S., and Zhang, D. (2008). Liquid Drop Impact on Solid Surface with Application to Water Drop Erosion on Turbine Blades, Part I: Nonlinear Wave Model and Solution of One-Dimensional Impact. *Int. J. Mech. Sci.* 50, 1526–1542. doi:10.1016/j.ijmecsci.2008.08.001

Liu, N., Yu, Z., Zhu, T., Yin, X., and Zhang, H. (2020). Effects of Microstructured Surface and Mixed Surfactants on the Heat Transfer Performance of Pulsed spray Cooling. *Int. J. Therm. Sci.* 158, 106530. doi:10.1016/j.ijthermalsci.2020.106530

Park, Y., Park, H.-K., Pusey, A., Hong, J., Park, J., Chung, B.-J., et al. (2019). Heat Transfer Augmentation in Two-phase Flow Heat Exchanger Using Porous Microstructures and a Hydrophobic Coating. *Appl. Therm. Eng.* 153, 433–447. doi:10.1016/j.applthermaleng.2019.03.030

Peng, W., and Cao, X. (2016). Numerical Simulation of Solid Particle Erosion in Pipe Bends for Liquid-Solid Flow. *Powder Techn.* 294, 266–279. doi:10.1016/j.powtec.2016.02.030

Semenov, Y. A., and Wu, G. X. (2016). Liquid Impact on a Permeable Solid Body. *Eur. J. Mech. B Fluids* 57, 22–30. doi:10.1016/j.euromechflu.2016.02.004

Shi, H., Li, S., Zhong, D., Meng, J. a., Luo, X., Zhang, X., et al. (2021). CHF Enhancement of Downward-Facing Saturated Pool Boiling on the SCGS-Modified Surfaces with Multi-Scale Conical Pin Fin Structures. *Int. J. Heat Mass Transfer* 181, 121848. doi:10.1016/j.ijheatmasstransfer.2021.121848

Sun, X. Z., Li, Q., Li, W. X., Wen, Z. X., and Liu, B. (2022). Enhanced Pool Boiling on Microstructured Surfaces with Spatially-Controlled Mixed Wettability. *Int. J. Heat Mass Transfer* 183, 122164. doi:10.1016/j.ijheatmasstransfer.2021.122164

Tokunaga, A., and Tsuruta, T. (2020). Enhancement of Condensation Heat Transfer on a Microstructured Surface with Wettability Gradient. *Int. J. Heat Mass Transfer* 156, 119839. doi:10.1016/j.ijheatmasstransfer.2020.119839

Wagner, H. (1932). Über Stoß- und Gleitvorgänge an der Oberfläche von Flüssigkeiten. *Z. Angew. Math. Mech.* 12, 193–215. doi:10.1002/zamm.19320120402

Wang, L., Wang, Y., Cheng, W., Yu, H., and Xu, J. (2021). Boiling Heat Transfer Properties of Copper Surface with Different Microstructures. *Mater. Chem. Phys.* 267, 124589. doi:10.1016/j.matchemphys.2021.124589

Xiong, J., Koshizuka, S., and Sakai, M. (2010). Numerical Analysis of Droplet Impingement Using the Moving Particle Semi-implicit Method. *J. Nucl. Sci. Technol.* 47, 314–321. doi:10.1080/18811248.2010.9711960

Xiong, J., Koshizuka, S., and Sakai, M. (2011). Investigation of Droplet Impingement onto Wet Walls Based on Simulation Using Particle Method. *J. Nucl. Sci. Techn.* 48, 145–153. doi:10.1080/18811248.2011.9711689

Xiong, J., Koshizuka, S., Sakai, M., and Ohshima, H. (2012). Investigation on Droplet Impingement Erosion during Steam Generator Tube Failure Accident. *Nucl. Eng. Des.* 249, 132–139. doi:10.1016/j.nucengdes.2011.08.048

Zhou, Q., Li, N., Chen, X., Xu, T., Hui, S., and Zhang, D. (2008). Liquid Drop Impact on Solid Surface with Application to Water Drop Erosion on Turbine Blades, Part II: Axisymmetric Solution and Erosion Analysis. *Int. J. Mech. Sci.* 50, 1543–1558. doi:10.1016/j.ijmecsci.2008.08.002

Zhu, S., Zhi, X., Gu, C., Wang, K., and Qiu, L. (2021). Enhancing Heat Transfer Performance of Nitrogen Condensation on Vertical Plate with Microstructure. *Int. J. Heat Mass Transfer* 172, 121219. doi:10.1016/j.ijheatmasstransfer.2021.121219

Zhukov, V. I., Pavlenko, A. N., and Shvetsov, D. A. (2020). The Effect of Pressure on Heat Transfer at Evaporation/boiling in Horizontal Liquid Layers of Various Heights on a Microstructured Surface Produced by 3D Laser Printing. *Int. J. Heat Mass Transfer* 163, 120488. doi:10.1016/j.ijheatmasstransfer.2020.120488

Conflict of Interest: The authors declare that the research was conducted in the absence of any commercial or financial relationships that could be construed as a potential conflict of interest.

Publisher's Note: All claims expressed in this article are solely those of the authors and do not necessarily represent those of their affiliated organizations, or those of the publisher, the editors and the reviewers. Any product that may be evaluated in this article, or claim that may be made by its manufacturer, is not guaranteed or endorsed by the publisher.

Copyright © 2022 Huang, Yue, Yuan, Zhu, Wang, Liu, Huang, Li and Li. This is an open-access article distributed under the terms of the Creative Commons Attribution License (CC BY). The use, distribution or reproduction in other forums is permitted, provided the original author(s) and the copyright owner(s) are credited and that the original publication in this journal is cited, in accordance with accepted academic practice. No use, distribution or reproduction is permitted which does not comply with these terms.

frontiers | Frontiers in Energy Research

ORIGINAL RESEARCH
published: 13 April 2022
doi: 10.3389/fenrg.2022.873731

Investigation of Nodal Numerical Adjoints From CMFD-Based Acceleration Methods

*Taesuk Oh and Yonghee Kim**

Korea Advanced Institute of Science and Technology (KAIST), Daejeon, Korea

In this work, the attribute of mathematical adjoints acquired from various CMFD (coarse-mesh finite difference) accelerated nodal methods based on the nodal expansion method (NEM) is presented. The direct transposition is implemented to the NEM-CMFD system matrix that includes correction factors to acquire the adjoint flux. Three different acceleration schemes are considered in this paper, which are, namely, CMFD, pCMFD, and one-node CMFD methods, and the self-adjoint attribute of migration operator for each acceleration scheme is studied. With regard to the one-node CMFD acceleration, a mathematical description for encountering negative adjoint flux values is given alongside an adjusted one-node CMFD scheme that stifles such an occurrence. The overall features of the aforementioned acceleration methods are recognized through analyses of 2D reactor problems including the KWU PWR 2D benchmark problem. Further systematic assessment is conducted based on the first-order perturbation theory, where the obtained adjoint fluxes are applied as weighting functions. It is clearly shown that the adjusted one-node CMFD scheme results in an improved reactivity estimation by excluding the presence of negative adjoint flux values.

Keywords: adjoint flux, CMFD accelerated nodal method, pCMFD, one-node CMFD, first-order perturbation theory

OPEN ACCESS

Edited by:
Shripad T. Revankar,
Purdue University, United States

Reviewed by:
Chen Hao,
Harbin Engineering University, China
Ndolane Sene,
Cheikh Anta Diop University, Senegal

***Correspondence:**
Yonghee Kim
yongheekim@kaist.ac.kr

Specialty section:
This article was submitted to Nuclear Energy, a section of the journal Frontiers in Energy Research

Received: *11 February 2022*
Accepted: *21 March 2022*
Published: *13 April 2022*

Citation:
Oh T and Kim Y (2022) Investigation of Nodal Numerical Adjoints From CMFD-Based Acceleration Methods. Front. Energy Res. 10:873731. doi: 10.3389/fenrg.2022.873731

INTRODUCTION

The adjoint flux is often referred to as an importance function since it signifies the importance of a neutron source at a certain phase-space contributing to fission reaction. Mathematically, it could be shown that the first-order errors can be removed when the adjoint flux is utilized as a weighting function, rendering it to be a preferred choice for perturbation theory–based analyses and generation of point kinetic parameters (Ott and Neuhold, 1985). The appraisal of adjoint flux can be performed by solving either the balance equation for itself or the transpose of a balance equation for the forward flux. The acquired adjoint fluxes from the former and latter methods are usually referred to as physical and mathematical adjoint fluxes, respectively.

Notwithstanding the presented advantages of an adjoint flux, its acquisition related to nodal methods is often regarded to be obscure. It is worthwhile to articulate that the reactor balance equation of interest is a well-defined problem, which implies the accuracy of nodal solution can be retained when corresponding current information is preserved. From such a perspective, correction factors for the finite difference method (FDM) can be envisioned, which forces the net current acquired from FDM-like representation to concur with that of the standalone nodal solution. Whereupon, acceleration in the nodal calculation can be met, which is known as the coarse-mesh finite difference (CMFD) method (Smith, 1983).

The meaning of the physical adjoint flux, which is obtained through discretization of balance equation for the adjoint flux itself, is still subjected to ambiguity issues (Lewins, 1965). The inclusion of discontinuity factors or super homogenization factors, i.e., nodal equivalence theory, additionally complicates the proper interpretation of physical adjoint.

On the contrary, the mathematical adjoint, which can be harnessed via solving the transposed balance equation for the forward flux, can be envisaged (Lawrence, 1984). However, the direct transposition of continuous balance equation is not practical and rather ambiguous for nodal methods that rely on the usage of transverse leakage (Hong and Cho, 1995). A different measure can be taken by transposing the discretized balance equation under CMFD accelerated nodal methods, where transverse leakage and its associated complexities are incorporated via the correction factors in the system matrix. The former and the latter ones are often referred to as direct-mathematical adjoint and indirect-mathematical adjoint, respectively. It is the latter approach that is widely implemented, which will be cited as numerical adjoint throughout this work.

A previous work states that negative adjoint flux values could occur for the conventional CMFD method, which utilized the analytic nodal method (ANM) solution while deducing the correction factor (Müller, 2014). To overcome such an unphysical anomaly, an additional correction was proposed; however, it deteriorates the consistency of CMFD formulation. In addition, no systematic evaluation of numerical adjoints from different CMFD schemes has been conducted.

In this paper, the characteristics of numerical adjoint fluxes obtained from nodal expansion method (NEM) solutions accelerated via various CMFD schemes are investigated. Especially, a systematic comparison is conducted between each adjoint flux obtained from different CMFD schemes, e.g., conventional CMFD, partial current–based CMFD, and one-node CMFD, based on the first-order perturbation theory. In *Coarse-Mesh Finite Difference–Based Acceleration Methods*, the basic concept and mathematical formulas regarding various CMFD acceleration schemes are depicted. In *Nodal Expansion Method*, a brief explanation concerning the nodal expansion method is given. In *Attributes of Numerical Adjoint Flux*, mathematical descriptions for attributes of numerical adjoints are depicted including the occurrence of negative adjoint flux. In *Numerical Results*, numerical results are presented alongside first-order perturbation theory–based comparison. Finally, conclusions are given in *Conclusion*.

COARSE-MESH FINITE DIFFERENCE–BASED ACCELERATION METHODS

The philosophy of the CMFD acceleration scheme is the preservation of the reference net current information while retaining the formulation of the finite difference method (FDM), which is the simplest numerical measure to be taken. Three different CMFD-based acceleration methods are considered in this work, which are, namely, 1) conventional CMFD, 2) partial current–based CMFD (pCMFD), and 3) one-node CMFD.

Conventional CMFD Method

Figure 1 illustrates the balance for neutron flux within a node of interest i, and its associated balance equation is expressed as follows:

$$\bar{J}_{i,i+1} - \bar{J}_{i-1,i} + \Sigma_{ri}\Delta x_i \bar{\phi}_i = \frac{1}{k}\nu\sum_{fi}\Delta x_i \bar{\phi}_i \tag{1}$$

where $\bar{J}_{i,i+1}$ denotes the net neutron current from node i toward its adjacent node i+1, k represents the multiplication factor, and all the other notations are those of the convention. By approximating the gradient of the flux to be linear in the diffusion theory, one garners the following equation which is known as the finite difference method (FDM):

$$\bar{J}_{i,i+1} = -\tilde{D}_{i,i+1}\left(\bar{\phi}_{i+1} - \bar{\phi}_i\right) \tag{2}$$

$$\tilde{D}_{i,i+1} = \frac{2\left(\frac{D_i}{\Delta x_i}\right)\left(\frac{D_{i+1}}{\Delta x_{i+1}}\right)}{\frac{D_i}{\Delta x_i} + \frac{D_{i+1}}{\Delta x_{i+1}}} \tag{3}$$

The correction factor $\hat{D}_{i,i+1}$ can be envisioned for **Eq. 2** which alters the net current to be the reference current as follows:

$$\bar{J}^{ref}_{i,i+1} = -\tilde{D}_{i,i+1}\left(\bar{\phi}_{i+1} - \bar{\phi}_i\right) - \hat{D}_{i,i+1}\left(\bar{\phi}_{i+1} + \bar{\phi}_i\right), \tag{4}$$

$$\hat{D}_{i,i+1} = \frac{-\tilde{D}_{i,i+1}\left(\bar{\phi}_{i+1} - \bar{\phi}_i\right) - \bar{J}^{ref}_{i,i+1}}{\left(\bar{\phi}_{i+1} + \bar{\phi}_i\right)}. \tag{5}$$

The neutron balance equation, i.e., **Eq. 1**, is known to be a well-defined problem, in which a single solution (eigenvalue) exists for a certain current value. Hence, the inclusion of **Eqs 4**, **5** while implementing the FDM would provide an equivalent solution to that of the reference, which is exploited for acquiring $\bar{J}^{ref}_{i,i+1}$ (Smith, 1983). The simplicity of the FDM with its coarse node size will manifest as a reduction in the computing burden (acceleration), hence attaining the name of coarse-mesh finite difference (CMFD) method.

Partial Current–Based CMFD Method

It is apparent that the preservation of partial currents will guarantee retaining net current. From such a perspective, two correction factors for incoming and outgoing partial currents can be considered as depicted in **Figure 2**, attaining the name of partial current–based CMFD (pCMFD) method (Cho et al., 2003):

$$\bar{J}^{+ref}_{i,i+1} = -\frac{\tilde{D}_{i,i+1}\left(\bar{\phi}_{i+1} - \bar{\phi}_i\right) + 2\hat{D}^{+}_{i,i+1}\bar{\phi}_i}{2} \tag{6}$$

$$\bar{J}^{-ref}_{i,i+1} = \frac{\tilde{D}_{i,i+1}\left(\bar{\phi}_{i+1} - \bar{\phi}_i\right) + 2\hat{D}^{-}_{i,i+1}\bar{\phi}_{i+1}}{2} \tag{7}$$

The net current can be expressed as

$$\bar{J}^{ref}_{i,i+1} = \bar{J}^{+ref}_{i,i+1} - \bar{J}^{-ref}_{i,i+1} = -\tilde{D}_{i,i+1}\left(\bar{\phi}_{i+1} - \bar{\phi}_i\right) - \left(\hat{D}^{+}_{i,i+1}\bar{\phi}_i + \hat{D}^{-}_{i,i+1}\bar{\phi}_{i+1}\right) \tag{8}$$

$$\bar{J}_{i,i+1} - \bar{J}_{i-1,i} + \Sigma_{ri}\Delta x_i \bar{\phi}_i = \frac{1}{k}\nu\Sigma_{fi}\Delta x_i \bar{\phi}_i \,,$$

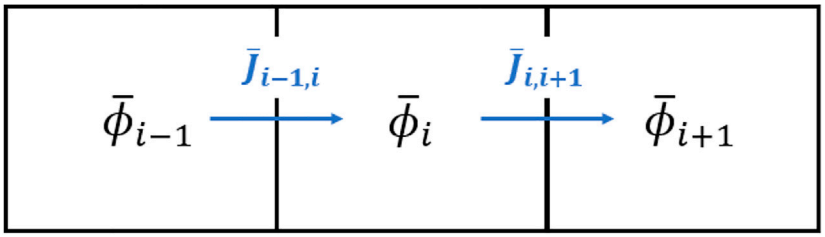

FIGURE 1 | Balance within a node of interest.

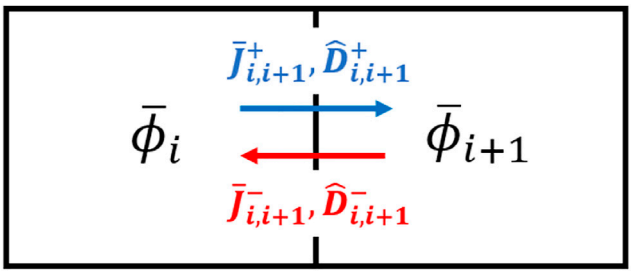

FIGURE 2 | Visualization of pCMFD correction schemes.

where

$$\hat{D}^{+}_{i,i+1} = -\frac{\tilde{D}_{i,i+1}\left(\bar{\phi}_{i+1} - \bar{\phi}_i\right) + 2\bar{J}^{+ref}_{i,i+1}}{2\bar{\phi}_i} \tag{9}$$

$$\hat{D}^{-}_{i,i+1} = -\frac{\tilde{D}_{i,i+1}\left(\bar{\phi}_{i+1} - \bar{\phi}_i\right) - 2\bar{J}^{-ref}_{i,i+1}}{2\bar{\phi}_{i+1}} \tag{10}$$

One-Node CMFD Method

The correction factors for the preservation of net current and surface flux could be introduced separately for each node as shown in **Figure 3**, where incoming partial current acts as a boundary condition for invoking kernel calculation (Shin and Kim, 1999). Such an approach differs from the conventional CMFD and pCMFD methods which introduce correction alongside two contiguous nodes:

$$\bar{J}_{i,i+1} = -\frac{2D_i}{\Delta x_i}\left(\bar{\phi}_s - \bar{\phi}_i\right) - \frac{2\hat{D}^{R}_{i}}{\Delta x_i}\left(\bar{\phi}_s + \bar{\phi}_i\right) \tag{11}$$

$$\bar{J}_{i,i+1} = -\frac{2D_{i+1}}{\Delta x_{i+1}}\left(\bar{\phi}_{i+1} - \bar{\phi}_s\right) - \frac{2\hat{D}^{L}_{i+1}}{\Delta x_{i+1}}\left(\bar{\phi}_s + \bar{\phi}_{i+1}\right) \tag{12}$$

Equating **Eqs 11**, **12** yields the following expression for the surface flux:

$$\bar{\phi}_s = \frac{\Delta x_{i+1}\left(D_i - \hat{D}^{R}_{i}\right)\bar{\phi}_i + \Delta x_i\left(D_{i+1} + \hat{D}^{L}_{i+1}\right)\bar{\phi}_{i+1}}{\Delta x_{i+1}\left(D_i + \hat{D}^{R}_{i}\right) + \Delta x_i\left(D_{i+1} - \hat{D}^{L}_{i+1}\right)} \tag{13}$$

where

$$\hat{D}^{R}_{i} = -\frac{\Delta x_i\,\bar{J}^{ref}_{i,i+1} + 2D_i\left(\bar{\phi}^{ref}_s - \bar{\phi}_i\right)}{2\left(\bar{\phi}^{ref}_s + \bar{\phi}_i\right)} \tag{14}$$

$$\hat{D}^{L}_{i+1} = -\frac{\Delta x_{i+1}\,\bar{J}^{ref}_{i,i+1} + 2D_{i+1}\left(\bar{\phi}_{i+1} - \bar{\phi}^{ref}_s\right)}{2\left(\bar{\phi}^{ref}_s + \bar{\phi}_{i+1}\right)} \tag{15}$$

Originally devised for parallel acceleration, the aforementioned acceleration scheme, which is referred to as one-node CMFD, can still be applied in a similar manner to that of the conventional CMFD or pCMFD method. Note that, for such an implementation, preservation of net current becomes irrelevant to surface flux values.

NODAL EXPANSION METHOD

As aforementioned, the underlying philosophy of CMFD-based acceleration is retaining current information from higher-order solutions, which is often the nodal calculation for whole-core analyses. In this work, the well-known nodal expansion method (NEM) was implemented as a kernel calculation, which is an assessment of current information and its corresponding correction factors for the neighboring two-node configuration. The correction factor is then considered during the formulation of discretized migration operator being analogous to that of the simple FDM, and the overall procedure is often referred to as NEM-CMFD calculation (Downar et al., 2009).

The detailed 1D flux and the transverse leakage term for a certain direction of interest are expanded via fourth-order and second-order polynomial basis functions (Legendre polynomials), respectively:

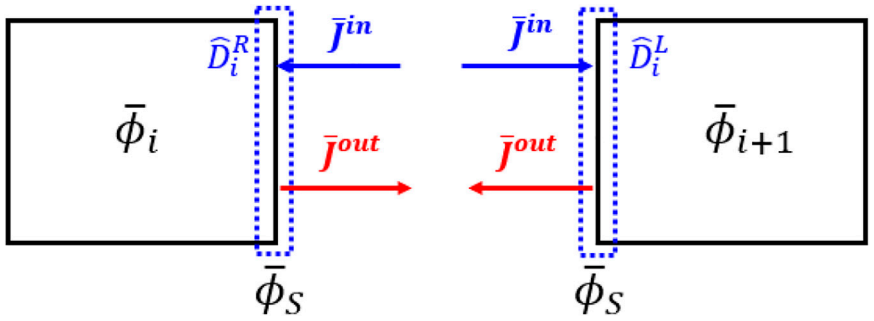

FIGURE 3 | Visualization of one-node CMFD correction factors.

TABLE 1 | Migration matrix entries for CMFD methods.

Method	$a_{i,i}$	$a_{i,i-1}$	$a_{i,i+1}$
FDM	$\tilde{D}_{i-1,j} + \tilde{D}_{i,j+1}$	$-\tilde{D}_{i-1,j}$	$-\tilde{D}_{i,j+1}$
CMFD	$\tilde{D}_{i-1,j} + \hat{D}_{i-1,j} + \tilde{D}_{i,j+1} - \hat{D}_{i,j+1}$	$-\tilde{D}_{i-1,j} + \hat{D}_{i-1,j}$	$-\tilde{D}_{i,j+1} - \hat{D}_{i,j+1}$
pCMFD	$\tilde{D}_{i-1,j} + \hat{D}^{-}_{i-1,j} + \tilde{D}_{i,j+1} - \hat{D}^{+}_{i,j+1}$	$-\tilde{D}_{i-1,j} + \hat{D}^{+}_{i-1,j}$	$-\tilde{D}_{i,j+1} - \hat{D}^{-}_{i,j+1}$
One-node CMFD	$\frac{2(D_{i-1}+\hat{D}^R_{i-1})(D_i+\hat{D}^L_i)}{\Delta x_{i-1}(D_i-\hat{D}^L_i)+\Delta x_i(D_{i-1}+\hat{D}^R_{i-1})} + \frac{2(D_i-\hat{D}^R_i)(D_{i+1}-\hat{D}^L_{i+1})}{\Delta x_{i+1}(D_{i+1}-\hat{D}^L_{i+1})+\Delta x_{i+1}(D_i+\hat{D}^R_i)}$	$-\frac{2(D_{i-1}-\hat{D}^R_{i-1})(D_i-\hat{D}^L_i)}{\Delta x_{i-1}(D_i-\hat{D}^L_i)+\Delta x_i(D_{i-1}+\hat{D}^R_{i-1})}$	$-\frac{2(D_i+\hat{D}^R_i)(D_{i+1}+\hat{D}^L_{i+1})}{\Delta x_i(D_{i+1}-\hat{D}^L_{i+1})+\Delta x_{i+1}(D_i+\hat{D}^R_i)}$

$$\phi_g(\xi) = a_{g,0}P_0(\xi) + a_{g,1}P_1(\xi) + a_{g,2}P_2(\xi) + a_{g,3}P_3(\xi) + a_{g,4}P_4(\xi) \tag{16}$$

$$L_g(\xi) = L_{g,0}P_0(\xi) + L_{g,1}P_1(\xi) + L_{g,2}P_2(\xi) \tag{17}$$

$$P_0(\xi) = 1,\ P_1(\xi) = \xi,\ P_2(\xi) = \xi^2 - \frac{1}{12},\ P_3(\xi) = \xi^3 - \frac{1}{4}\xi,\ P_4(\xi) = \xi^4 - \frac{3}{10}\xi^2 + \frac{1}{80} \tag{18}$$

where ξ is the direction of interest, $a_{g,i}$ is the ith-order flux expansion coefficient for group g, and $L_{g,i}$ is the ith-order transverse leakage expansion coefficient for group g. The determination of net current then corresponds to calculation of flux expansion coefficients, where transverse leakage information must be pre-determined before invoking the NEM kernel calculation. Note that it is the presence of transverse leakage that complicates the assessment of direct-mathematical adjoint flux.

For a two-node NEM calculation, a total of 8G (G = number of groups) coefficients must be determined, which requires the same number of governing equations. Flux continuity (1G), current continuity (1G), and zeroth, first, and second moment node balance equations (2G for each) are envisioned for such a case, which results in a generation of 8G by 8G matrix equation. In contrast, a 4G by 4G matrix equation is formulated for a node at the boundary, where incoming partial current information is used in lieu of continuity equations.

ATTRIBUTES OF NUMERICAL ADJOINT FLUX

Accompanied by proper usage of nodal kernel(s), either aided by transverse leakage or not, CMFD-based acceleration provides an FDM-like matrix where correction factors retain the net current information, rendering the solution to be that of the nodal calculation. The numerical adjoint can be readily calculated through the transpose of such a matrix representation; however, the correction factors manifest as a non-self-adjoint issue. Hence, the acquired numerical adjoint deviates from the reference one that possesses the self-adjoint property, where the extent of deviation depends on the type of CMFD acceleration scheme being utilized.

Self-Adjoint Issue

The multigroup diffusion equation can be written as follows:

$$M_g\phi_g = \frac{\chi_g}{k}\sum_{g'=1}^{G}\nu\Sigma_{f,g'}\phi_{g'} + \sum_{\substack{g'=1 \\ (g'\neq g)}}^{G}\Sigma_{s,g'\to g}\phi_{g'} \tag{19}$$

where G and k represent the number of energy groups and multiplication factor, M_g denotes the migration operator for group g ($M_g\phi_g := -\nabla\cdot D_g\nabla\phi_g + \Sigma_{r,g}\phi_g$), and all the other notations are those of the convention. Note that, through proper discretization, the given equation can be represented in a matrix form. The numerical adjoint flux can then be calculated by transposing **Eq. 19**:

$$M_g^\dagger\phi_g^\dagger = \frac{1}{k}\sum_{g'=1}^{G}\chi_{g'}\nu\Sigma_{f,g}\phi_{g'}^\dagger + \sum_{\substack{g'=1 \\ (g'\neq g)}}^{G}\Sigma_{s,g\to g'}\phi_{g'}^\dagger \tag{20}$$

where superscript dagger (†) signifies the adjoint operation.

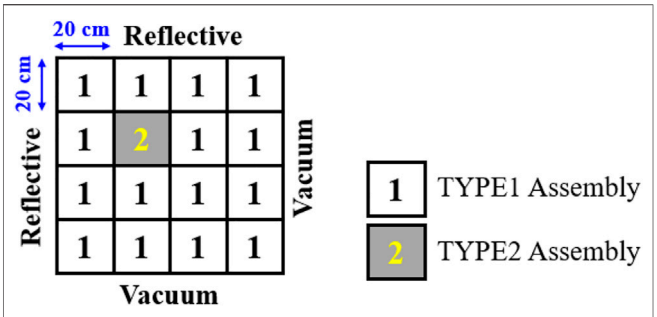

FIGURE 4 | One-group reactor problem.

TABLE 2 | Cross-section (XS) for the one-group reactor problem.

Assembly	Σ_{tr}	Σ_a	$\nu\Sigma_f$
TYPE 1	0.3650	0.0650	0.0700
TYPE 2	0.3650	0.0750	0.0700

TABLE 3 | Calculated multiplication factors for the one-group reactor problem.

Method	K-EFF	K-EFF (ADJ)
NEM-CMFD (1 × 1)	1.071408	1.071408
NEM-pCMFD (1 × 1)	1.071408	1.071408
NEM-1NCMFD (1 × 1)	1.071408	1.071408
FDM (50 × 50)	1.071408	1.071408

**(1 × 1) and (50 × 50) represent fuel assembly nodalization.*

Mathematically, it could be shown that the continuous migration operator for a certain group is self-adjoint (Ott and Neuhold, 1985). Such a feature is retained for the FDM approach, however, but not for the CMFD accelerated nodal calculation due to the presence of correction factors. The discretized balance equation can be generalized as follows:

$$a_{i,i-1}\bar{\phi}_{i-1} + a_{i,i}\bar{\phi}_i + a_{i,i+1}\bar{\phi}_{i+1} = s_i \tag{21}$$

where $a_{i,j}$ represents the contribution from $\bar{\phi}_j$ for the neutron balance concerning $\bar{\phi}_i$ and s_i denotes the source term for node i containing both scattering and fission. **Table 1** summarizes the matrix entries for the FDM and CMFD methods, where only the FDM approach retains the self-adjoint of the migration matrix, i.e., $a_{i-1,i} = a_{i,i-1}$ and $a_{i,i+1} = a_{i+1,i}$.

It could be observed that all the enumerated CMFD methods do not retain the self-adjoint property for the group-wise migration matrix. In addition, for the conventional CMFD and one-node CMFD, it could be easily shown that the absolute magnitude of corrections factors will dwindle with a decrease in the mesh size, i.e., numerators for **Eqs 5**, **14**, and **15** converge to zero:

$$-\tilde{D}_{i,i+1}\left(\bar{\phi}_{i+1} - \bar{\phi}_i\right) \to \bar{J}^{ref}_{i,i+1} \tag{22}$$

$$-\frac{D_i}{\Delta x_i/2}\left(\bar{\phi}^{ref}_s - \bar{\phi}_i\right) \to \bar{J}^{ref}_{i,i+1} \tag{23}$$

However, correction factors for pCMFD do not converge to zero like the other two CMFD-based acceleration schemes:

$$\hat{D}^{+}_{i,i+1} = -\frac{\tilde{D}_{i,i+1}\left(\bar{\phi}_{i+1} - \bar{\phi}_i\right) + 2\bar{J}^{+ref}_{i,i+1}}{2\bar{\phi}_i}$$
$$\cong \frac{J^{ref}_{i,i+1} - 2\bar{J}^{+ref}_{i,i+1}}{2\bar{\phi}_i} = \frac{\left(\bar{J}^{+ref}_{i,i+1} - \bar{J}^{-ref}_{i,i+1}\right) - 2\bar{J}^{+ref}_{i,i+1}}{2\bar{\phi}_i} = -\frac{\bar{J}^{+ref}_{i,i+1} + \bar{J}^{-ref}_{i,i+1}}{2\bar{\phi}_i}. \tag{24}$$

The inclusion of correction factors can be expressed in the following manner:

$$(M + \delta M_1 + \delta M_2)\phi_{CMFD} = \frac{1}{k}F\phi_{CMFD} \tag{25}$$

where ϕ_{CMFD} represents the CMFD-based flux and δM_1 and δM_2 denote diagonal and off-diagonal correction entries, respectively. The transpose of **Eq. 25** can be written as

$$\left(M^{\dagger} + \delta M^{\dagger}_1 + \delta M^{\dagger}_2\right)\phi^{\dagger}_{CMFD} = \frac{1}{k}F^{\dagger}\phi^{\dagger}_{CMFD} \tag{26}$$

Since the diagonal matrix is self-adjoint, i.e., $\delta M_1 = \delta M^{\dagger}_1$, subtraction of the two equations above garners

$$(M + \delta M_1)\left(\phi_{CMFD} - \phi^{\dagger}_{CMFD}\right) + \left(\delta M_2\phi_{CMFD} - \delta M^{\dagger}_2\phi^{\dagger}_{CMFD}\right)$$
$$= \frac{1}{k}F\left(\phi_{CMFD} - \phi^{\dagger}_{CMFD}\right). \tag{27}$$

If $\delta M_2 \cong \delta M^{\dagger}_2$ is satisfied, $\phi_{CMFD} = \phi^{\dagger}_{CMFD}$ becomes the solution for **Eq. 27**, which corresponds to the preservation of self-adjoint feature.

Since CMFD-induced and one-node CMFD–induced correction factors converge to zero with an increase in the number of nodes, their corresponding numerical adjoints would also converge to the reference, which is not expected for the pCMFD-based numerical adjoint flux.

Negative Adjoint Flux Issue

The correction factors in the discretized balance equation could result in the occurrence of negative numerical adjoint flux values as pointed out in previous studies which implemented the analytic nodal method (ANM) while deducing correction factors (Müller, 2014). Such an anomaly ensues when the off-diagonal and its corresponding diagonal entry of the migration matrix attain the same sign, which cannot be prevented for the conventional CMFD method. To circumvent such an issue, a different formula for net current preservation can be partially utilized under certain conditions; however, such an approach deteriorates the consistency in the CMFD formulation, i.e., ad hoc up to a certain extent.

Recalling that the usage of one-node CMFD in a two-node manner, i.e., not parallelized, could preserve the net current regardless of its surface flux values, one could exclude the occurrence of negative adjoint flux values through proper adjustment of the surface flux values. It is noteworthy to articulate that consistent usage of the same surface flux value while

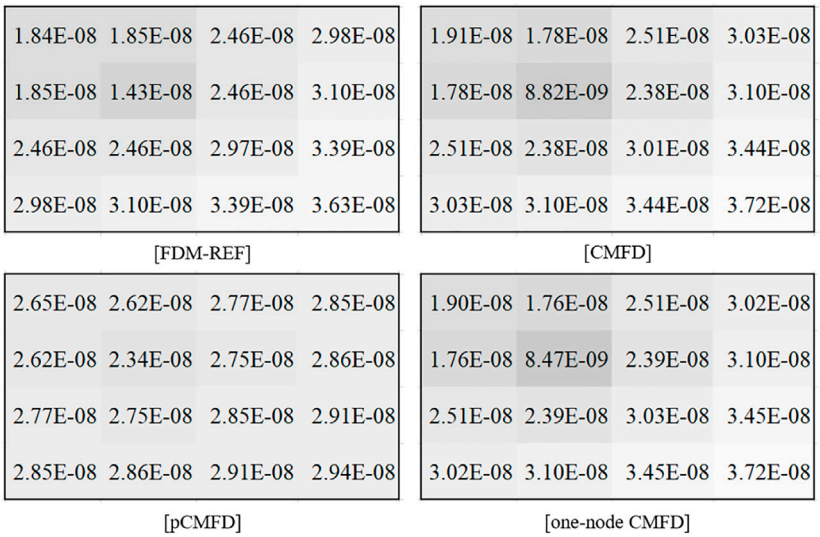

FIGURE 5 | CMFD-based numerical adjoint fluxes.

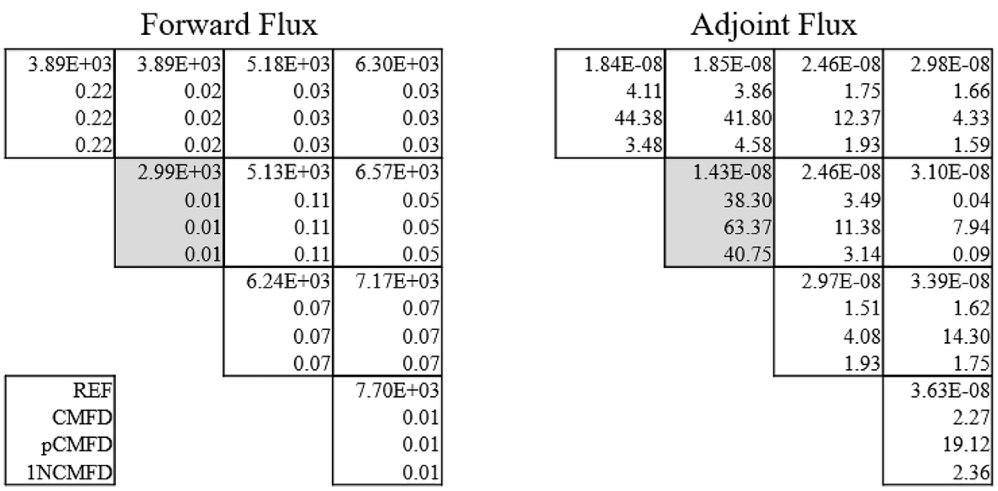

FIGURE 6 | Percentage error for forward and adjoint fluxes with a node size of 20 cm.

formulating the correction factors is responsible for the preservation of the current.

From **Eqs 14**, **15**, it could be recognized that the one-node CMFD correction factors have the same unit as the diffusion coefficient. Since it is unphysical for the correction factor–included diffusion coefficient to be negative, the following conditions can be envisioned:

$$\bar{\phi}_s^{ref} \le \frac{\Delta x_i}{4D_i}\left|\bar{J}_{i,i+1}^{ref}\right| \tag{28}$$

$$\bar{\phi}_s^{ref} \le \frac{\Delta x_{i+1}}{4D_{i+1}}\left|\bar{J}_{i,i+1}^{ref}\right| \tag{29}$$

Eqs 28, **29** represent the criterion for correction factors $\hat{D}_i^R$ and $\hat{D}_{i+1}^L$ being less than their associated diffusion coefficient in magnitude, respectively. Through adjustment of surface flux to suffice **Eqs 28**, **29**, the occurrence of negative numerical adjoint flux can be stifled.

NUMERICAL RESULTS

One-Group Reactor Problem

To test the deviation in the self-adjoint feature for various CMFD-based numerical adjoint fluxes, a simple one-group two-dimensional reactor problem was considered as shown in **Figure 4**. Two types of assemblies with a length of 20 cm are considered as shown in the cartoon, where their cross-section (XS) values are enumerated in **Table 2**.

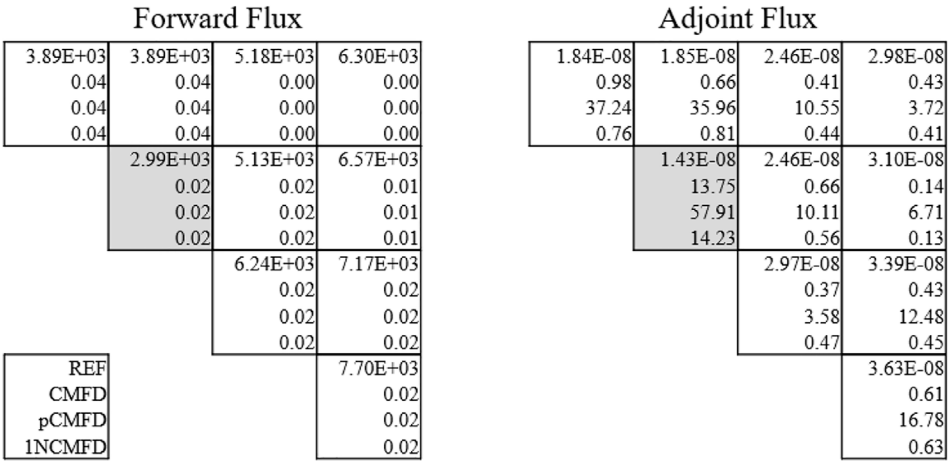

FIGURE 7 | Percentage error for forward and adjoint fluxes with a node size of 10 cm.

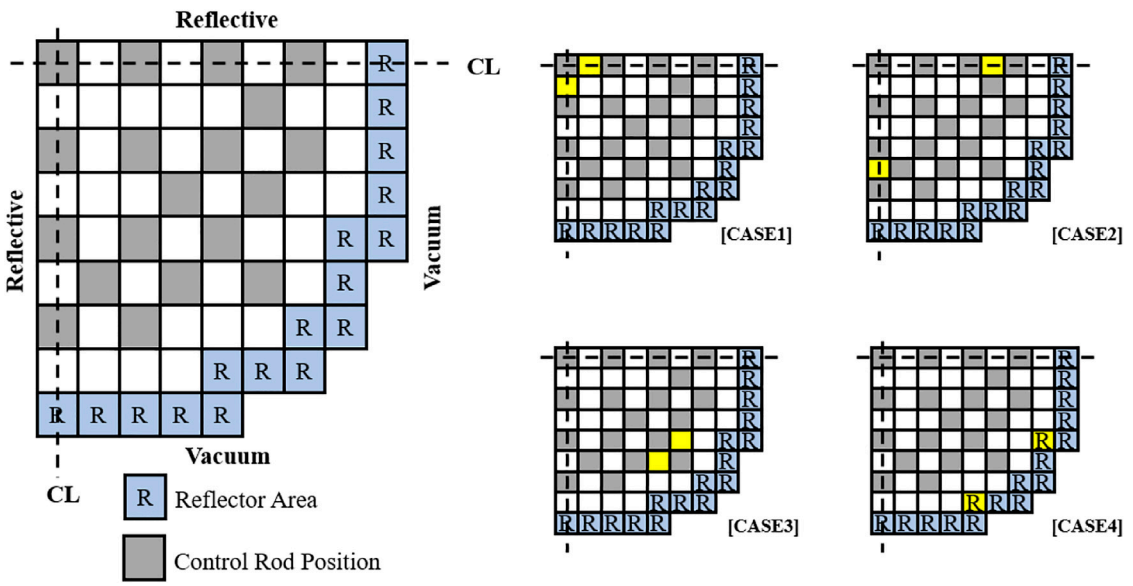

FIGURE 8 | KWU 2D core configuration.

TABLE 4 | Calculated multiplication factors for the KWU 2D problem.

Method	K-EFF	K-EFF (ADJ)
NEM-CMFD (1 × 1)	1.165863	1.165863
NEM-pCMFD (1 × 1)	1.165863	1.165863
NEM-1NCMFD (1 × 1)	1.165863	1.165863
FDM (100 × 100)	1.165694	1.165694

**(1 × 1) and (100 × 100) represent fuel assembly nodalization.*

For the acquisition of numerical adjoints, the nodal expansion method (NEM) kernel was utilized, whereas the reference adjoint flux was obtained via the FDM while dividing each assembly into equally spaced 2,500 nodes (50 × 50 per assembly). Since the FDM-based numerical adjoint always retains the self-adjoint feature, the acquired fine node-based result was regarded as a reference after condensing into an assembly-wise value according to the following equation (Downar et al., 2009):

$$\int_0^\infty dE \int_V dV \phi^\dagger(\boldsymbol{r}, E')\phi(\boldsymbol{r}, E') = 1.0 \tag{30}$$

The acquired multiplication factors for both forward and adjoint calculations are given in **Table 3**, where all the cases exhibit the same value.

TABLE 5 | Reactivity change (pcm) estimation for perturbation case 1.

Case 1	$\Delta\Sigma_{a,g}$ = +30%			$\Delta\Sigma_{a,g}$ = −30%		
Method	**$\Delta\rho$ (direct)**	**$\Delta\rho$ (first order)**	**Difference**	**$\Delta\rho$ (direct)**	**$\Delta\rho$ (first order)**	**Difference**
CMFD	516.46	598.99	82.53	−414.69	−481.39	−66.70
pCMFD	516.46	406.11	−110.35	−414.69	−298.90	115.79
1NCMFD	516.46	598.27	81.82	−414.69	−480.97	−66.28
1NCMFD*	516.46	598.27	81.82	−414.69	−480.97	−66.28
Uniform	516.46	296.91	−219.55	−414.69	−212.99	201.70

TABLE 6 | Reactivity change (pcm) estimation for perturbation case 2.

Case 2	$\Delta\Sigma_{a,g}$ = +30%			$\Delta\Sigma_{a,g}$ = −30%		
Method	**$\Delta\rho$ (direct)**	**$\Delta\rho$ (first order)**	**Difference**	**$\Delta\rho$ (direct)**	**$\Delta\rho$ (first order)**	**Difference**
CMFD	11.74	12.88	1.14	−10.02	−10.95	−0.93
pCMFD	11.74	40.09	28.35	−10.02	−34.40	−24.38
1NCMFD	11.74	12.41	0.66	−10.02	−10.55	−0.53
1NCMFD*	11.74	12.41	0.67	−10.02	−10.55	−0.53
Uniform	11.74	40.77	29.03	−10.02	−35.17	−25.15

TABLE 7 | Reactivity change (pcm) estimation for perturbation case 3.

Case 3	$\Delta\Sigma_{a,g}$ = +30%			$\Delta\Sigma_{a,g}$ = −30%		
Method	**$\Delta\rho$ (direct)**	**$\Delta\rho$ (first order)**	**Difference**	**$\Delta\rho$ (direct)**	**$\Delta\rho$ (first order)**	**Difference**
CMFD	10.12	11.31	1.19	−8.04	−8.95	−0.91
pCMFD	10.12	48.55	38.43	−8.04	−38.58	−30.54
1NCMFD	10.12	11.01	0.89	−8.04	−8.71	−0.67
1NCMFD*	10.12	11.01	0.88	−8.04	−8.71	−0.67
Uniform	10.12	52.95	42.82	−8.04	−42.32	−34.28

TABLE 8 | Reactivity change (pcm) estimation for perturbation case 4.

Case 4	$\Delta\Sigma_{a,g}$ = +80%			$\Delta\Sigma_{a,g}$ = −80%		
Method	**$\Delta\rho$ (direct)**	**$\Delta\rho$ (first order)**	**Difference**	**$\Delta\rho$ (direct)**	**$\Delta\rho$ (first order)**	**Difference**
CMFD	6.93	−0.26	−7.19	−1.04	−0.03	1.01
pCMFD	6.93	293.16	286.23	−1.04	−33.88	−32.84
1NCMFD	6.93	−0.31	−7.24	−1.04	−0.01	1.03
1NCMFD*	6.93	1.18	−5.75	−1.04	−0.21	0.83
Uniform	6.93	980.98	974.05	−1.04	−109.64	−108.60

Figure 5 illustrates the acquired adjoint fluxes from each acceleration scheme, where normalization according to **Eq. 30** was performed for comparison. It could be recognized that only the pCMFD-based numerical adjoint flux exhibits a different distribution. **Figure 6** summarizes the calculation result where the absolute value of percentage error for each case is given for both forward and adjoint fluxes. Note that the numerical adjoint flux exhibits the most conspicuous error for the TYPE 2 assembly region due to its enlarged absorption XS value:

$$ERR(\%) = \left|\frac{\phi^{ref} - \phi^{CMFD}}{\phi^{ref}}\right| \times 100. \tag{31}$$

As aforementioned, the deviation from the self-adjoint feature weakens as the size of the node dwindles. A similar analysis was

4.69E-19	5.21E-19	3.77E-19	3.24E-19	1.74E-19	8.33E-20	4.63E-20	3.61E-20	9.54E-21
3.34E-19	5.24E-19	2.65E-19	3.20E-19	1.18E-19	7.74E-20	3.88E-20	4.37E-20	1.87E-21
3.18E-19	3.38E-19	3.06E-19	3.11E-19	2.68E-19	2.45E-19	2.17E-19	2.17E-19	1.51E-19
3.36E-19	5.24E-19	2.68E-19	3.21E-19	1.19E-19	7.45E-20	3.60E-20	4.05E-20	8.70E-22
	5.44E-19	4.13E-19	3.31E-19	1.84E-19	7.38E-20	4.75E-20	3.77E-20	9.69E-21
	6.63E-19	4.12E-19	3.93E-19	1.72E-19	5.95E-20	5.09E-20	5.28E-20	2.13E-21
	3.47E-19	3.25E-19	3.18E-19	2.82E-19	2.35E-19	2.25E-19	2.22E-19	1.53E-19
	6.60E-19	4.13E-19	3.93E-19	1.74E-19	5.57E-20	4.73E-20	4.90E-20	8.42E-22
		2.83E-19	2.18E-19	1.17E-19	6.11E-20	3.77E-20	3.03E-20	7.97E-21
		1.96E-19	2.05E-19	7.99E-20	5.71E-20	3.10E-20	3.52E-20	1.54E-21
		2.92E-19	2.90E-19	2.51E-19	2.32E-19	2.09E-19	2.09E-19	1.47E-19
		1.99E-19	2.08E-19	8.04E-20	5.53E-20	2.91E-20	3.28E-20	6.95E-22
			1.13E-19	7.05E-20	4.24E-20	3.87E-20	2.59E-20	5.88E-21
			9.02E-20	6.63E-20	3.36E-20	4.71E-20	3.25E-20	1.70E-21
			2.54E-19	2.39E-19	2.13E-19	2.20E-19	2.06E-19	1.41E-19
			8.79E-20	6.53E-20	3.22E-20	4.45E-20	3.09E-20	4.32E-22
				4.19E-20	3.56E-20	3.28E-20	1.14E-20	1.69E-21
				3.36E-20	3.54E-20	4.18E-20	2.96E-21	3.59E-22
				2.14E-19	2.12E-19	2.14E-19	1.60E-19	1.14E-19
				3.22E-20	3.40E-20	3.97E-20	2.12E-21	1.26E-22
					2.37E-20	1.76E-20	4.66E-21	
					1.84E-20	1.81E-20	9.83E-22	
					1.92E-19	1.89E-19	1.33E-19	
					1.76E-20	1.73E-20	4.95E-22	

REF	5.27E-21	9.95E-22
CMFD	2.06E-21	2.28E-22
pCMFD	1.41E-19	1.02E-19
1NCMFD	1.03E-21	8.19E-23

FIGURE 9 | Fast group numerical adjoint flux for the KWU 2D problem.

5.24E-19	6.83E-19	4.21E-19	4.24E-19	1.95E-19	1.06E-19	5.32E-20	4.98E-20	2.82E-21
3.49E-19	6.85E-19	2.77E-19	4.18E-19	1.23E-19	1.01E-19	4.23E-20	6.09E-20	-4.17E-23
3.76E-19	4.39E-19	3.62E-19	4.04E-19	3.17E-19	3.09E-19	2.59E-19	2.90E-19	7.21E-20
3.53E-19	6.84E-19	2.81E-19	4.20E-19	1.25E-19	9.69E-20	3.94E-20	5.65E-20	-7.66E-23
	7.66E-19	5.43E-19	4.65E-19	2.42E-19	8.22E-20	6.15E-20	5.59E-20	3.14E-21
	9.39E-19	5.38E-19	5.56E-19	2.23E-19	6.28E-20	6.66E-20	8.00E-20	-5.05E-23
	4.71E-19	4.22E-19	4.31E-19	3.65E-19	2.76E-19	2.88E-19	3.11E-19	7.71E-20
	9.35E-19	5.39E-19	5.57E-19	2.25E-19	5.85E-20	6.18E-20	7.42E-20	-1.28E-22
		3.17E-19	2.85E-19	1.31E-19	7.76E-20	4.23E-20	4.18E-20	2.36E-21
		2.05E-19	2.66E-19	8.37E-20	7.42E-20	3.28E-20	4.91E-20	-3.04E-23
		3.45E-19	3.74E-19	2.96E-19	2.93E-19	2.47E-19	2.79E-19	6.97E-20
		2.09E-19	2.70E-19	8.43E-20	7.19E-20	3.07E-20	4.58E-20	-6.25E-23
			1.26E-19	8.94E-20	4.73E-20	5.34E-20	3.79E-20	1.91E-21
			9.51E-20	8.62E-20	3.54E-20	6.58E-20	4.91E-20	1.04E-23
			2.98E-19	3.01E-19	2.51E-19	2.96E-19	2.85E-19	6.97E-20
			9.24E-20	8.50E-20	3.39E-20	6.22E-20	4.67E-20	-9.37E-23
				4.65E-20	4.62E-20	4.85E-20	4.02E-21	7.97E-23
				3.52E-20	4.63E-20	6.32E-20	-1.09E-22	-6.71E-25
				2.50E-19	2.72E-19	2.99E-19	8.64E-20	2.42E-20
				3.38E-20	4.44E-20	6.01E-20	-1.13E-22	-1.18E-24
					2.74E-20	2.42E-20	1.33E-21	
					2.01E-20	2.52E-20	-7.86E-24	
					2.30E-19	2.48E-19	6.00E-20	
					1.93E-20	2.40E-20	-3.26E-23	

REF	1.70E-21	4.52E-23
CMFD	5.52E-23	2.61E-25
pCMFD	7.05E-20	2.05E-20
1NCMFD	-4.37E-23	-2.82E-25

FIGURE 10 | Thermal group numerical adjoint flux for the KWU 2D problem.

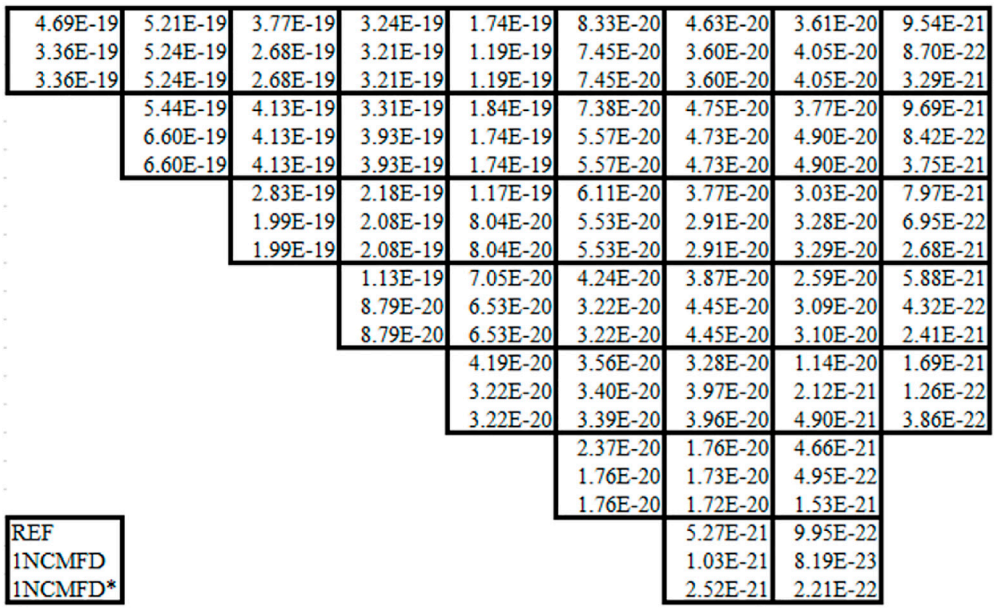

FIGURE 11 | One-node CMFD–based fast group numerical adjoint flux for the KWU 2D problem. The adjusted result is denoted with an asterisk (*).

performed by imposing a node size of 10 cm, where reduction in the adjoint flux error is observed for both CMFD and one-node CMFD (1NCMFD) cases as depicted in **Figure 7**.

KWU 2D Benchmark Problem

The KWU PWR 2D benchmark problem has been considered while excluding the presence of soluble boron under fully rodded conditions (Benchmark Source Situation, 1985). The configuration of the reactor problem is given in **Figure 8** alongside four different positions for imposing localized perturbation in the absorption XS.

The attainment of reference adjoint flux was done in a similar fashion to that of *one-group reactor problem* while dividing each assembly into equally spaced 10,000 nodes (100 × 100 per assembly). **Table 4** juxtaposes the calculated multiplication factors, where the same values are obtained regardless of the CMFD acceleration schemes as expected. Note that each assembly was taken as a single node during the CMFD accelerated nodal calculation.

The acquired numerical adjoint fluxes for both fast and thermal groups are shown in **Figures 9**, **10**, where pCMFD-based results do not conform with the other results. In addition, negative adjoint flux values (red color) are observed for the thermal group adjoint flux in the peripheral regions as depicted in **Figure 10**, where the surface flux attained from the NEM kernel calculation was directly utilized for one-node CMFD acceleration, i.e., no correction was made for acquisition of correction factors.

In order to stifle the occurrence of negative adjoint flux as shown in **Figure 10**, the surface flux was adjusted as follows to alter the correction factor to be zero when one of **Eqs 28**, **29** is met during a one-node CMFD calculation. The resulting numerical adjoint is illustrated in **Figures 11**, **12**, where no negative values are observed:

$$\bar{\phi}_s^{ref} = -\frac{1}{2}\cdot\frac{\Delta x_i\,\bar{J}_{i,i+1}^{ref}}{D_i} + \bar{\phi}_i \;\; for\; \hat{D}_i^R \tag{32}$$

$$\bar{\phi}_s^{ref} = \frac{1}{2}\cdot\frac{\Delta x_{i+1}\,\bar{J}_{i,i+1}^{ref}}{D_{i+1}} + \bar{\phi}_{i+1} \; for\; \hat{D}_{i+1}^L \tag{33}$$

For a systematic comparison between the numerical adjoint fluxes, the first-order perturbation theory was utilized, where assessment in the change of reactivity was made and compared with the reference value. Note that the reference reactivity change was evaluated via a direct solution of the perturbed system. The reactivity change can be estimated as follows:

$$\Delta\rho = \frac{\int_0^\infty \int_V dEdV\phi_0^\dagger(\mathbf{r},E)\,(\lambda_0\Delta\mathbf{F}-\Delta\mathbf{M})\phi_0(\boldsymbol{r},E)}{\int_0^\infty \int_V dEdV\phi_0^\dagger(\mathbf{r},E)\mathbf{F}_0\phi_0(\mathbf{r},E)} \tag{34}$$

where λ denotes the reciprocal of multiplication factor, F and M represent augmented fission and migration operators, respectively, and all the other notations are those of the convention.

Four different perturbation scenarios are envisaged as shown in **Figure 8**, where a change in the absorption XS was locally imposed (yellow colored assemblies). The extent of variation in the XS compared to its original value was set to be 30% for cases 1 to 3 and 80% for case 4. Two different adjoint fluxes are considered for the one-node CMFD method, namely, the original and the adjusted one. Note that the former result is subjected to a negative value issue. The calculated results are enumerated from **Tables 5**–**8**.

Where the asterisk denotes the adjusted one-node CMFD numerical adjoint and UNIFORM indicates the usage of unit vector while estimating reactivity change according to the first-

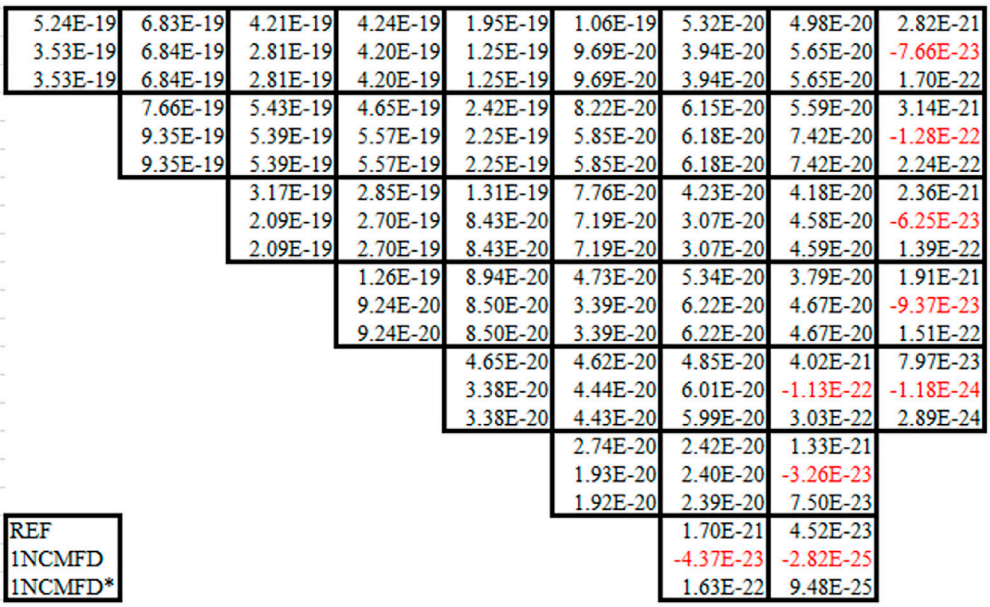

FIGURE 12 | One-node CMFD–based thermal group numerical adjoint flux for the KWU 2D problem. The adjusted result is denoted with an asterisk (*).

order perturbation theory. It could be observed that the exploitation of one-node CMFD–based adjoint flux renders the estimation to be more accurate compared to other approaches. Especially, for the perturbation in the reflector region, i.e., case 4, only the negative adjoint flux issue–resolved one-node CMFD exhibits a reliable result.

CONCLUSION

In this work, attributes of numerical adjoint fluxes that are obtained from various CMFD-based acceleration methods, e.g., conventional CMFD, pCMFD, and one-node CMFD, are investigated alongside a thorough mathematical description. It is noteworthy to mention that one-node CMFD formulation was employed under the two-node configuration, i.e., not in a parallelized manner. With the exploitation of the NEM kernel, the CMFD correction factors that are introduced in the migration operator matrix render such a matrix to be non-self-adjoint for all the presented CMFD acceleration schemes. Especially, it was found that the pCMFD-based numerical adjoint flux cannot retain the self-adjoint feature of a migration operator regardless of its mesh size, insinuating its inherent limitation for acquiring a reliable estimation for adjoint information. In addition, the occurrence of negative adjoint flux values was encountered for both conventional CMFD and one-node CMFD methods, which result in an erroneous reactivity estimation when employed as a weighting function for the first-order perturbation theory.

Mathematically, the preservation of net current information is independent of the choice of surface flux value if it is consistently applied for the generation of correction factors regarding the one-node CMFD method under the two-node configuration. Nevertheless, the magnitude of such correction factors, which has a unit of length, must not exceed the given diffusion coefficient to prevent encountering negative adjoint flux values. Hence, an adjustment scheme in the surface flux to circumvent such an issue while deducing the correction factors was proposed regarding the one-node CMFD method. A systematic analysis based on the first-order perturbation theory vividly attests to the effectiveness of employing the adjusted one-node CMFD–based numerical adjoint flux concerning a localized perturbation where a negative adjoint flux originally appeared. The stability analysis for the proposed surface flux–adjusted one-node CMFD acceleration scheme will be deliberated in the near future.

DATA AVAILABILITY STATEMENT

The original contributions presented in the study are included in the article/Supplementary Material, and further inquiries can be directed to the corresponding author.

AUTHOR CONTRIBUTIONS

TO wrote the first draft of the manuscript. TO and YK contributed to conception and design of the study. YK provided overall supervision.

FUNDING

This work was supported by the National Research Foundation of Korea Grant funded by the Korean government (NRF-2016R1A5A1013919) and BK21 FOUR (Fostering Outstanding Universities for Research; project No. 4120200313637).

REFERENCES

Benchmark Source Situation (1985). *Tech. Rep. ANL-7416*. Argonne, IL: National Energy Software Center.

Cho, N. Z., Lee, G. S., and Park, C. J. (2003). *On a New Acceleration Method for 3D Whole-Core Transport Calculations*. Sasebo: Annual Meeting of the Atomic Energy Society of Japan.

Downar, T., Xu, Y., and Seker, V. (2009). *PARCS NRC Core Neutronics Simulator THEOTY MANUAL*. Ann Arbor, MI.

Hong, S. G., and Cho, N. Z. (1995). Mathematical Adjoint Solution to the Analytic Expansion Nodal (AFEN) Method. *J. Korean Nucl. Soc.* 27, 374–384.

Lawrence, R. D. (1984). Perturbation Theory within the Framework of a Higher-Order Nodal Method. *Trans. Am. Nucl. Soc.* 46, 402.

Lewins, J. (1965). *'IMPORTANCE: The Adjoint Function'*. Oxford: Pergamon Press.

Müller, E. (2014). On the Non-uniqueness of the Nodal Mathematical Adjoint. *Ann. Nucl. Energ.* 64, 333–342. doi:10.1016/j.anucene.2013.10.019

Ott, K. O., and Neuhold, R. J. (1985). *Introductory Nuclear Reactor Dynamics*. American Nuclear Society.

Shin, H. C., and Kim, Y. (1999). *A Nonlinear Combination of CMFD and FMFD Methods*. Pohang: Proceedings of Korean Nuclear Society Spring Meeting.

Smith, K. S. (1983). Nodal Method Storage Reduction by Nonlinear Iteration. *Trans. Am. Nucl. Soc.* 44, 265.

Conflict of Interest: The authors declare that the research was conducted in the absence of any commercial or financial relationships that could be construed as a potential conflict of interest.

Publisher's Note: All claims expressed in this article are solely those of the authors and do not necessarily represent those of their affiliated organizations, or those of the publisher, the editors, and the reviewers. Any product that may be evaluated in this article, or claim that may be made by its manufacturer, is not guaranteed or endorsed by the publisher.

Copyright © 2022 Oh and Kim. This is an open-access article distributed under the terms of the Creative Commons Attribution License (CC BY). The use, distribution or reproduction in other forums is permitted, provided the original author(s) and the copyright owner(s) are credited and that the original publication in this journal is cited, in accordance with accepted academic practice. No use, distribution or reproduction is permitted which does not comply with these terms.

frontiers | Frontiers in Energy Research

ORIGINAL RESEARCH
published: 20 April 2022
doi: 10.3389/fenrg.2022.864821

Scalability of Nek5000 on High-Performance Computing Clusters Toward Direct Numerical Simulation of Molten Pool Convection

Boshen Bian[1]*, *Jing Gong*[2] and *Walter Villanueva*[1]

[1]Division of Nuclear Power Safety, Royal Institute of Technology (KTH), Stockholm, Sweden, [2]EuroCC National Competence Center Sweden (ENCCS), Uppsala University, Uppsala, Sweden

In a postulated severe accident, a molten pool with decay heat can form in the lower head of a reactor pressure vessel, threatening the vessel's structural integrity. Natural convection in molten pools with extremely high Rayleigh (Ra) number is not yet fully understood as accurate simulation of the intense turbulence remains an outstanding challenge. Various models have been implemented in many studies, such as RANS (Reynolds-averaged Navier–Stokes), LES (large-eddy simulation), and DNS (direct numerical simulation). DNS can provide the most accurate results but at the expense of large computational resources. As the significant development of the HPC (high-performance computing) technology emerges, DNS becomes a more feasible method in molten pool simulations. Nek5000 is an open-source code for the simulation of incompressible flows, which is based on a high-order SEM (spectral element method) discretization strategy. Nek5000 has been performed on many supercomputing clusters, and the parallel performance of benchmarks can be useful for the estimation of computation budgets. In this work, we conducted scalability tests of Nek5000 on four different HPC clusters, namely, JUWELS (Atos Bullsquana X1000), Hawk (HPE Apollo 9000), ARCHER2 (HPE Cray EX), and Beskow (Cray XC40). The reference case is a DNS of molten pool convection in a hemispherical configuration with Ra = 10^{11}, where the computational domain consisted of 391 million grid points. The objectives are (i) to determine if there is strong scalability of Nek5000 for the specific problem on the currently available systems and (ii) to explore the feasibility of obtaining DNS data for much higher Ra. We found super-linear speed-up up to 65536 MPI-rank on Hawk and ARCHER2 systems and around 8000 MPI-rank on JUWELS and Beskow systems. We achieved the best performance with the Hawk system with reasonably good results up to 131072 MPI-rank, which is attributed to the hypercube technique on its interconnection. Given the current HPC technology, it is feasible to obtain DNS data for Ra = 10^{12}, but for cases higher than this, significant improvement in hardware and software HPC technology is necessary.

Keywords: direct numerical simulation, internally heated natural convection, Nek5000, high-performance computing, scalability

OPEN ACCESS

Edited by:
Jun Wang,
University of Wisconsin-Madison, United States

Reviewed by:
Vitali Morozov,
Argonne Leadership Computing Facility (ALCF), United States
Luteng Zhang,
Chongqing University, China

***Correspondence:**
Boshen Bian
boshen@kth.se

Specialty section:
This article was submitted to Nuclear Energy, a section of the journal Frontiers in Energy Research

Received: *28 January 2022*
Accepted: *21 March 2022*
Published: *20 April 2022*

Citation:
Bian B, Gong J and Villanueva W (2022) Scalability of Nek5000 on High-Performance Computing Clusters Toward Direct Numerical Simulation of Molten Pool Convection. Front. Energy Res. 10:864821. doi: 10.3389/fenrg.2022.864821

INTRODUCTION

In a postulated severe accident scenario of a light water reactor, the reactor core can melt down and relocate to the lower head of the reactor pressure vessel. Due to the decay heat and oxidation, the debris, also called corium, can form a molten pool with heat fluxes that can threaten the integrity of the pressure vessel. One of the strategies to keep the corium inside the pressure vessel by maintaining the vessel's structural integrity is called in-vessel retention (IVR), which is performed by cooling the external surface of the lower head. To ensure the success of the IVR strategy (Fichot et al., 2018; Villanueva et al., 2020; Wang et al., 2021), it is crucial to analyze the heat flux distribution imposed by the corium on the vessel. First, the heat fluxes must not exceed the given critical heat flux (CHF) of the vessel. Second, such heat flux distributions can be used to assess the structural response of the vessel.

Numerous studies have been conducted on the molten pool simulation, both experimentally (Asfia and Dhir, 1996; Bernaz et al., 1998; Sehgal et al., 1998; Helle et al., 1999; Fluhrer et al., 2005) and numerically (Shams, 2018; Whang et al., 2019; Dovizio et al., 2022). However, many challenges remain in the numerical simulation of molten pool convection. One of them is to properly reproduce the intensive turbulence caused by the strong heat source inside the molten pool. **Figure 1** shows the observation of thermo-fluid behavior of the BALI molten pool experiment (Bernaz et al., 1998). It is shown that the flow domain can be divided into three regions. Turbulent Rayleigh–Bénard convection (RBC) cells are observed in the upper part of the fluid domain. The second region is the damped flow in the lower part of the domain, where the flow is mainly propelled by shear forces. The third is the flow that descends along the curved wall, which is known as the ν-phenomenon (Nourgaliev et al., 1997).

The Reynolds-averaged Navier–Stokes (RANS) models are commonly utilized to model turbulent flows (Chakraborty, 2009). However, Dinh and Nourgaliev pointed out that RANS models such as the $k-\varepsilon$ model are not suitable for modeling the turbulent natural convection flow (Dinh and Nourgaliev, 1997) because the thermo-fluid behavior in the molten pool is characterized as internally heated (IH) natural convection, which is different from the force convection flow. Large-eddy simulation (LES) has also been implemented to simulate molten pool convection, but more qualification and quantification are needed (Zhang et al., 2018). On the other hand, direct numerical simulation (DNS) can provide the most accurate simulation results because it does not have assumption models on the turbulence flows (Grötzbach and Wörner, 1999; Yildiz et al., 2020). But, it requires much more computational results than those of the RANS and LES models. Recently Bian et al. (2022a), Bian et al. (2022b) conducted a DNS of molten pool convection with Rayleigh number $Ra = 10^{11}$ in a hemispherical configuration using an open-source code Nek5000 (Fischer et al., 2016). The results of the thermo-fluid behavior, shown in **Figures 2** and **3**, are consistent with the observations in the BALI experiment, which are the RBC flow in the upper region, the damped flow in the lower region that facilitates thermal stratification, and the descending flow on the curved region that effectively transfer heat to the bottom. Although the Rayleigh number in this case (which is already the highest Ra value to date in a hemispherical geometry) is significantly less than the prototypic value of 10^{16}–10^{17}, the DNS data can offer valuable information on the thermo-fluid behavior of internally heated molten pools. In addition, it can serve as reference data for the assessment of RANS and LES models, such as the turbulent quantities that cannot be obtained from experiments. However, if DNS data can be generated for even higher Rayleigh numbers, better insights and understanding can be attained relevant to the prototypic case. It is important to note, though, that the higher the Rayleigh number, the required computational resources for a DNS calculation rise exponentially. Hence, such calculations must use high-performance computing (HPC) systems, which can also support the computational tool of choice. In this study, we explore the feasibility of obtaining DNS data for higher Ra numbers using Nek5000.

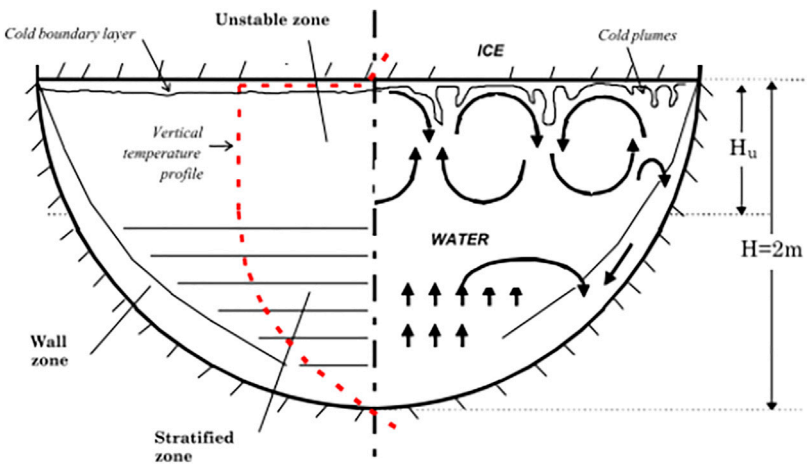

FIGURE 1 | General flow observations in BALI experiments (Bernaz et al., 1998).

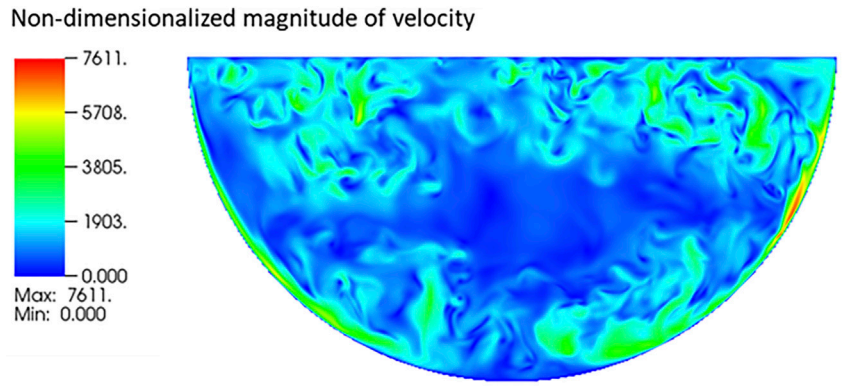

FIGURE 2 | Instantaneous distribution of the magnitude of the velocity of an internally heated natural convection with Ra = 10^{11} (Bian et al., 2022).

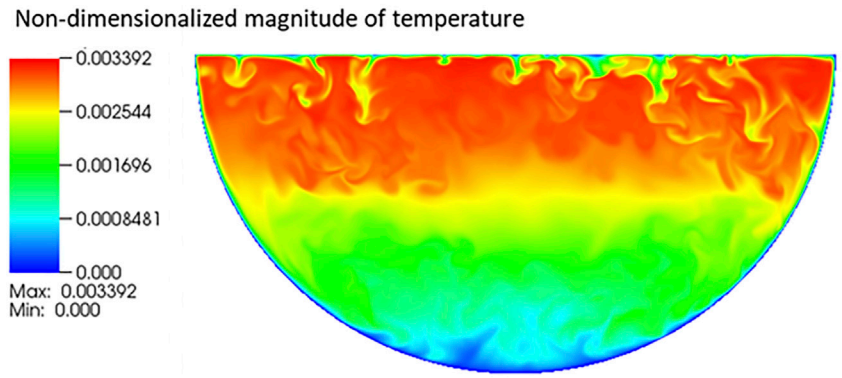

FIGURE 3 | Instantaneous temperature distribution of an internally heated natural convection with Ra = 10^{11} (Bian et al., 2022).

Nek5000 is an open-source computational fluid dynamics (CFD) code with spatial discretization based on the spectral element method (SEM), which features scalable algorithms to be faster and more efficient. Goluskin et al. (2016) conducted a series of DNS simulations of internally heated natural convection with different Rayleigh numbers in a box geometry using Nek5000. We also used Nek5000 to analyze molten pool convection in different geometries (Bian et al., 2022). Since the DNS works usually demand large computational resources, it is necessary to compute the budget based on the scalability performance of the code. Recently, few scalability tests of Nek5000 have been performed by Fischer et al., (2015); Fischer et al., (2015); Offermans et al., (2016); Merzari et al., (2016); Merzari et al., (2020) analyzing the algorithms for performance characteristics on large-scale parallel computers. Offermans et al. (2016) discussed in detail the scalability of pipe flow simulations on Petascale systems with CPUs. Furthermore, Merzari et al. (2016) compared the LES with RANS calculations for a wire-wrapped rod bundle. In addition, Merzari et al. (2020) studied the weak scaling performances for Taylor–Green vortex simulation on a heterogenous system (Summit at Oak Ridge National Laboratory).

In this study, we perform scalability tests of Nek5000 based on the molten pool simulation using four different high-performance computing (HPC) clusters, namely, JUWELS[1], ARCHER2[2], Hawk[3], and Beskow[4]. The objective of this work is two-fold. The first is to determine if there is strong scalability of Nek5000 for molten pool natural convection on the available HPC systems. This is carried out by running the benchmark case having a specific Ra number with different MPI ranks. The second is to explore the feasibility of obtaining DNS data for much higher Ra number. In the following, **Section 2** gives a description of the benchmark case and the governing equations. **Section 3** briefly introduces the discretization scheme in Nek5000 and presents the mesh used in the simulations. **Section 4** illustrates the scalability result of the benchmark tests on the four different HPC clusters and estimates the feasibility of performing DNS of molten pool convection at extremely high

[1]https://www.fz-juelich.de/ias/jsc/EN/Expertise/Supercomputers/JUWELS/JUWELS_news.html
[2]https://www.archer2.ac.uk/
[3]https://kb.hlrs.de/platforms/index.php/HPE_Hawk
[4]https://www.pdc.kth.se/hpc-services/computing-systems/beskow-1.737436

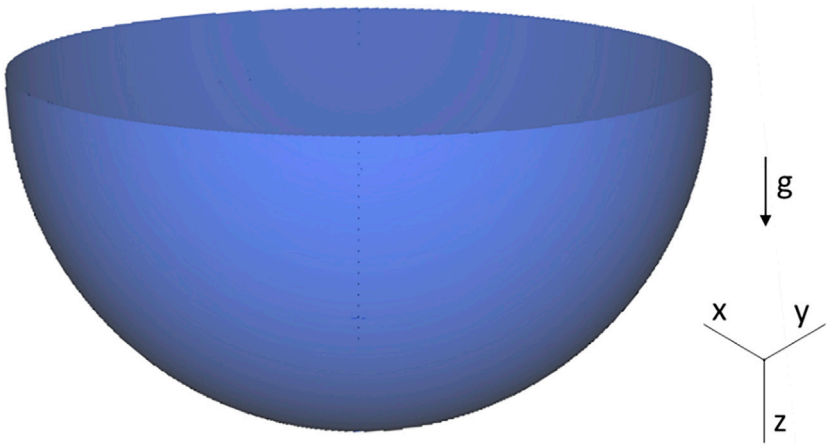

FIGURE 4 | Computational domain.

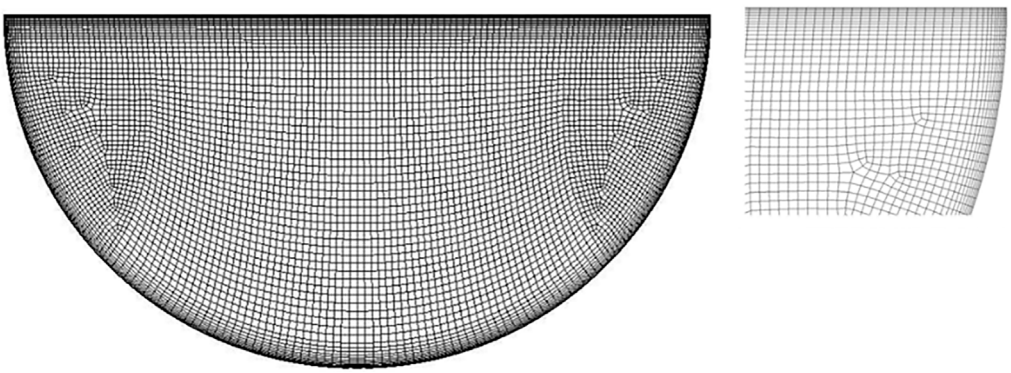

FIGURE 5 | Mesh on a middle slice of the computational domain.

Rayleigh numbers. Finally, the concluding remarks are given in **Section 5**.

BENCHMARK CASE

In this work, a DNS simulation of the internally heated molten pool in the hemispherical domain is selected as the benchmark case for the scalability test. The 3D hemispherical cavity is shown in **Figure 4**, which represents the lower head of the reactor pressurized vessel. The cavity contains two no-slip boundaries, the top wall and the curved wall. The isothermal condition is specified on the boundaries. To simulate the decay heat effect in the corium, a homogenous volumetric heat source is arranged inside the domain. The gravity field is parallel with the vertical z-direction, as shown in **Figure 4**. The thermo-fluid behavior in the molten pool is characterized as an internally heated natural convection where the flow motion is propelled by buoyancy force induced by the density difference of the fluid due to the internal heat source.

The Oberbeck–Boussinesq approximation (Oberbeck, 1879; Rajagopala et al., 2009) is commonly used to model the natural convection, which is mainly propelled by the buoyancy force. With this approximation, the density variation of the fluid is assumed to only depend on the change of temperature such that

$$\frac{\rho - \rho_*}{\rho_*} = -\beta(T - T_*),$$

where ρ is the density, ρ_* is the reference density at the reference temperature T_*, and β is the expansion coefficient. Incorporating this assumption, the governing equations of the thermo-fluid behavior are given below (Goluskin, 2016)

$$\nabla \cdot \boldsymbol{u} = 0,$$
$$\frac{\partial \boldsymbol{u}}{\partial t} + \boldsymbol{u} \cdot \nabla \boldsymbol{u} = -\frac{1}{\rho_*}\nabla p + \nu \nabla^2 \boldsymbol{u} + g\beta T\vec{z},$$
$$\frac{\partial T}{\partial t} + \boldsymbol{u} \cdot \nabla T = k\nabla^2 T + \frac{Q}{\rho_* c_p},$$

where $\boldsymbol{u}$, p, and T are the velocity, pressure, and temperature field, respectively. The parameters ν, g, k, and c_p are the kinematic viscosity, gravity acceleration, thermal diffusivity, and thermal capacity, respectively. The first one is the mass equation which

TABLE 1 | Summary of key simulation parameters.

Rayleigh number	1×10^{11}
Prandtl number	0.8
Element number	~764 K
Number of grid points	~391 M
Polynomial order	7
Target CFL	3.6
Maximum timestep	1×10^{-6}

controls the divergence free of the incompressible flow. The second equation is the momentum equation which solves the flow motion within the molten pool. On the right hand, the terms represent the pressure, shear and buoyancy effect, respectively. The last equation is the energy equation which solves the temperature field, and the terms on the right hand are the diffusive term and heat source term. To generalize the problem, the equations can be normalized using a characteristic length $l\,[m]$, time scale $\frac{l^2}{\alpha}\,[s]$, and temperature scale $\Delta = \frac{l^2 Q}{\alpha \rho_* c_p}\,[K]$. The normalized equations of the molten pool convection are shown below

$$\nabla \cdot \boldsymbol{u}^* = 0.$$

$$\frac{\partial \boldsymbol{u}^*}{\partial t^*} + \boldsymbol{u}^* \cdot \nabla \boldsymbol{u}^* = -\nabla p* + \mathrm{Pr}\nabla^2 \boldsymbol{u}^* + Ra\mathrm{Pr}T^*\vec{z}.$$

$$\frac{\partial T^*}{\partial t^*} + \boldsymbol{u}^* \cdot \nabla T^* = \nabla^2 T^* + 1.$$

In the equations, the variables with the star notation are the corresponding nondimensional fields. There are two nondimensional numbers in the normalized equation, namely, the Rayleigh number $Ra = \frac{g\beta l^3 \Delta}{\alpha \nu}$ and the Prandtl number $\mathrm{Pr} = \frac{\nu}{\alpha}$. The Rayleigh number indicates the ratio of the fluid inertial force to the viscous force, which can be treated as the primary control number of the IH natural convection. When the Rayleigh number increases, the natural convection will first change from laminar flow to turbulent flow and the intensity of the turbulence will become stronger. Therefore, with the larger Rayleigh number, more detail of the flow need to be solved in the DNS simulations, and correspondingly larger resources are required. The Prandtl number is a material-dependent parameter, representing the ratio of momentum diffusion to heat diffusion.

NUMERICAL SETTINGS

The equations are solved using Nek5000, which is based on the SEM discretization method. The SEM can be treated as the combination of the finite element method (FEM) and spectral method (SM), which absorbs both the generality of the former and the accuracy of the latter. When using the SEM, the computational domain will be divided into elements, similar to the FEM. Within each element, the SEM is implemented in such a manner that unknown in each element can be represented by using a chosen function space and the weights on the collocation points in the element. In Nek5000, for the convenience of numerical integration, the Gauss–Legendre–Lobatto (GLL) points are used as the collocation points. In this study, the Pn–Pn method (Tomboulides et al., 1997; Guermond et al., 2006) is selected as the solver for the governing Navier–Stokes equations in Nek5000, and the time discretization method is an implicit–explicit BDFk-EXTk (backward difference formula and EXTrapolation of order k). The Helmholtz solver is used for the passive scalar equation. Details about the discretization of the governing equations can be found in the theory guide of Nek5000 (Deville et al., 2002).

When generating the DNS mesh of the IH natural convection in the molten pool, the smallest dissipation length scale of both the bulk flow and boundary layer should be considered, which puts the highest restriction on the computational effort. In a turbulence natural convection, the mesh requirement depends on the Rayleigh number and the Prandtl number (Shishkina et al., 2010). A Rayleigh number of 10^{11} is set in this study. If the Rayleigh number increases by 10, the mesh resolution should also practically increase by 10. It should be mentioned that the computational domain comprises elements in Nek5000, and the elements are divided by the GLL grid points on the element edges according to the polynomial order. In this case, it is the distance between adjusting grid points that satisfy the mesh size.

After the pre-estimation of the DNS mesh, the total element number in the computational domain is about 764K. The mesh on a sample middle plane is shown in **Figure 5**, and it is shown that the boundary layers have been refined. In this approach, the polynomial order or the order of the function space used is 7, which yields a total of 391M GLL grid points in the whole domain. The overall settings of the simulation are listed in **Table 1**. A quasi-steady state is first established, which means that an energy balance of the system has been attained. After that, we conduct the scalability tests starting from the steady-state simulations on the four different HPC clusters.

BENCHMARK TESTS

We performed the benchmark tests on three different European Petascale systems, namely, JUWELS at Julich Supercomputing Centre, ARCHER2 at EPCC, the University of Edinburgh, and Hawk at HLRS High-Performance Computing Center Stuttgart, as shown in **Table 2**. JUWELS is an Intel Xeon–based system and has a total of 2,271 compute nodes with Intel processors. The interconnect used is a Mellanox InfiniBand EDR fat-tree network. ARCHER2 is an HPE Cray EX system and has 5,860 compute nodes with AMD processors. The HPE Cray slingshot with 2x100 Gbps bi-directional per node is used as the interconnection. Hawk is an HPE Apollo 9000 system and has 5,632 AMD EPYC compute nodes. The interconnect is InfiniBand HDR200 with a bandwidth of 200 Gbit/s and an MPI latency of ~1.3us per link. In addition to the EU Petascale systems, the Beskow cluster at KTH PDC is also used. It is a Cray XC40 system based on Intel Haswell and Broadwell processors and Cray Aries interconnect technology. The cluster has a total of 2,060 compute nodes.

The corresponding software, including compilers and MPI libraries on these systems, is presented in **Table 3**. On ARCHER2,

TABLE 2 | HPC systems overview.

	JUWELS	Archer2	Hawk	Beskow
Peak performance	73 Pflops	28 Pflops	26 Pflops	2.44 Pflops
Total number of compute nodes	2271	5860	5632	2060
Compute node	2x 24 core Intel Xeon Platinum 8168@2.7 GHz CPU	2x64 core AMD EPYC 7742@2.25 GHz processors	2 x 64 core AMD EPYC 7742 @2.25GHz processors	2x Intel Hasell Xeon E5-2698v3@2.3 GHz
Memory	96 GB	256 GB	256 GB	64 GB
Interconnection	InfiniBand EDR with fat-tree network	HPC Cray Slingshot with 2x100 Gbps bi-direction per node	InfiniBand HDR200 with 9-dimensional hypercube	Cray Aries with dragonfly topology
Queue system	SLURM	SLURM	PBS	SLURM
Location	Jülich, Germany	EPCC, UK	HLRS, Germany	PDC, Sweden

TABLE 3 | Overview of the software environment of the HPC systems.

System	Operating system	Compiler	MPI libraries
JUWELS	CentOS v8.4	Intel v2021.2.0	ParaStationMPI v5.4.10
ARCHER2	SUSE v15.1	Cray CCE v11.0.4	Cray MPICH v8.1.4
Hawk	CentOS v8.4	GCC v9.2.0	HPE MPI MPT v2.23
Beskow	SUSE v15.1	Intel v18.0.0.128	Cray MPICH v7.7.14

TABLE 4 | Overview of latencies and bandwidths on the systems used.

	T_a (μs)	α	β
JUWELS	$1.4 \cdot 10^{-4}$	26925	8.9
ARCHER2	$7.3 \cdot 10^{-5}$	11866	2.9
Hawk	$9.3 \cdot 10^{-5}$	23161	3.5
Beskow	$1.5 \cdot 10^{-4}$	17000	5.5

the compiler flags for AMD CPU architectures have been loaded by default using the module *"craype-x86-rome"*. The default compiler flags *"-march = znver2 –mtune = znver2 –O3"* for GCC has been adapted to AMD CPU architectures on Hawk. Only pure MPI runs are performed on fully occupied nodes for all systems, and even using few cores per node used can accelerate the performances for general CFD applications, that is, one MPI process is used per core on the node.

One linear interprocessor communication model has been developed by Fischer et al. (2015),

$$T_c(m) = (\alpha + \beta m) T_a,$$

where T_c is the communication time, α and β are two dimensionless parameters, m is the message length, and T_a is the inverse of the observed flop rate. We used the model to measure the latencies and bandwidths on these systems. The latencies and bandwidths for a word with 64-bit length for these systems using 512 MPI-rank are presented in **Table 4**.

The benchmark case consists of 763,904 elements with the 7th polynomial order. The total number of grid points is around 391 million. We run the case with different MPI-ranks up to 1,000 steps. The speed-up for the strong scalability tests is measured following the same method used by Offermans et al. (2016). In addition, we only consider the execution times during the time-integration phase without I/O operations.

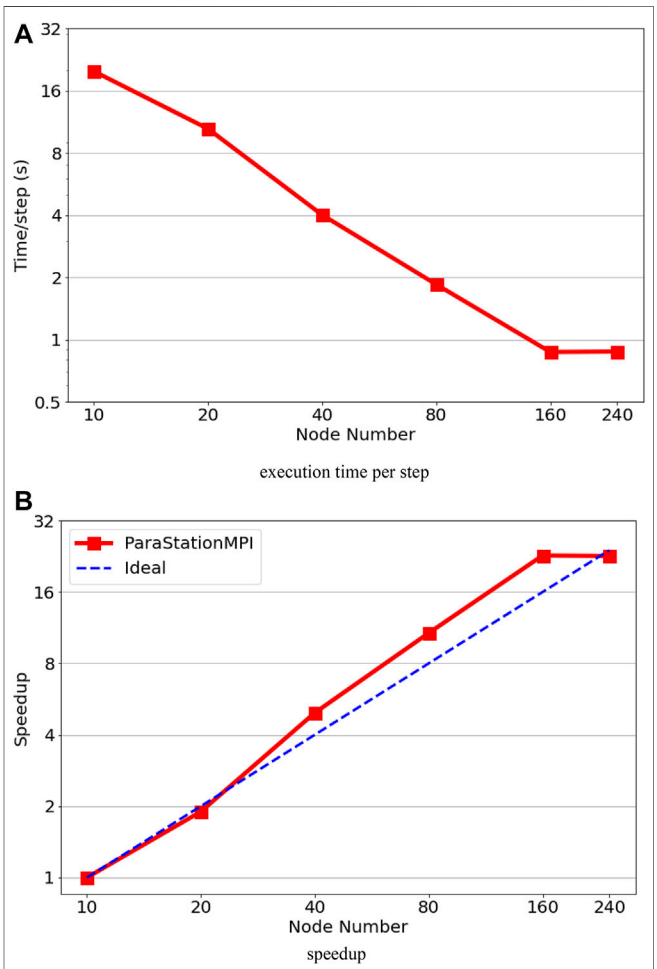

FIGURE 6 | Performance results on the JUWELS system. **(A)** Execution time per step. **(B)** Speedup.

Figures 6A,B shows the execution time in second per step and speedup on the JUWELS cluster. The test was performed from 480 MPI-rank (i.e., fully occupied 10 nodes) to 11520 MPI-rank (i.e., fully occupied 240 nodes). The maximum speed-up of 20.5 can be achieved with 160 nodes (7680 MPI-rank), and then the performance becomes worse with increase in the number of node number. We observe super-linear speedup with increasing

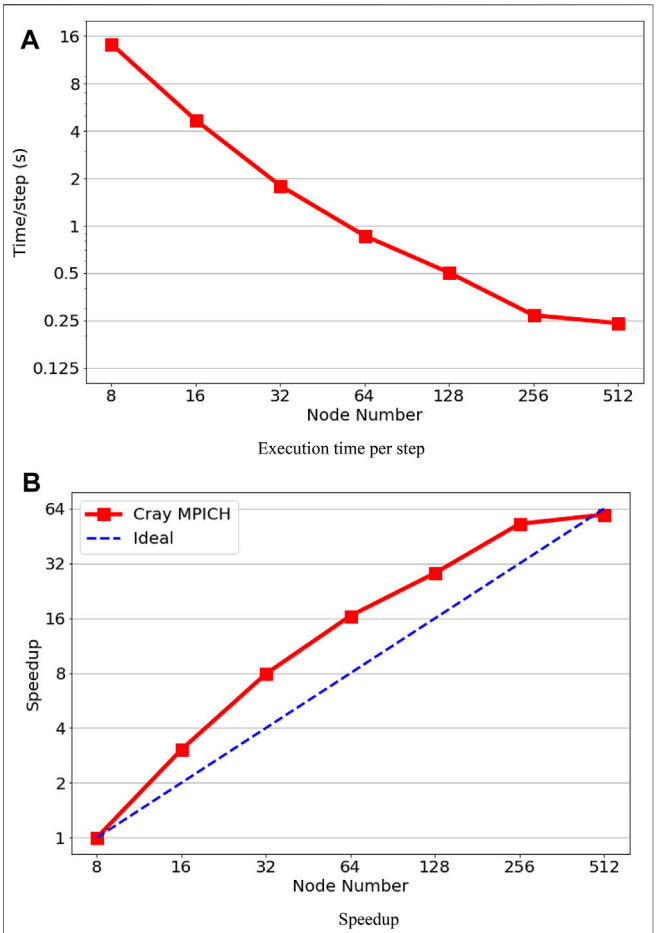

FIGURE 7 | Performance results on the ARCHER2 system. **(A)** Execution time per step. **(B)** Speedup.

number of MPI-rank until 7680 MPI-rank. The super-linear speedup is not surprising for Nek5000's strong scalability test due to cache memory usage and SIMD (simple instruction multiple data); for a more detailed analysis, see Offermans et al. (2016).

The performance results on ARCHER2 are presented in **Figures 7A,B**. We also observed a super-linear speedup on the AMD CPU based system. The execution time per step continually reduces from 8 nodes (1024 MPI-rank) to 256 nodes (32768 MPI-rank), and then the performance improves slightly with doubted MPI-rank to 65536. The performances are limited to around 8,000–16000 grid points. By comparing with MPI-rank on JUWELS, which is an Intel CPU–based system, the performance on the JUWELS system is better. However, we obtain better node-to-node performances and strong scaling on the ARCHER system.

The performance results on Hawk are shown in **Figures 8A,B**. By comparing with ARCHER2, we observe that the execution times per step are very similar to those on ARCHER2 using 8 nodes (1024 MPI-rank) to 256 nodes (32768 MPI-rank), mostly due to the factor that both systems have the same AMD CPUs. On the other hand, the performance can be sped up from 32768 to 65536 MPI-rank on Hawk, that is, the execution time per step reduces from 0.22 to 0.16 s. From the log files, we found that the main difference between the two systems is the communication time. A 9-dimensional enhanced hypercube topology is used for the interconnecting on Hawk, which means that less bandwidth is available if the dimension of the hypercube is higher (Dick et al., 2020). With 16 computer nodes connected to a common switch as one hypercube node, the case of 65536 MPI-rank with 512 nodes corresponds to 2^5 hypercube nodes (i.e., 5-dimensional binary cube topology). In addition, the gather–scatter operation in the Nek5000's crystal router for MPI global communication supports to exchange messages of arbitrary length between any nodes within a hypercube network (Fox et al., 1988; Schliephake and Larue, 2015). As a result, the required communication time can be reduced, especially for irregular applications.

The performance results on the Beskow cluster are shown in **Figure 9**. The test started from 64 nodes (2048 MPI-rank) due to the memory limitation (64GB RAM/node) on the compute nodes. Then the MPI-rank increases by 1024, and it is found that the execution time per time step achieves the minimum at 256 nodes (8192 MPI-rank), and the maximum speed-up here is 4.9. After 8192 MPI-rank, the performance becomes worse when

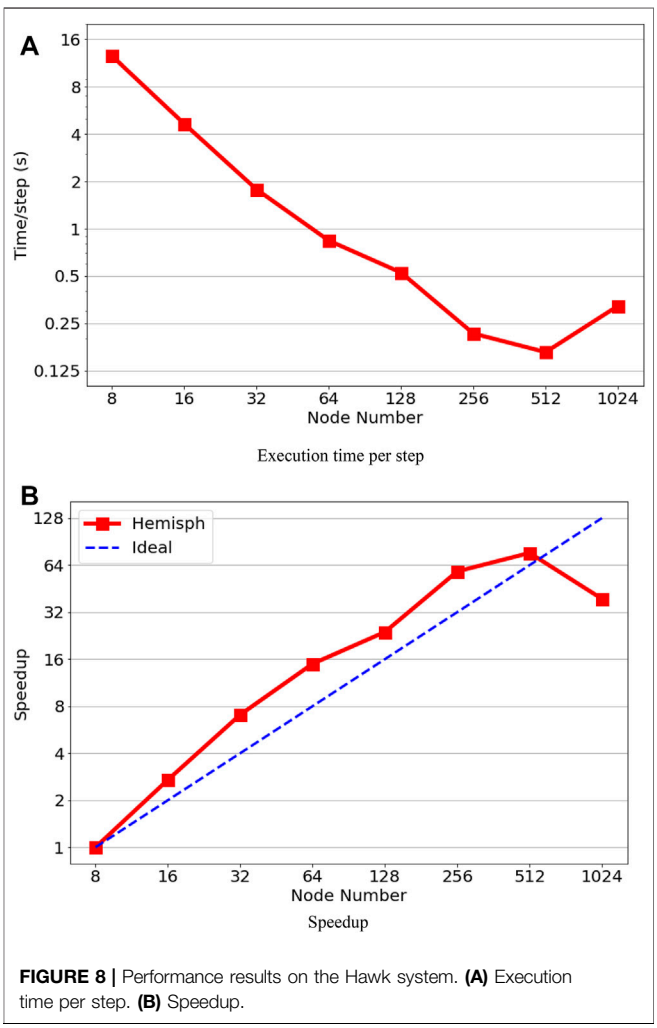

FIGURE 8 | Performance results on the Hawk system. **(A)** Execution time per step. **(B)** Speedup.

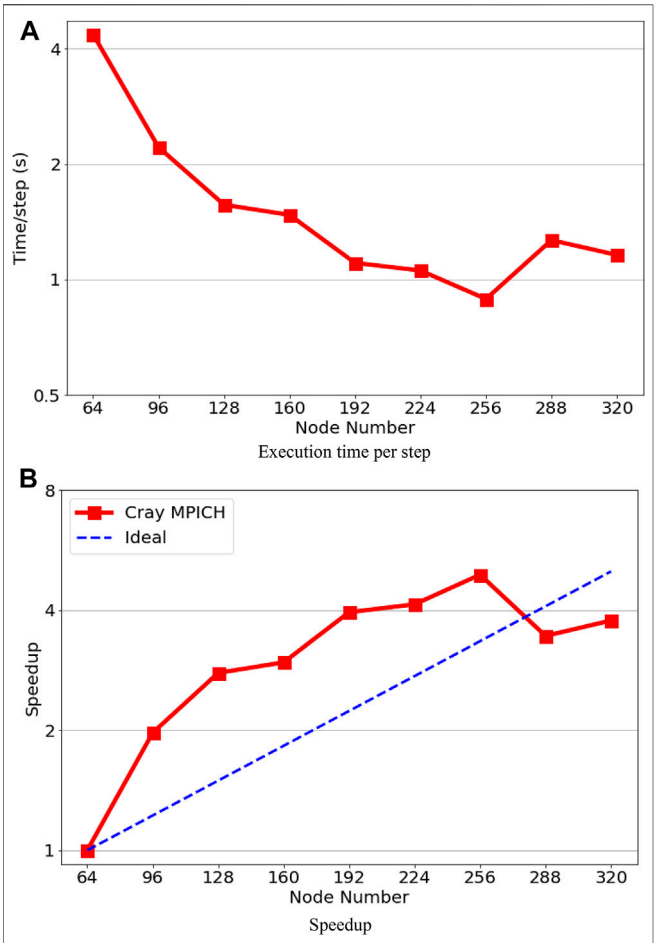

FIGURE 9 | Performance results on the Beskow system. **(A)** Execution time per step. **(B)** Speedup.

the MPI-rank continually increases. Like in previous systems, a super-linear performance has been observed on the Beskow cluster before the maximum speedup point.

In general, the benchmark case simulated using Nek5000 can achieve super-linear speed-up in all the tested HPC systems, although within certain MPI-rank ranges due to communication requirements (Offermans et al., 2016). The ARCHER2 and Hawk systems have the highest speed-up upper bound (65536 MPI rank), while Hawk has relatively smaller execution time per timestep than ARCHER2. The super-linear scalability means that one can save calculation time by increasing the MPI rank within the linear speed-up range. However, after the speedup limitation, the performance of the code would become worse and inefficient.

The case with Ra = 10^{11} in reaching a quasi-steady state took about 2M core-hour computational resources. This includes ramping up the Ra from 10^{10} to the target 10^{11}. Since the Rayleigh number of the prototypic corium or the prototypic molten pool experiments is higher than the benchmark case in this study, we need to consider the available computational resources of DNS simulations of the molten pool with higher Rayleigh numbers in the future. From the numerical aspect, when the Rayleigh number increases 10 times to 10^{12}, the mesh size of the computational domain is supposed to be 10 times. In addition, the velocity magnitude of the flow is expected to be $10^{1/2}$ times larger. If the CFL condition number is kept the same, the time step is then reduced to about 3% of the case with Rayleigh number 10^{11}. From the computed aspect, the required minimum MPI ranks for a certain simulation are limited by the maximum element number capacity on each core. By taking the ARCHER2 system as an example, the minimum MPI rank of the simulation with Ra = 10^{11} is 1024. When the Rayleigh number increases to 10^{12}, the minimum MPI rank should be 10240 because the total element number of the simulation becomes 10 times larger. Therefore, if the Rayleigh becomes 10^{12}, the whole simulation will require about 300 times core-hours than the original case, which is about 600M core-hours.

Practically, given the highest allocation that can be made available to any research group, which is in the order of 200M core-hours per year, the amount of time needed to reach a quasi-steady state at Ra = 10^{12} is estimated to be about 3 years. If this is again projected for an order of magnitude higher Rayleigh number, 10^{13}, with the required mesh, the amount of time needed is about 900 years. Hence, for the ultimate case of 10^{17}, such DNS is rendered unfeasible given the current technology. In the meantime, before the needed development of both hardware and software technology happens, we need to rely on less accurate models such as LES or RANS. However, these models need to be modified and verified with the help of available reference DNS data with the highest Ra.

To aim for DNS for Ra = 10^{12} to 10^{13}, exascale supercomputer systems with a capacity of more than 1 exaflops (10^{18} flops) will be required. However, all exascale supercomputers will be heterogenous systems with emerging architecture[5]. In this case, the GPU-based Nek5000 code, namely, NekRS (Fischer et al., 2021) must be utilized.

CONCLUSION

We have presented the scalability of Nek5000 on four HPC systems toward the DNS of molten pool convection. As low latencies of MPI communication and memory bandwidth are essential for CFD applications, the linear communication models for the four systems have been addressed. The case can be scaled up to 65536 MPI-rank on the Hawk and ARCHER2 systems. But, the best performance can be achieved on the Hawk system in comparison with the others. This is attributed to its lower latency in global communication and the hypercube technique that was used for the interconnection, which both accelerates the embedded crystal algorithm in Nek5000 for global MPI communication. Furthermore, we also observed that super-linear speed-up can be achieved using fewer MPI-ranks on both Intel and AMD CPUs.

For the reference case Ra = 10^{11}, current CPU-based Petascale systems are sufficient for obtaining DNS data using Nek5000. Depending on the resources available, the choice of MPI-rank to obtain the data as efficiently as possible can be guided by the

[5]https://eurohpc-ju.europa.eu

scalability of the specific system, as shown in this article. For an order of magnitude higher Ra, that is, 10^{12}, the required resources can readily increase two orders of magnitude. To obtain better efficiency, the relatively new GPU-based NekRS can also be used, but further development is needed, and sufficient GPU resources must be made available. For the prototypic Ra, about 10^{16} to 10^{17}, current HPC technology is not up to task in obtaining DNS data. In this case, less accurate LES or RANS should be used. However, such models must be verified with the help of available reference DNS data with the highest Ra, and possible modifications might be necessary.

DATA AVAILABILITY STATEMENT

The raw data supporting the conclusions of this article will be made available by the authors, without undue reservation.

AUTHOR CONTRIBUTIONS

BB: methodology, calculation, data processing, writing and review; JG: methodology, calculation, data processing, writing and review; WV: supervision, methodology, writing and review, funding and computer resources acquisition.

FUNDING

The funding support is partially from EU-IVMR Project No. 662157, Boshen Bian's PhD scholarship from China Scholarship Centre (CSC), the EuroCC project, which has received funding from the European Union's Horizon 2020 research and innovation program under Grant 951732, and the Swedish e-Science Research Center (SeRC) through the SESSI program.

ACKNOWLEDGMENTS

The authors would like to acknowledge the funding support from EU-IVMR. Boshen Bian appreciates the PhD scholarship from China Scholarship Centre (CSC). We also acknowledge DECI and PRACE projects for granting us access to the ARCHER2 system at EPCC, JUWELS system at JSC, and Hawk system at HLRS. Part of the computations was enabled on Beskow at PDC provided by the Swedish National Infrastructure for Computing (SNIC).

REFERENCES

Asfia, F. J., and Dhir, V. K. (1996). An Experimental Study of Natural Convection in a Volumetrically Heated Spherical Pool Bounded on Top with a Rigid wall. *Nucl. Eng. Des.* 163 (3), 333–348. doi:10.1016/0029-5493(96)01215-0

Bernaz, L., Bonnet, J. M., Spindler, B., and Villermaux, C. (1998). "Thermal Hydraulic Phenomena in Cerium Pools: Numerical Simulation with TOLBIAC and Experimental Validation with BALI," in OECD/CSNI Workshop on In-vessel Core Debris Retention and Coolability, Garching, Germany, March 3-6.

Bian, B., Villanueva, W., and Dovizio, D. (2022a). Direct Numerical Simulation of Molten Pool Convection in a 3D Semicircular Slice at Different Prandtl Numbers. *Nucl. Eng. Des.*.

Bian, B., Villanueva, W., and Dovizio, D. (2022b). Direct Numerical Simulation of Molten Pool Natural Convection in A Hemispherical Configuration. in Proceedings of the Ninth International Topical Meeting on Nuclear Reactor Thermal-Hydraulics, NURETH-19, Brussels, Belgium, March 6-11, 2022

Chakraborty, N. (2009). The Effects of Turbulence on Molten Pool Transport during Melting and Solidification Processes in Continuous Conduction Mode Laser Welding of Copper-Nickel Dissimilar Couple. *Appl. Therm. Eng.* 29, 3618–3631. doi:10.1016/j.applthermaleng.2009.06.018

Deville, M. O., Fischer, P. F., and Mund, E. H. (2002). *High-Order Methods for Incompressible Fluid Flow*. Cambridge: Cambridge University Press.

Dick, B., Bonisch, T., and Krischok, B. (2020). Hawk Interconnect Network. Available at: https://kb.hlrs.de/platforms/upload/Interconnect.pdf (Accessed January 20, 2022).

Dinh, T. N., and Nourgaliev, R. R. (1997). Turbulence Modelling for Large Volumetrically Heated Liquid Pools. *Nucl. Eng. Des.* 169, 131–150. doi:10.1016/s0029-5493(96)01281-2

Dovizio, D., Komen, E. M. J., Bian, B., and Villanueva, W. (2022). "RANS Validation of a Corium Pool in a Hemispherical," in Proceedings of the Ninth International Topical Meeting on Nuclear Reactor Thermal-Hydraulics, NURETH-19, Brussels, Belgium, March 6-11, 2022.

Fichot, F., Carénini, L., Villanueva, W., and Bechta, S. (2018). "A Revised Methodology to Assess In-Vessel Retention Strategy for High-Power Reactors," in Proceedings of the 26th International Conference on Nuclear Engineering (ICONE-26), London, UK, July 22-26. doi:10.1115/icone26-82248

Fischer, P., Heisey, K., and Min, M. (2015). "Scaling Limits for PDE-Based Simulation," in 22nd AIAA Computational Fluid Dynamics Conference, 22-26 June 2015, Dallas, TX (Du Page County: American Institute of Aeronautics and Astronautics).

Fischer, P., Kerkemeier, S., Min, M., Lan, Y., Phillips, M. T., Rathnayake, E. M., et al. (2021). *NekRS, a GPU-Accelerated Spectral Element Navier-Stokes Solver*. CoRR abs/2104.05829.

Fischer, P., Lottes, J., Kerkemeier, S., Marin, O., Heisey, K., Obabko, A., et al. (2016). *Nek5000: User's Manual*. Argonne National Laboratory.

Fluhrer, B., Alsmeyer, H., Cron, T., Messemer, G., Miassoedov, A., and Wenz, T. (2005). "The Experimental Programme LIVE to Investigate In-Vessel Core Melt Behaviour in the Late Phase," in Proceedings of Jahrestagung Kerntechnik 2005, Nürnberg, German, May 10 (INFORUM GmbH).

Fox, G. (1988). *Solving Problems on Concurrent Processors: General Techniques and Regular Problems* 1. Englewood Cliffs, NJ: Prentice-Hall.

Goluskin, D. (2016). *Internally Heated Convection and Rayleigh-Bénard Convection*. Cham: Springer Briefs in Thermal Engineering and Applied Science.

Goluskin, D., Van der Poeland Erwin, P. (2016). Penetrative Internally Heated Convection in Two and Three Dimensions. *J. Fluid Mech.* 791, R6. doi:10.1017/jfm.2016.69

Grötzbach, G., and Wörner, M. (1999). Direct Numerical and Large Eddy Simulations in Nuclear Applications. *Int. J. Heat Fluid Flow* 20 (3), 222–240. doi:10.1016/S0142-727X(99)00012-0

Guermond, J. L., Minev, P., and Shen, J. (2006). An Overview of Projection Methods for Incompressible Flows. *Comp. Methods Appl. Mech. Eng.* 195, 6011–6045. doi:10.1016/j.cma.2005.10.010

Helle, M., Kymäläinen, O., and Tuomisto, H. (1999). "Experimental COPO II Data on Natural Convection in Homogenous and Stratified Pools," in Proceedings of the Ninth International Topical Meeting on Nuclear Reactor Thermal-Hydraulics, NURETH-9, San Francisc, USA, October 3-8.

Merzari, E., Fischer, P., Min, M., Kerkemeier, S., Obabko, A., Shaver, D., et al. (2020). Toward Exascale: Overview of Large Eddy Simulations and Direct Numerical Simulations of Nuclear Reactor Flows with the Spectral Element Method in Nek5000. *Nucl. Tech.* 206, 1308–1324. doi:10.1080/00295450.2020.1748557

Merzari, E., Fischer, P., Yuan, H., Van Tichelen, K., Keijers, S., De Ridder, J., et al. (2016). Benchmark Exercise for Fluid Flow Simulations in a Liquid Metal Fast

Reactor Fuel Assembly. *Nucl. Eng. Des.* 298, 218–228. doi:10.1016/j.nucengdes.2015.11.002

Nourgaliev, R. R., Dinh, T. N., Sehgal, B. R., Nourgaliev, R. R., Dinh, T. N., and Sehgal, B. R. (1997). Effect of Fluid Prandtl Number on Heat Transfer Characteristics in Internally Heated Liquid Pools with Rayleigh Numbers up to 1012. *Nucl. Eng. Des.* 169 (1-3), 165–184. doi:10.1016/s0029-5493(96)01282-4

Oberbeck, A. (1879). Ueber die Wärmeleitung der Flüssigkeiten bei Berücksichtigung der Strömungen infolge von Temperaturdifferenzen. *Ann. Phys. Chem.* 243, 271–292. doi:10.1002/andp.18792430606

Offermans, N., Marin, O., Schanen, M., Gong, J., Fischer, P., and Schlatter, P. (2016). "On the strong Scaling of the Spectral Elements Solver Nek5000 on Petascale Systems," in Exascale Applications and Software Conference, EASC 2016, Stockholm, Sweden, April 25-29, 2016. article id a5.

Rajagopal, K. R., Saccomandi, G., and Vergori, L. (2009). On the Oberbeck-Boussinesq Approximation for Fluids with Pressure Dependent Viscosities. *Nonlinear Anal. Real World Appl.* 10, 1139–1150. doi:10.1016/j.nonrwa.2007.12.003

Schliephake, M., and Laure, E. (2015). "Performance Analysis of Irregular Collective Communication with the Crystal Router Algorithm," in Proceedings of the 2014 Exascale Applications and Software Conference, Cham: (Springer), 130–140. doi:10.1007/978-3-319-15976-8_10

Sehgal, B. R., Bui, V. A., Dinh, T. N., Green, J. A., and Kolb, G. (1998). "SIMECO Experiments on In-Vessel Melt Pool Formation and Heat Transfer with and without a Metallic Layer," in Proceedings of the OECD/CSNI Workshop, Garching, Germany, March 3-6.

Shams, A. (2018). Towards the Accurate Numerical Prediction of thermal Hydraulic Phenomena in Corium Pools. *Annals Nucl. Energ.* 117117, 234234–246246. doi:10.1016/j.anucene.2018.03.031

Shishkina, O., Stevens, R. J. A. M., Grossmann, S., and Lohse, D. (2010). Boundary Layer Structure in Turbulent thermal Convection and its Consequences for the Required Numerical Resolution. *New J. Phys.* 12 (7), p.075022. doi:10.1088/1367-2630/12/7/075022

Tomboulides, A. G., Lee, J. C. Y., and Orszag, S. A. (1997). Numerical Simulation of Low Mach Number Reactive Flows. *J. Scientific Comput.* 12, 139–167.

Villanueva, W., Filippov, A., Jules, S., Lim, K., Jobst, M., Bouydo, A., et al. (2020). "Thermo-mechanical Modelling of Reactor Pressure Vessel during Core Melt In-Vessel Retention," in Proceedings of the International Seminar on In-vessel retention: outcomes of the IVMR project, Juan-les-Pins, France, January 21-22.

Wang, H., Villanueva, W., Chen, Y., Kulachenko, A., and Bechta, S. (2021). Thermo-mechanical Behavior of an Ablated Reactor Pressure Vessel wall in a Nordic BWR under In-Vessel Core Melt Retention. *Nucl. Eng. Des.* 351, 72–79. doi:10.1016/j.nucengdes.2021.111196

Whang, S., Park, H. S., Lim, K., and Cho, Y. J. (2019). Prandtl Number Effect on thermal Behavior in Volumetrically Heated Pool in the High Rayleigh Number Region. *Nucl. Eng. Des.* 351, 72–79. doi:10.1016/j.nucengdes.2019.05.007

Yildiz, M. A., Botha, G., Yuan, H., Merzari, E., Kurwitz, R. C., and Hassan, Y. A. (2020). Direct Numerical Simulation of the Flow through a Randomly Packed Pebble Bed. *J. Fluids Eng.* 142 (4), 041405. doi:10.1115/1.4045439

Zhang, L., Luo, S., Zhang, Y., Tian, W., Su, G. H., and Qiu, S. (2018). Large Eddy Simulation on Turbulent Heat Transfer in Reactor Vessel Lower Head Corium Pools. *Ann. Nucl. Energ.* 111, 293–302. doi:10.1016/j.anucene.2017.08.055

Conflict of Interest: The authors declare that the research was conducted in the absence of any commercial or financial relationships that could be construed as a potential conflict of interest.

Publisher's Note: All claims expressed in this article are solely those of the authors and do not necessarily represent those of their affiliated organizations, or those of the publisher, the editors, and the reviewers. Any product that may be evaluated in this article, or claim that may be made by its manufacturer, is not guaranteed or endorsed by the publisher.

Copyright © 2022 Bian, Gong and Villanueva. This is an open-access article distributed under the terms of the Creative Commons Attribution License (CC BY). The use, distribution or reproduction in other forums is permitted, provided the original author(s) and the copyright owner(s) are credited and that the original publication in this journal is cited, in accordance with accepted academic practice. No use, distribution or reproduction is permitted which does not comply with these terms.

frontiers | Frontiers in Energy Research

ORIGINAL RESEARCH
published: 27 April 2022
doi: 10.3389/fenrg.2022.841631

Improved Radiation Heat Transfer Model in RELAP5 for Compact Fuel Rod Bundles by the Absorption Factor Modification

*Qian Sun, Yu Ji and Jun Sun**

Institute of Nuclear and New Energy Technology, Collaborative Innovation Center of Advanced Nuclear Energy Technology, Key Laboratory of Advanced Reactor Engineering and Safety of Ministry of Education, Tsinghua University, Beijing, China

OPEN ACCESS

Edited by:
Yue Jin,
Massachusetts Institute of Technology, United States

Reviewed by:
Shanfang Huang,
Tsinghua University, China
Zeyun Wu,
Virginia Commonwealth University, United States
Anil Singh Yadav,
Lakshmi Narain College of Technology (LNCT), India

***Correspondence:**
Jun Sun
sunjun@tsinghua.edu.cn

Specialty section:
This article was submitted to Nuclear Energy, a section of the journal Frontiers in Energy Research

Received: *22 December 2021*
Accepted: *11 April 2022*
Published: *27 April 2022*

Citation:
Sun Q, Ji Y and Sun J (2022) Improved Radiation Heat Transfer Model in RELAP5 for Compact Fuel Rod Bundles by the Absorption Factor Modification. Front. Energy Res. 10:841631. doi: 10.3389/fenrg.2022.841631

Simulations of radiation heat transfer in fuel rod bundles are necessary for the thermal hydraulic design and safety analysis of open lattice gas-cooled reactors, which always operate at high temperatures. To save the computational costs, existing radiation models in system codes such as RELAP5 commonly assume each fuel rod to own the uniform radiosity over the rod surface. Previous research studies have indicated that the uniform radiosity assumption could overestimate the heat transfer flux and under-predict the maximum fuel rod temperature, and the anisotropic correction was tried by dealing with non-uniform reflected radiation. To better model the non-uniform radiosity effect, the Gehart's method based on the non-uniform absorbed radiation is introduced in this study. By dividing the surface of each rod into six segments, the one-sixth rod view factors are derived in specific rod and near wall sections to generate the segment-to-segment absorption factors. By summarizing those segment-to-segment absorption factors, the rod-to-rod and rod-to-wall absorption factors are modified and implemented into RELAP5 to improve the radiation heat transfer model. The two-dimension radiation heat transfer problem in the nuclear fuel rod bundle is simulated in FLUENT as the benchmark and in RELAP5 for comparison. Fuel rod bundles in hexagonal arrays were investigated with various surface emissivity and pitch-to-diameter ratios (p/d). The simulations indicated that the method of rod segment division and absorption factor modification could reflect the non-uniform radiosity, and the results were related to the values of p/d and surface emissivity. The modified radiation heat transfer model in RELAP5 validated that the deviations of the maximum temperature were reduced from around 20% to 1%,3%,8% for p/d = 1.1, 1.2, and 1.3, respectively. Rod bundles with larger p/d required more radiative rods in the analyses of absorption factor modifications. The present radiation heat transfer model should be studied and tested in three-dimension cases to further prove that it is appropriate for the nuclear rod bundles.

Keywords: fuel rod bundles, radiation heat transfer, non-uniform radiosity, absorption factor, RELAP5

1 INTRODUCTION

Human beings have always maintained a strong curiosity about deep space exploration. For deep space exploration, an efficient and reliable space power is critically important. Among all realizable technologies, the space nuclear reactor power shows a superior performance compared to chemical energy battery, solar battery, and radioisotope nuclear power due to its long-term maintenance at a high power level in complex space environment. As the power level requirement of space facilities increases rapidly, the gas-cooled reactor combined with the closed Brayton cycle provides the most promising energy conversion pathway for megawatt applications (Stanculescu, 2005; Zika and Wollman, 2006; Tournier et al., 2006; El-Genk and Tounier, 2008). Both the United States and Russia have developed megawatt-class, gas-cooled space reactor concepts. In 2003, NASA started the Prometheus project (Zika and Wollman, 2006) which adopts a helium xenon mixture cooled reactor with a thermal power rating of 1 MW. The fuel is mainly UO_2 or UN. The design outlet temperature of the reactor is about 1150K. Several core configurations have been investigated, including the open lattice, pin in block, and monoblock, as shown in **Figure 1**. The Prometheus Project Reactor Module Final Report (Zika and Wollman, 2006) points out that the open lattice design provides the lowest mass, which is a huge advantage for space missions. Russia announced its new space nuclear project with thermal power up to 3.5 MW (Dragunov, 2015). It is also cooled by helium xenon mixture and adopts traditional UO_2 as the fuel. The designed reactor outlet temperature was 1500K. However, other details are not available. Recently, the open lattice core design has attracted considerable interest as it can greatly reduce the system mass (Meng et al., 2019; Qin et al., 2020).

In the open lattice core, the coolant channel is the gap between hundreds of fuel rods. Normally, the outlet temperature of the coolant in these gas-cooled reactors should be raised to 1,100–1,500 K to ensure an acceptable thermal-to-electricity conversion efficiency and the temperature on the surface of the fuel rods could be extremely high (Ashcroft and Eshelman, 2006; Dragunova, 2021). Hence, thermal radiation in fuel rod bundles plays a vital role in the heat transfer processes inside the core. In addition, under certain postulated accident scenarios such as loss of coolant, the only way of heat rejection is the radiation heat transfer from the fuel rod bundles to the pressure vessel and, finally, to the space. Therefore, the study of radiation heat transfer between rod bundles is of the determinate essence for the thermal design and safety analysis of the open-lattice reactor.

To investigate the radiation heat transfer between rod bundles, the Computational Fluid Dynamics (CFD) methods can provide detailed and accurate simulation results, but for the open-lattice core, it is extremely time-consuming and inefficient because of the complex geometry. Traditionally, the system codes including ICARE, MELCOR, and RELAP5 are adopted for the transient and accident analysis of the nuclear system. These codes are all based on a network of 1-D or 0-D volumes and some assumptions and approximations have to be employed to ensure an acceptable computational speed. Therefore, when using the system code to study the radiative heat exchange in an open-lattice core, it is very important to establish a reasonable radiation heat transfer model for rod bundles to balance the accuracy and cost.

Existing radiation models implemented in codes such as ICARE, MELCOR, and RELAP5 are based on the net radiation method. The net radiation method assumes each radiation surface has a uniform radiosity, viz., a uniform radiation leaving the surface, and the radiosity exchange is accounted for by a "view factor," which is related to the size, separation distance, and orientation of involved surfaces. When using the net radiation method to model the radiation heat transfer of rod bundles in the reactor, a fuel rod surface is usually treated as a single unit with uniform circumferential radiosity (sum up of self-emitted radiation and reflected part of the incident radiation). However, the uniform radiosity assumption is usually not realized for the rod surface in reactor core. When there is a temperature gradient around a fuel rod, as shown in **Figure 2**, the temperature of rod No. 1 is higher than that of rod No. 3, and then the incident radiation on the left part of rod No. 2 from rod No. 1 is greater than the right part from rod No. 3. Consequently, the reflected radiation of rod No. 2 would be non-uniform since most of the incident radiation returns along the original direction as seen in **Figure 2A**. Meanwhile, if the uniform radiosity assumption is adopted,

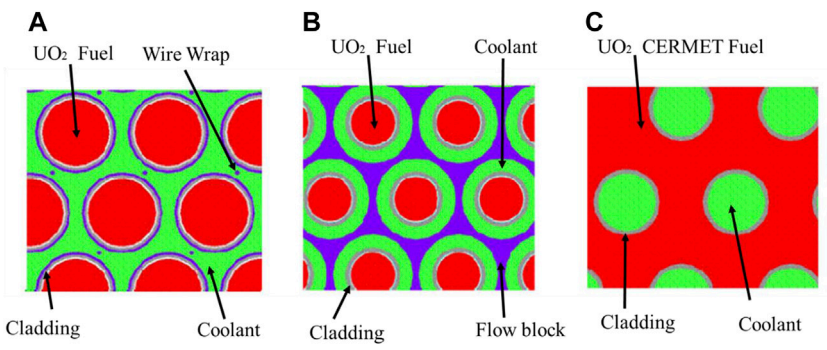

FIGURE 1 | Core arrangement options [Ashcroft, J., and C. Eshelman. 2006]. **(A)** Open lattice, **(B)** Pin in block, **(C)** Monoblack.

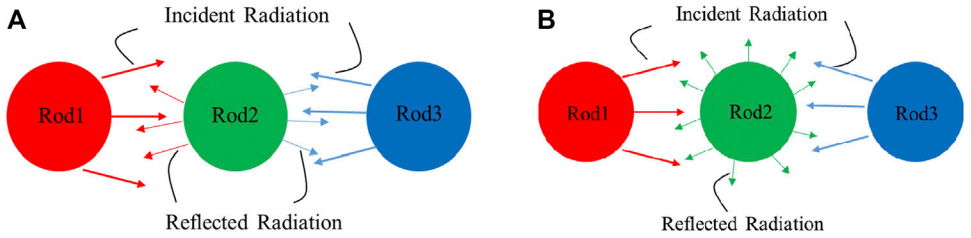

FIGURE 2 | Radiosity amoung rod bundles. **(A)** Non-uniform radiosity. **(B)** Uniform radiosity.

the projected radiation from rod No. 1 to rod No. 2 will be reflected isotopically around the circumference; thus, part of it will reach to rod No. 3, as shown in **Figure 2B**. The uniform model virtually enhances the radiation heat transfer between rod No. 1 and rod No. 3, because of a "penetration" through rod No. 2 to rod No. 3, thus leading to an overestimated effect between different surfaces of the system (Naitoh et al.,1977; Watson, 1963; Cox, 1977).

To compensate the overestimation of the radiation heat transfer rate between rod bundles, anisotropic correction was proposed by Andersen and Tien (1979) to account for the non-uniform reflected radiation. Subsequently, the correction was further improved by Tien et al. (1979) and was implemented in the safety analysis code SCDAP. However, little has been done to investigate the effect of anisotropic correction (Sohal, 1986). Clearly, multiple units performed in the circumferential direction of each fuel rod would reduce the non-uniform radiosity error. Naitoh et al. (1977) suggested for the square rod bundle that it is necessary to divide at least 4 units. Rector (1987) developed the software RANGEN for calculating the view factors between rod bundles in which a rod on a square pitch is divided into 4 parts, and a rod on a triangular pitch is divided into 6 parts. More subdivision of each rod surface would improve the prediction. However, this will greatly increase the computational cost for large arrays of rods.

The uniform radiosity assumption substantially arises from the use of view factors in the net radiation method. Meanwhile, another method for analyzing radiation heat transfer between surfaces, Gebhart's method (Gebhart, 1959, 1971), which is based on the absorption factors, does not require a uniform radiosity assumption, but needs an accurate absorption factors matrix. Compared with the view factor, which is purely geometrical, the absorption factors are a combination of geometry and surface emissivities. Hence, absorption factors totally characterize radiation heat transfer. The absorption factors can be obtained by matrix transformation from the view factors. It can also be gained through the ray tracing method or Monte Carlo method.

Klepper (1963) first used the ray tracing method to obtain the radiation absorption factors between rod bundles arranged in squares and equilateral triangles. His research results were adopted by Cox (1977), who abandoned his rod-to-rod view factors and improved the agreement between the predicted temperature results with the profiles that were experimentally measured. However, Klepper did not discuss the absorption factors around the wall region. Manteufel (1991) used the Monte Carlo method to calculate the view factors on the basis of more finely divided surface areas for each rod and then applied the matrix-inversion technology to calculate the rod-to-rod and rod-to-wall absorption factors and produced much more accurate results. Meanwhile, the Monte Carlo calculation step in Manteufel, D's procedure increased the computational cost.

Based on the previous research studies, it can be seen that the assumption of uniform radiosity around the circumference of the fuel rod is not met in practice, and it is recommended that the radiation heat transfer equations be solved using Gebhart's method with the accurate absorption factors. However, to get the absorption factors, the ray tracing method or Monte Carlo method is time consuming. Thus, in this study, the absorption factors derived from the one-sixth rod for compact fuel rod bundles is introduced, and Gebhart's method is implemented in RELAP5 to improve the radiation heat transfer model for rod bundles. The article is organized as follows. Theory of radiation exchange between the surfaces is introduced in **Section 2**. The construction of absorption matrices developed in this study is provided in **Section 3**. The radiation heat transfer simulations in enclosed hexagonal rod arrays are shown in **Section 4**. The conclusion and future work are given in **Section 5**.

2 THEORY OF RADIATION EXCHANGE BETWEEN THE SURFACES

In this section, both the net radiation method and Gebhart's method will be introduced.

2.1 The Net Radiation Method

Almost all the engineering radiation heat transfer calculations are based on the net radiation or radiosity method.

For the surface i, the radiosity R_i refers to the total radiant energy leaving a unit surface in a unit time:

$$R_i = \varepsilon_i \sigma T_i^4 + \rho_i J_i. \tag{1}$$

The radiosity R_i not only includes the surface self-radiation $\varepsilon_i \sigma T_i^4$ of the surface but also includes the part of the incident radiation that is reflected by the surface.

The energy incident on surface i for an enclosure containing n surfaces is as follows:

$$A_i J_i = \sum_{j=1}^{n} A_j F_{j,i} R_j, \tag{2}$$

where A_i is the area of surface i, incident radiation J_i refers to the total radiant energy input to a unit surface in a unit time, and $F_{j,i}$ is the view factor, which represents the proportion of radiant energy leaving from surface j to arrive at surface i. With the interchangeability of view factor $A_j F_{j,i} = A_i F_{i,j}$, the **Eqn. 2** can be expressed as follows:

$$A_i J_i = \sum_{j=1}^{n} A_j F_{j,i} R_j = \sum_{j=1}^{n} A_i F_{i,j} R_j . \tag{3}$$

Therefore,

$$J_i = \sum_{j=1}^{n} F_{i,j} R_j. \tag{4}$$

Elimination of J_i from **Eqn. 1** by using **Eqn. 4** gives the following:

$$R_i = \varepsilon_i \sigma T_i^4 + \rho_i \sum_{j=1}^{n} F_{i,j} R_j. \tag{5}$$

The net radiant heat flux of surface i can be expressed as follows:

$$q_i = R_i - J_i = R_i - \sum_{j=1}^{n} F_{i,j} R_j. \tag{6}$$

Combining **Eqs 5**, **6**, the following equation is obtained:

$$q_i = R_i - \left(R_i - \varepsilon_i \sigma T_i^4\right) / \rho_i. \tag{7}$$

Eqn. 5 are the general equations for determining radiation exchange in a gray, diffuse enclosure of n surfaces by using the net radiation method. After solving the effective radiation R of each surface, the net radiant heat flux of each surface can be obtained according to **Eqn. 7**.

2.2 Gebhart's Method

For analyzing the radiation heat transfer between surfaces, Gebhart introduced the concept of absorption factor $G_{i,j}$, which represents the fraction of the energy finally absorbed by the surface j from the emission of surface i, including reflections by other surfaces.

For surface i in an enclosure containing n surfaces, the radiation heat transfer equation can be expressed as follows:

$$Q_i = A_i \varepsilon_i \sigma T_i^4 - \sum_{j=1}^{n} \varepsilon_j \sigma T_j^4 A_j G_{j,i}, \tag{8}$$

where ε_i, A_i, and T_i represent the emissivity, area, and temperature of surface i. Q_i is the net energy loss from surface i. The first term on the right-hand side of **Eqn. 8** is the energy emitted by surface i, and the second term is the sum of the energy absorbed by surface i from all other surfaces.

Similar to the view factor, the absorption factor has reciprocity and conservation properties. For two surfaces i and j, the energy rate radiated from i to j is $\varepsilon_i A_i G_{i,j} T_i^4$ and the energy rate radiated from j to i is $\varepsilon_j A_j G_{j,i} T_j^4$. If $T_i = T_j$, there will be no radiation heat transfer between i and j, which means $\varepsilon_i A_i G_{i,j} T_i^4 = \varepsilon_j A_j G_{j,i} T_j^4$. Therefore, we have the following:

$$\varepsilon_i A_i G_{i,j} = \varepsilon_j A_j G_{j,i}. \tag{9}$$

For a closed system, all radiation emitted from any surface must fall on surfaces of the system.

Thus

$$\sum_{j=1}^{n} G_{i,j} = 1. \tag{10}$$

Because of $\varepsilon_j A_j G_{j,i} = \varepsilon_i A_i G_{i,j}$, **Eqn. 8** can be expressed as follows:

$$Q_i = A_i \varepsilon_i \sigma T_i^4 - \sum_{j=1}^{n} \sigma T_j^4 \varepsilon_i A_i G_{i,j}. \tag{11}$$

The net radiant heat flux of surface i can be expressed as follows:

$$q_i = \varepsilon_i \sigma T_i^4 - \sum_{j=1}^{n} \sigma T_j^4 \varepsilon_i G_{i,j}. \tag{12}$$

It can be seen from **Eqn. 12** that the key issue of Gebhart's method to solve the radiation heat transfer is to obtain the absorption factors.

The concept of absorption factor and view factor are similar, but their meanings are different.

The view factor $F_{i,j}$ represents the proportion of the radiant energy leaving the surface i directly reaching the surface j, regardless of the reflection through other surfaces.

The absorption factor $G_{i,j}$ represents the portion of the radiant energy emitted from the surface i that is finally absorbed by the surface j, including multiple reflections through other surfaces.

The theoretical derivation of the view factor is introduced in many literatures or textbooks, but the theoretical derivation of the absorption factor is rarely introduced.

For a closed system containing n surfaces, the absorption factors can be generated from the view factors as follows:

$$G_{i,j} = F_{i,j} \varepsilon_j + \sum_{k=1}^{n} F_{i,k} (1 - \varepsilon_k) G_{k,j}. \tag{13}$$

The derivation of this formula can be explained as follows: the left term of **Eqn. 13** is the fraction of the radiation energy absorbed by surface j from surface i. The first term on the right side is the radiation energy that surface i directly projects to surface j and is absorbed by surface j. The other items can be understood as the radiation energy that the surface i directly projects to the surface k and is reflected by surface k and absorbed by surface j.

The net radiation method is computationally expensive when calculating the radiation and view factors for a large number of surfaces. Generally, there are 200~500 fuel rods in the open-lattice core. When modeling the radiation heat transfer between rod bundles, each rod surface is usually assumed as a single unit with uniform circumferential radiosity to reduce the computational cost. However, an actual non-uniform radiosity usually exists due to a great temperature gradient between the fuel rod bundles, which nullifies the assumption and causes much error during the calculation, as shown in **Figure 2A**. More subdivisions of the rod surface along the circumferential direction will reduce the error, but this treatment will

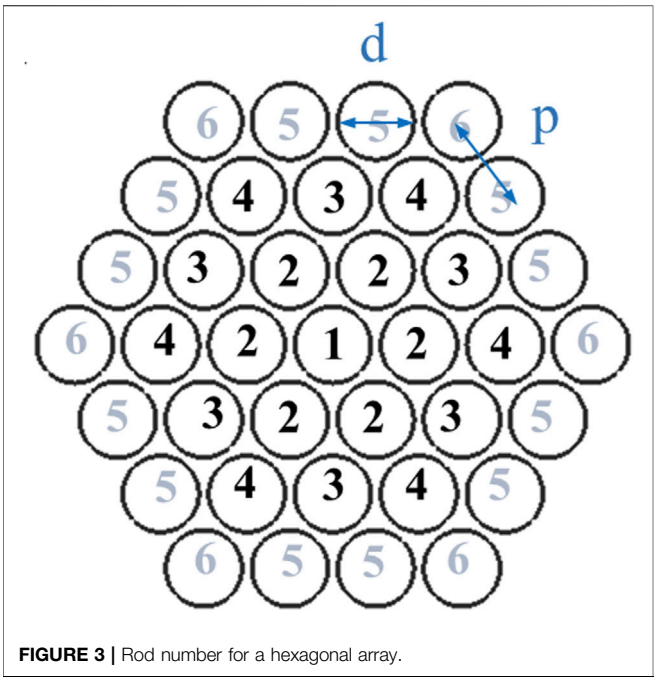

FIGURE 3 | Rod number for a hexagonal array.

complicate the construction of view factor matrices and also greatly increase the computational cost.

Instead, Gebhart's method does not rely on a uniform radiosity assumption, which could better solve the above problem related to the net radiation method. Differently, Gebhart's method needs an accurate absorption factors matrix. So, in the next section, we focus on getting the appropriate absorption factors without increasing the number of radiation heat transfer equations that need to be solved.

3 DERIVATION OF ABSORPTION FACTORS IN THIS STUDY

In this section, the absorption factors for the interior of the rod bundles and the enclosing wall were derived for hexagonal arrays. To reduce the error caused by the uniform radiosity assumption, the absorption factor in this study is obtained by dividing a single rod into six segments in the circumferential direction, while the radiation heat transfer equation is still based on every individual fuel rod. Hence, the computation time will not increase compared with the net radiation method.

The detailed calculation step for the interior of the rod bundles and the enclosing wall will be described in **Section 3.1** and **Section 3.2**. The construction of absorption matrices for enclosed arrays and the implement of Gebhart's method in RELAP5 is introduced in **Section 3.3**.

3.1 Rod-to-Rod Basic Absorption Factor

For a hexagonal array, the relative spatial position of each fuel rod and its surrounding rods can be indicated by No. 1 and No. 2/No. 3/No. 4/No. 5/No. 6 in **Figure 3**. It is assumed that the radiation heat transfer of rod No. 1 only occurs with itself and the surrounding rods No. 2, No. 3, and No. 4. For compact rod packing (for the space open-lattice reactor, p/d < 1.2), this assumption is reasonable. But for larger p/d (> 1.3), farther-traveling radiation heat transfer needs to be considered, for example, connections with rod No. 5 and rod No. 6 or even more.

The absorption factors in a hexagonal array as shown in **Figure 3** are defined as follows:

g11 is the fraction of the energy absorbed by rod No. 1 from the emission of rod No. 1.

g12/g13/g14 are the fraction of the energy absorbed by rod No. 2/No. 3/No. 4, respectively, from the emission of rod No. 1.

The absorption matrices for enclosed hexagonal arrays can be constructed from g11/g12/g13/g14. So next, we will introduce the derivation process to get these basic absorption factors.

The basic unit for studying the rod-to-rod absorption factor is illustrated in **Figure 4A**. In this unit, every individual rod is divided into six segments in the circumferential direction, and the surface 2/6/8/12/14/18 are the imaginary surfaces introduced to form an enclosure.

The computational procedure for rod-to-rod basic absorption factors can be described as follows:

First, calculating the segment-to-segment view factors F (18 × 18) (surfaces 1/2/. . ./18, the detailed expressions are

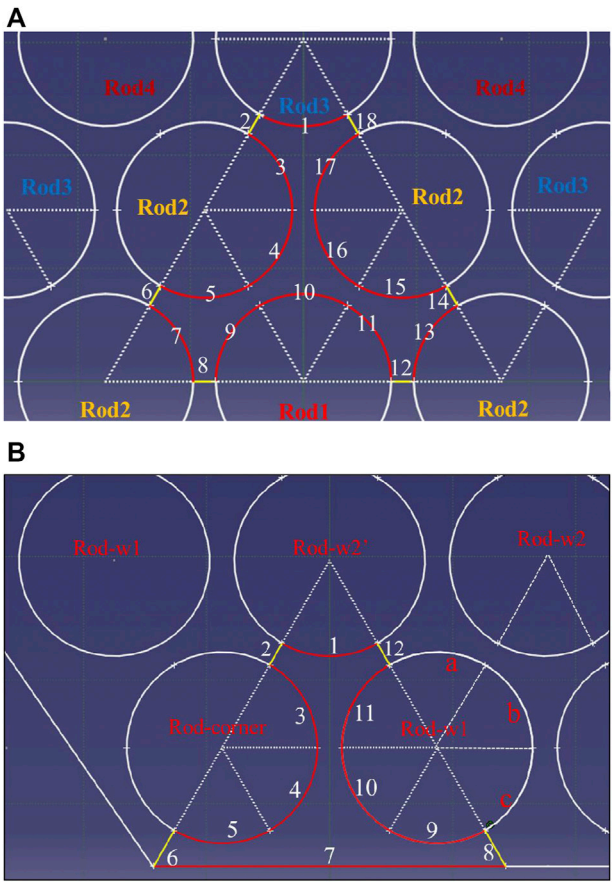

FIGURE 4 | Basic unit for analyzing **(A)** the rod-to-rod absorption factors and **(B)** the rod-to-wall absorption factors.

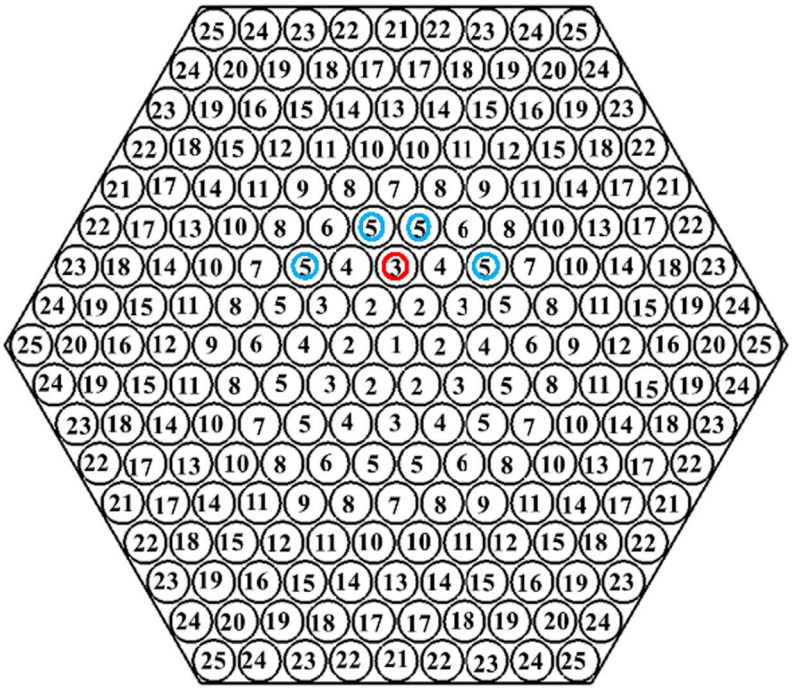

FIGURE 5 | Cross-section of an enclosed hexagonal array and rod numbers.

described in the **Supplementary Appendix A**, which is only related to p/d).

Next, calculating the segment-to-segment absorption factors SG (18 × 18) by using the matrix relationship **Eqn. 13**.

Then, calculating the basic absorption factors (g11/g12/g13/g14) by summing the corresponding segment-to-segment absorption factors:

$$g11 = SG(10,9) + SG(10,10) + SG(10,11) + [SG(10,8) + SG(10,12)]/2, \quad (14)$$

$$g12 = \frac{[SG(10,7) + SG(10,5) + SG(10,4) + SG(10,3) + SG(10,17) + SG(10,16) + SG(10,15) + SG(10,13)]}{6} + [SG(10,8) + SG(10,12)]*(1/2)\Big/6 + [SG(10,6) + SG(10,14)]*\left(\frac{2}{3}\right)\Big/6 + [SG(10,2) + SG(10,18)]*\left(\frac{1}{3}\right)\Big/6, \quad (15)$$

$$g13 = SG(10,1)\Big/6 + [SG(10,6) + SG(10,14)]*\left(\frac{1}{3}\right)\Big/6 + [SG(10,2) + SG(10,18)]*\left(\frac{1}{3}\right)\Big/6, \quad (16)$$

$$g14 = (1 - g11 - g12*6 - g13*6)/6. \quad (17)$$

In the above equations for calculating g11-g14, the segment-to-segment absorption factor related to surfaces 2/6/8/12/14/18 is an approximate treatment. For compact arrangement, the areas of surfaces 2/6/8/12/14/18 are relative small comparing with 1/6 rod segments. The unaccounted fraction absorbed by these areas is added to the neighboring rods. For example, the factor 1/2 in **Eqs. 14**, **15** can be explained using the energy absorbed by surface 8 and surface 12 from the emission of surface 10 being added to the two neighboring rods, Rod1 and Rod2. The factor 2/3 in **Eqn. 15** can be explained using the energy absorbed by surface 6 and surface 14 from the emission of surface 10 being added to the three neighboring rods, among which two are Rod2 and the other one is Rod3. By the same token, 1/3 is chosen for surface 2 and surface 18 in **Eqs. 15**, **16**. The reason for 1/6 in **Eqs. 15–17** is that there are 6 rods marked as Rod2/Rod3/Rod4 around Rod1 in **Figure 3**.

The derivation here only goes to g14. Therefore, g14 is derived from g11 + 6*g12 + 6*g13 + 6*g14 = 1 according to the conservation of energy. It should be mentioned that the basic rod-to-rod absorption factor derived from **Figure 4A** is only applicable for compact rod bundles (p/d < 1.2). As p/d increase, a larger fraction of radiation energy will escape through these imaginary surfaces, but the basic unit shown in **Figure 4A** will limit the dispersal of radiation energy. For larger p/d (> 1.3), more radiative rods in the basic unit analyses need to be considered.

3.2 Rod-to-Wall Basic Absorption Factor

Figure 4B is the basic unit for analyzing the rod-to-wall absorption factors.

Defining Wg1, Wg2, and Wgcorner are the fraction of the energy absorbed by the wall from the emission of the rod near the wall in the first row, the second row, and the diagonal corners, respectively.

The computational procedure for rod-to-wall basic absorption factors is the same as the steps for rod-to-rod basic absorption factors.

First, calculating the segment-to-segment view factors F (12 × 12) (surfaces 1/2/. . ./12, the detailed expressions are described in the **Supplementary Appendix B**).

A

i \ j	1	2	3	4	5	6	7	8	9	10	11	12
1	g11	6g12	6g13	6g14	0.0	0	0	0	0	0	0	0
2		g11+g14 2(g12+g13)	2g12+2g14	g12+2g13	2g13+2g14	g14	0	0	0	0	0	0
3			g11+2g13	2g12	2g12+2g14	2g13	g13	2g14	0	0	0	0
4				g11 +2g14	2g12+2g13	g12	2g14	2g13	g14	0	0	0
5					g11+g12+g13	g12+g14	g12	g12+g13+g14	g13	g13+g14	g14	0
6						g11	2g13	2g12	g12	2g14	2g13	g14
7							g11	2g12	2g14	2g12	2g13	0
8								g11+g13+g14	g12	g12+g13	g12+g14	g13
9									g11	2g13	2g12	g12
10										g11+g12	g12+g14	g14
11											g11+g13	g12
12												g11

$$G_{i,j} = \frac{A_j \varepsilon_j}{A_i \varepsilon_i} G_{j,i}$$

B

13	14	15	16	17	18	19	20	21	22	23	24	25	26	j / i
g11	2g12	2g14	0	2g12	2g13	0	0	g13	2g14	0	0	0	1-∑i=13	13
	g11+g14	g12	g14	g12+g13	g12	g13	0	g14	g13	g14	0	0	1-∑i=14	14
		g11+g13	g12	g13	g12	g12+g14	g13	0	g14	g13	g14	0	1-∑i=15	15
			g11	0	2g13	2g12	g12	0	0	2g14	2g13	g14	1-∑i=16	16
				1-∑i=17	g12+g14	g14	0	g12	g12+g13	g13	0	0	Wg2	17
					1-∑i=18	g12	g14	g13	g12	g12	g13	0	Wg2	18
						1-∑i=19	g12	0	g13	g12	g12+g14	g13	Wg2	19
							1-∑i=20	0	0	2g13	2g12	g12	2*Wg2	20
								1-∑i=21	2g12	2g14	0	0	Wg1	21
									1-∑i–22	g12	g14	0	Wg1	22
										1-∑i=23	g12	g14	Wg1	23
											1-∑i–24	g12	Wg1	24
												1-∑i=25	Wgcorner	25
													1-∑i=26	26

$$G_{i,j} = \frac{A_j \varepsilon_j}{A_i \varepsilon_i} G_{j,i}$$

FIGURE 6 | Absorption factor matrix for a hexagonal array: **(A)** interior and **(B)** near the wall.

Next, calculating the segment-to-segment absorption factors SG (12 × 12) by using the matrix relationship **Eqn. 13**.

Then, calculating the basic absorption factors (Wg1, Wg2, and Wgcorner) by summing the corresponding segment-to-segment absorption factors:

$$\mathrm{Wg1} = [SG(3,7) + SG(4,7) + SG(9,7) + SG(10,7) + SG(11,7)] * (1/6), \quad (18)$$

$$\mathrm{Wg2} = SG(1,7)/6, \quad (19)$$

$$\mathrm{Wgcorner} = [SG(3,7) + SG(4,7) + SG(5,7)]/3. \quad (20)$$

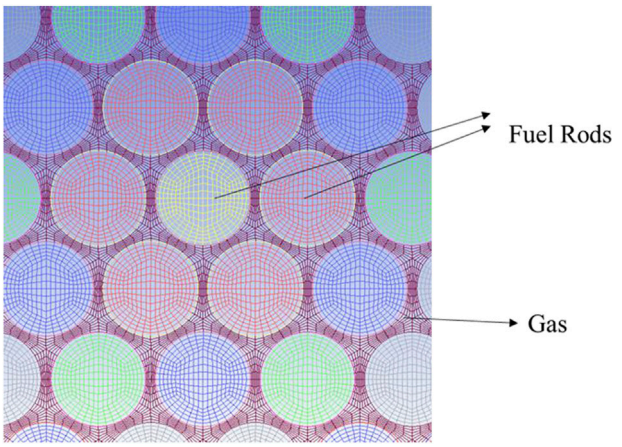

FIGURE 7 | Schematic diagram of CFD mesh.

For Rod-w1 in **Figure 4B**, the fraction of the energy absorbed by the wall should be the average fraction of six surfaces 9/10/11/a/b/c. While the surface a is totally on the opposite side of the wall, its contribution to Wg1 can be ignored. The contribution of surfaces b and c are equal to the part of surfaces 3 and 4. So, Wg1 is expressed as **Eqn. 18**.

For Rod-w2 in **Figure 4B**, the fraction of the energy absorbed by the wall should be one-sixth of the fraction of surface 1. But for Rod-w2', the absorption factor should be 2*Wg2.

For Rod-corner, the total fraction absorbed by the wall should be the average fraction of surfaces 3, 4, and 5.

Similarly, the rod-to-wall absorption factor calculation shown here is only suitable for tight wall distance. The improvement of wall effect will be introduced in subsequent studies.

3.3 Construction of Absorption Matrices

After getting the basic rod–rod and rod–wall absorption factor, we can construct the absorption factor matrices for enclosed hexagonal arrays.

Figure 5 is a schematic diagram of the cross-section of fuel rod bundles in an enclosed hexagonal array. There are 217 fuel rods in total. The rod surfaces can be numbered as 1–25 when the heat generation and boundary temperature are uniform, where rods with the same number are considered as one surface of uniform temperature.

$G_{i,j}$ represents the absorption factor matrices for the hexagonal arrays. For compact fuel rod bundles, it is assumed that the radiation heat transfer within three rows is important. Then all the absorption factors $G_{i,j}$ can be calculated from g11/g12/g13/g14. For example, $G_{3,5}$ = 2*g12 + 2*g14. For each of the rods labeled as No. 3 as shown in **Figure 5**, two surfaces labeled as No. 5 have the same relative relationship with No. 3 as that between No. 2 and No. 1. Another two

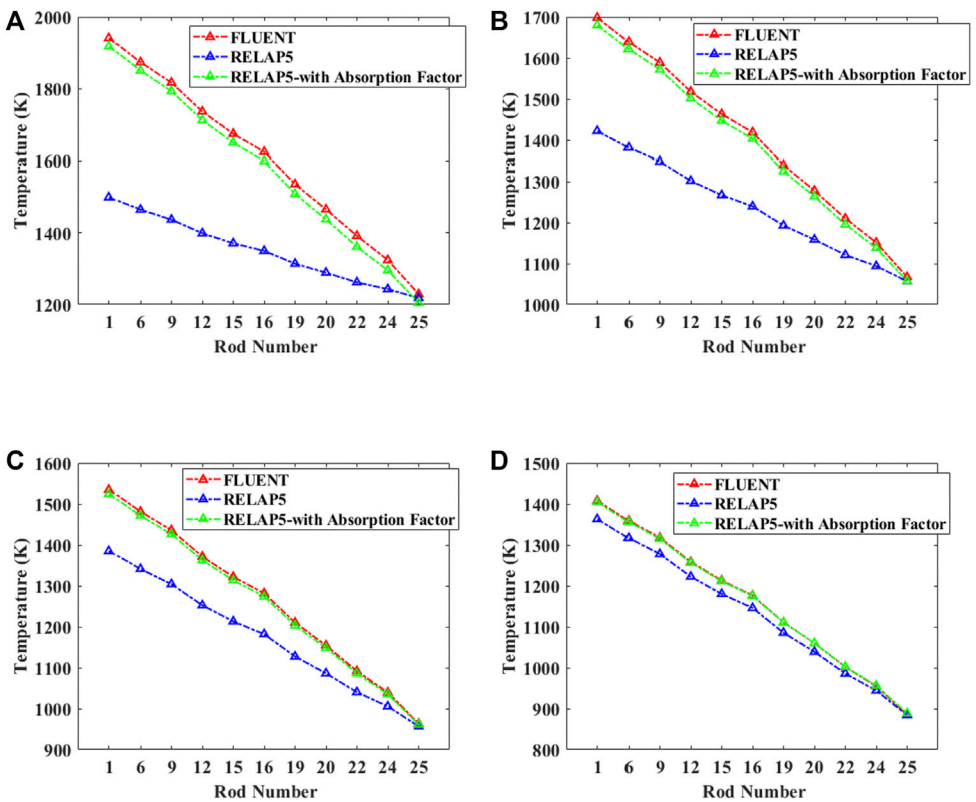

FIGURE 8 | Temperature results for p/d = 1.1: **(A)** emissivity = 0.3, **(B)** emissivity = 0.5, **(C)** emissivity = 0.7, and **(D)** emissivity = 0.9.

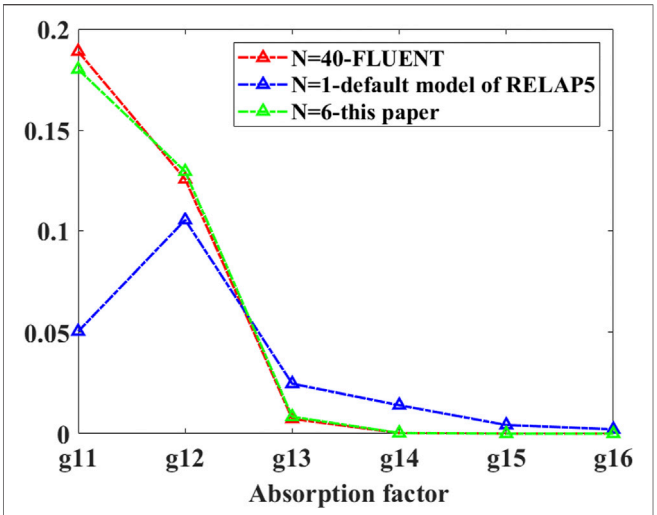

FIGURE 9 | Absorption factors from different N for p/d = 1.1 and emissivity = 0.5.

surfaces labeled as No. 5 have the same relative relationship with No. 3 as that between No. 4 and No. 1.

According to the fuel rods arrangement, the absorption factor matrix of the whole array constructed from g11/g12/g13/g14 to construct are presented in **Figure 6**.

The default model of RELAP5 for solving radiation heat transfer is based on the net heat method with the view factors (Information Systems Laboratories, 2003). We have modified its code and expanded its capability. The absorption factors matrix can be written in the input cards, and Gebhart's method can be chosen to solve the radiation heat transfer between the surfaces.

4 RADIATION HEAT TRANSFER SIMULATION

In this part, Gebhart's method is used to simulate the radiation heat transfer between rod bundles using the absorption factor matrix derived from **Section 3**.

The hexagonal array shown in **Figure 5** was considered. In the preliminary research stage, it is simplified as a two-dimensional problem, which means the fuel rod bundles are infinitely long in the axial direction. The modeling details are outlined as follows: the diameter of each fuel rod d is 15.5 mm and the center distance between the fuel rods p = 1.1*d. The fuel rods are given a uniform power of 0.8 MW/m^3 and a steady state solution was obtained with an imposed wall temperature of 573.0 K. The thermal conductivity of the material is assumed to be 1.0e6 W/(m·K) to eliminate temperature variations around the circumference of each rod. Each rod surface can be thought as isothermal.

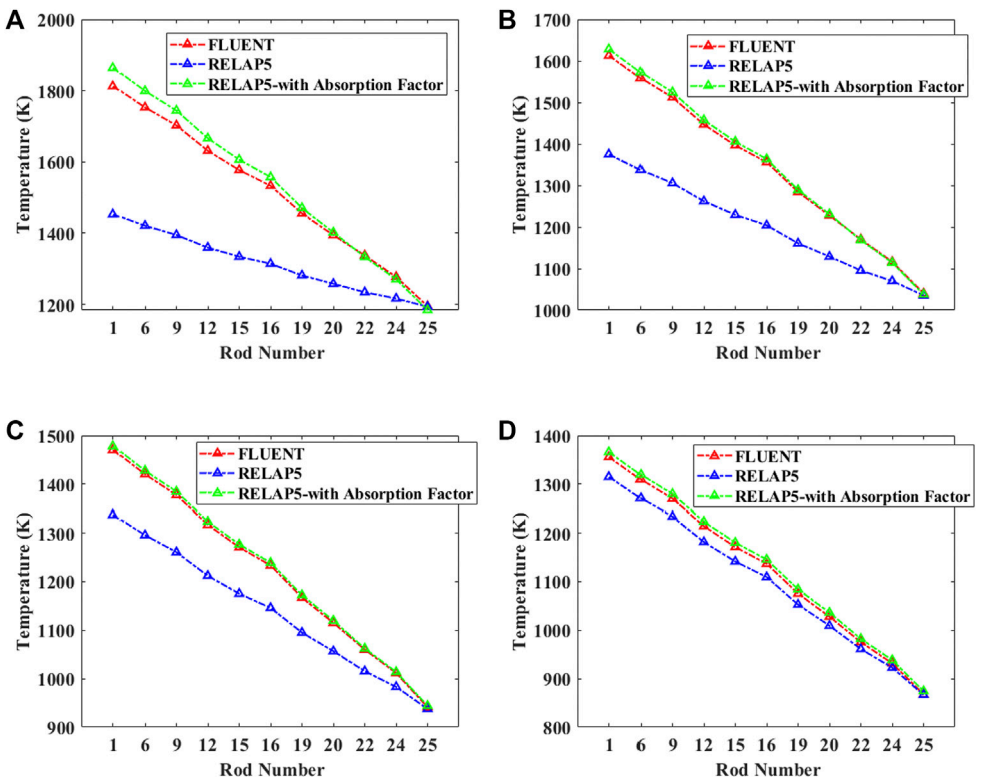

FIGURE 10 | Temperature results for p/d = 1.2: **(A)** emissivity = 0.3, **(B)** emissivity = 0.5, **(C)** emissivity = 0.7, and **(D)** emissivity = 0.9.

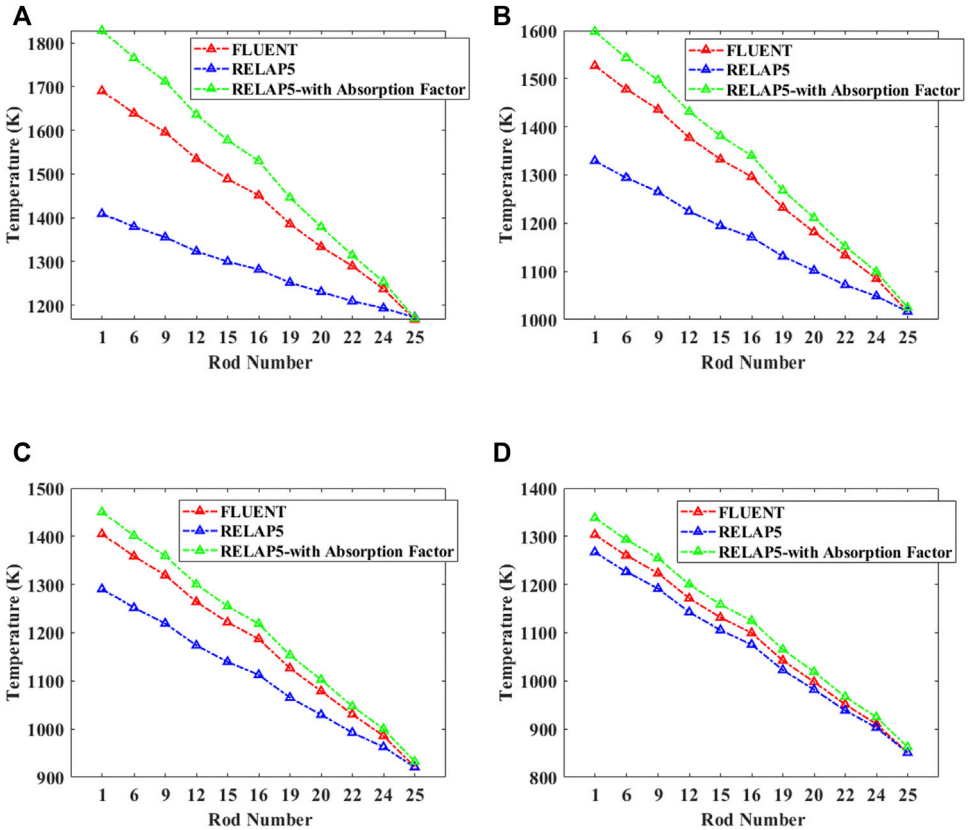

FIGURE 11 | Temperature results for p/d = 1.3: **(A)** emissivity = 0.3, **(B)** emissivity = 0.5, **(C)** emissivity = 0.7, and **(D)** emissivity = 0.9.

TABLE 1 | Relative temperature error of rod No.1.

Relative error	emissivity = 0.3		emissivity = 0.5		emissivity = 0.7		emissivity = 0.9	
	Uniform radiosity	This study	Uniform radiosity	This study	Uniform radiosity	This study	Uniform radiosity	This study
p/d = 1.1	−22.76%	−1.17%	−16.26%	−1.07%	−9.76%	−0.69%	−3.20%	−0.23%
p/d = 1.2	−19.84%	2.93%	−14.74%	1.02%	−9.04%	0.57%	−3.02%	0.74%
p/d = 1.3	−16.65%	8.29%	−12.93%	4.71%	−8.14%	3.27%	−2.78%	2.67%

Both the net radiation method (RELAP5) and Gebhart's method (RELAP5 with Absorption Factor) were chosen for calculation. In addition, a detailed modeling of the radiation heat exchange was also carried out using CFD software FLUENT. For the RELAP5 and FLUENT simulation, the coolant should be included but the coolant in the enclosure neither emits nor absorbs radiant thermal energy. The surface-to-surface (S2S) radiation model based on the net radiation method was chosen in FLUENT, if N is considered as the number of subdivisions of a single rod surface. When using FLUENT to simulate the thermal radiation for hexagonal array shown in **Figure 5**, the number of mesh elements is 100,872, and the mesh schematic diagram is displayed in **Figure 7**. Each single rod is subdivided into N = 40 areas along the circumferential direction. Meanwhile, for the simulation of the default RELAP5 (the net radiation method) and the modified RELAP5 (Gebhart's method with absorption factor), each individual fuel rod is treated as a unit; therefore, 25 + 1 = 26 elements are adopted, in which the additional one is the enclosed wall. The pair view factors of infinite parallel cylinders for the default RELAP5 simulation can be obtained from the work of Cox (1977). It is worth noting that in the default RELAP5 (the net radiation method), N is equal to 1 as the uniform radiosity over the entire circumferential surface of individual rod is assumed. Whereas, in the modified RELAP5 (Gebhart's method with absorption factor), N is equal to 6 as the absorption factor matrix derived from **Section 3** is based on the one-sixth rod.

Figure 8 shows the surface temperature distribution of rod bundles calculated from RELAP5, the modified RELAP5 (with absorption factor), and FLUENT. It can be found that the temperature gradient between rod bundles calculated by RELAP5 is much lower than that calculated

by FLUENT, which demonstrates that the uniform radiosity assumption over the entire rod overestimates the radiation heat transfer effect between rod bundles and thus under-predicts the rod temperature. The max error is up to 23% (~440K). This is undesirable for the safety analysis of the reactor. With the increase in emissivity, the error will gradually decrease. The source of the error in uniform radiosity assumption is that the reflected radiation on the surface over the entire rod is not uniform. The radiosity due to reflection is proportional to the surface reflectivity ρ. Therefore, with the emissivity ε increase, the error caused by the uniform reflection assumption will decrease ($\rho = 1 - \varepsilon$).

In contrast, the temperature gradient calculated with the modified RELAP5 based on the absorption factors derived in this study is much closer to the CFD results under different emissivity. Which means that the calculation procedure proposed in this study can reduce the non-uniform radiosity error greatly.

Figure 9 presents the comparison of rod-to-rod absorption factors from different N for ε = 0.5 at p/d = 1.1. It can be seen that N = 6 in this study obtains a reasonable accuracy compared with the benchmark, that is, N = 40. In addition, the figure also indicates that a higher proportion of the radiation to be absorbed by the radiating rod itself and neighboring rods for compact rod arrangement. However, the default model (N = 1) overestimated the radiation domain of the radiating rod. In consequence, the predicted temperature is much flatter than the more divided results.

Figure 10 describes the simulation results when p/d = 1.2. It can be seen that the simulation results based on the absorption factor are still much closer to CFD. **Figure 11** shows the simulation results for p/d = 1.3. With the increase of P/d, the simulation results based on the absorption factor gradually deviate from the CFD results.

The relative temperature error of Rod 1 was summarized in **Table 1**. The uniform radiosity assumption over the entire rod overestimates the radiation heat transfer effect between rod bundles and thus under-predict the rod temperature. The max temperature under-predictions are about 23%, 20% for p/d = 1.1, 1.2, respectively. While using the absorption factor matrix derived in this study, the maximum temperature deviation can be reduced to around 1% for p/d = 1.1 and 3% for p/d = 1.2.

As p/d increase, the radiation heat will transfer farther; thus, the temperature gradient between rod bundles decreases. As a result, the non-uniform radiosity error will gradually decrease, but still underestimate the temperature around 17% for p/d = 1.3. The absorption factor derived in this study will overestimate the maximum temperature about 8% for p/d = 1.3. The reason has been explained in **Section 3**. With the increase in p/d, there is actually a wider dispersal of energy, but our derivation only goes to g14. So, the temperature results calculated with the absorption factors for p/d = 1.3 are steeper and higher than that calculated by CFD. Rod bundles with larger p/d required more radiative rods in the deprivation of absorption factors.

5 CONCLUSION

Radiation heat transfer is an important heat transfer mechanism in the open-lattice gas-cooled reactors. The uniform radiosity assumption of each fuel rod will overestimate the heat transfer and thus under-predict the maximum fuel rod temperature, which is not expected in safety analysis. To reduce the non-uniform radiosity error, construction of absorption factor matrices based on 1/6 rod segments have been developed in this study.

Gebhart's method was implemented in RELAP5 and was used to simulate the radiation heat transfer between rod bundles. It is found that the simulation results based on the absorption factor matrices deprived in this study can reduce the non-uniform radiosity error greatly for compact rod bundle arrangement (p/d < = 1.2). Rod bundles with larger p/d required more radiative rods in the analyses of basic absorption factor modifications. The present radiation heat transfer model should be studied and tested in three-dimension cases to further prove that it is appropriate for the nuclear rod bundles.

DATA AVAILABILITY STATEMENT

The original contributions presented in the study are included in the article/**Supplementary Material**, further inquiries can be directed to the corresponding author.

AUTHOR CONTRIBUTIONS

All authors contributed to the article and approved the submitted version.

FUNDING

This work was supported by NSFC No. 52106256, the China Postdoctoral Science Foundation (2020M680586), and the CNSA program (D010501).

SUPPLEMENTARY MATERIAL

The Supplementary Material for this article can be found online at: https://www.frontiersin.org/articles/10.3389/fenrg.2022.841631/full#supplementary-material

REFERENCES

Andersen, J., and Tien, C. L. (1979). "Radiation Heat Transfer in a BWR Fuel Bundle under LOCA Conditions," in Fluid Flow and Heat Transfer over Rod or Tube Bundles Conference at ASME, Simulation, New York, NY, December 2-7, 1979, 199–207.

Ashcroft, J., and Eshelman, C. (2006). Summary of NR Program Prometheus Efforts. *Naval Reactors Program* 3, 83–87. doi:10.2172/881290

Cox, R. L. (1977). *Radiative Heat Transfer in Arrays of Parallel Cylinders*. [dissertation]. Knoxville (Tennessee): University of Tennessee.

Dragunov, Y. G. (2015). Fast-neutron Gas-Cooled Reactor for the Megawatt-Class Space Bimodal Nuclear thermal System. *Eng. Autom. Probl.* 2, 117–120.

Dragunov, Y. G. (2021). Space Nuclear Power. *Her. Russ. Acad. Sci.* 91, 327–334. doi:10.1134/s1019331621030035

El-Genk, M. S., and Tournier, J.-M. (2008). Noble Gas Binary Mixtures for Gas-Cooled Reactor Power Plants. *Nucl. Eng. Des.* 238 (6), 1353–1372. doi:10.1016/j.nucengdes.2007.10.021

Gebhart, B. (1959). A New Method for Calculating Radiant Exchanges. *Trans. ASHRAE* 65, 321–332.

Gebhart, B. (1971). *Heat Transfer*. 2d ed.. New York: McGraw-Hill.

Information Systems Laboratories (2003). *RELAP5/MOD3.3 Code Manual, Vol. 1: Code Structure, System Models, and Solution Methods. NUREG/CR-5535/Rev P3-Vol I*. Idaho: National Engineering Laboratory.

Klepper, O. H. (1963). *Radiant Interchange Factors for Heat Transfer in Parallel Rod Arrays, ORNL-TM-583*. Oak Ridge, TN: Oak Ridge National Laboratory.

Manteufel, R. D. (1991). *Heat Transfer in an Enclosed Rod Array*. [dissertation]. Cambridge (Massachusetts): Massachusetts Institute of Technology.

Meng, T., Zhao, F., Cheng, K., Zeng, C., and Tan, S. (2019). Neutronics Analysis of Megawatt-Class Gas-Cooled Space Nuclear Reactor Design. *J. Nucl. Sci. Technol.* 56, 1–10. doi:10.1080/00223131.2019.1644244

Naitoh, M., Kawabe, R., and Chino, K. (1977). Analysis of Radiant Heat Transfer in a BWR Fuel Assembly. *Nucl. Eng. Des.* 44 (3), 315–321. doi:10.1016/0029-5493(77)90167-4

Qin, H., Zhang, R., Guo, K., Wang, C., and Qiu, S. (2020). Thermal-hydraulic Analysis of an Open-Grid Megawatt Gas-Cooled Space Nuclear Reactor Core. *Int. J. Energ. Res.* 45, 11616–11628. doi:10.1002/er.5329

Rector, D. R. (19871987). *RADGEN: A Radiation Exchange Factor Generator for Rod Bundles*. Richland, Washington: Pacific Northwest Laboratory.

Sohal, M. S. (1986). Radiation Heat Transfer Model for the SCDAP Code. *Nucl. Technol.* 75, 2. doi:10.13182/NT86-A33862

Stanculescu, A. (2005). *The Role of Nuclear Power and Nuclear Propulsion in the Peaceful Exploration of Spac*. Vienna: International Atomic Energy Agency.

Tien, C. L., Sanchez, R. A., Mandell, D. A., and McDaniel, C. T. (1979). Surface Radiative Exchange in Rod Bundles. *Trans. Asme, J. Heat Transfer* 101, 378–379. doi:10.1115/1.3450981

Tournier, J. M., El-Genk, M., and Gallo, B. (2006). "Best Estimates of Binary Gas Mixtures Properties for Closed Brayton Cycle Space Applications," in 4th International Energy Conversion Engineering Conference and Exhibit (IECEC), San Diego, California, June 26 - 29, 2006.

Watson, J. S. (1963). *Heat Transfer from Spent Reactor Fuels during Shipping: A Proposed Method for Predicting Temperature Distribution in Fuel Bundles and Comparison with Experimental DataORNL-3439*. Oak Ridge TN: Oak Ridge National Laboratory.

Zika, M. J., and Wollman, M. J. (2006). *Prometheus Project Reactor Module Final Report, for Naval Reactors Information. Knolls Atomic Power Laboratory (KAPL)*. West Mifflin, PA: Bettis Atomic Power Laboratory.

Conflict of Interest: The authors declare that the research was conducted in the absence of any commercial or financial relationships that could be construed as a potential conflict of interest.

The reviewer SH declared a shared affiliation, with no collaboration, with the authors to the handling editor at the time of the review.

Publisher's Note: All claims expressed in this article are solely those of the authors and do not necessarily represent those of their affiliated organizations, or those of the publisher, the editors, and the reviewers. Any product that may be evaluated in this article, or claim that may be made by its manufacturer, is not guaranteed or endorsed by the publisher.

Copyright © 2022 Sun, Ji and Sun. This is an open-access article distributed under the terms of the Creative Commons Attribution License (CC BY). The use, distribution or reproduction in other forums is permitted, provided the original author(s) and the copyright owner(s) are credited and that the original publication in this journal is cited, in accordance with accepted academic practice. No use, distribution or reproduction is permitted which does not comply with these terms.

frontiers | Frontiers in Energy Research

ORIGINAL RESEARCH
published: 05 May 2022
doi: 10.3389/fenrg.2022.848799

An Improved Model of the Heat Pipe Based on the Network Method Applied on a Heat Pipe Cooled Reactor

Yuchuan Guo[1], Zilin Su[1], Zeguang Li[1], Kan Wang[1] and Xuanyi Liu[2]*

[1]Department of Engineering Physics, Tsinghua University, Beijing, China, [2]Department of Physics, Beijing Normal University, Beijing, China

As the unique piece of heat transport equipment in a heat pipe cooled reactor, an accurate simulation of the heat pipe is helpful for understanding the real behavior of the reactor core and the reactor system. Based on the network method, an improved model for the heat pipe which considers the heat conductance in the wall, the vapor flow in the vapor space, and the liquid flow in the wick is proposed. Meanwhile, the gravity term is also added to the flow equation. Compared with the experimental results of a copper-water heat pipe, the validity of this model is verified. Then, a high-temperature sodium heat pipe of 1.0 m length is selected as the study object. Based on the analysis, it can be found that the total temperature difference of the heat pipe is 31.7 K, and the temperature drop caused by the vapor flow is only 2.6 K. As for the flow pressure drop in the heat pipe, the pressure drop is mainly concentrated in the wick region, which is 8,422.47 Pa, and the pressure drop in the vapor space is only 896.68 Pa. In cases of non-uniform heating and cooling, high heat leakage, and inclined operation, results indicate that the greater the non-uniformity of heating or cooling, the greater will be the temperature drop of the heat pipe. With the increase of heat leakage, the operating temperature of the heat pipe decreases significantly, and the total temperature drop increases. The heat pipe can operate at all positive inclination angles, but when the inclination angle exceeds–30°, the heat pipe will reach the capillary limit, and it may be damaged. All of these results can provide support for the design and simulation of a heat pipe cooled reactor.

Keywords: heat pipe, network method, heat leakage, gravity, inclined operation

OPEN ACCESS

Edited by:
Fulvio Mascari,
ENEA Bologna Research Centre, Italy

Reviewed by:
Fulong Zhao,
Harbin Engineering University, China
Juan Manuel Belman-Flores,
University of Guanajuato, Mexico
Andrea Bersano,
Italian National Agency for New Technologies, Energy and Sustainable Economic Development (ENEA), Italy

****Correspondence:***
Zeguang Li
lizeguang@tsinghua.edu.cn

Specialty section:
This article was submitted to Nuclear Energy, a section of the journal Frontiers in Energy Research

Received: *05 January 2022*
Accepted: *29 March 2022*
Published: *05 May 2022*

Citation:
Guo Y, Su Z, Li Z, Wang K and Liu X (2022) An Improved Model of the Heat Pipe Based on the Network Method Applied on a Heat Pipe Cooled Reactor. Front. Energy Res. 10:848799. doi: 10.3389/fenrg.2022.848799

1 INTRODUCTION

Benefiting from the compact structure, low weight, and high reliability, a heat pipe cooled reactor can be widely used in aerospace, mobile power stations, deep-water exploration, and other fields. Many preliminary designs of heat pipe cooled reactor systems have been proposed, such as the Kilopower system (Poston et al., 2019), the Heatpipe-Operated Mars Exploration Reactor (HOMER) system (Poston, 2001), the (Heat Pipe-Segmented Thermoelectric Module Converter (HP-STMC) system (El-Genk and Tournier, 2004), the MegaPower reactor system (McClure et al., 2015), the eVinci reactor system (Swartz et al., 2021), and the Aurora reactor (Kadak, 2017). As the unique piece of equipment of fission heat absorption, the stable operation of the heat pipe is critical for the safety of the reactor system. Operating characteristics of the heat pipe can directly affect the power variation and temperature distribution of the reactor core. The accurate simulation of the heat pipe is important for reactor simulation and reactor design.

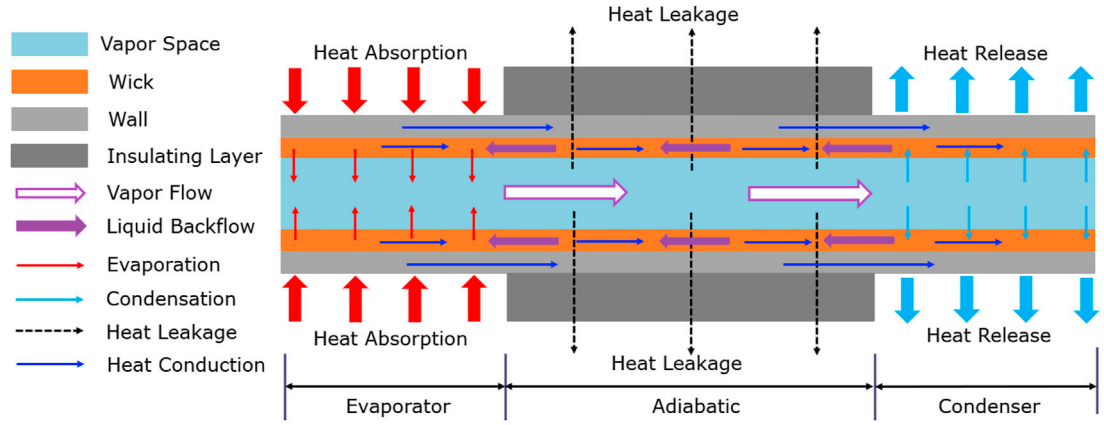

FIGURE 1 | Basic diagram of the heat pipe structure and main heat transfer process.

During the operation, the phenomena of heat conductance, heat convection, evaporation, and condensation exist in the heat pipe. **Figure 1** shows the basic composition and the heat transport of the heat pipe. It is composed of a wall, wick, vapor space, and insulating layer. The wick consists of a porous structure and liquefied working medium. As for the porous structure, it can be wrapped screen, sintered metal, groove, open artery, or other types. Along the axial direction, it is divided into an evaporator, adiabatic section, and condenser. When it is heated, the working medium evaporates and generates vapor flows to the condenser with the effective pressure head. Then, the latent heat released by condensation transfers to the secondary by axial heat conduction and heat convection. With the pumping head of capillarity, the liquefied working medium flows back to the evaporator, thus completing the heat transfer circulation. Because of the temperature difference between the heat pipe and the environment, there will be a certain amount of heat lost to the environment through the insulating layer. Moreover, the heat transfer capacity of the heat pipe is always limited by heat transfer limitations such as the capillary limit, sonic limit, boiling limit, and entrainment limit (Busse, 1973), (Faghri, 1995), (Levy and Chou, 1973).

So far, many theoretical analyses (Tournier and El-Genk, 1994; Tournier and El-Genk, 1996; Rice and Faghri, 2007) and experimental studies (El-Genk and Lianmin, 1993; Kim and Peterson, 1995; Xu and Zhang, 2005) have been carried out. In 1965, Cotter (1965) proposed the theory of the heat pipe for the first time, which laid the foundation for theoretical analyses of heat pipes. Cao and Faghri (1991) and (Cao and Faghri, 1993a) described vapor flow using two-dimensional Navier–Stokes (N–S) equations of compressible vapor and derived mass and energy transfer equations at the vapor–liquid interface. In the early startup period of high-temperature heat pipe operations, Cao and Faghri (1993b) adopted the self-diffusion model of rarefied vapor to describe vapor flow. The Knudsen number was chosen to judge the flow type of the vapor. However, this model still assumed that there was only heat conduction in the wick region. Heat transport caused by the backflow was also ignored. Faghri and Harley (1994) presented a transient lumped formulation for heat pipes. Because of the "isothermal" characteristics of the heat pipe, Faghri et al. treated the heat pipe as a control volume with uniform temperature distribution. Although this method greatly simplified modeling, only the lumped temperature was calculated which was insufficient to understand the operation characteristics of a heat pipe. Zuo and Faghri (1998) simplified the heat transportation of a heat pipe as heat conduction, ignoring the backflow in the wick and the temperature drop in the vapor space. The network model was established. Compared with the lumped model, it took the actual process of heat transportation into consideration and could obtain more information about the operation of the heat pipe. Therefore, it was widely used for the fast calculation of heat pipe performance. However, this model could not calculate the fluid flow and pressure drop during the operation. Ferrandi et al. (2013), inheriting the basic idea of the network model, regarded vapor flow as an adiabatic flow of compressible fluid to preliminarily analyze the vapor flow. However, in this model, the heat transfer between the vapor space and the wick in the adiabatic region and fluid backflow were both ignored, leading to the incapability of calculating the real temperature distribution of the heat pipe.

In recent years, many researchers have used the computational fluid dynamics (CFD) method to simulate the heat transport characteristics of heat pipes. Alizadehdakhel et al. (2010) had investigated the effect of input heat flow and fill ratio on the performance of the thermosiphon. They showed that the CFD method was useful for calculating the complex flow and heat transfer in the thermosiphon. Annamalai and Ramalingam (2011) had analyzed the characteristics of heat pipes using ANSYS CFX. They concluded that for efficient operation of the heat pipe; the condenser surface should be exposed to circulating water with a high convective coefficient, or a higher heat transfer area is required with the addition of fins in the condenser section. Lin et al. (2013) had studied the heat transfer mechanism of a miniature oscillating heat pipe (MOHP) using ANSYS FLUENT. The volume of the fluid (VOF) model and a mixture model were used for comparison. Results showed

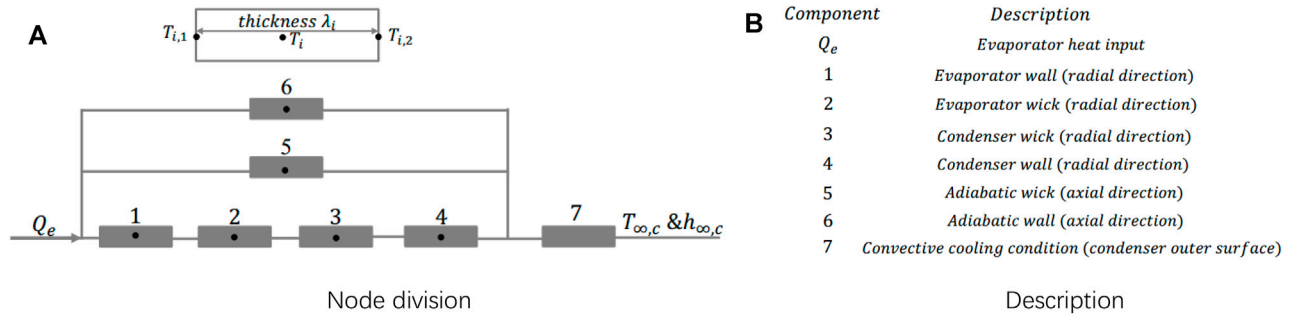

FIGURE 2 | Traditional network model for a heat pipe.

that the mixture model was more suitable for the two-phase flow simulation in an MOHP. Boothaisong et al. (2015) had established a three-dimensional model to simulate the heat transfer on heat pipes. The governing equation based on the shape of the pipe was numerically simulated using the finite element method. Yue et al. (2018) had executed the CFD simulation on the heat transfer and flow characteristics of micro-channel separate heat pipes under different filling ratios. The CFD method can realize the three-dimensional modeling of heat pipes. Important phenomena of the two-phase flow, evaporation, condensation, and entrainment can also be simulated. However, it consumes a lot of computing resources and calculates slowly. Moreover, for different sizes and types of heat pipes, geometry establishment and mesh generation have to be carried out which means that the flexibility of the model is poor.

For heat pipe cooled reactor systems, situations of non-uniform heating and cooling, heat leakage, and inclined operation may occur. The existing models either cannot consider these factors comprehensively or have shortcomings of a low calculation efficiency. In this study, an improved model based on the network method is proposed. It realizes the fast and flexible calculation of the heat pipe performance, and it can obtain the variation of temperature, flow rate, pressure drop, and other parameters. After verifying the validity of the model by comparing with the experimental results of the copper-water heat pipe, the operating characteristics of high-temperature sodium heat pipes are analyzed in different cases. The effects of a non-uniform heat transfer, heat leakage, and gravity on heat pipe operations are discussed in detail.

2 DESCRIPTION OF THE IMPROVED NETWORK MODEL

First, both the method and main limitations of a network model are described in **Section 2.1**. In **Section 2.2**, the improved model is demonstrated, and the conservation equations of each region are established. According to the modification of this model, it can calculate the temperature distribution of the heat pipe and can obtain the flow characteristics and pressure distribution.

2.1 Network Model for Heat Pipes

Zuo and Faghri (1998) had proposed the classical network model for heat pipes in 1996 (**Figure 2**), which had been widely used in heat pipe cooled reactor simulation (Yuan et al., 2016). For this model, it was considered that the heat absorbed in the evaporator was transported to the condenser through heat conductance, and the temperature drop caused by the vapor flow was ignored. Meanwhile, it ignored the high-speed vapor flow in the vapor space, the fluid backflow in the wick, and the evaporation/condensation at the vapor–liquid interface. Since only six temperature variables need to be calculated, it can obtain the fast calculation of heat pipe performance. But the information on fluid flow and pressure distribution is lost.

2.2 Improved Network Model for Heat Pipe

Figure 3 shows the node division for this improved model. To account for the non-uniform heat transfer and heat leakage, several temperature nodes are set in each region. The actual number of nodes can be flexibly adjusted based on the actual length of each region and the requirement of computational accuracy. Both the axial and the radial heat conductance are included at each node. Particularly, the heat transportation of the liquid backflow in the wick and evaporation or condensation between the wick and the vapor space are contained to realize the simulation of heat pipe operations as real as possible. Meanwhile, the gravity term is added to the flow equations to preliminarily analyze the operating characteristics under different angles of inclination. Particularly, if the fluid flow, evaporation, condensation, and heat leakage were all ignored, this model would degenerate into the network model. It should be mentioned that this model cannot be used for the transient calculation on heat pipe startups because the melting and redistribution of the working medium are not included in this model.

To simplify the modeling difficulty, there are some assumptions:

1) Heat conduction is two-dimensional;
2) Vapor flow is a one-dimensional, compressible, and adiabatic flow;

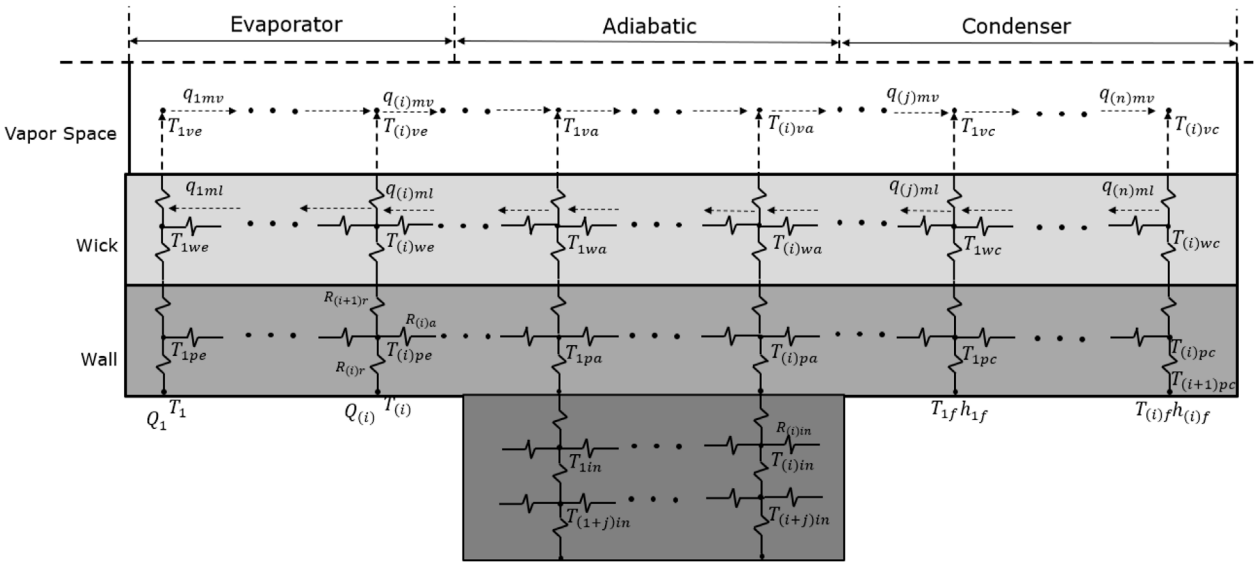

FIGURE 3 | Schematic diagram of the improved heat pipe model.

3) Vapor is treated as a compressible ideal gas;
4) Liquid in the wick is incompressible, and the wick volume is constant;
5) Gravity does not cause the redistribution of the working medium;
6) The temperature at the vapor–liquid interface is always the saturated temperature.

Actually, when the working medium is completely melted, there will be an accumulation of the working medium caused by gravity. The redistribution of the working medium may affect the operation of the heat pipe. Further studies will be executed to discuss the effect of gravity.

In this model, there are radial thermal resistance, axial thermal resistance, and convective thermal resistance. They are defined as follows:

$$\text{Radial thermal resistance}: R_{(i)r} = \frac{\ln(r_{out}/r_{in})}{2\pi k_{(i)} L_{(i)}}, \tag{1}$$

$$\text{Axial thermal resistance}: R_{(i)a} = \frac{L_{(j)}}{\pi(r_{out}^2 - r_{in}^2)k_{(i)}}, \tag{2}$$

$$\text{Convective thermal resistance}: R_{(i)f} = \frac{1}{2\pi r_{out} L_{(k)} \lambda_{(i)}}. \tag{3}$$

2.2.1 Modeling in the Wall Region

Along the axial direction, the wall is divided into three regions. The Neumann boundary condition is set on the boundary surface of the evaporator. There can be different heating powers for each node. The conservation equation can be written as follows:

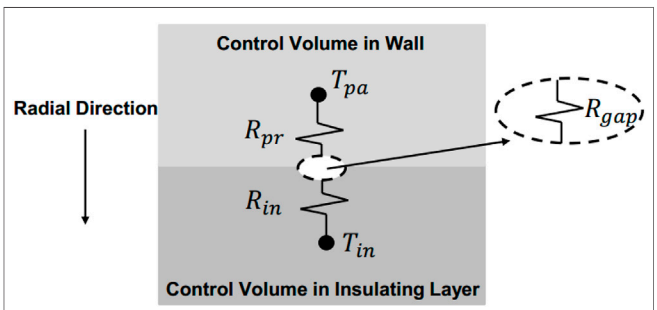

FIGURE 4 | Contact heat transfer between the wall and insulating layer.

$$\rho_{(i)pe} C_{(i)pe} \frac{dT_{(i)pe}}{dt} = Q_{(i)in} + \frac{T_{(i-1)pe} - T_{(i)pe}}{R_{(i-1)a}} - \frac{T_{(i)pe} - T_{(i+1)pe}}{R_{(i)a}} - \frac{T_{(i)pe} - T_{(i)we}}{R_{(i+1)r} + R_{(i+2)r}}. \tag{4}$$

As for the wall region in the adiabatic section, there is heat conduction between the wall and the insulating layer. Thermal contact resistance between two regions is ignored.

$$\rho_{(i)pa} C_{(i)pa} \frac{dT_{(i)pa}}{dt} = \frac{T_{(i-1)pa} - T_{(i)pa}}{R_{(i-1)a}} + \frac{T_{(i)wa} - T_{(i)pa}}{R_{(i+1)r} + R_{(i+2)r}} - \frac{T_{(i)pa} - T_{(i+1)pa}}{R_{(i)a}} - \frac{T_{(i)pa} - T_{(i)in}}{R_{(i)r} + R_{(i)in}}. \tag{5}$$

Actually, if it is needed to consider the contact conductance, adding the thermal contact resistance on the radial heat transfer path between two regions is feasible (**Figure 4**). The thermal contact resistance can be obtained through empirical relations or

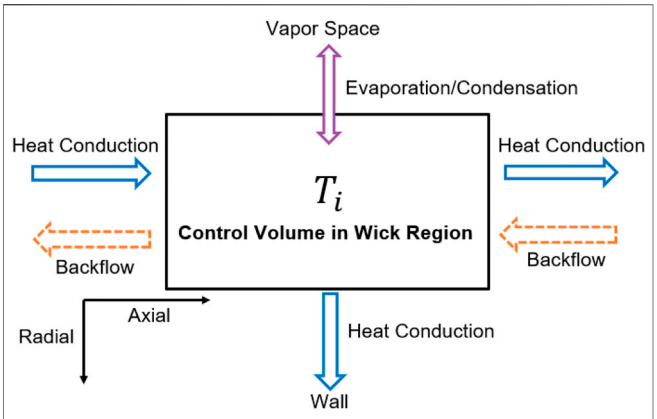

FIGURE 5 | Heat transfer process in the wick.

contact heat transfer models (Song and Yovanovich, 1988) (Kumar and Ramamurthi, 2001).

$$Q_{radial} = \frac{T_{pa} - T_{in}}{R_{pr} + R_{in} + R_{gap}}. \tag{6}$$

On the condenser wall surface, the Robin boundary condition is adopted as follows:

$$\rho_{(i)pc} C_{(i)pc} \frac{dT_{(i)pc}}{dt} = \frac{T_{(i-1)pc} - T_{(i)pc}}{R_{(i-1)a}} + \frac{T_{(i)wc} - T_{(i)pc}}{R_{(i+1)r} + R_{(i+2)r}} - \frac{T_{(i)pc} - T_{(i+1)pc}}{R_{(i)a}} - \frac{T_{(i)pc} - T_{(i)f}}{R_{(i)r} + R_{(i)f}}. \tag{7}$$

For the surface temperature of the wall, the continuous heat flow criterion is used for deducing the temperature:

$$Q_{(i)in} = A_{(i)pe} k_{(i)pe} \frac{T_{(i)} - T_{(i)pe}}{Thick_{(i)}}, \tag{8}$$

$$\frac{T_{(i)pc} - T_{(i)f}}{R_{(i)r} + R_{(i)f}} = \frac{T_{(i)pc} - T_{(i+1)pc}}{R_{(i)r}}. \tag{9}$$

Thus, the surface temperature can be obtained as follows:

$$T_{(i)} = T_{(i)pe} + \frac{Q_{(i)in}}{A_{(i)pe} k_{(i)pe}} Thick_{(i)}, \tag{10}$$

$$T_{(i+1)pc} = T_{(i)pc} - \frac{T_{(i)pc} - T_{(i)f}}{R_{(i)r} + R_{(i)f}} R_{(i)r}. \tag{11}$$

2.2.2 Modeling in the Insulating Layer

Similarly, the temperature nodes in this region can be increased or decreased based on the calculation requirement. Conservation equations can be obtained as follows:

$$\rho_{(i)in} C_{(i)in} \frac{dT_{(i)in}}{dt} = \frac{T_{(i-1)in} - T_{(i)in}}{R_{(i-1)in}} + \frac{T_{(i)pa} - T_{(i)in}}{R_{(i+1)r} + R_{(i+2)r}} - \frac{T_{(i)in} - T_{(i+1)in}}{R_{(i)in}} - \frac{T_{(i)in} - T_{(i+j)in}}{R_{(i)r}}. \tag{12}$$

2.2.3 Modeling in the Wick Region

2.2.3.1 Temperature Equations

Heat transfer in the wick is shown in **Figure 5**. It includes evaporation/condensation, radial heat conduction, axial heat conduction, and heat transport of the working medium backflow. Evaporation/condensation between the vapor space and the wick can be expressed, as shown in **Figure 6**. According to the assumptions (2) and (6), the vapor temperature is considered to be equal to the vapor–liquid interface temperature.

$$T_v = T_f, \tag{13}$$

$$Q_{evap/cond} = \frac{T_i - T_f}{R_i} = \frac{T_i - T_v}{R_i}. \tag{14}$$

Heat transfer by evaporation/condensation can be obtained as follows:

$$\text{Evaporator}: Q_{evap} = \frac{T_{(i)we} - T_{(i)ve}}{R_{(i+1)r}}, \tag{15}$$

$$\text{Adiabatic section}: Q_{adia} = \frac{T_{(i)va} - T_{(i)wa}}{R_{(i+1)r}}, \tag{16}$$

$$\text{Condenser}: Q_{cond} = \frac{T_{(i)vc} - T_{(i)wc}}{R_{(i+1)r}}. \tag{17}$$

The mass flow rate can also be obtained as follows:

$$\text{Evaporator}: q_{evap} = \frac{T_{(i)we} - T_{(i)ve}}{R_{(i+1)r} h_v (T_{(i)ve})}, \tag{18}$$

$$\text{Adiabatic section}: q_{adia} = \frac{T_{(i)va} - T_{(i)wa}}{R_{(i+1)r} h_v (T_{(i)va})}, \tag{19}$$

$$\text{Condenser}: q_{cond} = \frac{T_{(i)vc} - T_{(i)wc}}{R_{(i+1)r} h_v (T_{(i)vc})}. \tag{20}$$

According to the assumption (4), the backflow rate in the wick core can be obtained as follows:

$$q_{(i)ml} = \sum_{j=i+1}^{12} q_{(j)v}, \begin{cases} q_{(j)v} < 0 & evaporation, \\ q_{(j)v} > 0 & condensation. \end{cases} \tag{21}$$

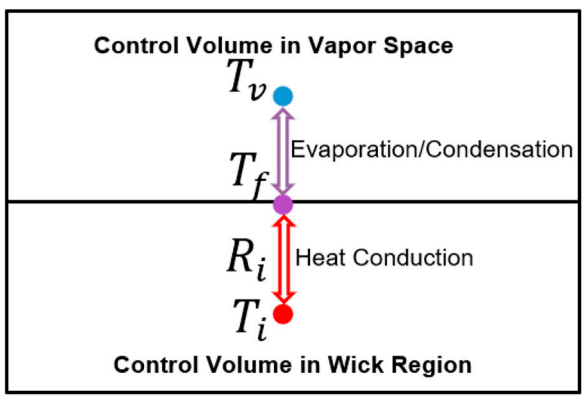

FIGURE 6 | Evaporation/condensation between the wick and the vapor space.

Therefore, the energy equation can be summarized as follows:

$$\rho_{(i)we}C_{(i)we}\frac{dT_{(i)we}}{dt} = \frac{T_{(i-1)we}-T_{(i)we}}{R_{(i-1)a}} - \frac{T_{(i)we}-T_{(i+1)we}}{R_{(i)a}} - \frac{T_{(i)we}-T_{(i)ve}}{R_{(i+1)r}} - \frac{T_{(i)we}-T_{(i)pe}}{R_{(i)r}+R_{(i-1)r}} + q_{(i)ml}h_{(i)l} - q_{(i-1)ml}h_{(i-1)l}. \tag{22}$$

2.2.3.2 Flow Equations

The wick is regarded as a porous structure. The porous medium model is used for describing the flow of the working medium. In addition, the gravity term is added in the equation as follows:

$$\rho g + \nabla P = -\frac{\mu}{K}u. \tag{23}$$

Definition of the liquid flow rate is

$$q_{ml} = \rho_f \varepsilon\pi\left(r_{out}^2 - r_{in}^2\right)u. \tag{24}$$

Combining **Eq. 23** with **Eq. 24** and integrating on length L_{eff} we obtain the following equation:

$$\frac{\mu L_{eff}}{K\rho_f}\frac{1}{\varepsilon\pi\left(r_{out}^2 - r_{in}^2\right)}q_{ml} = P_1 - P_2 + \rho_f g L_{eff} sin\theta. \tag{25}$$

In other words,

$$P_2 - P_1 = \nabla P = \frac{\mu L_{eff}}{K\rho_f}\frac{1}{\varepsilon\pi\left(r_{out}^2 - r_{in}^2\right)}q_{ml} - \rho_f g L_{eff} sin\theta. \tag{26}$$

The permeability parameter K can be estimated using the following empirical correlation.

$$K = \frac{4r_g^2\varepsilon^2}{150(1-\varepsilon)^2}. \tag{27}$$

Therefore, the pressure drop caused by the flow in the wick can be solved when the flow rate is known.

2.2.3.3 Physical Parameter Calculation in the Wick

The wick is composed of a porous structure and liquefied working medium. In this model, two different materials are regarded as the equivalent material. The physical parameters such as density, specific heat capacity, and thermal conductivity coefficient can be calculated by the following formula (Bowman, 1991):

$$\rho_{equ} = \varepsilon\rho_f + (1-\varepsilon)\rho_w, \tag{28}$$

$$C_{equ} = \varepsilon C_f + (1-\varepsilon)C_w, \tag{29}$$

$$k_{equ} = k_l\frac{(k_l+k_w) - (1-\varepsilon)(k_l-k_w)}{(k_l+k_w) + (1-\varepsilon)(k_l-k_w)}. \tag{30}$$

2.2.4 Modeling in the Vapor Space

2.2.4.1 Vapor Density Equations

In the vapor space, there are evaporation, condensation, and vapor flow. Using the law of conservation of mass, the vapor density equation can be obtained as follows:

$$V_{(i)v}\frac{d\rho_{(i)v}}{dt} = q_{(i)v} + q_{(i-1)mv} - q_{(i)mv}. \tag{31}$$

2.2.4.2 Vapor Pressure Equations

Based on the assumption (2), the relation between pressure and density can be obtained by the following equation:

$$\frac{\partial P_v}{\partial \rho_v} = \gamma R_g T_v. \tag{32}$$

So

$$\frac{d\rho_v}{dt} = \frac{1}{\gamma R_g T_v}\frac{dp_v}{dt}. \tag{33}$$

Taking this correlation into **Eq. 31**, the vapor pressure equation can be obtained:

$$\frac{dP_{(i)v}}{dt} = \frac{\gamma R_g T_{(i)v}}{V_{(i)v}}\left(q_{(i)v} + q_{(i-1)mv} - q_{(i)mv}\right). \tag{34}$$

2.2.4.3 Vapor Temperature Equations

Similarly, according to the assumptions, the relationship between the pressure and temperature can be obtained:

$$\frac{\gamma}{\gamma-1}\frac{P_v}{T_v}\frac{dT_v}{dt} = \frac{dP_v}{dt}. \tag{35}$$

Combined with **Eq. 34**, the vapor temperature equation can be written as follows:

$$\frac{dT_{(i)v}}{dt} = \frac{(\gamma-1)R_g}{V_{(i)v}}\frac{T_{(i)v}^2}{P_{(i)v}}\left(q_{(i)v} + q_{(i-1)mv} - q_{(i)mv}\right). \tag{36}$$

2.2.4.4 Vapor Flow Equations

For the vapor flow in the vapor space, it is assumed to be a one-dimensional, unsteady, and compressible laminar flow. In the N–S equation, it contains the time term, gravity axial term, convective transport term, surface friction term, and pressure gradient term. It can be seen as follows (Bowman, 1991):

$$\frac{\partial(\rho u)}{\partial t} = \rho g sin\theta - \frac{\partial(\rho u^2)}{\partial x} - \frac{2\tau_w}{R} - \frac{\partial P}{\partial x}. \tag{37}$$

Integrating this equation on length L_v, it can be concluded as follows:

$$\frac{L_v}{\pi r_i^2}\frac{dq_v}{dt} = \rho_v g L_v sin\theta + \left(\frac{q_v^2}{\rho_v\pi^2 r_i^4}\right)_{1v} - \left(\frac{q_v^2}{\rho_v\pi^2 r_i^4}\right)_{2v} - \frac{8\mu L_v}{\rho_v\pi r_i^4}q_v + P_{1v} - P_{2v}. \tag{38}$$

Appling **Eq. 38** into the calculation of the working medium flow in the vapor space, we obtain the following equation:

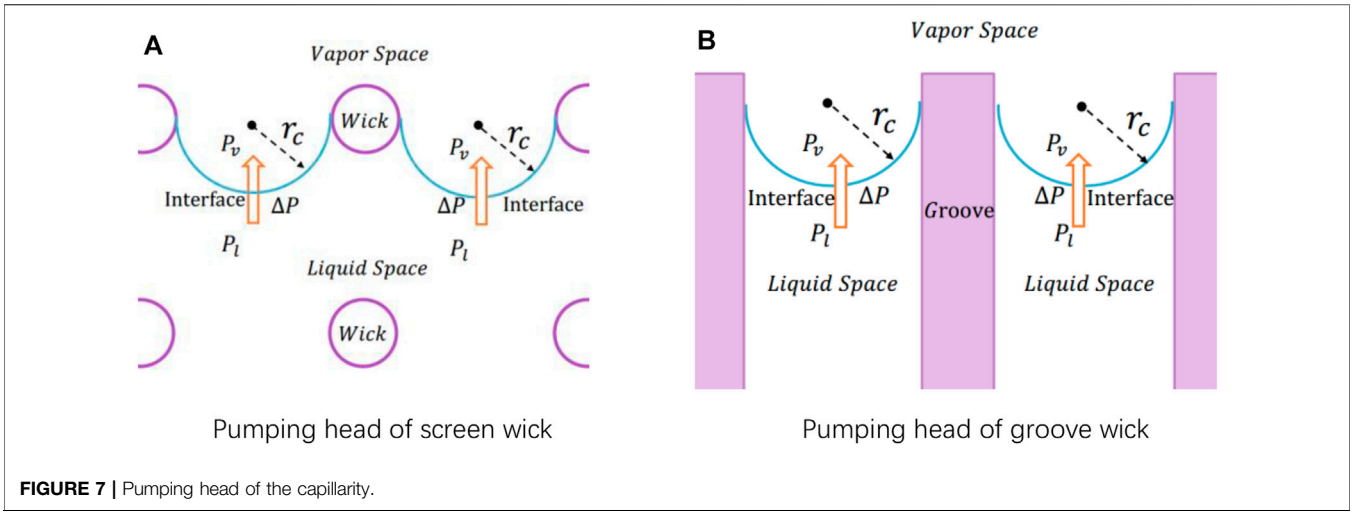

FIGURE 7 | Pumping head of the capillarity.

$$\frac{L_{(i)v}}{\pi r_{in}^2}\frac{dq_{(i)mv}}{dt} = -\frac{8\mu L_{(i)v}}{\rho_{(i)v}\pi r_{in}^4}q_{(i)mv} + \frac{1}{\rho_{(i)v}\pi^2 r_{in}^4}q_{(i)in}^2 - \frac{1}{\rho_{(i+1)v}\pi^2 r_{in}^4}q_{(i)out}^2 + P_{(i)v} - P_{(i+1)v} + \rho_{(i)v}gL_{(i)v}sin\theta. \tag{39}$$

2.3 Judgment of the Capillary Limit

At the vapor–liquid interface between the wick and vapor space, the concave vapor–liquid surface can form the pumping head of the capillarity (**Figure 7**). The pumping head acts as the power of the stable flow. When the heat absorption of the evaporator exceeds a certain limitation, the liquid returned by the pumping head cannot meet the required flow rate of evaporation, and the temperature in the evaporator will rise rapidly as a consequence of drying up in the wick. The heat pipe may be damaged.

The maximum pumping head of the capillarity provided by the heat pipe is as follows:

$$P_v - P_l = \frac{2\sigma}{r_c}. \tag{40}$$

To ensure that the heat pipe is always below the capillary limit, the following relation needs to be met:

$$\frac{2\sigma}{r_c} \geq \sum_{i=1}^{11} P_{(i)v} + \sum_{j=1}^{11} P_{(j)l} + \int_0^L \rho_l g sin\theta dl - \int_0^L \rho_v g sin\theta dl. \tag{41}$$

According to **Eqs. 26**,**34**, the pressure drop on each flow path can be calculated. When the angle of inclination is known, **Eq. 41** can be adopted to judge whether the heat pipe reaches the capillary limit.

2.4 Numerical Algorithm of the Improved Model

The presented heat pipe model can be expressed as follows:

TABLE 1 | Basic description of a copper-water heat pipe (Huang et al., 1993).

Description	Value
Length of the evaporator (*mm*)	600.0
Length of the adiabatic section (*mm*)	90.0
Length of the condenser (*mm*)	200.0
Outer diameter of the heat pipe (*mm*)	19.1
Inner diameter of the vapor space (*mm*)	17.3
Wall thickness (*mm*)	0.15
Wick thickness (*mm*)	0.75
Effective porosity of the wick	0.5
Initial temperature (*K*)	296.3
Inlet coolant temperature in secondary (*K*)	294.5
Convective coefficient in secondary ($W/(m^2 \cdot K)$)	1800.0
Mass flow rate in secondary (*g*/s)	11.33
Electric power (*W*)	575.0
Efficient power (*W*)	443.0
Leakage power (*W*)	132.0

$$\begin{cases} \frac{dY}{dt} = f(t, Y) \\ Y(t_0) = Y_0 \end{cases}. \tag{42}$$

Unknown variables including the temperature, density, pressure, and flow rate can be calculated as follows:

$$Y = \left[T_{(i)pe}, T_{(i)pa}, T_{(i)pc}, T_{(i)we}, T_{(i)wa}, T_{(i)wc}, T_{(i)ve}, T_{(i)va}, T_{(i)vc}, \rho_{(i)ve}, \rho_{(i)va}, \rho_{(i)vc}, P_{(i)ve}, P_{(i)va}, P_{(i)vc}, q_{(j)mv}, T_{(k)in}\right]. \tag{43}$$

Methods for solving this type of differential equation can be the Euler algorithm, Runge–Kutta algorithm, linear multistep method, and so on. In this study, the implicit Runge–Kutta algorithm is used. The basic solving process of this algorithm is as follows:

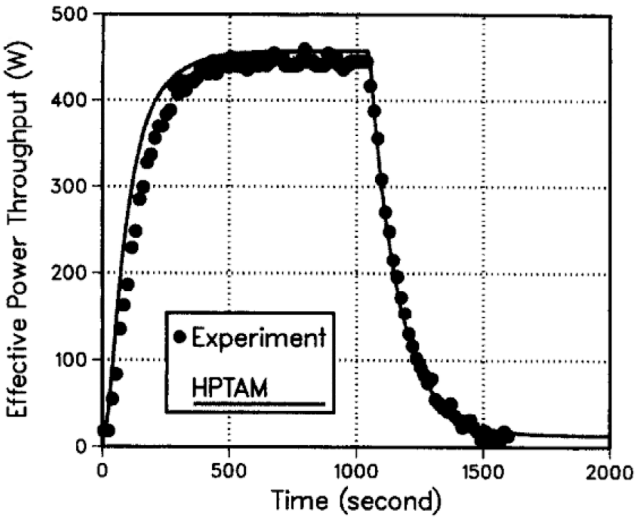

FIGURE 8 | Original data of effective power (Tournier and El-Genk, 1994).

$$\begin{cases} Y_{n+1} = Y_n + h\sum_{i=1}^{m} b_i k_i \\ k_{i,j} = f\left(t_n + \tau_i h, Y_n + h\sum_{j=1}^{m} a_{ij} k_j\right) i = 1, 2, \cdots m \end{cases}. \quad (44)$$

here, $t_n = t_0 + nh(n = 0, 1, \cdots)$, h is the transient time step, $b = [b_1, b_2, \cdots b_m]$ is the weight coefficient vector, $\tau = [\tau_1, \tau_2, \cdots \tau_m]$ is the node coefficient vector, and $a = [a_{11}, a_{12}, \cdots a_{1m}, a_{21}, a_{22}, \cdots a_{2m}, \cdots a_{mm}]$ is the coefficient matrix.

3 MODEL VALIDATION

To verify the correctness of this model, experimental results of a copper-water heat pipe (Tournier and El-Genk, 1994) (Huang et al., 1993) are chosen. The description of this heat pipe is shown in **Table.1**.

In calculation, the effective power is regarded as the real power in the evaporator. It is assumed that the heat pipe system is well insulated, and there is no heat leakage. For the evaporator, heat source distribution is assumed to be uniform. For the condenser, the convective coefficient is constant, and the fluid temperature at the corresponding node is calculated according to the law of conservation of energy.

$$T_{(i)f} = \sum_{j=1}^{i-1}\left(\frac{T_{(j)pc} - T_{(j)f}}{R_{(j)pc} + R_{(j)f}}\right) \Big/ C_f + T_{1f} \quad i = 1, 2, 3, 4. \quad (45)$$

The model predictions are compared with the experimental results of Huang et al. (1993) and the calculated results using the proposed heat pipe transient analysis model (HPTAM) of Tournier and El-Genk (1994) for horizontal water heat pipes (**Figure 8**). Based on the experimental data, the variation of effective power in the evaporator is fitted linearly, and the fitting

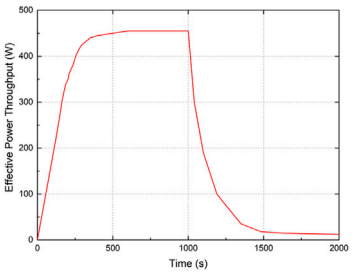

FIGURE 9 | Fitted curve of effective power.

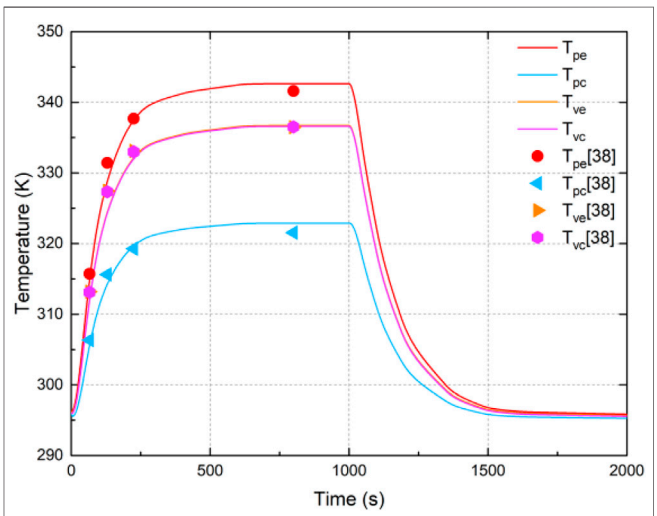

FIGURE 10 | Comparison with experimental results.

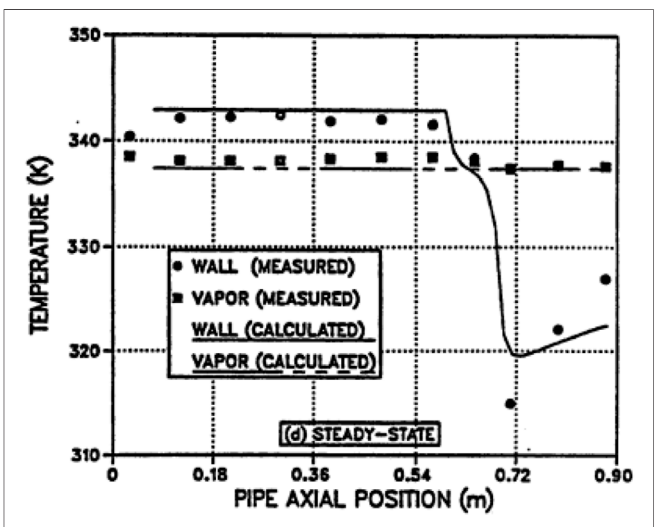

FIGURE 11 | Temperature distribution in the steady state (Tournier and El-Genk, 1994).

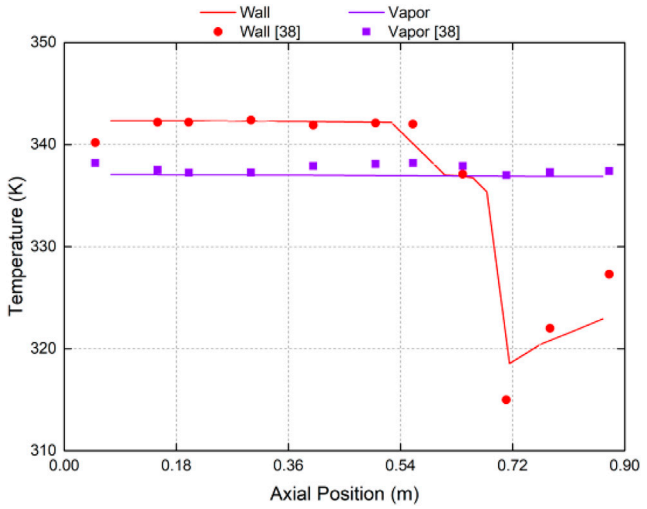

FIGURE 12 | Calculated temperature distribution in the steady state.

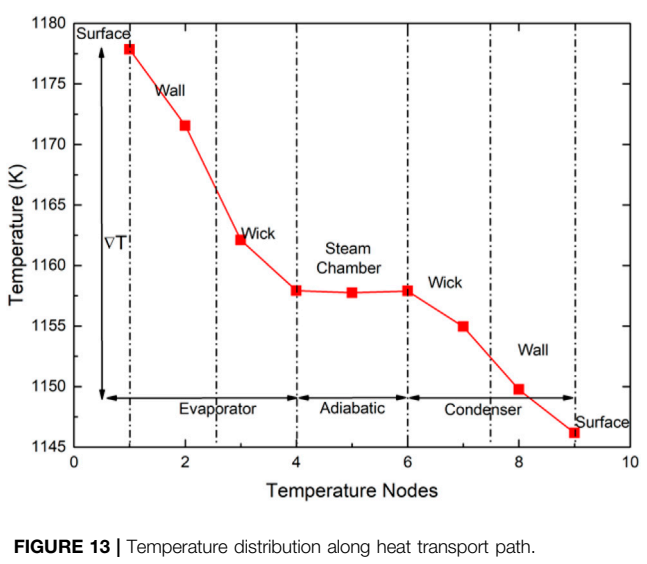

FIGURE 13 | Temperature distribution along heat transport path.

TABLE 2 | Parameter description of a sodium heat pipe.

Description	Value
Length of the evaporator (*mm*)	300.0
Length of the adiabatic section (*mm*)	200.0
Length of the condenser (*mm*)	500.0
Outer diameter of the heat pipe (*mm*)	25.0
Inner diameter of the vapor space (*mm*)	19.0
Wall thickness (*mm*)	2.0
Wick thickness (*mm*)	1.0
Thickness of the insulating layer (*mm*)	70.0
Wick porosity	0.96
Wick structure	Screen wick
Wick grain radius (*mm*)	0.01
Wall material	316-L stainless steel
Wick material	316-L stainless steel
Working medium	Sodium
Density of the insulating layer (kg/m^3)	230.0
Heat capacity of the insulating layer ($J/(kg \cdot K)$)	900.0
Thermal conductivity of the insulating layer ($W/(m \cdot K)$)	0.1
Absorbed power (W)	3,000.0
Coolant temperature in secondary (K)	650.0
Convective coefficient in secondary ($W/(m^2 \cdot K)$)	152.7
Environment temperature (K)	300.0
Convective coefficient in the insulating layer ($W/(m^2 \cdot K)$)	20.0

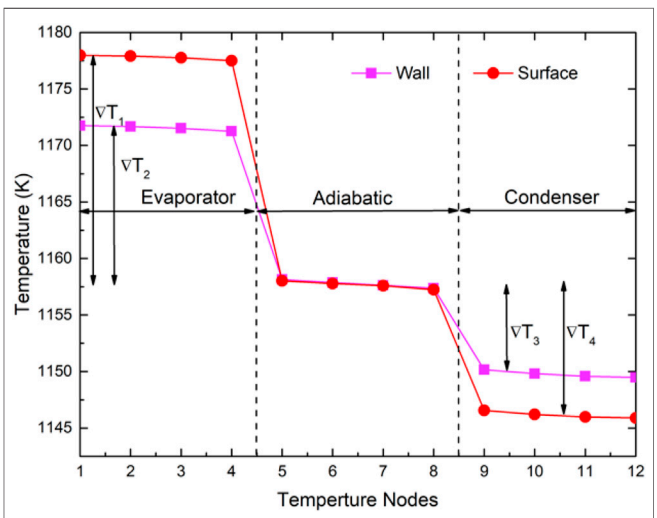

FIGURE 14 | Temperature distribution along the heat transport path.

formula is used for describing the real change of the heating power in the model (**Figure 9**).

In this model, each region contains multiple temperature nodes. The arithmetic mean value of the temperature nodes in the corresponding region is selected for the comparison between these results. **Figure 10** shows the temperature variation of the heat pipe with time. The curve shows the calculated results using this model, and the scatter is the measuring results by experiment. From the figure, it can be found that the calculated results are in good agreement with the experimental results. Meanwhile, it can be seen that there is little difference between the vapor temperature in the evaporator and that in the condenser. For the water heat pipe, the temperature drop in the vapor space can indeed be ignored. **Figures 11**, **12** show the temperature distribution in a steady state. Benefiting from the capability of describing non-uniform cooling, this model can calculate the temperature rise on the wall surface of the condenser section, causing the rise of the wall temperature. As a consequence, the correctness of this model is validated.

4 CASE ANALYSIS

Four cases of standard operation, non-uniform heat transfer, heat leakage, and inclined operation are respectively carried out to analyze the operating characteristics of the heat pipe. They are

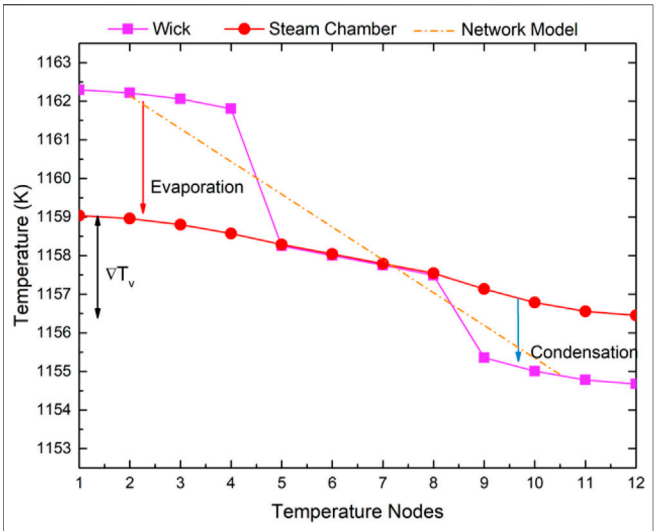

FIGURE 15 | Temperature distribution of the wall and the surface in the axial direction.

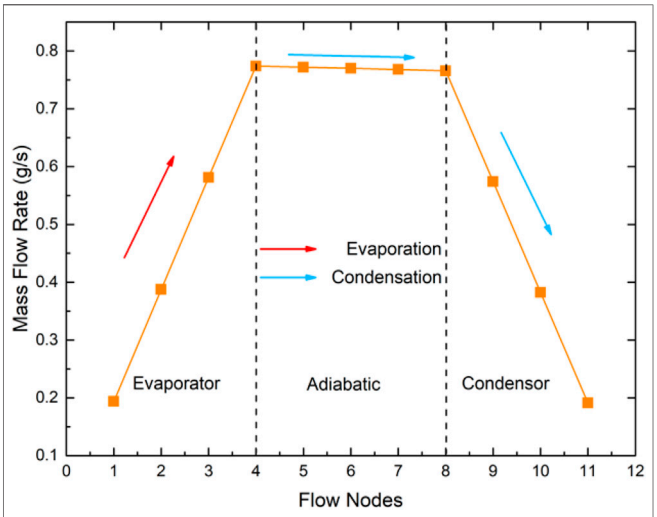

FIGURE 16 | Temperature distribution of the wick and the vapor space.

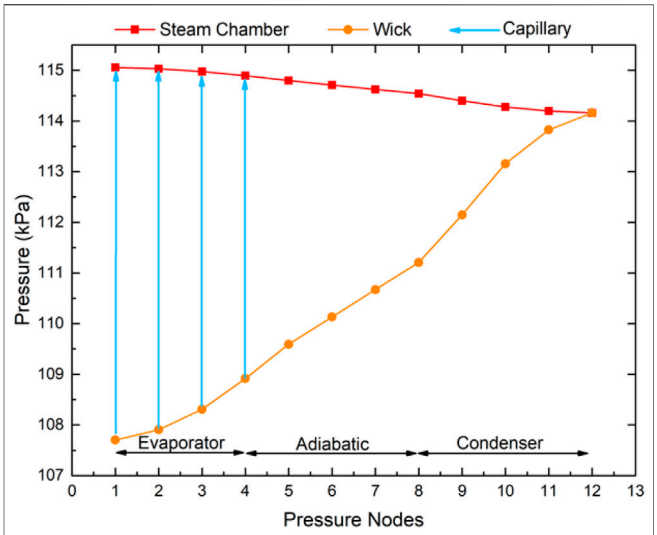

FIGURE 17 | Mass flow rate in the vapor space.

also the situations that may occur during the operation of the heat pipe cooled reactor. A hypothetical high-temperature sodium heat pipe is taken as the research object. The basic description of this heat pipe is listed in **Table 2**. As for the physical parameters of sodium, such as density, heat capacity, thermal conductivity, enthalpy, and surface tension, they can be found in the report published by the Argonne National Laboratory (Fink and Leibowitz, 1995).

4.1 Case With Standard Operation

In this case, it is assumed that the heat pipe is uniformly heated and uniformly cooled. The insulating layer is treated as natural convection with the environment. **Figure 13** shows the temperature distribution along the heat transport path. The arithmetic mean value of the corresponding region is chosen as the characteristic temperature. The surface temperature of the wall is calculated by **Eqs. 10**, **11** and considers this influence on the temperature distribution of the heat pipe. From **Figure 13**, it can be seen that the total temperature drop of this heat pipe is 31.7 K. The temperature drop in the evaporator is more obvious than that in the condenser. It is because the shorter length of the evaporator causes higher radial thermal resistance, and the higher thermal resistance leads to a larger temperature drop.

As shown in **Figure 14**, the temperature distribution in each region is generally uniform, and the temperature drop in the axial direction is mainly concentrated in the transition section between different regions. The wall temperature difference between the evaporator and the adiabatic section is 13.8 K, and the temperature difference between the adiabatic section and the condenser is 8.1 K. As for the surface temperature differences, they are 19.1 and 13.6 K.

Figure 15 shows the temperature distribution of the wick and the vapor space along the axial direction. The broken line represents the wick temperature distribution using the network model. In that model, the evaporation, condensation, and working medium backflow are all ignored, which means only axial heat conduction exists in the wick. Therefore, the calculated temperature distribution of the wick is linear. From **Figure 15**, it can be found that the results of the improved model are more reasonable. In the evaporator and condenser, there is always a temperature difference between the wick and vapor space due to the evaporation and condensation of the liquid medium. The wick temperature in the adiabatic section remains basically the same as that of the vapor space, with only a temperature difference of about 0.04 k. The reason is shown in **Figure 5**. Heat transfer modes in the wick include axial heat conduction, radial heat conduction, evaporation/condensation heat transfer, and heat transport of fluid backflow. In this case, the axial heat

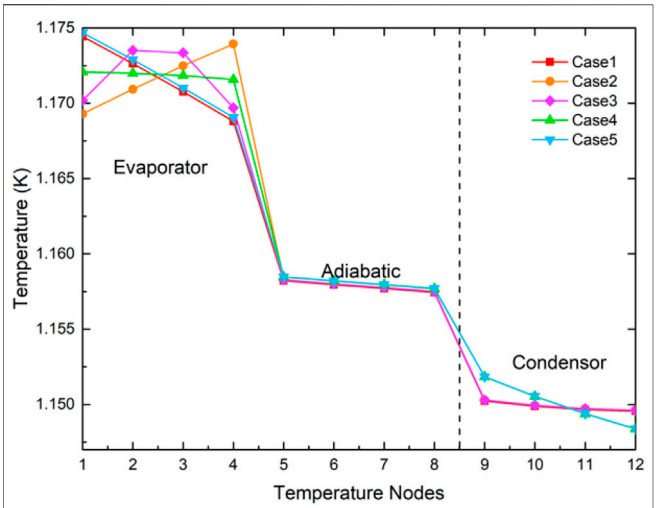

FIGURE 18 | Pressure variation in circulation.

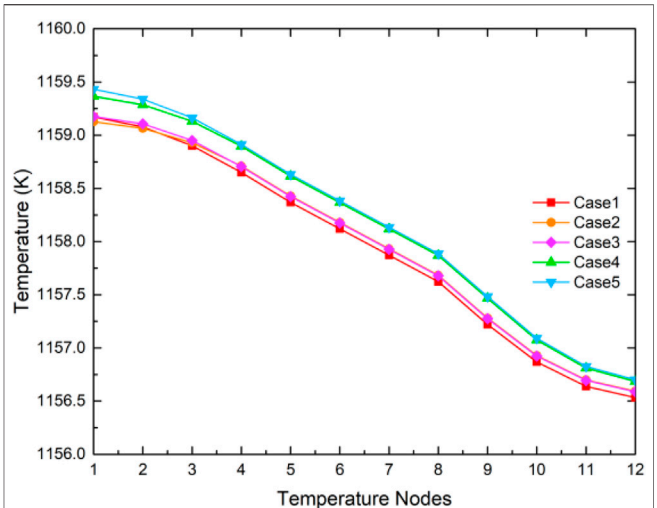

FIGURE 19 | Wall temperature distribution in different cases (1).

TABLE 3 | Description of a non-uniform heat transfer boundary condition.

	Q_{1in} (W)	Q_{2in} (W)	Q_{3in} (W)	Q_{4in} (W)	h_{1f} (W/m^2)	h_{2f} (W/m^2 · K)	h_{3f} (W/m^2 · K)	h_{4f} (W/m^2 · K)
Case 1	900.0	800.0	700.0	600.0	152.7	152.7	152.7	152.7
Case 2	600.0	700.0	800.0	900.0	152.7	152.7	152.7	152.7
Case 3	650.0	850.0	850.0	650.0	152.7	152.7	152.7	152.7
Case 4	750.0	750.0	750.0	750.0	122.7	142.7	162.7	182.7
Case 5	900.0	800.0	700.0	600.0	122.7	142.7	162.7	182.7

conduction is not obvious. The radial heat conduction due to heat leakage and the working medium backflow causes a heat loss of the control volume. The heat release of condensation between the vapor space and wick can compensate for such heat loss to keep the temperature constant. Because the heat loss is not obvious, the condensing flow is small, causing only a small temperature difference between the wick and the vapor space. In addition, it can be found that the temperature difference in the vapor space is about 2.6 K due to the energy dissipation caused by high-speed flow and wall friction.

This model can also simulate the flow distribution and pressure variation during the flow circulation. In this case, it is assumed that the heat pipe is uniformly heated, and the vapor flow rate increases linearly along the axial direction (**Figure 16**). Because of the good insulation of the adiabatic section, the condensation in this area is negligible. When the vapor flows to the condenser, the flow rate decreases sharply because of the condensation. **Figure 17** shows the pressure variation in flow circulation. Although the vapor density is lower, there is still a pressure drop of about 897.2 Pa in the vapor chamber due to the accelerated pressure drop and frictional pressure drop of the vapor flow. In the wick region, caused by the viscous flow in the porous medium, the pressure drop is about 6,159.1 Pa. Then, with the pumping head of capillarity, the pressure rises to maintain the stable flow.

4.2 Case With Non-Uniform Heating and Cooling

In a heat pipe cooled reactor, heating and cooling to a high-temperature heat pipe are always non-uniform. In this section, these effects on a heat pipe are preliminarily discussed. The steady-state performance of heat pipes under different boundary conditions is discussed. A detailed description of different cases is shown in **Table 3**.

Figure 18 shows the temperature distribution of the wall in different cases. From the figure, it can be seen that the non-uniform boundary condition does change the temperature distribution in the corresponding regions. The actual temperature distribution is determined by the specific boundary condition. In general, the higher the heating power, the higher will be the temperature. The more the cooling power, the lower temperature will be. Meanwhile, it can be found that non-uniform heating and non-uniform cooling both lead to a larger temperature difference in the heat pipe. The greater the non-uniformity is, the larger the temperature difference will be. In case 5, the total temperature difference is 33.76 K, which is up to 19.54% compared with the standard case.

Combining **Figures 18**, **19**, it can be concluded that non-uniform heating does not affect the temperature distribution of the condenser and non-uniform cooling does not change the temperature distribution of the evaporator. It is because the non-

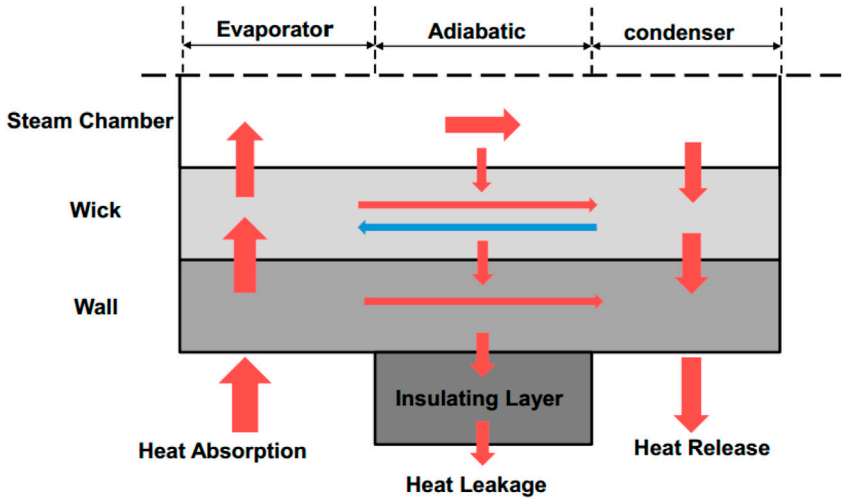

FIGURE 20 | Vapor temperature distribution in different cases.

uniformity of heating or cooling does not obviously change the vapor temperature in the vapor space. For the heat transport between the evaporator and condenser, it is achieved through flow heat transfer of the vapor. The high-speed flow of the vapor can effectively eliminate the influence of non-uniform heat transfer on the operation of the heat pipe.

4.3 Case With Heat Leakage

In a heat pipe cooled reactor, because of the large number of heat pipes used, heat leakage through the insulating layer will be regarded as an important part of the system's heat dissipation. In this section, the operating characteristics of heat pipes under different heat leakage conditions are preliminarily analyzed. Because of the heat convection between the insulating layer and the environment, obvious condensation between the vapor space and the wick will exist. The latent heat released by condensation will be transferred to the environment through radial heat conduction (**Figure 20**).

In the calculations, the thermal conductivity of the insulating layer is modified to $3W/(m \cdot K)$ (case 6), $6W/(m \cdot K)$ (case 7), and $12W/(m \cdot K)$ (case 8), respectively. Other parameters remain unchanged.

Figure 21 shows the temperature distribution of the wall in cases of high heat leakage. When heat leakage increases, the operating temperature decreases obviously. Compared with **Figure 14**, the increase in heat leakage leads to a temperature decrease from about 1160 to 970 K (case 8). Moreover, the heat leakage causes an obvious temperature gradient between the

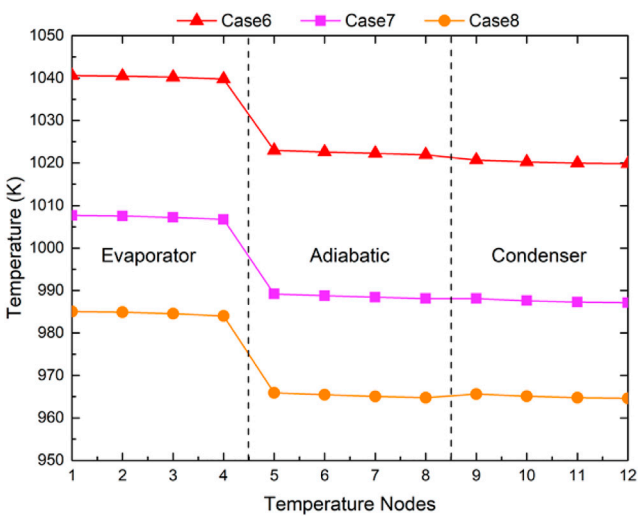

FIGURE 21 | Schematic diagram of heat leakage of the heat pipe.

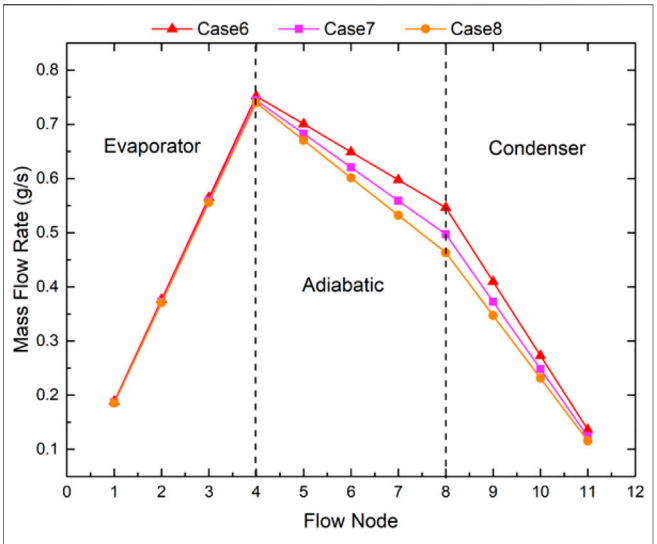

FIGURE 22 | Wall temperature distribution in different cases (2).

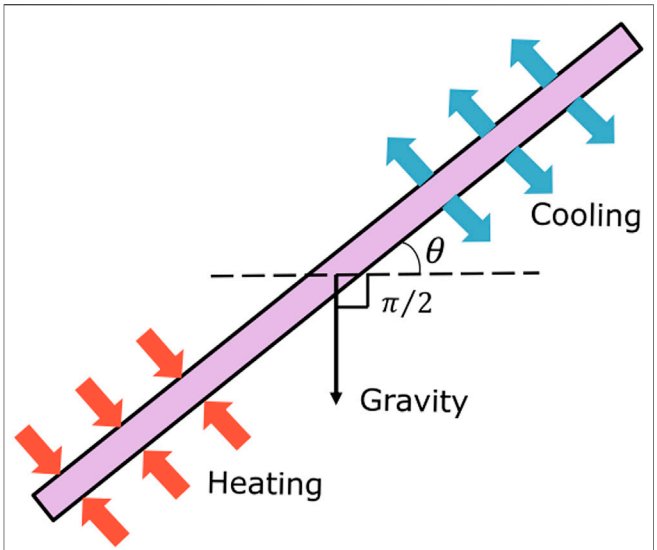

FIGURE 23 | Mass flow rate in the vapor space.

evaporator and the adiabatic section. Because of the poor insulation of the adiabatic section, it can be regarded as the "cold" source and the evaporator is the "heat" source. Therefore, the axial heat conduction causing a significant temperature gradient in the axial direction becomes non-negligible. As for heat conduction between the adiabatic section and the condenser, the temperature difference is inconspicuous because the heat transferred from the evaporator is mainly lost to the environment through the insulating layer rather than to the condenser, leading to a small temperature gradient. If the thermal conductivity of the insulating layer is high enough, the surface temperature in the adiabatic section will be even lower than that of the condenser, resulting in the reverse heat conduction from the condenser to the adiabatic section (cases 7 and 8).

From **Figure 22**, it can be found that because of the heat leakage, more condensation occurs in the adiabatic section, leading to the decrease of vapor flow in the condenser. The reduction of heat transfer in the condenser is the root cause of the temperature drop of the heat pipe. From these results, it can be concluded that it is essential to keep the heat preservation performance of the heat pipe system.

4.4 Case With Inclined Operation

For mobile power stations such as the eVinci reactor, an inclined operation may occur (**Figure 23**). In this section, the working medium flow and temperature distribution at different inclined angles are simulated, and the capillary limit of the heat pipe is judged.

From **Table 4**, the influence of gravity on the flow mainly shows in the pressure drop in the wick, but the influence on the vapor flow is not obvious. It is because the working medium in the wick is a high-density liquid, and the density of the vapor in the vapor space is low enough. When the angle is positive, gravity provides the effective pressure head for the flow, reducing the total pressure drop. The larger the inclination angle of the heat pipe, the more effective the pressure head is provided by gravity. Particularly, when the angle is 90°, the pressure drop in the wick is less than that in the vapor space. However, when the angle is negative, the working medium has to overcome the influence of gravity. According to the calculation, when the inclination angle is −30°, the total pressure drop of the working medium exceeds the pumping head of the

TABLE 4 | Pressure drop and heat transfer of a heat pipe at different inclined angles.

angle (◦)	Steam∇P (Pa)	Liquid∇P (Pa)	Total∇P (Pa)	Wall temperature in evaporator + (K)	Wall temperature in condensor + (K)	Capillary limit
0	896.678	8,422.472	9,319.150	1,171.545	1,149.754	NO
15	897.483	6,434.366	7,331.849	1,171.402	1,149.611	NO
30	898.141	4,529.731	5,427.872	1,171.403	1,149.611	NO
45	898.702	2,993.146	3,891.848	1,171.404	1,149.610	NO
60	899.139	1773.228	2,672.367	1,171.404	1,149.610	NO
75	899.412	1,006.355	1905.767	1,171.405	1,149.609	NO
90	899.505	744.789	1,644.294	1,171.405	1,149.609	NO
-15	896.070	10,407.946	11,304.016	1,171.401	1,149.613	NO
−30[a]	NULL	NULL	NULL	NULL	NULL	YES

[a]*When the angle is −30°, the capillary limit occurs.*
+Arithmetic mean value.

capillary, and the capillary limit occurs. It should be mentioned that the model is built on the assumption that gravity does not cause the redistribution of the working medium. In fact, this assumption may not be believable at a large inclined angle. When the inclined angle is large enough, the working medium will accumulate at the lower region, resulting in the increase of the working medium in the evaporator and a change in the vapor–liquid interface shape, affecting the actual heat transfer of the heat pipe.

5 CONCLUSION

The accurate calculation of heat pipes will affect the reliability of the analysis results of the heat pipe cooled reactor system. Based on the network method, an improved model is proposed. It can calculate more realistic temperature distributions and obtain information on fluid flow and pressure distribution.

For the high-temperature sodium heat pipe of 1.0 m length, based on the analysis, it can be concluded that non-uniform heating and cooling can change the temperature distribution of the heat pipe. The greater the non-uniformity is, the larger the temperature difference will be. When the heat leakage is obvious, it will not only reduce the operating temperature but also lead to a large temperature gradient between the evaporator and the adiabatic section. As for the gravity term, the influence on the flow depends on the inclination degree. When the angle is positive, gravity will provide an effective pressure head for the flow. When the angle is negative, the fluid needs to overcome its influence. When the inclination angle exceeds −30°, the heat pipe may reach the capillary limitation, and it may be damaged.

It should be highlighted that gravity may lead to the redistribution of the working medium in the heat pipe, which is ignored in this model. In the future, numerical analyses and experimental investigations of gravity effects on heat pipes will be carried out. Coupling simulation with the reactor core will also be investigated.

DATA AVAILABILITY STATEMENT

The original contributions presented in the study are included in the article/Supplementary Material, further inquiries can be directed to the corresponding author.

AUTHOR CONTRIBUTIONS

YG and ZL contributed to the conception and design of this study. ZS performed the statistical analysis. All authors contributed to the writing of the manuscript.

FUNDING

This research was funded by the National Key Research and Development Project of China, (No. 2020YFB1901700), the Science Challenge Project (TZ2018001), Project 11775126/11775127 by the National Natural Science Foundation of China, and the Tsinghua University Initiative Scientific Research Program.

REFERENCES

Alizadehdakhel, A., Rahimi, M., and Alsairafi, A. A. (2010). CFD Modeling of Flow and Heat Transfer in a Thermosyphon. *Int. Commun. Heat Mass Transfer* 37 (3), 312–318. doi:10.1016/j.icheatmasstransfer.2009.09.002

Annamalai, S., and Ramalingam, V. (2011). Experimental Investigation and CFD Analysis of a Air Cooled Condenser Heat Pipe. *Therm. Sci.* 15 (3), 759–772. doi:10.2298/tsci100331023a

Boothaisong, S., Rittidech, S., Chompookham, T., Thongmoon, M., Ding, Y., and Li, Y. (2015). Three-dimensional Transient Mathematical Model to Predict the Heat Transfer Rate of a Heat Pipe[J]. *Adv. Mech. Eng.* 7 (2), 1687814014567811. doi:10.1177/1687814014567811

Bowman, W. J. (1991). Numerical Modeling of Heat-Pipe Transients. *J. Thermophys. Heat transfer* 5 (3), 374–379. doi:10.2514/3.273

Busse, C. A. (1973). Theory of the Ultimate Heat Transfer Limit of Cylindrical Heat Pipes. *Int. J. Heat Mass Transfer* 16 (1), 169–186. doi:10.1016/0017-9310(73)90260-3

Cao, Y., and Faghri, A. (1993). A Numerical Analysis of High-Temperature Heat Pipe Startup from the Frozen State. *J. Heat Transfer* 115 (1), 247–254. doi:10.1115/1.2910657

Cao, Y., and Faghri, A. (1993). Simulation of the Early Startup Period of High-Temperature Heat Pipes from the Frozen State by a Rarefied Vapor Self-Diffusion Model. *J. Heat Transfer* 115 (1), 239–246. doi:10.1115/1.2910655

Cao, Y., and Faghri, A. (1991). Transient Two-Dimensional Compressible Analysis for High-Temperature Heat Pipes with Pulsed Heat Input. *Numer. Heat Transfer, A: Appl.* 18 (4), 483–502. doi:10.1080/10407789008944804

Cotter, T. P. (1965). *Theory of Heat pipes[M]*. Los Alamos Scientific Laboratory of the University of California.

El-Genk, M. S., and Tournier, J. M. (2004). Conceptual Design of HP-STMCs Space Reactor Power System for 110 kWe[C]. *AIP Conf. Proc. Am. Inst. Phys.* 699 (1), 658–672.

El-Genk, M. S., and Lianmin, H. (1993). An Experimental Investigation of the Transient Response of a Water Heat Pipe. *Int. J. Heat Mass Transfer* 36 (15), 3823–3830. doi:10.1063/1.1649628

Faghri, A. (1995). Heat pipe science and technology. *Fuel Energy Abst.* 36 (4), 285–285. doi:10.1016/0140-6701(95)95609-9

Faghri, A., and Harley, C. (1994). Transient Lumped Heat Pipe Analyses. *Heat Recovery Syst. CHP* 14 (4), 351–363. doi:10.1016/0890-4332(94)90039-6

Ferrandi, C., Iorizzo, F., Mameli, M., Zinna, S., and Marengo, M. (2013). Lumped Parameter Model of Sintered Heat Pipe: Transient Numerical Analysis and Validation. *Appl. Therm. Eng.* 50 (1), 1280–1290. doi:10.1016/j.applthermaleng.2012.07.022

Fink, J. K., and Leibowitz, L. (1995). *Thermodynamic and Transport Properties of Sodium Liquid and vapor[R]*. United States: N. p., 1995. Web. doi:10.2172/94649

Huang, L., El-Genk, M. S., and Tournier, J. M. (1993). Transient Performance of an Inclined Water Heat Pipe with a Screen Wick[J]. *ASME-PUBLICATIONS-HTD* 236, 87.

Kadak, A. C. (2017). *A Comparison of Advanced Nuclear technologies[M]*. Columbia University in the City of New York.

Kim, B. H., and Peterson, G. P. (1995). Analysis of the Critical Weber Number at the Onset of Liquid Entrainment in Capillary-Driven Heat Pipes. *Int. J. Heat mass transfer* 38 (8), 1427–1442. doi:10.1016/0017-9310(94)00249-u

Kumar, S. S., and Ramamurthi, K. (2001). Prediction of Thermal Contact Conductance in Vacuum Using Monte Carlo Simulation. *J. Thermophys. Heat transfer* 15 (1), 27–33. doi:10.2514/2.6592

Levy, E. K., and Chou, S. F. (1973). The Sonic Limit in Sodium Heat Pipes. *Heat Transfer* 95, 218–223. doi:10.1115/1.3450029

Lin, Z., Wang, S., Shirakashi, R., and Winston Zhang, L. (2013). Simulation of a Miniature Oscillating Heat Pipe in Bottom Heating Mode Using CFD with Unsteady Modeling. *Int. J. Heat Mass Transfer* 57 (2), 642–656. doi:10.1016/j.ijheatmasstransfer.2012.09.007

McClure, P., Poston, D., Rao, D., and Reid, R. (2015).*Design of Megawatt Power Level Heat Pipe Reactors*. Technical Report. Los Alamos, NM (United States): Los Alamos National Lab. LA-UR-15-28840.

Poston, D. I., Gibson, M., and McClure, P. (2019). "Kilopower Reactors for Potential Space Exploration Missions[C]," in Proceeding of the Nuclear and Emerging Techologies for Space, May 2019 (American Nuclear Society Topical Meeting. ANS.).

Poston, D. I. (2001). The Heatpipe-Operated Mars Exploration Reactor (HOMER) [C]. *AIP Conf. Proc. Am. Inst. Phys.* 552 (1), 797–804. doi:10.1063/1.1358010

Rice, J., and Faghri, A. (2007). Analysis of Screen Wick Heat Pipes, Including Capillary Dry-Out Limitations. *J. Thermophys. Heat transfer* 21 (3), 475–486. doi:10.2514/1.24809

Song, S., and Yovanovich, M. M. (1988). Relative Contact Pressure - Dependence on Surface Roughness and Vickers Microhardness. *J. Thermophys. Heat transfer* 2 (1), 43–47. doi:10.2514/3.60

Swartz, M. M., Byers, W. A., Lojek, J., and Blunt, R. (2021). "Westinghouse eVinci™ Heat Pipe Micro Reactor Technology Development[C]," in International Conference on Nuclear Engineering, October 2021 (American Society of Mechanical Engineers), 85246. V001T04A018.

Tournier, J.-M., and El-Genk, M. S. (1994). A Heat Pipe Transient Analysis Model. *Int. J. Heat Mass Transfer* 37 (5), 753–762. doi:10.1016/0017-9310(94)90113-9

Tournier, J. M., and El-Genk, M. S. (1996). A Vapor Flow Model for Analysis of Liquid-Metal Heat Pipe Startup from a Frozen State. *Int. J. Heat mass transfer* 39 (18), 3767–3780. doi:10.1016/0017-9310(96)00066-x

Xu, J. L., and Zhang, X. M. (2005). Start-up and Steady thermal Oscillation of a Pulsating Heat Pipe. *Heat Mass. Transfer* 41 (8), 685–694. doi:10.1007/s00231-004-0535-3

Yuan, Y., Shan, J., Zhang, B., Gou, J., Zhang, B., Lu, T., et al. (2016). Study on Startup Characteristics of Heat Pipe Cooled and AMTEC Conversion Space Reactor System. *Prog. Nucl. Energ.* 86, 18–30. doi:10.1016/j.pnucene.2015.10.002

Yue, C., Zhang, Q., Zhai, Z., and Ling, L. (2018). CFD Simulation on the Heat Transfer and Flow Characteristics of a Microchannel Separate Heat Pipe under Different Filling Ratios. *Appl. Therm. Eng.* 139, 25–34. doi:10.1016/j.applthermaleng.2018.01.011

Zuo, Z. J., and Faghri, A. (1998). A Network Thermodynamic Analysis of the Heat Pipe. *Int. J. Heat Mass Transfer* 41 (11), 1473–1484. doi:10.1016/s0017-9310(97)00220-2

Conflict of Interest: The authors declare that the research was conducted in the absence of any commercial or financial relationships that could be construed as a potential conflict of interest.

The handling editor (FM) declared a past co-authorship with one of the authors (WV).

Publisher's Note: All claims expressed in this article are solely those of the authors and do not necessarily represent those of their affiliated organizations, or those of the publisher, the editors and the reviewers. Any product that may be evaluated in this article, or claim that may be made by its manufacturer, is not guaranteed or endorsed by the publisher.

Copyright © 2022 Guo, Su, Li, Wang and Liu. This is an open-access article distributed under the terms of the Creative Commons Attribution License (CC BY). The use, distribution or reproduction in other forums is permitted, provided the original author(s) and the copyright owner(s) are credited and that the original publication in this journal is cited, in accordance with accepted academic practice. No use, distribution or reproduction is permitted which does not comply with these terms.

NOMENCLATURE

A area (m^2)

C specific heat capacity $(J/(kg \cdot K))$

$\mathbf{g}$ acceleration of gravity (m/s^2)

h specific enthalpy (J/kg)

k heat conductivity $(W/(m \cdot K))$

K permeability

L length (m)

P pressure (Pa)

q mass flow rate (kg/s)

Q heating power (W)

r radius (m)

R thermal resistance (K/W)

R_g gas constant $(J/(kg \cdot K))$

T temperature (K)

$Thick$ thickness (m)

u velocity (m/s)

V volume (m^3)

ρ density (kg/m^3)

μ dynamic viscosity $(Pa \cdot m)$

ε porosity

λ convective heat transfer coefficient $(W/(m^2 \cdot K))$

γ heat capacity ratio

Y variable vector

b weight coefficient vector

τ node coefficient vector

a coefficient matrix

Subscripts

pe wall region in the evaporator/radial direction (1)

pr radial direction (2)

pc wall region in the condenser/radial direction (3)

we wick region in the evaporator/radial direction (4)

wr radial direction (5)

wc wick region in the condenser/radial direction (6)

pa wall region in the adiabatic section/axial direction (1)

wa wick region in the adiabatic section/axial direction (2)

ve vapor space region in the evaporator

va vapor space region in the adiabatic section

vc vapor space region in the condenser

in insulating layer/inner radius/heat absorption

gap contact gap

$evap$ evaporationevaporator

$cond$ condensationcondenser

mv mass flow rate of vapor

ml mass flow rate of liquid

out outer radius

equ equivalent parameter

eff effective parameter

$evap$ evaporationevaporator

$adia$ adiabatic section

$cond$ condensationcondenser

f fluid

v vapor

w wick mesh

c capillary

frontiers | Frontiers in Energy Research

TYPE Original Research
PUBLISHED 10 August 2022
DOI 10.3389/fenrg.2022.859622

Check for updates

OPEN ACCESS

EDITED BY
Haomin Yuan,
Argonne National Laboratory (DOE), United States

REVIEWED BY
Jiankai Yu,
Massachusetts Institute of Technology, United States
Tengfei Zhang,
Shanghai Jiao Tong University, China

*CORRESPONDENCE
Yonghee Kim,
yongheekim@kaist.ac.kr

SPECIALTY SECTION
This article was submitted to Nuclear Energy, a section of the journal Frontiers in Energy Research

RECEIVED 21 January 2022
ACCEPTED 11 July 2022
PUBLISHED 10 August 2022

CITATION
Kim I, Kim I and Kim Y (2022), An iDTMC-based Monte Carlo depletion of a 3D SMR with intra-pin flux renormalization. *Front. Energy Res.* 10:859622. doi: 10.3389/fenrg.2022.859622

COPYRIGHT
© 2022 Kim, Kim and Kim. This is an open-access article distributed under the terms of the Creative Commons Attribution License (CC BY). The use, distribution or reproduction in other forums is permitted, provided the original author(s) and the copyright owner(s) are credited and that the original publication in this journal is cited, in accordance with accepted academic practice. No use, distribution or reproduction is permitted which does not comply with these terms.

An iDTMC-based Monte Carlo depletion of a 3D SMR with intra-pin flux renormalization

Inhyung Kim, Inyup Kim and Yonghee Kim*

Nuclear and Quantum Engineering, Korea Advanced Institute of Science and Technology, Daejeon, South Korea

Improved deterministic truncation of the Monte Carlo (iDTMC) solution method has been applied to neutronic depletion analyses of a nuclear reactor in this work. The theoretical background on the iDTMC method and material depletion calculation is briefly discussed, and the concept of an intra-pin renormalization scheme is presented to determine the detailed power and flux profiles with the pin-wise homogenized iDTMC solutions. The iDTMC method is applied and evaluated in a 100 MWth 3-dimensional small modular reactor (SMR) problem. Burnup-dependent multiplication factors, pin power distributions, and material densities are estimated by the iDTMC method and compared with the reference and standard Monte Carlo solutions. Numerical performance is investigated in terms of real standard deviation, root-mean-square and relative errors, computing time, and figure-of-merit. The numerical results demonstrate that the iDTMC method is superior to the standard MC method in estimating the burnup-dependent reactor eigenvalue and 3D pin-wise power distribution.

KEYWORDS

Monte Carlo method, iDTMC, p-CMFD, depletion analysis, intra-pin reconstruction

Introduction

A depletion calculation in nuclear reactor analyses is essential for evaluating burnup-dependent reactor parameters and material compositions of nuclear fuels. Recently, the Monte Carlo (MC) method has been extended to the depletion analysis in response to the demand for high-fidelity physics solutions (Romano et al., 2021; Haeck and Verboomen 2007; Ebiwonjumi et al., 2020; Davidson et al., 2018; A. Isotalo 2015). For a practical application of the MC method in commercial reactor problems, a whole core depletion calculation should be affordable in terms of memory and computing time. Despite of advances in computational resources, an intra-pin level burnup calculation in large-scale whole core problems is still excessively demanding.

Many research groups have studied to enhance the efficiency of the MC-based depletion calculation. Fission and surface source iteration algorithm has been suggested to efficiently utilize the given memory storage based on a domain decomposition approach (Y. G. Jo et al., 2020). In a multi-core cluster, each group of processors independently simulates particle sources within local domains evenly decomposing a whole core and

corrects the fission and surface sources by a non-blocking communication between the groups. The predictor-corrector method has been applied in the depletion analysis to improve the accuracy and stability of the established burnup calculation (A. E. Isotalo and Aarnio 2011; Dufek et al., 2013; Cosgrove, Shwageraus, and Parks 2020). This method solves multiple neutronic calculations at every depletion time step, and then it can provide corrected material compositions and neutron fluxes by considering continuously changing reaction rates over an interval. The Chebyshev rational approximation method (CRAM) has been popularly used in solving the exponential matrix to enhance the computational accuracy and efficiency by examining the characteristics of the eigenvalues of the burnup matrix (Pusa and Leppänen 2010; A. E. Isotalo and Aarnio 2011; Pusa 2016).

In the meantime, the amount of computational burden in Monte Carlo burnup calculation is largely consumed in the neutronic transport calculation than in the material depletion calculation in large-scale whole core problems. Reducing the numerical cost for the neutronic simulation is still strongly required for the practical and affordable whole core depletion analyses.

The improved deterministic truncation of the Monte Carlo solution (iDTMC) method has been previously developed to decrease the computing time and stochastic uncertainties for the steady-state MC eigenvalue analysis (Kim and Kim 2020; Kim, Kim, and Kim 2020; Kim and Kim 2022). It was shown that the iDTMC method can improve the accuracy and reliability of the pin-wise power and flux profiles compared to the conventional MC method. Recently, preliminary studies were carried out for the application of the iDTMC method to lattice (fuel assembly) depletion calculations (Kim and Kim, 2021a; 2021b).

In this study, the iDTMC method is applied to the depletion calculation in a small modular reactor (SMR) whole core problem. First, an overview of the iDTMC method and material depletion calculation is briefly presented, and the concept of an intra-pin flux renormalization scheme is provided. In numerical analysis, burnup-dependent criticalities, pin power distributions, and material densities through the burnup are estimated by an in-house MC code called iMC (Kim 2021) for both the standard MC and iDTMC approaches. Moreover, computational performance is evaluated by examining the real standard deviation (SD), root-mean-square (RMS) and relative errors, computing time, and figure-of-merit (FOM).

Methods

Improved deterministic truncation of Monte Carlo solution method

The iDTMC method is a numerical algorithm to reduce statistical uncertainty and computing time in the MC transport simulation by maximizing the utilization of deterministic solutions (Kim and Kim 2020; Kim and Kim 2021a; Kim and Kim 2022). The MC method can provide high-fidelity neutronic solutions, while the deterministic method is numerically cheap. Therefore, the accurate reactor solutions can be quickly calculated by strategically combining the deterministic and MC methods and employing the advantages of each method.

In the iDTMC method, the deterministic solutions are calculated by the partial-current coarse mesh finite difference (p-CMFD) method (Cho, 2012). The p-CMFD method is a nonlinear iterative acceleration scheme popularly used in neutronic analyses. This method can give MC-equivalent high-fidelity solutions by solving a one-group diffusion-like neutron balance equation with surface current correction. The one-group neutron balance equation can be simply expressed in the Cartesian coordinate:

$$\sum_i \frac{A}{V_i}\left(J_{i+1/2} - J_{i-1/2}\right) + \Sigma_a^i \phi_i = \frac{1}{k_{eff}} \nu\Sigma_f^i \phi_i \tag{1}$$

where i is the node index, A is surface area, V is the volume of the node, J is the net current, Σ_a is the absorption cross section, $\nu\Sigma_f$ is the fission cross section times the number of neutrons per fission, k_{eff} is the effective multiplication factor, and ϕ is the neutron flux. The net current can be represented by the partial currents, and the partial currents can be expressed by the neighboring neutron fluxes:

$$J_{i+1/2} = J_{i+1/2}^{+} - J_{i+1/2}^{-} = -\tilde{D}_{i+1/2}\left(\phi_{i+1} - \phi_i\right) + \hat{D}_{i+1/2}^{+}\phi_i - \hat{D}_{i+1/2}^{-}\phi_{i+1}, \tag{2}$$

where $\tilde{D}_{i+1/2}$ is the interface diffusion coefficient, and $\hat{D}_{i+1/2}$ are the correction factors:

$$\tilde{D}_{i+1/2} = \frac{2D_iD_{i+1}}{(D_i + D_{i+1})\Delta}, \text{ and} \tag{3}$$

$$\hat{D}_{i+1/2}^{\pm} = \frac{J_{i+1/2}^{\pm} \pm 0.5 \cdot \tilde{D}_{i+1/2}\left(\phi_{i+1} - \phi_i\right)}{\phi_{i+1/2 \mp 1/2}}. \tag{4}$$

The group constants for equation formation and the currents and fluxes for the correction factors are obtained from the MC simulation. Then, the subset of the eigenvalue equation can be derived in reference to the MC simulation. By solving the matrix equation, deterministic solutions such as the multiplication factor and neutron flux distribution can be obtained with a convergence tolerance of 1E-9 for the relative errors between criticalities.

In the iDTMC method, these deterministic solutions are used not only to accelerate the convergence of the fission source distribution but also to predict the system solutions. The assembly-wise p-CMFD calculation is implemented during inactive cycles coupled with the MC simulation. In this stage, the deterministic solutions update the fission source of the MC simulation by adjusting particles' weight. In the meantime, the pin-wise p-CMFD calculation is carried out during active cycles

to solely acquire the reactor solutions like the eigenvalue and detailed power distribution.

Depletion analysis

The isotopic changes can be characterized by the Bateman depletion equation taking into account neutron-induced reactions and spontaneous radioactive decay:

$$\frac{dN_i}{dt} = \sum_{i \neq j} \lambda_{ij} N_j - (\lambda_i + \phi\sigma_i) N_i, \tag{5}$$

where i and j are the indices for the nuclides, N_i is the concentration of nuclide i, λ_{ij} is the coefficient characterizing the production of the nuclide i from the nuclide j through decay, transmutation, and fission reactions, λ_i is the decay constant of the nuclide i, and σ_i is the disappearance cross section.

The first-order linear differential equations for the isotopes can be represented in a matrix form assuming the coefficients are constant in a time:

$$\mathbf{n}' = \mathbf{A}\mathbf{n}, \tag{6}$$

where $\mathbf{A}$ is the burnup matrix including the transmutation and decay coefficients of the nuclides and $\mathbf{n}$ is the isotope concentration vector. This equation can be solved by the matrix exponential method having the simple solution:

$$\mathbf{n}(t) = e^{\mathbf{A}t}\mathbf{n}_0, \tag{7}$$

where $\mathbf{n}_0 = \mathbf{n}(t = 0)$. In our study, the CRAM is applied to compute the matrix exponential solutions using the constant extrapolation method. Meanwhile, the burnup matrix is determined based on ORIGEN and ACE-formatted libraries (Rearden and Jessee 2018). The libraries contain one-group fission yields and decay characteristics for 1,306 nuclides, and the transmutation cross-section is tallied for 301 nuclides during the MC transport calculation.

In general, the burnup calculation of nuclear fuels in reactor cores is performed by sequentially solving the steady-state neutronics and changes of material compositions in a quasi-static manner. From the MC simulation, the one-group effective cross sections for each isotope are calculated and the one-group neutron flux is updated via the iDTMC method at every time step. These are used for the input parameters in the depletion calculation. The Bateman equation gives the material compositions and isotopic concentrations. Then, the MC simulation is again implemented with the changed materials. This process is repeated over a fuel depletion cycle.

Intra-pin renormalization scheme

In the neutronic depletion calculation, the material compositions and neutron flux are considered spatially constant within each burnup zone. However, in reality, nuclear fuels are pretty heterogeneous due to the spatial self-shielding effect particularly in a radial direction in terms of both the materials and neutron flux. Neutrons are mainly absorbed at the outer periphery of a fuel pellet resulting in the highest thermal flux at the rim and lowest one at the center, and this flux gradient also affects the distribution of fission products and fissionable nuclides. Therefore, fuel rods are generally divided into several rings for a reliable computer simulation of fuel depletion.

However, the iDTMC method only can provide the homogenized pin-cell flux distribution. The detailed flux distribution inside the fuel pin is essential to apply the iDTMC method to the neutronic depletion calculation. In this study, the intra-pin flux distribution on the designated geometry of the pin interior is reproduced with the iDTMC solutions by the intra-pin renormalization scheme (Nguyen and Kim 2018; Kim and Kim 2021b). A form function upon pin cells is calculated from the MC simulation, and then the intra-pin flux and power distributions are renormalized by adjusting the magnitude with the iDTMC solutions.

The form function is generated based on the MC flux distribution, and normalized for the summation to be unity at each pin cell:

$$ff_{i,r} = \frac{\phi_{i,r}^{MC}}{\sum_{r}^{N_r} \phi_{i,r}^{MC}}, \tag{8}$$

where i and r are the indices for the pin and ring nodes respectively, and N_r is the number of rings. When it comes to the number of rings, the fuel rod is generally divided into 1 to 5 rings and the burnable absorber rods are divided into 3 to 10 concentric rings. The flux distribution is normalized to the actual reactor power:

$$\phi_i^{iDTMC'} = C \cdot \phi_i^{iDTMC}, \tag{9}$$

where C is the normalization factor

$$C = \frac{P\ [\mathrm{MW}]}{\sum_i \kappa\Sigma_f^i \phi_i^{iDTMC} V_i\ [\mathrm{MeV}] \times 1.602\mathrm{E}-19}$$

Then, the intra-pin flux distribution on each pin cell can be finally calculated by multiplying the pin homogenized flux and form function as follows (see Figure 1):

$$\phi_{i,r} = ff_{i,r} \times \phi_i^{iDTMC'} \tag{10}$$

The neutron balance can be exactly preserved by the iDTMC method on each pin cell as well as the whole core.

Numerical results

Problem description

A small modular reactor (SMR) core has been considered for numerical analysis. The detailed configurations of the reactor

FIGURE 1
Intra-pin renormalization with the MC tally and iDTMC solution.

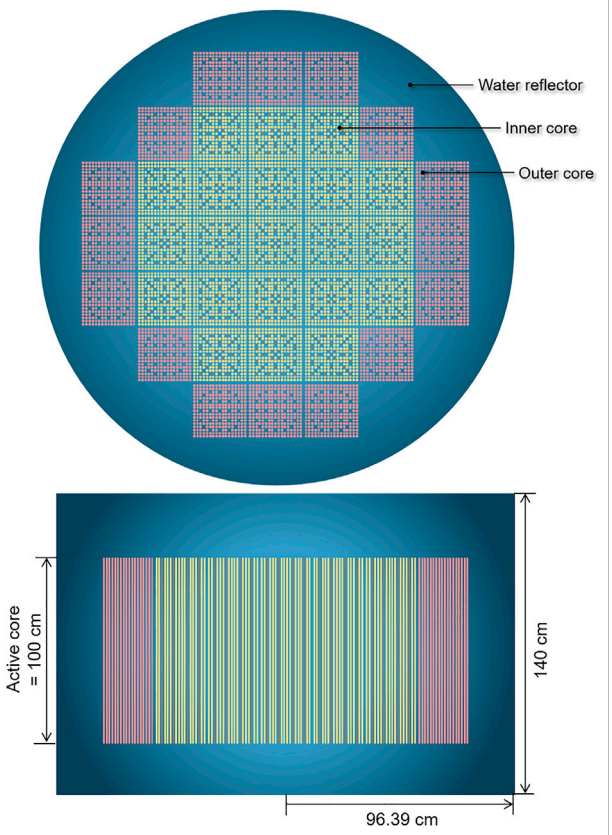

FIGURE 2
Configuration of SMR core; **(A)** radial **(B)** axial.

core are presented in Figures 2A,B. Total 37 fuel assemblies are loaded in the core. There are two different types of fuel assembly. One fuel assembly contains higher-enriched U fuel rods and Gadolinia (Gd_2O_3) burnable absorber pins, while the other one solely consists of lower enriched fuel rods. The fuel rods are arranged in a 17 by 17 array and the fuel assembly includes 25 guide tubes and 264 fuel rods. Among them, 24 fuel rods contain Gadolinia burnable absorbers as shown in Figure 3. The core is surrounded by a water reflector. The diameter and height of the core are 192.78 cm and 140 cm, respectively. The reactor power is 100 MW thermal. The detailed specifications of the SMR core can be found in Table 1.

The reactor core was depleted over 650 effective full power days (EFPDs) with a power level of 100 MWth. For the burnup calculation, the fuel pins are axially divided into 10 subdivisions by 10 cm. The fuel rods without the Gd_2O_3 burnable absorber are not divided radially in the standard MC and iDTMC calculations, while they are radially divided into 2 rings in the reference calculation for a more accurate solution. In the meantime, since the flux gradient is larger in the Gadolinia-loaded fuel rods due to the strong spatial self-shielding, those are radially divided into equivolumetric 5 rings to account for the spatial self-shielding effect.

Neutronic analysis has been implemented by an in-house MC code named iMC (Kim 2021) with ENDF/B-VII.1 nuclear data library (Chadwick et al., 2011). A reference solution was calculated with 30 inactive cycles, 200 active cycles, and 1,500,000 histories per cycle. For the standard MC and iDTMC methods, 30 inactive cycles, 10 active cycles, and 1,500,000 histories per cycle were used at every time step. For the estimation of the real SD of the reactor parameters, 20 independent batches were simulated with the different random seeds. All the calculations were carried out with a total of 112 cores of Xeon E5-2697.

Source convergence

The convergence of the fission source distribution has been characterized by the Shannon entropy. Figures 4A,B show the behavior of the Shannon entropy at the first (0 EFPD) and second (0.25 EFPD) time steps, respectively. The entropy value is highest at the first transport cycle because of uniformly distributed particles and gradually decreases along with the simulation at the first time step. The entropy in the standard MC method

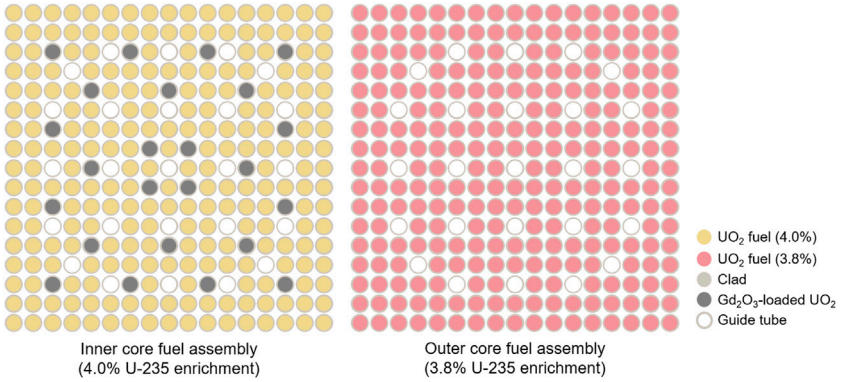

FIGURE 3
Detailed configuration of fuel assemblies.

TABLE 1 Specifications of the SMR core.

Parameters	Values
No. of fuel assemblies	37
Weight fraction of Gd_2O_3 in fuel	4%
Fuel pellet radius	0.5 cm
Pin pitch size	1.26 cm
Assembly pitch size	21.42 cm
UO_2 density	10.4 g/cm^3
Cladding thickness	0.3 mm
Cladding density	6.5 g/cm^3
Reflector	Water
Water density	0.9 g/cm^3
Reactor diameter	192.78 cm
Reactor height	140 cm
Reactor thermal power	100 MW

reaches a stationary state at around cycle 25, while the iDTMC method more quickly attains the source convergence at around cycle 15 due to the CMFD acceleration. The fission source distribution does not change significantly with the fuel burnup, so the entropy values are already close to the stationary state from the initial transport cycle after the first time step as shown in Figure 4B.

Burnup dependent criticality

The multiplication factors were calculated at certain time steps over 650 EFPDs. The SMR core was depleted with the short time bin at the beginning of the cycle to properly take into account the depletion of the burnable absorber and the buildup of the neutron-absorbing fission products. Figure 5 describes the burnup-dependent criticalities and the differences compared to the reference solution. The criticality quickly decreases over the early depletion steps due to Xe build-up, and gradually decreases after 10 EFPDs. The RMS error for the burnup dependent criticalities is estimated to be 12.8 pcm for the iDTMC method and 17.1 pcm for the standard MC method. In short, the iDTMC method shows a better agreement with the reference solution compared to the standard MC method.

The same reactor problem was also analyzed by Serpent 2.1.29 code (A. Isotalo and Sahlberg 2015; A. Isotalo 2015) for comparison, and the results are also given in Figure 5. For the Serpent calculation, 100 inactive cycles, 10 active cycles, and 1,500,000 particles per cycle were simulated. Although Serpent uses different fission yield and decay libraries from iMC and deals with a lot more nuclides including meta-stable isotopes, the iMC results are quite close to the Serpent values. The difference of criticalities between iMC and Serpent is 17.4 pcm for the initial condition. Since the one standard deviation of the multiplication factor is 5.6 pcm for the iMC reference and 20 pcm for the Serpent results, their results agree well within the stochastic uncertainty. The largest discrepancy between the iMC and Serpent through the depletion is only about 220 pcm.

Figure 6 shows the standard deviations of the burnup dependent multiplication factor. The reference solution provides the apparent SDs, while the standard MC and iDTMC methods give the real SDs estimated by the batch calculation. The apparent SD for the reference solution is estimated to be around 5 pcm on average. According to the figure, the iDTMC method clearly shows smaller stochastic uncertainties throughout the simulation than the standard MC. The average of values at each time step is estimated to be 9.4 pcm in the iDTMC method and 21.6 pcm in the standard MC method.

Meanwhile, the iDTMC method has shown the effectiveness of the early truncation of the MC solutions in many steady-state

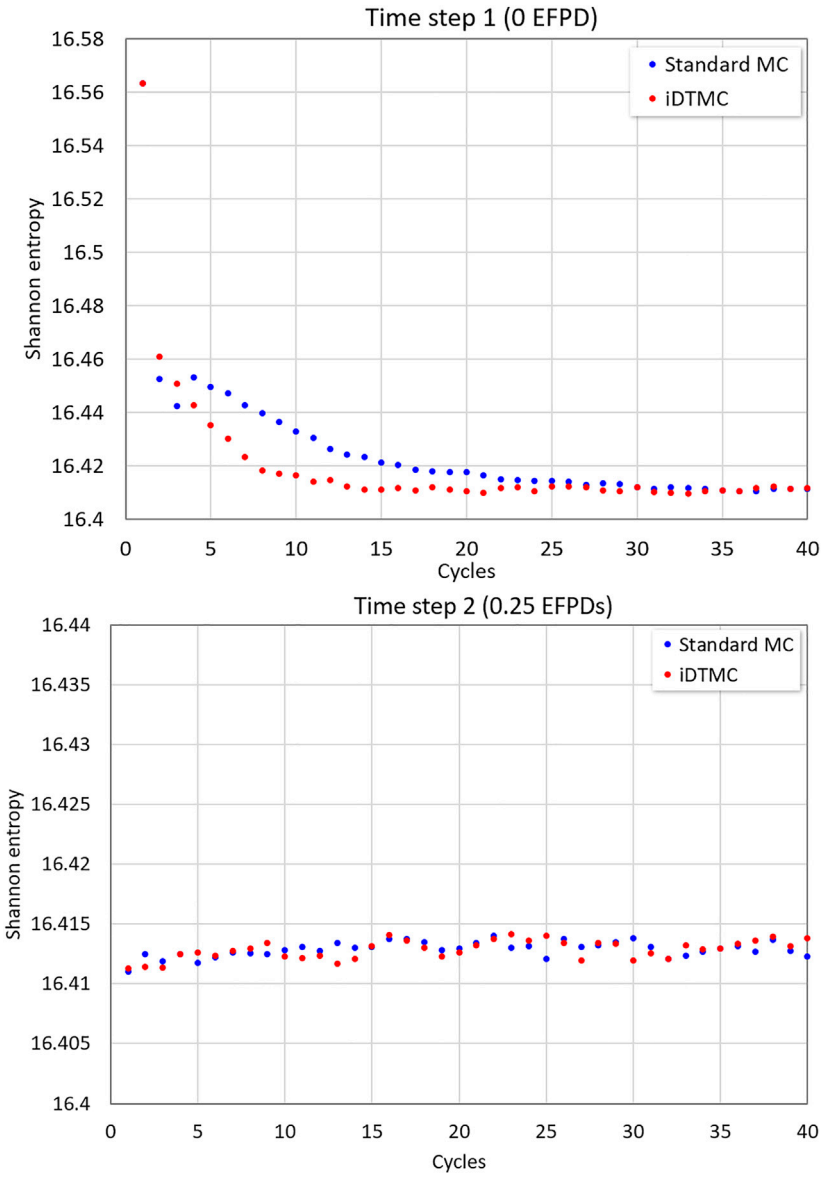

FIGURE 4
Shannon entropies at the different time steps; **(A)** 0 EFPD **(B)** 0.25 EFPD

neutronic analyses (Kim, Kim, and Kim 2020; Kim and Kim 2022). It means that the iDTMC method can provide accurate and reliable solutions even within 3 active cycles. This characteristic also has been evaluated in this depletion calculation by assessing the statistical errors at the different active cycles. Figure 7 describes the real SDs of the criticality at the specific active cycle 1, 3, 5, and 10, respectively. The standard MC method shows higher SDs at the earlier active cycles. On the other hand, the iDTMC method has consistently smaller SDs even from the early active cycles and seems not significantly affected by the number of active cycles. This implies that the computational burden for the active cycles can be possibly reduced by decreasing the number of cycles.

Power distribution

A 2-D pin power distribution has been evaluated and compared with each other. The original 3D powers were axially summed up and normalized for the average to be unity. Figure 8 describes the RMS and relative errors of the 2-D pin power profile. The RMS error is 3.2% in the standard MC

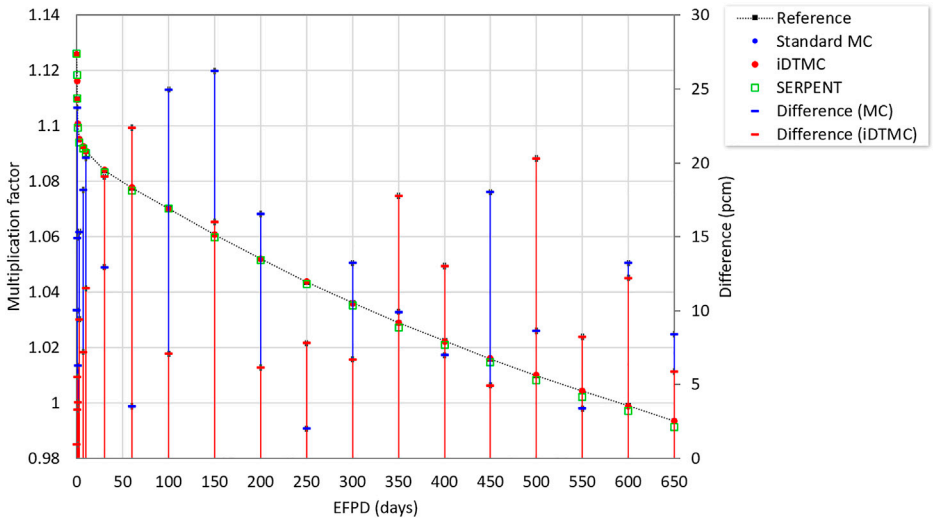

FIGURE 5
Burnup dependent criticalities of the SMR core problem.

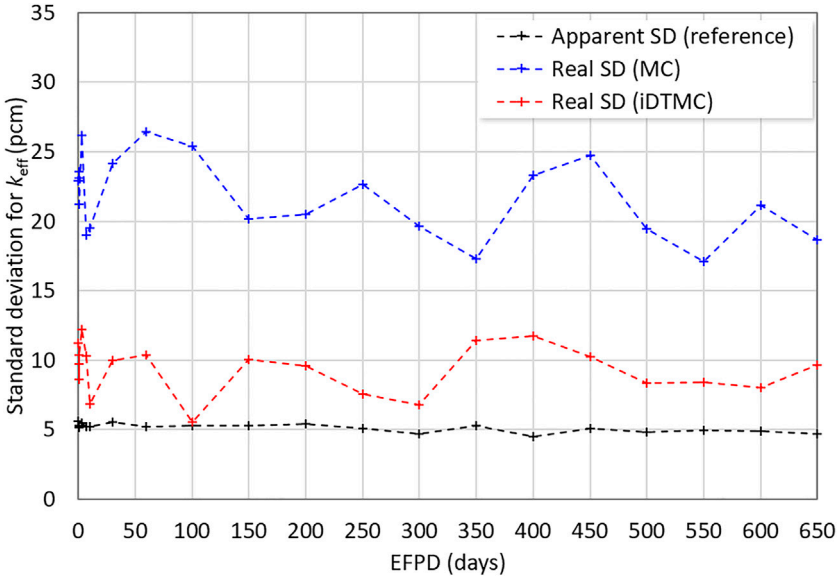

FIGURE 6
Standard deviations for burnup dependent criticality (active cycle 10)

and 2.1% in the iDTMC method. The maximum errors were reduced by 40% in the iDTMC method compared to the standard MC method. The pin power distribution was also calculated with the Serpent for comparison. The Serpent solution shows a 4% discrepancy from the iMC-based reference distribution in terms of the RMS errors.

Figure 9 shows the average of real standard deviations of the 2-D pin power distribution at each burnup step. The real standard deviation for the pin power was also calculated with 15 independent runs. The iDTMC method shows smaller stochastic uncertainties for the pin power distribution. The iDTMC method reduces the real standard deviation by 40%

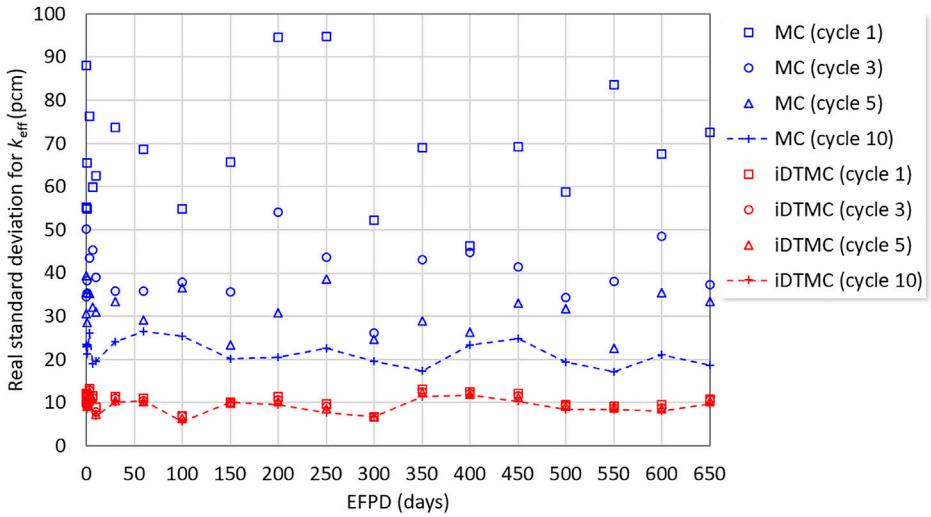

FIGURE 7
Real standard deviations for burnup dependent criticality at different active cycles.

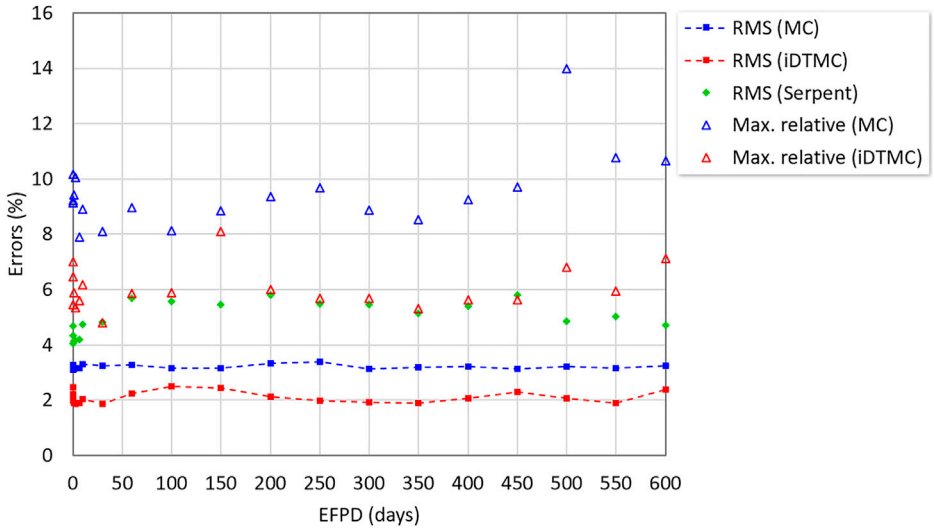

FIGURE 8
Errors for pin power distribution (active cycle 10)

compared to the standard MC method with the same calculation condition. Figure 10 shows the RMS errors for the 2-D intra-pin power distribution. The ring-wise intra-pin power distribution was normalized for the average to be unity. The iDTMC method has similar RMS errors with the standard MC method, indicating that the intra-pin power profile was properly determined by the intra-pin renormalization scheme.

The effectiveness of the early truncation of the MC solutions also has been assessed with the pin power profile. The RMS errors were estimated at the different active cycles (i.e. 1, 3, 5, and 10 cycles) in Figure 11. The RMS errors of the standard MC were more than 9% at the first active cycle and gradually decreased with the cycle accumulation. On the other hand, the RMS errors of the iDTMC method were already low from the first active cycle and slowly decreases with the active cycles. The iDTMC RMS errors of the pin-power profile are consistently lower than in the standard MC case in all active cycles and the difference gets smaller with active cycles.

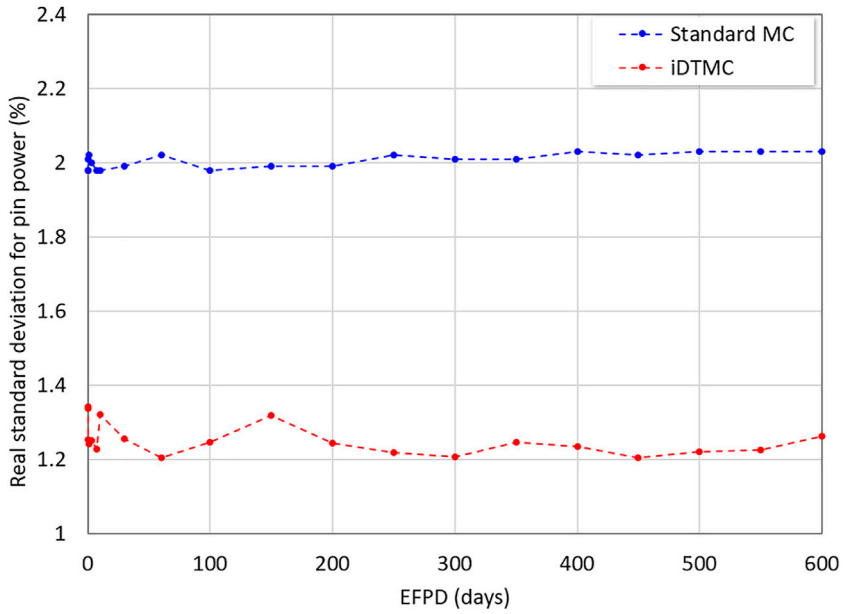

FIGURE 9
Average of real standard deviations for pin power (active cycle 10)

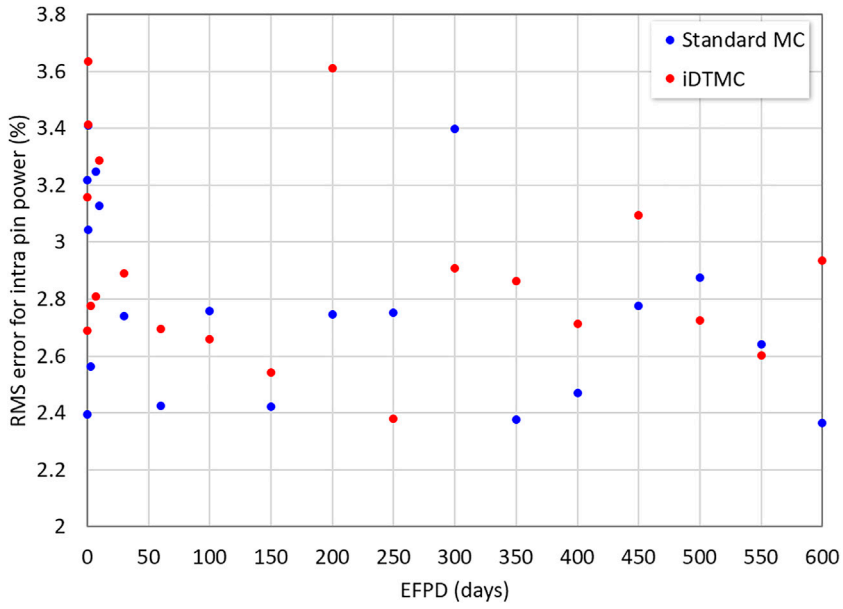

FIGURE 10
RMS errors for intra-pin power distribution (active cycle 10)

Material density

Figure 12 presents the change of the total number density of all the low-enriched uranium fuel rods for several nuclides. The number densities of the gadolinium, uranium, and plutonium isotopes were estimated and compared. U-235 was steadily depleted, while Pu-239 was quickly produced and reaches an equilibrium state. Gadolinium isotopes were

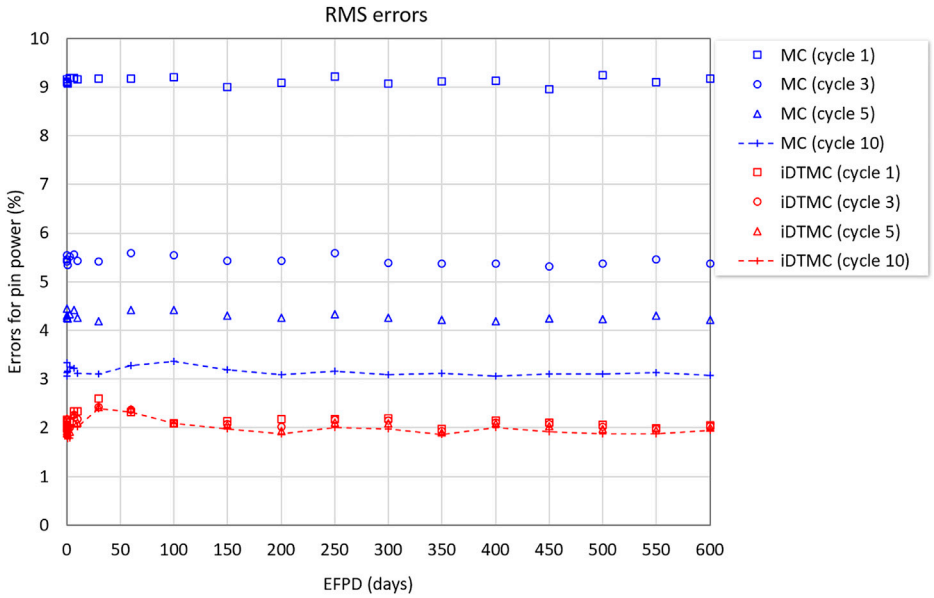

FIGURE 11
Cycle-wise RMS errors for the pin power profile.

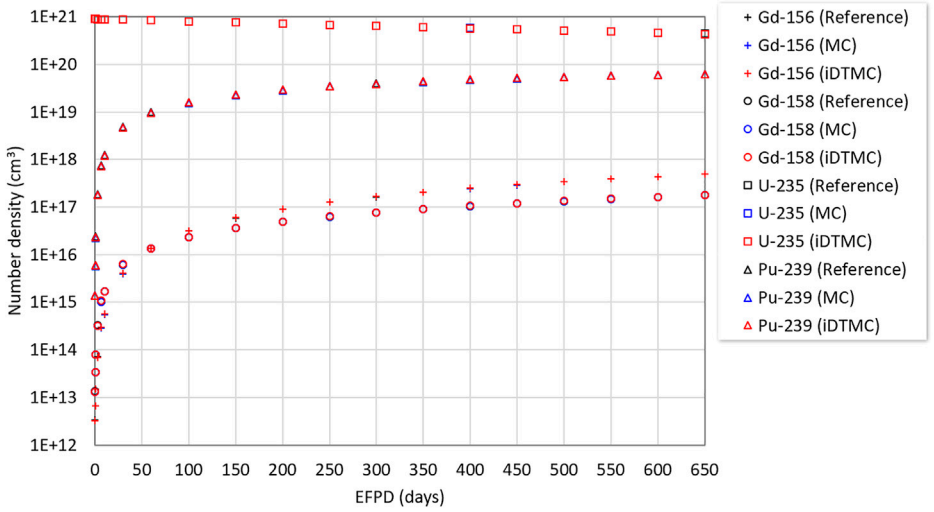

FIGURE 12
Number densities of the several isotopes in the fuel.

also quickly produced as fission products. The nuclide number densities are basically identical within the statistical uncertainties for the two schemes. The results prove that the production and loss of the nuclides in the reactor core have been correctly modeled by the standard MC and iDTMC calculations.

Numerical performance

Table 2 compares the computing time consumed during the transport and depletion calculations. The standard MC took 16.8 h, while the iDTMC method took 17.3 h. The iDTMC method requires a slightly more running time due to the additional deterministic

TABLE 2 Total computing time for the whole core depletion calculation.

Computing time (hr.)		Reference	Standard MC	iDTMC	Serpent
Transport	Inactive	21.1	9.4	9.8	—
	Active	208.8	4.6	4.8	—
	Total	229.9	14.0	14.5	22.6
Depletion		5.0	2.7	2.7	47.4
Total (transport + depletion)		234.9	16.8	17.3	70.0

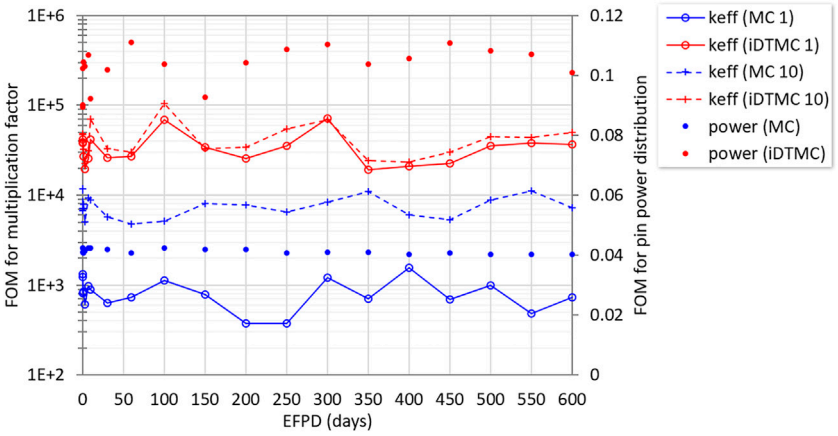

FIGURE 13
Figure of merits for the multiplication factor and pin power profile.

calculations, but it can be reckoned that the numerical overhead for the iDTMC calculation accounting for ~3% of the total time is affordable when considering the more accurate and reliable solutions. The computing time of the Serpent calculation is also included only for information, but the Serpent depletion calculation has not been optimized for the large-scale burnup problem involving more than 20,000 depletion zones, and a lot more nuclides are handled in the Serpent depletion.

The iDTMC method requires more memory for the deterministic calculation. The additional memory size necessary for the iDTMC calculation considerably depends on the problem size. In this SMR problem, the iDTMC method utilized 17.7 MB more memory than the standard MC method.

Lastly, numerical performance has been measured in view of the FOM for the multiplication factor and pin power as shown in Figure 13. The FOM was calculated with the real variance (σ^2) at the active cycle 10 and corresponding total transport computing time (T).

$$FOM = \frac{1}{\sigma^2 T}. \tag{11}$$

Although the computing time is longer in the iDTMC method, the iDTMC method significantly reduces the stochastic uncertainties. Therefore, the iDTMC method shows much bigger FOMs. The FOM of the iDTMC method is 5.2 times higher for the multiplication factor and 2.5 times higher for the pin power distribution.

The FOM of the multiplication factor is also calculated at the first active cycle to demonstrate the effectiveness of the early truncation in the iDTMC method. The iDTMC shows even higher FOM from the beginning of the active cycle. The FOM of the iDTMC method at the first active cycle is shown to be comparable to that at the active cycle 10. On the other hand, the FOM of the standard MC at the first active cycle is clearly lower than that of the 10th active cycle. The average FOM of the standard MC for the multiplication factor is 8.6E+2 at the first cycle and 3.5E+4 at the last cycle, while it is 7.6E+3 at the 1st cycle and 4.3E+4 at the 10th cycle for the iDTMC method, respectively. The iDTMC FOM is ~40 times higher at the 1st active cycle and ~6 times higher at the 10th cycle than that of the standard MC.

Conclusion

Improved deterministic truncation of the Monte Carlo solution (iDTMC) method has been applied to the neutronic

depletion calculation in a small modular reactor core problem. The intra-pin flux distribution has been properly determined by the renormalization scheme combined with the iDTMC solutions. From numerical analyses, the iDTMC method showed better agreement with the reference solution and superior numerical performance compared to the standard MC method. For the burnup dependent multiplication factors, the iDTMC method showed the smaller discrepancy on average and reduced the real standard deviation almost by 50%. In particular, the iDTMC method produced reliable solutions even from the first active cycle having consistently smaller stochastic uncertainties regardless of the number of active cycles. When it comes to the pin power distribution, the iDTMC method achieved a 40% reduction both in the stochastic uncertainties and errors. The average real standard deviations for the pin power distribution have been estimated to be 1.3% in the iDTMC method but 2.0% in the standard MC method. Moreover, the RMS error for the iDTMC method was shown to be 2.1%, while that for the standard MC method was shown to be 3.2%. In the meantime, the computing time is marginally longer in the iDTMC method due to the additional deterministic calculation. As a result, the iDTMC method provides quite larger FOMs in terms of the multiplication factor and pin power distribution.

Data availability statement

The raw data supporting the conclusions of this article will be made available by the authors, without undue reservation.

Author contributions

IK (1st author) and YK developed the theoretical basis. IK (1st author) performed the numerical simulations and IK (2nd author) helped performing the simulations. Both IK (1st author) and IK (2nd author) contributed to the final version of the manuscript with consultation of YK. YK supervised the project.

Funding

This work was supported by the National Research Foundation of Korea Grant funded by the Korean government NRF-2016R1A5A1013919.

Conflict of interest

The authors declare that the research was conducted in the absence of any commercial or financial relationships that could be construed as a potential conflict of interest.

Publisher's note

All claims expressed in this article are solely those of the authors and do not necessarily represent those of their affiliated organizations, or those of the publisher, the editors and the reviewers. Any product that may be evaluated in this article, or claim that may be made by its manufacturer, is not guaranteed or endorsed by the publisher.

Reference

Chadwick, M. B., Herman, M., Obložinský, P., Dunn, M. E., Danon, Y., Kahler, A. C., et al. (2011). ENDF/B-VII.1 nuclear data for science and Technology: Cross sections, covariances, fission product yields and decay data. *Nucl. Data Sheets* 112 (12), 2887–2996. doi:10.1016/j.nds.2011.11.002

Cho, N. Z. (2012). "The partial current-based CMFD (p-CMFD) method revisited," in Transactions of the Korean Nuclear Society, Gyeongju, Republic of Korea, October 25–26.

Cosgrove, P., Shwageraus, E., and Parks, G. T. (2020). Stability analysis of predictor-corrector schemes for coupling neutronics and depletion. *Ann. Nucl. Energy* 149, 107781. doi:10.1016/j.anucene.2020.107781

Davidson, Gregory G., Pandya, Tara M., Johnson, Seth R., Evans, Thomas M., Isotalo, Aarno E., Gentry, Cole A., et al. (2018). Nuclide depletion capabilities in the shift Monte Carlo code. *Ann. Nucl. Energy* 114, 259–276. doi:10.1016/j.anucene.2017.11.042

Dufek, Jan, Kotlyar, Dan, Shwageraus, Eugene, and Leppänen, Jaakko (2013). Numerical stability of the predictor-corrector method in Monte Carlo burnup calculations of critical reactors. *Ann. Nucl. Energy* 56, 34–38. doi:10.1016/j.anucene.2013.01.018

Ebiwonjumi, Bamidele, Lee, Hyunsuk, Kim, Wonkyeong, and Lee, Deokjung (2020). Validation of nuclide depletion capabilities in Monte Carlo code MCS. *Nucl. Eng. Technol.* 52, 1907–1916. doi:10.1016/j.net.2020.02.017

Haeck, W., and Verboomen, B. (2007). An optimum approach to Monte Carlo burnup. *Nucl. Sci. Eng.* 156 (2), 180–196. doi:10.13182/NSE07-A2695

Isotalo, Aarno (2015). Comparison of neutronics-depletion coupling schemes for burnup calculations-continued study. *Nucl. Sci. Eng.* 180 (3), 286–300. doi:10.13182/NSE14-92

Isotalo, Aarno, and Sahlberg, Ville (2015). Comparison of neutronics-depletion coupling schemes for burnup calculations. *Nucl. Sci. Eng.* 179 (4), 434–459. doi:10.13182/NSE14-35

Isotalo, A. E., and Aarnio, P. A. (2011). Higher order methods for burnup calculations with bateman solutions. *Ann. Nucl. Energy* 38, 1987–1995. doi:10.1016/j.anucene.2011.04.022

Jo, Yu Gwon, Kim, Hyeon Tae, Kim, Yonghee, and Cho, Nam Zin (2020). Whole-core depletion calculation using domain decomposed continuous-energy Monte Carlo simulation via McBOX with p-CMFD acceleration and inline feedback. *Ann. Nucl. Energy* 139, 107245. doi:10.1016/j.anucene.2019.107245

Kim, Inhyung (2021). "Development of a deterministic truncation of Monte Carlo solution for a pin-resolved nuclear reactor analysis,". KAIST, Ph.D. Dissertation.

Kim, Inhyung, Kim, Hyeon Tae, and Kim, Yonghee (2020). Deterministic truncation of the Monte Carlo transport solution for reactor eigenvalue and pinwise power distribution. *Nucl. Sci. Eng.* 194 (1), 14–31. doi:10.1080/00295639.2019.1654815

Kim, Inhyung, and Kim, Yonghee (2020). "A new deterministic truncation of Monte Carlo solution using decoupled fine-mesh finite difference method," in Proceedings of American Nuclear Society Winter Meeting, November 16–19. Online.

Kim, Inhyung, and Kim, Yonghee (2021a). "A study on reconstruction of intra fuel pin power and flux distribution with the IDTMC method in the Monte Carlo reactor analyses," in Transactions of the Korean Nuclear Society Spring Meeting, Jeju, Korea, May 13–14.

Kim, Inhyung, and Kim, Yonghee (2022). An improved deterministic truncation of Monte Carlo solution for pin-resolved nuclear reactor analysis. *Ann. Nucl. Energy* 166, 108723. doi:10.1016/j.anucene.2021.108723

Kim, Inhyung, and Kim, Yonghee (2021b). "Depletion analysis of fuel assembly with the IDTMC method," in Transactions of the Korean Nuclear Society Autumn Meeting, Changwon, Korea, October 21–22.

Nguyen, Xuan Ha, and Kim, Yonghee (2018). A study on reconstruction of intrapin power distribution in pinwise two-group diffusion analysis. *Nucl. Sci. Eng.* 189 (3), 224–242. doi:10.1080/00295639.2017.1394086

Pusa, Maria (2016). Higher-order Chebyshev rational approximation method and application to burnup equations. *Nucl. Sci. Eng.* 182 (3), 297–318. doi:10.13182/NSE15-26

Pusa, Maria, and Leppänen, Jaakko (2010). Computing the matrix exponential in burnup calculations. *Nucl. Sci. Eng.* 164 (2), 140–150. doi:10.13182/NSE09-14

Rearden, B. T., and Jessee, M. A. (2018). *SCALE code system. Ornl/Tm-2005/39*.

Romano, Paul K., Josey, Colin J., Johnson, Andrew E., and Liang., Jingang (2021). Depletion capabilities in the OpenMC Monte Carlo particle transport code. *Ann. Nucl. Energy* 152, 107989. doi:10.1016/j.anucene.2020.107989

frontiers | Frontiers in Energy Research

TYPE Original Research
PUBLISHED 02 September 2022
DOI 10.3389/fenrg.2022.875371

Check for updates

OPEN ACCESS

EDITED BY
Yue Jin,
Massachusetts Institute of Technology,
United States

REVIEWED BY
Jinyong Feng,
Massachusetts Institute of Technology,
United States
Pengcheng Zhao,
University of South China, China

*CORRESPONDENCE
Xiang Chai,
xiangchai@sjtu.edu.cn

SPECIALTY SECTION
This article was submitted to Nuclear Energy,
a section of the journal
Frontiers in Energy Research

RECEIVED 14 February 2022
ACCEPTED 11 July 2022
PUBLISHED 02 September 2022

CITATION
Li W, Guan C, Song H, Chai X and Liu X (2022), Numerical investigation of heat transfer characteristics of moderator assembly employed in a low-enriched uranium nuclear thermal propulsion reactor.
Front. Energy Res. 10:875371.
doi: 10.3389/fenrg.2022.875371

COPYRIGHT
© 2022 Li, Guan, Song, Chai and Liu. This is an open-access article distributed under the terms of the Creative Commons Attribution License (CC BY). The use, distribution or reproduction in other forums is permitted, provided the original author(s) and the copyright owner(s) are credited and that the original publication in this journal is cited, in accordance with accepted academic practice. No use, distribution or reproduction is permitted which does not comply with these terms.

Numerical investigation of heat transfer characteristics of moderator assembly employed in a low-enriched uranium nuclear thermal propulsion reactor

Wei Li, Chaoran Guan, Houde Song, Xiang Chai* and Xiaojing Liu

School of Nuclear Science and Engineering, Shanghai Jiao Tong University, Shanghai, China

The design of a nuclear thermal propulsion (NTP) reactor based on low-enriched uranium (LEU) requires additional moderator elements in the core to physically meet the critical requirements. This design softens the core energy spectrum and can provide more thermal neutrons for the fission reaction, but the heat transfer characteristics between the fuel and moderator assembly are more complex. Aiming at the typical LEU unit design, the heat transfer mathematical model is established using the principle of heat flow diversion and superposition. The model adopts the heat transfer relationship based on STAR-CCM+ simulation rather than the empirical expression used in the past literature to improve the applicability of the model. The heat transfer coefficients in the proposed model are evaluated under different Reynolds numbers and thermal power. The deviations between the proposed model and CFD simulation are analyzed. The results show that the calculation of the heat transfer coefficient between the proposed model and the CFD simulation maintains a good consistency, most of which are within 10%. It may provide a reliable and conservative temperature estimation model for future LEU core design.

KEYWORDS

low-enriched uranium, nuclear thermal propulsion, STAR-CCM+ simulation, heat transfer mathematical model, heat transfer coefficients

Introduction

The nuclear thermal propulsion (NTP) reactor has become a potential leading power option for NASA's crewed landing on Mars due to its much shorter transit time in a long-distance space mission (Hibberd and HEIN, 2021). NTP reactor designs are grouped into high-enriched uranium (HEU) and low-enriched uranium (LEU) designs according to the different enrichment of the nuclear fuel used. A few decades of the cold war between the United States and the Soviet Union had witnessed the amount of mature and effective numerical and experimental work (Belair et al., 2013; Khatry et al., 2019; Graham, 2020) on HEU design. However, recent efforts focus on designing a feasible engine that relies on

LEU fuel due to its lower cost and nuclear proliferation risk (Venneri and KIM, 2015a; Venneri and KIM, 2015b; Gates et al., 2018). In LEU design, moderator assembly is employed to cooperate with fuel assembly to support the whole structure and take some heat away. What is more, this design can slow down the fast neutrons produced from the latter and keep the system critical. These new LEU-based generations of NTP require geometrical modifications associated with the assemblies' thickness and pitch, as well as the core's length and configuration. These modifications may bring large uncertainties in using empirical models or correlations based on HEU design. Hence, it is essential to understand the influence of moderator assembly on heat transfer, which is required for a core design using a comprehensive analysis method involving neutronics, thermal-hydraulics, and dynamic characteristics of the NTP system.

Several numerical methods have been proposed to model NTP sub-elements over a few decades. Hall et al. (1992) analyzed the thermal-hydraulic performance of the gaseous flow using the KLAXON code. This was among the first computational sequences developed to study an NTP system. Nevertheless, only a simple 1D model was used to predict pressure distribution from the inlet of the reactor core to the exit of the converging-diverging nozzle. Cheng and Yen-Sen (2015) conducted 3D numerical simulations on NERVA-type engine FE using self-developed computational fluid dynamic code (UNIC). The simulation implemented a conjugate heat transfer (CHT) routine to couple the solid and flow regions. Husemeyer (2016) conducted the coupled neutronic-thermal-hydraulic analysis on a Pewee-type engine. The calculation routine relied on a self-developed 3D finite element method to capture temperature distributions across the core. However, most of the work above relied on empirical heat transfer correlations and focused on HEU objects instead of LEU ones. Recently, Wang and Kotlyar (2021) utilized a reduced-order 1.5D semi-analytic solution to implant the legacy heat transfer correlations for a 3D CHT numerical solver on the OpenFOAM platform. Moreover, the in-house 1.5D reduced-order solver, namely, THERMO, uses an inaccurate heat transfer model between fuel assembly and moderator assembly due to the current implementation limitation within THERMO (Krecicki and Kotlyar, 2020).

The purpose of this work is to introduce the heat transfer model of the LEU nuclear thermal propulsion assembly. The flow heat transfer in each coolant channel is simplified into one-dimensional axial heat transfer, characterized by the Newton cooling formula. The radial solid heat conduction is accurately expressed by a three-dimensional heat conduction equation. The heat conduction equation provides heat flux boundary conditions for axial convective heat transfer. The temperature distribution in the fuel assembly and moderating assembly can be obtained by solving the two heat transfer processes. This model can provide thermo-hydraulic compliance for the subsequent conceptual design of the core. Still, the accuracy of the model largely depends on the heat transfer coefficient in the expression. Therefore, referring to the empirical expression of legacy experimental data (Walton, 1992) and utilizing a large number of numerical simulations conducted by STAR-CCM+, the fitted heat transfer coefficient expressions are obtained, which covers as many working conditions as possible to improve the applicability of the correlation.

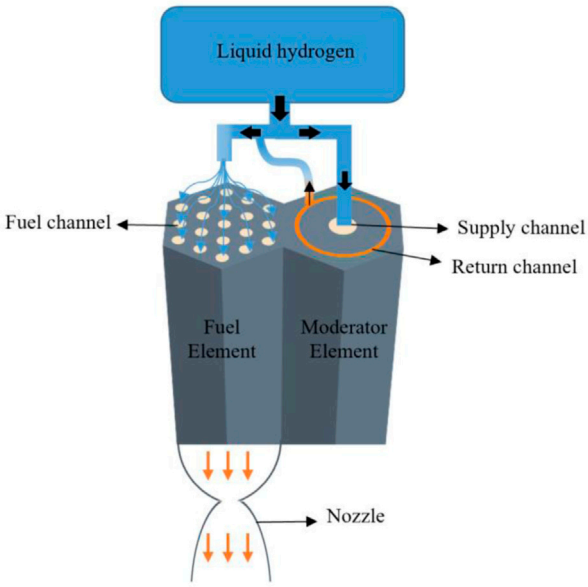

FIGURE 1
Schematic diagram of assemblies' structure and coolant flow within it.

Numerical configurations

Governing equation

The mathematical models in the calculation process comprise a continuity equation, a momentum equation, and an energy equation:

$$\frac{\partial \rho U_j}{\partial x_j} = 0 \tag{1}$$

$$\frac{\partial \left(\rho U_i U_j\right)}{\partial x_j} = -\frac{\partial P}{\partial x_i} + \frac{\partial}{\partial x_j}\left(\mu_{eff}\frac{U_i}{\partial x_j}\right) - \rho g_i \tag{2}$$

$$\frac{\partial \left(\rho U_j T\right)}{\partial x_j} = \frac{\partial}{\partial x_j}\left(\left(\frac{\mu}{Pr} + \frac{\mu_t}{Pr_t}\right)\frac{\partial T}{\partial x_j}\right) \tag{3}$$

where U, T, and P are velocity, temperature, and pressure, respectively. Pr and Pr_t are the Prandtl and turbulent Prandtl

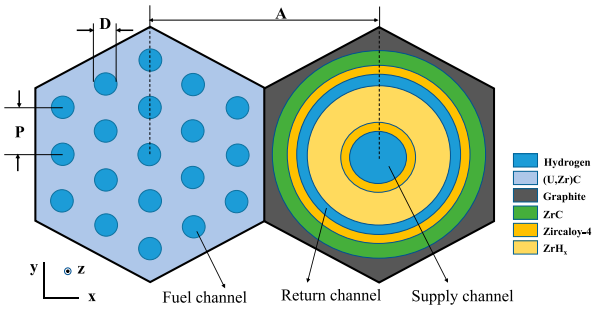

FIGURE 2
Schematic diagram of a hexagonal fuel and moderator assembly.

numbers, respectively. ρ is the density of the fluid, t is the time, and x is the Cartesian coordinate. In order to close the modeling, the effective viscosity, which is composed of laminar viscosity and turbulence viscosity, is calculated as follows:

$$\mu_{eff} = \mu + \mu_t \tag{4}$$

In the current study, the model proposed by Kays (1994) is employed to evaluate the value of the turbulent Prandtl number. Pe_t is the turbulent Peclet number indicating the relative importance of advective transport and diffusive transport:

$$Pr_t = 0.85 + \frac{0.7}{Pe_t} \tag{5}$$

The realizable k-ε two-layer model (Volkov, 2007) with all $y+$ wall treatment is adopted due to its robustness, accuracy, and computational efficiency. More details about the turbulence models and the corresponding wall treatment can be found in the user guide of STAR-CCM (Siemens Digital Industries Software, 2021).

Simulation domain

In the NTP system, as shown in Figure 1, part of the coolant (around 40% of total mass flow rate) flows out of the liquid hydrogen storage tank, first enters the supply channel at the lowest temperature, 35 K, and then flows back through the return channel from the bottom to top. After that, this part of the heated coolant merges with most of the initial coolant (around 60% of total mass flow rate) and flows through the fuel channel. Finally, the fully heated gas is ejected from the tail nozzle to generate thrust. It has been recognized that both fuel center temperature peaks and the moderator temperature peaks vary with the mass flow rate of hydrogen and heat power of the fuel assembly. However, an accurate prediction of peak temperature in the sensitive region remains a significant challenge due to the complex heat transfer mechanism involved in the two kinds of assemblies.

This study's fuel and moderator assembly geometry is based on the NERVA-derived design (Belair et al., 2013). The fuel assembly features 19 coolant channels with a diameter of 0.257 cm. The moderator assembly has seven layers from inside to outside: supply channel, inner cladding, ZrH_x, return channel, outer cladding, ZrC, and graphite, respectively. Figure 2 presents the fuel and moderator assembly geometry in detail, and Tables 1, 2 list their equivalent annulus dimensions.

Three different meshes were employed in the current study to consider the influence of the mesh resolution. As shown in Table 2, the number of meshes varied from 0.74 to 2.4 million, whereas the meshing diagram of case 2 is shown in Figure 3. The predicted results of the surface temperature of the diagonal line (z = 0.4445 m), as Figure 4 shows, clearly indicated that the influence of the mesh resolution could be neglected when the total number of meshes is more than 1.45 million. The third mesh is chosen in the current study. The total number of meshes is set to around 2.4 million. Based on this current mesh, the iteration convergence is analyzed in Figure 5. Figure 5A shows the fuel channel coolant temperature along with the line probes in the axial direction (x = 0.0001, y = 0) with different iterations by STAR-CCM+, whereas Figure 5B shows the temperature along with the diagonal line probes with different iterations by the software. Each case requires about 20,000 iteration steps to achieve a stable residual smaller than 10^{-4} for both momentum and energy equations.

The conductivity of graphite, ZrH_x, ZrC, and Zr was adapted from the work of Krecicki and Kotlyar (2020), (U, Zr)C, the nuclear fuel that we used in this study. Its density and conductivity come from Kubin and Presley (1964). The hydrogen material properties play a significant role in the simulation. Thus, almost all the properties are functions of temperature and pressure. The density of the hydrogen is referenced in Lyon (1973), and the other hydrogen properties such as dynamic viscosity, conductivity, and specific heat capacity were adapted by Bradley (2012).

Boundary conditions

The boundary conditions involved in coolant flow and solid heat conductions shown above are summarized in Table 3, which come from a typical case (Belair et al., 2013). As shown in Figure 6, 39.14% of the coolant first flows through the supply channel and return channels to protect the moderating assembly from overheating and ablating. Most coolant passes through fuel channels simultaneously and is heated to about 2,800 K (outlet temperature) in a small space and distance. The

TABLE 1 Assembly geometric dimensions.

	Items	Value, cm
Fuel assembly dimensions	Fuel assembly flat-to-flat, A	1.905
	Fuel assembly coolant channel diameter, D	0.257
	Fuel assembly pitch of coolant channel, P	0.441
	Length of the element, L	88.9
Moderator assembly equivalent annulus dimensions	Moderator assembly flat-to-flat	1.905
	Moderator assembly supply channel radius	0.2
	Moderator assembly supply channel cladding thickness	0.057
	Moderator ZrH_x thickness	0.393
	Moderator assembly return channel radius	0.08
	Moderator assembly return channel cladding thickness	0.057
	Moderator assembly insulator thickness	0.103

TABLE 2 Mesh independence analysis settings.

Case	Number of layers	Target surface size in fluid regions (mm)	Minimum surface size in fluid regions (mm)	Prism layer total thickness (mm)	Number of meshes
1	100	0.1	0.08	0.1	7,23,700
2	200	0.1	0.08	0.1	14,47,400
3	200	0.05	0.025	0.0125	23,98,600

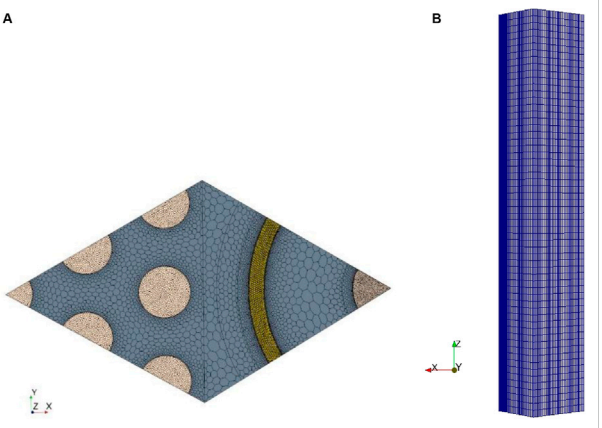

FIGURE 3
Mesh grids layout. **(A)** radial perspective. **(B)** axial perspective.

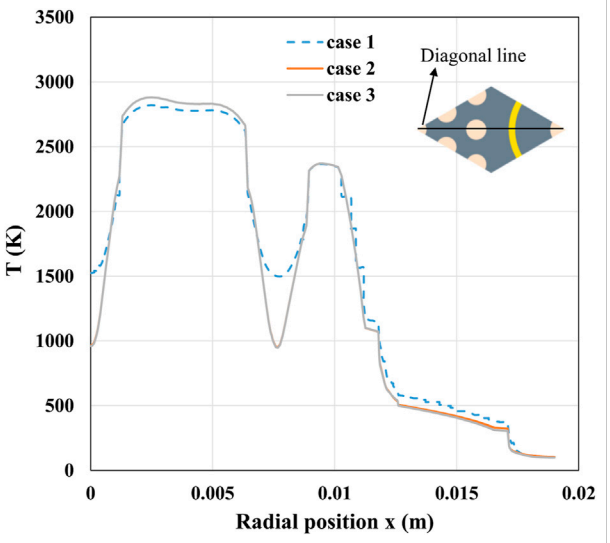

FIGURE 4
Temperature distribution on diagonal line at the half-length of the assemblies.

temperature span is so large that the influence of physical properties changing with temperature on the heat transfer process must be considered. Among them, hydrogen density and hydrogen-specific heat greatly influence the accuracy of the results. The specific heat as a function of temperature has been given in Bradley (2012). As for the density, this study uses the field function of STAR-CCM+ to accurately provide the density of hydrogen in the temperature range with drastic changes in physical properties.

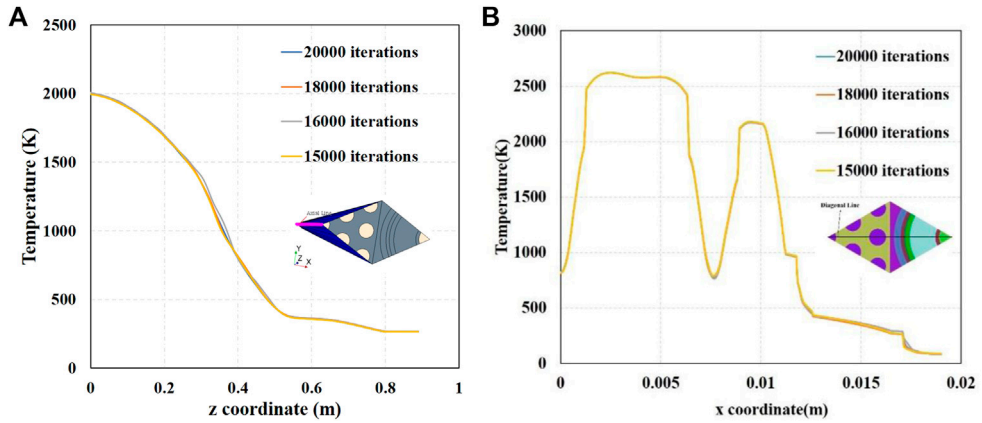

FIGURE 5
Temperature versus iterations. **(A)** axial distribution. **(B)** radial distribution.

TABLE 3 Summary of the boundary conditions.

Parameter	Unit	Value
Initial temperature of FE flow before mixing, T_0	K	35
Inlet temperature of the supply channel, T_{1_in}	K	35
Outlet temperature of the supply channel, T_{1_out}	K	—
Inlet temperature of the return channel, T_{2_in}	K	$h_{in_{return_{channel}}} = h_{out_{supply_{channel}}}$ $T_{2_in} = h^{-1}_{in_return_channel}(T)$
Outlet temperature of the return channel, T_{2_out}	K	
Inlet temperature of fuel channels, T_{in}	K	$h_{in} = \frac{\dot{m}_{FE_channel}h_1 + \dot{m}_{ME}h_2}{\dot{m}_{FE_channel} + \dot{m}_{ME}} T_{in} = h_{in}^{-1}(T)$
Power of each fuel assembly, Q	MW	0.1404
Inlet mass flow rate of the fuel channel, $\dot{m}_{FE_channel}$	kg/s	0.000162
Total mass flow per moderator assembly,$\dot{m}_{ME}$	kg/s	0.001208
Total mass flow rate per fuel assembly,$\dot{m}_{FE}$	kg/s	0.003078
Exit pressure of the fuel assembly, P_e	MPa	4

In the current case, the outlet temperature of the core is expected to be 2,800 K. Therefore, the power of the fuel assembly is 0.1404 MW based on energy conservation. Besides, a volumetric heat source with cosine distribution in the axial direction is employed in the simulation, which is considered closer to the reactor's actual power distribution. T_{in}, the inlet temperature of the fuel channel, can be evaluated by the following equation:

$$h_{in} = \frac{\dot{m}_{FE_channel}h_1 + \dot{m}_{ME}h_2}{\dot{m}_{FE_channel} + \dot{m}_{ME}} \tag{6}$$

where $\dot{m}_{FE_channel}$ is the mass flow rate of the fuel channel, $\dot{m}_{ME}$ the mass flow rate of the return channel, h_1 is the inlet enthalpy of the fuel channel, and h_2 is the outlet enthalpy of the return channel, respectively. The linear interpolation table is utilized in STAR-CCM+ to calculate the corresponding temperature, whereas the enthalpy of both the fuel channel and return channel is calculated by built-in functions.

Results and discussions

For NTP reactors, cores with different power levels are usually designed according to the mission to meet different mission requirements, such as a crewed lunar landing or crewed Mars landing. Different tasks correspond to different core power levels, and the fuel assembly as the basic unit of output power may operate at different power. It is essential to ensure that the fuel and moderator assembly operate safely within a reasonable power range. In order to ensure that the temperature does not exceed the limit,

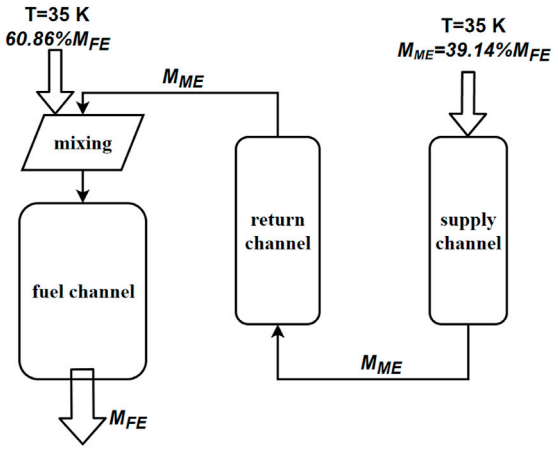

FIGURE 6
Flow distribution among the channels.

different output powers of components correspond to different flow characteristics (i.e., Reynolds number). As a typical case, the inlet Reynolds number of the simulation domain is around 1,00,000. According to this typical reference case (case 2), the other four cases are expanded, as shown in Table 4. In cases 1 and 3, the inlet Reynolds number is decreased and increased by 20%, respectively. In cases 4 and 5, 20% reduction and increment will occur, respectively, when the heating power is modified with other parameters of case 2.

Based on case 2, preliminary simulation can be first carried out by STAR-CCM+ to understand heat transfer between assemblies. Figures 7, 8 give the cross-sectional profiles of velocity (axial direction) and temperature at two assembly heights. They show that the velocity and temperature vary significantly among the channels, ranging from 23 to 537 m/s and from 45 to more than 2,200 K, respectively. The negative values shown in Figure 7 indicates that the fluid flow direction is perpendicular to the paper surface outward. The temperature of the coolant varies significantly in the axial direction. Therefore, the density, pressure, and speed vary greatly, and the speed of the drastic change, in turn, affects the temperature distribution. The influence between them is a two-way intense coupling process.

Significant temperature changes can be confirmed by the heat flow distribution in each component, as shown in Figure 9. It

TABLE 4 Simulation case settings considering different Reynolds numbers and heat power.

Cases	Heat power (W)	Inlet Re	Mass flow rate of fuel channel (kg/s)	Mass flow rate of return channel (kg/s)
1	140,400.7	80,000	0.0024647	0.0057880
2		100,000	0.0030808	0.0072350
3		120,000	0.0036970	0.0086821
4	112,320.6	100,000	0.0030808	0.0072350
5	168,480.8			

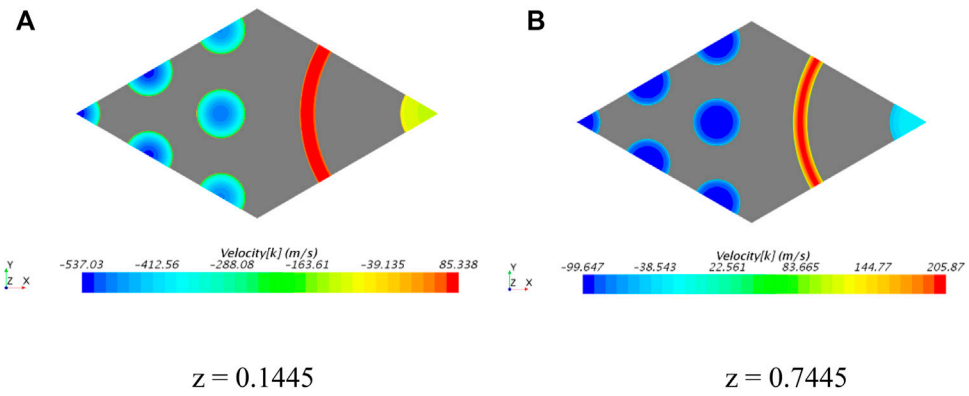

FIGURE 7
Cross-sectional profiles of velocity magnitude in case 2. **(A)** cross-sectional profile while height is equal to 0.1445. **(B)** cross-sectional profile while height is equal to 0.7445.

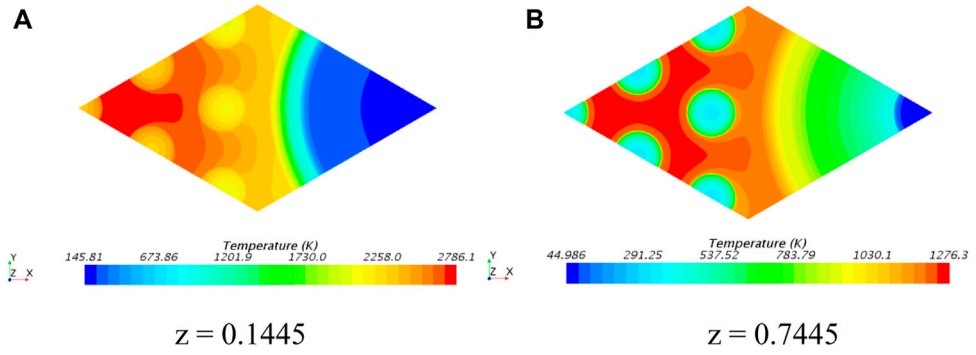

FIGURE 8
Cross-sectional profiles of temperature in case 2. **(A)** cross-sectional profile while height is equal to 0.1445. **(B)** cross-sectional profile while height is equal to 0.7445.

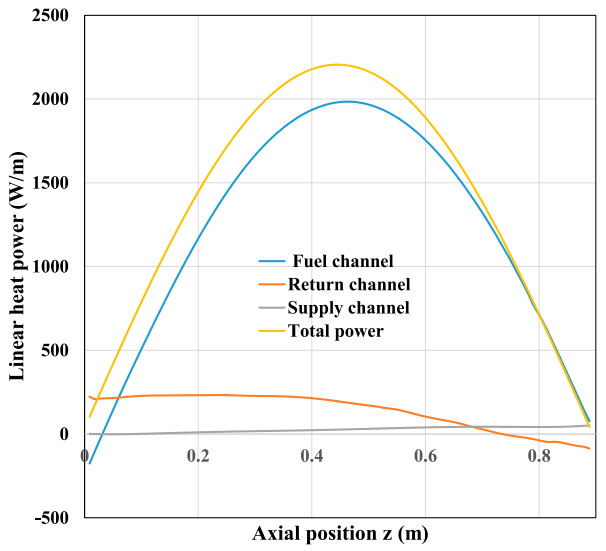

FIGURE 9
Axial linear heat power distribution of each channel in case 2.

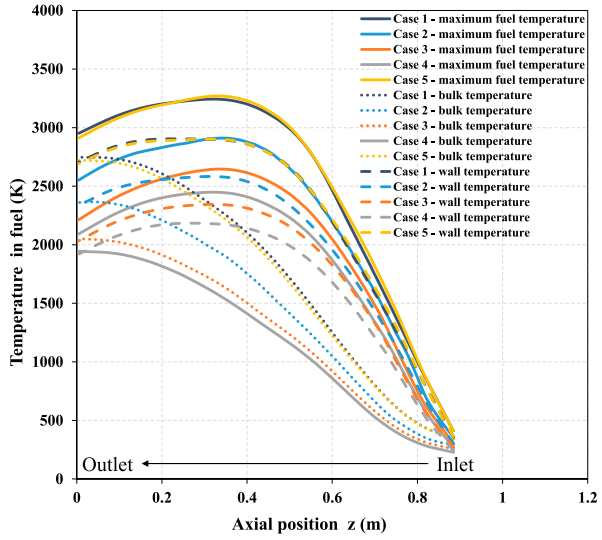

FIGURE 10
Maximum fuel center temperature, bulk temperature, and wall temperature in fuel channel vary among different cases.

shows axial linear heat power distribution of all channels, and it can be seen that most of the heat is taken away by the coolant in the fuel channel, so its temperature changes most violently, which can also be further confirmed by the axial temperature distribution of the fuel assembly, as shown in Figure 10. Besides, Figure 9 shows that the fuel assembly transfers heat to both the return channel and supply channel of the moderating assembly. The quantitative results show that this part of heat accounts for about 11.6% of the total. Moreover, the heating power of the return channel has some negative values near the outlet section, indicating that the coolant has an outward heat transfer process.

The reverse heat transfer can be seen from the axial distribution of the bulk and wall temperatures in the return channel, as shown in Figure 11, which also shows that the bulk temperature in the return channel increases and then decreases along the flow direction because the coolant flow direction of the return channel is contrary to that of other channels, which adds the complexity of finding the heat exchange law between assemblies. In case of the possible failure of the existing empirical correlation of heat transfer coefficient, it is necessary to establish a new inter-assembly heat transfer model. This model can be regarded as reliable for future core design by accurately predicting the fuel and moderator peak temperature. The above analysis reveals the general phenomenon of heat transfer between assemblies. However, the heat distribution in each channel and peak temperature inside the assembly under different working

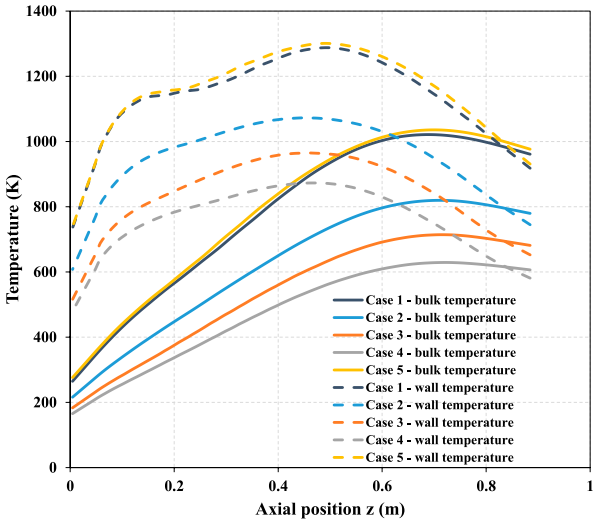

FIGURE 11
Bulk and wall temperatures in the return channel vary among different cases.

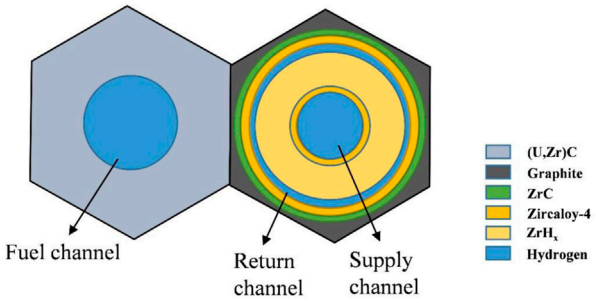

FIGURE 12
Schematic diagram of simplified assemblies.

conditions still need more profound concern. Before further discussion, a new heat transfer model between assemblies must be established. The following part will carefully deduce the heat transfer function based on the simplified axial convective heat transfer model and radial thermal resistance.

Figure 12 displays the equivalent FE and full ME model that preserves the hydraulic parameter and fuel volume. The equivalent FE model draws on the method by Wang and Kotlyar (2021). The method uses 1/19 of the full explicit FE model to get a conservative but quick result, although it is more suited for solving circular and annular pins instead of hexagonal prisms. As for the heat transfer mechanism between assemblies, different from the 1.5D conduction–convection solution (Krecicki and Kotlyar, 2020; Wang and Kotlyar, 2021), the current research focuses on deriving the heat transfer equations between the two assemblies according to the principle of heat flow diversion and superposition (Holman, 2010). Heat flux $Q_{2\to1}$ through the cylinder surface of the fuel channel can be deduced from the heat conduction differential equation and corresponding boundary conditions for the steady-state temperature distribution in the equivalent fuel assembly, shown as Eq. 7. In this equation, L represents the length of the assembly, k is the conductivity of fuel, T_2 means the maximum temperature of the fuel, $T_1$is the bulk temperature of the fuel channel, r_1 and r_2 are the equivalent fuel radius (distance from centroid to the position of maximum fuel temperature) and equivalent coolant channel radius, respectively. q_v is volumetric heat power. Eq. 7 contains two terms in total. The first term can be regarded as the heat flow generated by the internal and external temperature (T_1 on L_1 and T_2 on L_2) difference acting alone, and the second term can be regarded as the heat flow generated by the interval $[r_1, r_2]$ uniform heat source acting alone. Combining Eq. 7 with Newton's cooling theorem (Eq. 8) and eliminating T_1, Eq. 7 can be expressed as Eq. 9. The calculation $Q_{2\to3}$, the heat flux from the fuel to the moderator, is more complex than that of $Q_{2\to1}$ because the calculation process of $Q_{2\to1}$ is essentially a steady-state heat conduction problem of concentric rings with an internal heat source, and there are multi-layer structural materials between the return channel of moderator assembly and fuel assembly. Therefore, it is necessary to calculate the heat flux without an internal heat source. The sum of the two parts of heat flux is $Q_{2\to3}$, as shown in Eq. 10. In Eq. 10, T_3,is the temperature of the interface between fuel assembly and moderator assembly and r_3 is the equivalent radius of the fuel assembly. Combining Eq. 10 with Eq. 11 and eliminating the intermediate variable T_3, Eq. 12 can be obtained. In Eq. 12, T_{b4} is the bulk temperature of return channel. Δr_i, $i = 1, 2, 3$ are the corresponding thickness of graphite, ZrC, and Zr, respectively, and A_{li}, $i = 1, 2, 3, 4$ are the corresponding heat exchange area of graphite, ZrC, Zr, and ZrH_x, respectively:

$$Q_{2\to1} = \frac{2\pi Lk(T_2 - T_1)}{\ln r_2/r_1} + \frac{q_v \pi L r_1^2}{\ln r_2/r_1}\left\{\left(\frac{r_2}{r_1}\right)^2 \ln\frac{r_2}{r_1} - \frac{1}{2}\left[\left(\frac{r_2}{r_1}\right)^2 - 1\right]\right\} \quad (7)$$

$$Q_{2\to1} = hA(T_1 - T_{b1}) \quad (8)$$

$$Q_{2\to1} = \frac{(T_2 - T_{b1}) + \frac{q_v r_1^2}{2k}\left\{\left(\frac{r_2}{r_1}\right)^2 \ln\frac{r_2}{r_1} - \frac{1}{2}\left[\left(\frac{r_2}{r_1}\right)^2 - 1\right]\right\}}{\frac{\ln r_2/r_1}{2\pi Lk} + \frac{1}{h_1 A_2}} \quad (9)$$

$$Q_{2\to3} = \frac{2\pi Lk(T_2 - T_3)}{\ln r_3/r_2} + \frac{q_v \pi L r_2^2}{\ln r_3/r_2}\left\{\left(\frac{r_3}{r_2}\right)^2 \ln\frac{r_3}{r_2} - \frac{1}{2}\left[\left(\frac{r_3}{r_2}\right)^2 - 1\right]\right\} \quad (10)$$

$$Q_{2\to3} = \frac{T_3 - T_{b4}}{\frac{\Delta r_1}{k_1 A_{l1}} + \frac{\Delta r_2}{k_2 A_{l2}} + \frac{\Delta r_3}{k_3 A_{l3}} + \frac{1}{h_4 A_{l4}}} \quad (11)$$

$$Q_{2\to3} = \frac{(T_2 - T_{b4}) + \frac{q_v r_2^2}{2k}\left\{\left(\frac{r_3}{r_2}\right)^2 \ln\frac{r_3}{r_2} - \frac{1}{2}\left[\left(\frac{r_3}{r_2}\right)^2 - 1\right]\right\}}{\frac{\ln r_3/r_2}{2\pi Lk} + \frac{\Delta r_1}{k_1 A_{l1}} + \frac{\Delta r_2}{k_2 A_{l2}} + \frac{\Delta r_3}{k_3 A_{l3}} + \frac{1}{h_4 A_{l4}}} \quad (12)$$

$$Q_{fuel\ element} = Q_{2\to3} + Q_{2\to1} \quad (13)$$

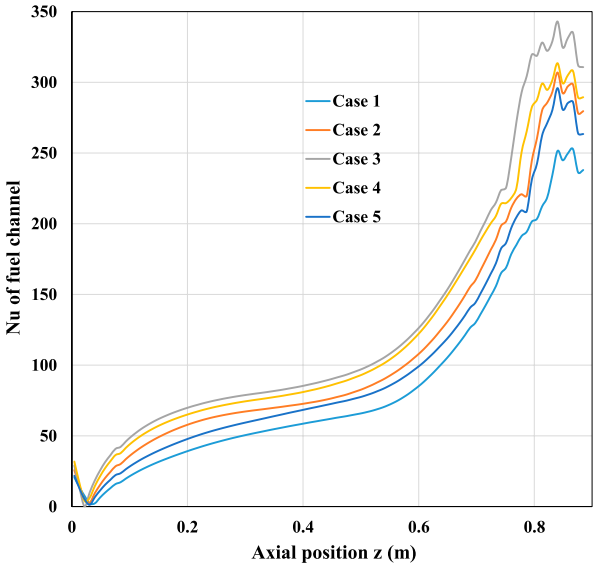

FIGURE 13
Axial distribution of the Nusselt number in fuel channel considering different Reynolds numbers and heat power.

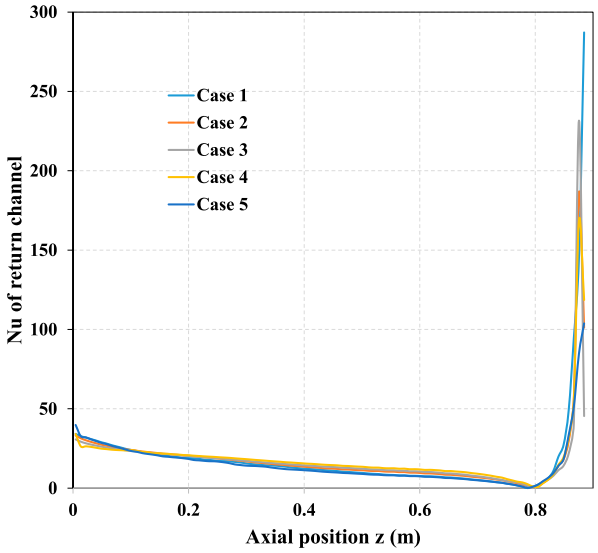

FIGURE 14
Axial distribution of the Nusselt number in the return channel considering different Reynolds numbers and heat power.

Eqs 9, 12 are only functions of the fuel center and bulk temperatures. If Eq. 13 is simultaneously used when the inlet and outlet temperature of the fuel channel and fuel assembly power (this is usually considered as boundary conditions) are known, the fuel center and bulk temperatures of the return channel can be calculated more conveniently. The maximum temperature limit of the fuel center is one of the criteria for future core design. Moreover, it is also essential to predict the maximum temperature of the moderator assembly, which can release the design margin of the coolant flow rate in the current LEU core design. Therefore, it is necessary to establish the relationship between the return channel's bulk temperature and the moderator's maximum temperature through STAR-CCM+ simulation so that the maximum temperature of the moderator can be predicted once the bulk temperature is known. Eqs 9, 12 provide an effective way to predict temperature, but the accuracy of the prediction depends on the selection of heat transfer coefficient. The usual practice is to select the empirical correction based on legacy experimental data. Nevertheless, it may not apply to LEU assembly, especially the flow and heat transfer of the return channel. In this work, the CFD method is used to simulate different working conditions, and the heat transfer coefficients are fitted from the simulation results concerning the form of general legacy empirical correction. The evaluated formula is substituted into Eqs 9, 12 for further calculations. The prediction effect evaluation will also be discussed subsequently.

Firstly, based on the CFD simulation, the Nusselt number distribution in the axial direction of the fuel channel under various working conditions is calculated, as shown in Figure 13. With the increase in height, the Nusselt number in the fuel channel increases gradually. The increase in Nu can be explained by the coolant flowing through the fuel assembly from top to bottom. With the decrease in height, the temperature difference between coolant and fuel gradually decreases, and the heat exchange process slows down. It is worth mentioning that when the coolant approaches the outlet, the Nusselt number first decreases and then increases, which is due to the outlet effect, and the bulk temperature of the fuel channel also presents a similar phenomenon.

Figure 14 shows that the Nusselt number in the return channel decreases slowly along the flow direction. However, when approaching the outlet section of the return channel, there is distortion in the Nusselt number curve due to the propellant flowing in two opposite directions in the fuel and return channels. The coolant in the fuel channel cools the fuel assembly from top to bottom. Thus, its temperature rises from top to bottom, as Figure 10 shows. Because the fuel power presents a cosine distribution in the axial direction, the fuel center temperature increases and decreases from top to bottom. Moreover, the fuel channel's coolant will make the fuel center's maximum temperature shift downstream along the axis. The coolant in the return channel cools the moderator assembly from bottom to top, and the temperature rises first and then decreases in Figure 11. Therefore, the so-called reverse heat transfer process will occur when the fuel center temperature drops below the return channel bulk temperature. This process occurs after about $z = 0.8$. Figure 15 shows that the linear heat flux has a negative

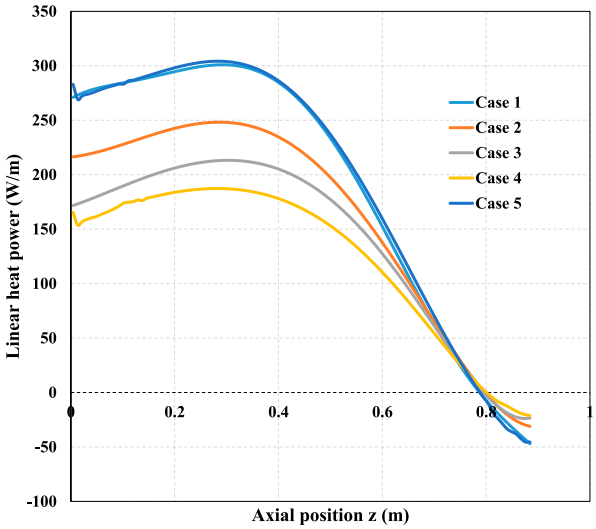

FIGURE 15
Axial linear heat power distribution of return channel considering different Reynolds numbers and heat power.

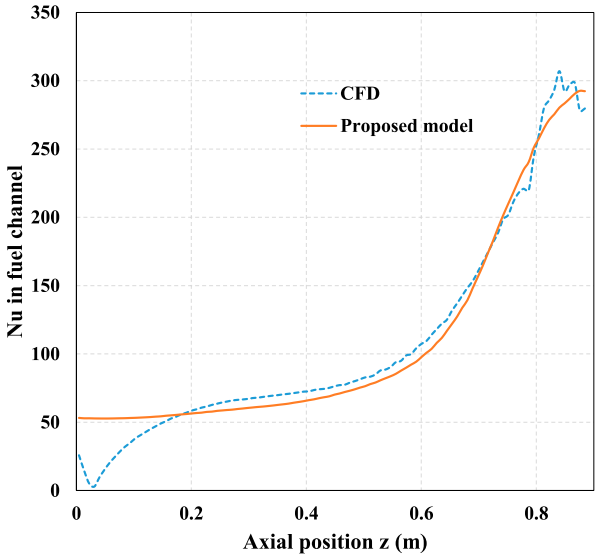

FIGURE 16
Nu calculation of the fuel channel in case 2.

value. Once reverse heat transfer occurs, the bulk temperature will continue to decrease, which can protect the moderator on the right from high-temperature damage. Further, for evaluating the heat transfer coefficient, only the heat transfer coefficient in the height range of 0–0.8 m can be considered without affecting the conservative estimation of the maximum temperature of the bulk temperature in the return channel.

$$Nu_{fuel\ channel} = 0.0095 \times Re_{b1}^{0.935} Pr_{b1}^{1.5236} \left(T_{w1}/T_{b1}\right)^{-0.0389}, \quad (14)$$

$$Nu_{return\ channel} = 0.023 \times Re_{b1}^{0.6257} Pr_{b1}^{1.3736} \left(T_{w4}/T_{b4}\right)^{0.742+1.3085*D_4/X} \quad (15)$$

Referring to the Dittus–Boelter correlation and approximating it according to the Nussle number curve in Case 2, the mathematical expression for the Nussle number can be obtained as shown in Eqs 14, 15, where Re_1 and Re_4 are the Reynolds numbers of the coolant in the fuel and return channels, Pr_1 and Pr_4 are the Prandtl numbers of the fuel and return channels, T_{w1} and T_{w4} are the wall temperature of the fuel and return channels, and T_{b1} and n are the bulk temperature of the fuel and return channels, respectively. Because the existing Dittus–Boelter correlation equation or Sieder–Tate equation is inapplicable to the operating conditions discussed in this study, our proposed correlation equation is equivalent to an extension of the Dittus–Boelter equation. These equations are all functions of independent variables, Re and Pr. For the expression of the Nusselt number in the return channel, the correction of the entrance effect as an exponential item is also considered. A Python script can realize this approximate process. With the two equations, the abovementioned closed calculation of Eqs 9, 13 can be carried out, and the assemblies' bulk temperature, wall temperature, and maximum fuel center temperature can be predicted conveniently and quickly with given boundary conditions. It can provide a convenient and fast calculation tool for reactor conceptual design. Nevertheless, from the Nusselt number curves shown in Figures 16, 17, the model curve should be consistent with the CFD calculation results as

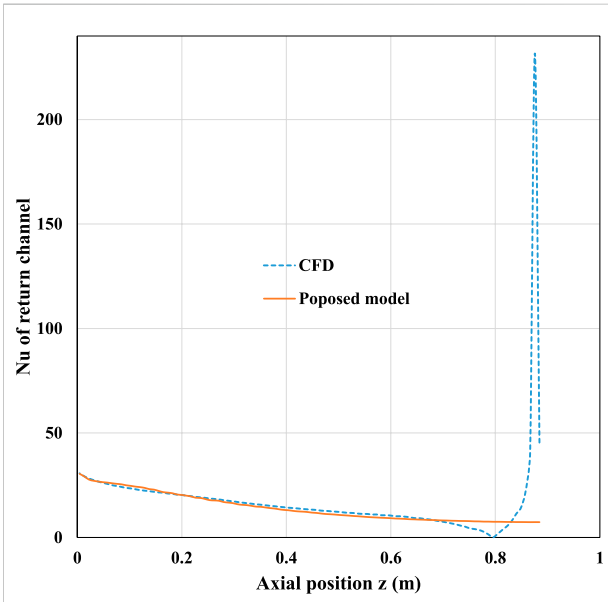

FIGURE 17
Nu calculation of the return channel in case 2.

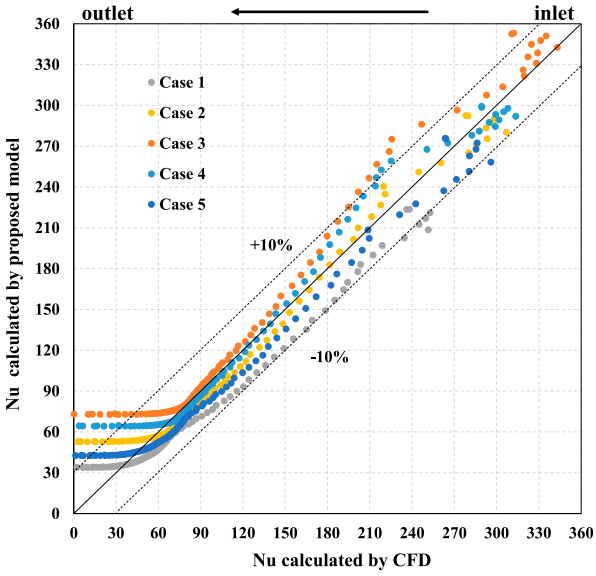

FIGURE 18
Comparison of the Nusselt number deviation in fuel channel by two methods.

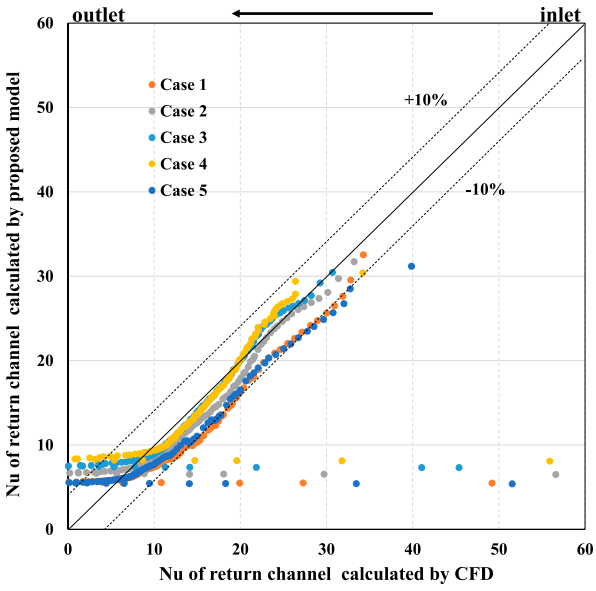

FIGURE 19
Comparison of the Nusselt number deviation in return channel by two methods.

much as possible. However, as the exit approaches, the consistency between the two models decreases, whether within the fuel or return channel.

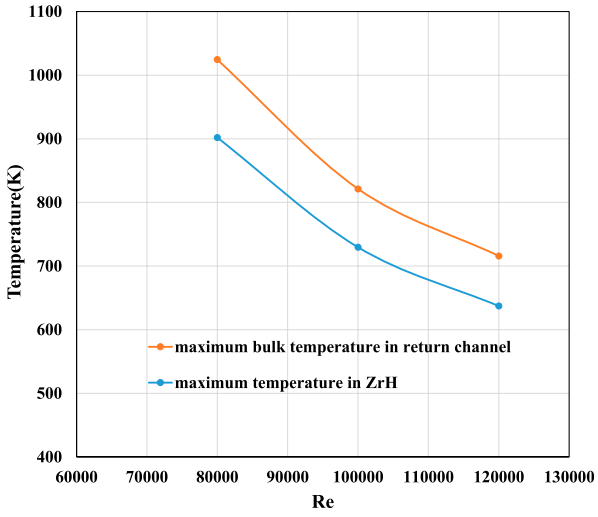

FIGURE 20
Maximum temperature comparison between return channel and ZrH_x.

Further analysis should be considered to prove the proposed model's reliability for temperature prediction. Firstly, the difference between the Nusselt number calculated by the two equations and the Nusselt number obtained by STAR-CCM+ numerical simulation is compared. Figures 18, 19 show that the deviations in the Nusselt number between the CFD model and the proposed model are mostly within 10%. The points with a relatively large coefficient deviation are located in the outlet section in the fuel channel. The height is less than 0.2 m, which can also be seen intuitively in Figure 16. In this area, the bulk and wall temperature difference first decreases and then increases. In other words, the bulk temperature increases slowly from low to high, and the wall temperature decreases slowly from high to low. When the two temperatures are approaching, the flow heat transfer capacity will decrease, leading to the falling of the heat transfer coefficient; the bulk temperature slightly exceeds the wall temperature in the approaching outlet section, where a reverse heat transfer process occurs. The heat transfer coefficient increases slightly, but this range is minimal (0–0.05 m), and the heat transfer coefficient changes little. For the two model coefficient evaluation curves in Figure 18, on the premise of ensuring that most of the deviation range is within 10%, the calculation curve of the heat transfer coefficient of the proposed model is lower than that of CFD, which can ensure a conservative estimation temperature prediction in this channel.

Heat transfer coefficient evaluation in the return channel should be considered as well. Figure 19 shows that the Nusselt number has a large deviation at the exit section. Therefore, the predicted value of the heat transfer coefficient in this narrow area

deviates greatly from the CFD result. Nevertheless, it does not affect the maximum temperature prediction of the return channel. Figure 11 shows that the bulk temperature in the return channel begins to drop at a height above 0.7 m. Thus, the prediction of the maximum bulk temperature of the return channel only needs to consider the temperature change at the height below 0.7 m. In addition, just like the evaluation of the heat transfer coefficient in the fuel channel, the return channel also ensures that the model calculation curve is lower than the CFD calculation curve, which can not only balance the deviation of the outlet section but also obtain the conservative prediction of the bulk temperature in the return channel.

The purpose of predicting the maximum bulk temperature of the return channel is to obtain a conservative estimate of the maximum ZrH_x moderator temperature. The limit of the maximum ZrH_x moderator temperature (around 1,000 K) is one of the criteria for the future NTP conceptual design. Figure 20 presents the maximum temperature comparison between the return channel and the ZrH_x moderator and shows that the maximum bulk temperature in the return channel is about 100 K higher than that of the ZrH_x moderator. There is a simple linear relationship between the two curves. Then, it can be concluded that it is appropriate to regard the prediction of the maximum bulk temperature of the return channel by the model as a conservative estimation of the maximum moderator temperature.

Conclusion

A simplified heat transfer model between LEU fuel assembly and moderator assembly is proposed by deriving the thermal resistance assumption between the assemblies. The model's correction evaluation of the heat transfer coefficient is conducted based on CFD simulations and legacy empirical formula. Furthermore, the calculation deviation of the model is calculated and analyzed under different Reynolds numbers and heating power. The results show that the model's evaluation curve of the axial distribution of heat transfer coefficient is in good agreement with the CFD calculation results, and the overall deviation of the axial distribution of heat transfer coefficient is less than 10%, whether in the fuel or return channel. The deviation near the outlet is large, but the overall evaluation curve is slightly lower than the CFD calculation curve to ensure that the temperature prediction of the model is conservative. The proposed model can be applied to the LEU core design in the future NTP concept design.

Data availability statement

The datasets presented in this article are not readily available because there are restrictions. Requests to access the datasets should be directed to WL, smartwei@sjtu.edu.cn.

Author contributions

WL: conceptualization, methodology, software, validation, formal analysis, data curation, visualization, and writing—original draft. CG: software, validation. HS: methodology, formal analysis, data curation. XC: supervision, conceptualization, investigation, resources, writing—original draft, writing—review and editing, project administration, and funding acquisition. XL: supervision, writing—review and funding acquisition.

Acknowledgments

The authors gratefully acknowledge the support provided by the National Key R&D Program of China under Grant no. 2020YFB1901900.

Conflict of interest

The authors declare that the research was conducted in the absence of any commercial or financial relationships that could be construed as a potential conflict of interest.

Publisher's note

All claims expressed in this article are solely those of the authors and do not necessarily represent those of their affiliated organizations or those of the publisher, the editors, and the reviewers. Any product that may be evaluated in this article, or claim that may be made by its manufacturer, is not guaranteed or endorsed by the publisher.

References

Belair, M. L., Sarmiento, C., and Lavelle, T. (2013). "Nuclear Thermal Rocket Simulation in NPSS," in proceedings of the 49th AIAA/ASME/SAE/ASEE Joint Propulsion Conference.

Bradley, A. (2012). Multiphysics design and simulation of a tungsten-cermet nuclear thermal rocket. Master's thesis. Texas A&M University. Available at: https://hdl.handle.net/1969.1/ETD-TAMU-2012-08-11649.

Cheng, G. C., and Yen-Sen, I. Y. (2015). Numerical Study of Single Flow Element in a Nuclear Thermal Thrust Chamber[J]. *J. Aeronautics Aerosp. Eng.* 04 (3).

Gates, J. T., Denig, A., Ahmed, R., Mehta, V., and Kotlyar, D. (2018). Low-Enriched Cermet-Based Fuel Options for a Nuclear Thermal Propulsion Engine. *Nucl. Eng. Des.* 33, 313–330. doi:10.1016/j.nucengdes.2018.02.036

Graham, C. (2020). The History of Nuclear Thermal Rocket Development [J]. *Reference Module Earth Syst. Environ. Sci.*

Hall, M. L., Rider, W. J., and Cappiello, M. W. (1992). Thermohydraulic Modeling of Nuclear Thermal Rockets: The KLAXON Code[J]. *Trans. Am. Nucl. Soc.*

Hibberd, A., and Hein, A. M. (2021). Project Lyra: Catching 1I/'Oumuamua–Using Nuclear Thermal Rockets. *Acta Astronaut.* 179, 594–603. doi:10.1016/j.actaastro.2020.11.038

Holman, J. P . (2010). *Heat Transfer*. Tenth Edition.

Husemeyer, P. J. A. (2016). *Design and Optimization of a Low-Enriched Uranium Nuclear Thermal Rocket Engine* (Cambridge, UK: Thesis for Doctoral Degree in Nuclear Engineering at University of Cambridge).

Kays, W. M . (1994). Turbulent Prandtl Number—Where Are We?[J]. *J. Heat. Transf.* 116 (2), 284–295. doi:10.1115/1.2911398

Khatry, J., Aydogan, F., Ilyas, M., and Houts, M. (2019). Modeling of Corrosion-induced Blockages on Radiation Heat Transfer by using RELAP5-3D. *Prog. Nucl. Energy* 112, 123–134. doi:10.1016/j.pnucene.2018.12.005

Krecicki, M., and Kotlyar, D. (2020). Low Enriched Nuclear Thermal Propulsion Neutronic, Thermal Hydraulic, and System Design Space Analysis[J]. *Nucl. Eng. Des.*, 363.

Kubin, R. F., and Presley, L. L. (1964). *Thermodynamic Properties And Mollier Chart For Hydrogen From 300deg k to 20,000deg k*. Washington, DC. Scientific and Technical Information Division, National Aeronautics and Space Administration.

Lyon, L. L. (1973). *Performance of (U,Zr)C-Graphite (Composite) and of (U,Zr)C (Carbide) Fuel Elements in the Nuclear Furnace 1 Test Reactor*. United States. doi:10.2172/4419566

Siemens Digital Industries Software (2021). *Simcenter STAR-CCM+, siemens*.

Venneri, P. F., and Kim, Y. (2015b). A Feasibility Study On Low Enriched Uranium Fuel For Nuclear Thermal Rockets – II: Rocket And Reactor Performance [J]. *Prog. Nucl. Energy*, 87.

Venneri, P. F., and Kim, Y. (2015a). A Feasibility Study On Low-Enriched Uranium Fuel For Nuclear Thermal Rockets – I: Reactivity Potential. *Prog. Nucl. Energy* 83, 406–418. doi:10.1016/j.pnucene.2015.05.003

Volkov, K. N. (2007). Application Of A Two-Layer Model Of Turbulence In Calculation Of A Boundary Layer With A Pressure Gradient. *J. Eng. Phys. Thermophys.* 80, 97–106. doi:10.1007/s10891-007-0013-0

Walton, J. T. (1992). *Program Elm: A Tool For Rapid Thermal-Hydraulic Analysis Of Solid-Core Nuclear Rocket Fuel Elements*. United States.

Wang, J. C., and Kotlyar, D. (2021). High-Resolution Thermal Analysis Of Nuclear Thermal Propulsion Fuel Element Using Openfoam[J]. *Nucl. Eng. Des.*, 372, 110957. doi:10.1016/j.nucengdes.2020.110957

Advantages of publishing in Frontiers

OPEN ACCESS
Articles are free to read for greatest visibility and readership

FAST PUBLICATION
Around 90 days from submission to decision

HIGH QUALITY PEER-REVIEW
Rigorous, collaborative, and constructive peer-review

TRANSPARENT PEER-REVIEW
Editors and reviewers acknowledged by name on published articles

Frontiers
Avenue du Tribunal-Fédéral 34
1005 Lausanne | Switzerland

Visit us: www.frontiersin.org
Contact us: frontiersin.org/about/contact

REPRODUCIBILITY OF RESEARCH
Support open data and methods to enhance research reproducibility

DIGITAL PUBLISHING
Articles designed for optimal readership across devices

FOLLOW US
@frontiersin

IMPACT METRICS
Advanced article metrics track visibility across digital media

EXTENSIVE PROMOTION
Marketing and promotion of impactful research

LOOP RESEARCH NETWORK
Our network increases your article's readership